University of Southampton
Faculty of Engineering, Science and Mathematics
School of Electronics and Computer Science

Development of a Micromachined Electrostatically Suspended Gyroscope

by

Badin Damrongsak

Thesis for the degree of Doctor of Philosophy

February 2009

UNIVERSITY OF SOUTHAMPTON

ABSTRACT

FACULTY OF ENGINEERING, SCIENCE AND MATHEMATICS
SCHOOL OF ELECTRONICS AND COMPUTER SCIENCE
Doctor of Philosophy

DEVELOPMENT OF A MICROMACHINED ELECTROSTATICALLY SUSPENDED GYROSCOPE

by Badin Damrongsak

In this thesis, a new approach based on an electrostatically suspended gyroscope (ESG) was explored in order to improve the performance of micromachined gyroscopes. Typically, a conventional micromachined gyroscope consists of a vibrating mass suspended on elastic beams that are anchored to a substrate. It measures the rotation rate of a body of interest by detecting rotation-induced Coriolis acceleration of a vibrating structure. Such a gyro is sensitive to fabrication imperfections and prone to cross-coupling signals between drive and sense modes, which degrade its performance. The micromachined ESG, on the other hand, employs a proof mass with no elastic beams connecting it to a substrate. The proof mass is levitated and spun electrostatically. In the presence of rotation, the spinning mass will rotate in the direction perpendicular to the spin and input axes. The displacement of the mass is capacitively sensed by a closed-loop electrostatic suspension system based on a sigma delta modulator (ΣΔM). The system, in turn, produces feedback forces to counteract the movement of the mass, moving it back to its nominal position. These feedback forces are equal to the precession torque and provide a measure of the rotation rate. Electrostatic levitation isolates the proof mass from unwanted inputs (for instance, mechanical friction, wear and stress), and thus the long-term stability of the gyroscope is expected to be improved. Furthermore, the micromachined ESG has a potential to achieve higher device sensitivity than that of a conventional vibrating-type micromachined gyroscope.

This thesis deals with three aspects of the development of the micromachined ESG: device design and analysis, design and simulation of an electrostatic suspension system and device fabrication. Analytical calculations and ANSYS simulations were carried out to predict the behaviour of the micromachined ESG. The micromachined ESG with an electrostatic suspension control system based on a sigma-delta modulator (ΣΔM) was modelled in Matlab/Simulink and OrCAD/PSPICE to evaluate the operation and performance of the closed-loop gyroscope. A front-end capacitive readout circuit was also developed. Initial tests were carried out and the measurement results showed a reasonable good agreement to both theoretical calculation and OrCAD/PSPICE simulation. The fabrication of the prototype micromachined ESG was developed using a triple-stack glass-silicon-glass anodic bonding in combination with a high-aspect-ratio DRIE process. Fabrication results and processing issues were discussed. However, it was found that the rotor of the fabricated gyroscopes was stuck to the substrate. Therefore, a fabricated prototype, which had not yet covered by a top substrate, was used to investigate an alternative approach to provide electrostatic levitation using sidewall electrodes. The analysis of this approach was investigated using 2D electrostatic finite element simulations in ANSYS. Initial tests were also carried out.

Contents

List of Figures

List of Tables

List of Abbreviations

2D	two dimensional
3D	three dimensional
AC	alternating current
ADC	analogue-to-digital converter
AM	amplitude modulation
APC	automatic pressure control
ARW	angle random walk
BOE	buffered oxide etch
BW	signal bandwidth
CPD	critical point dryer
DAC	digital-to-analogue converter
DAVED	decoupled angular velocity detector
DC	direct current
DI	deionised
DRIE	deep reactive ion etching
DSP	digital signal processing
EFAB	electrochemical fabrication developed by Microfabrica, Inc.
ESG	electrostatically suspended gyroscope
ESS	electrostatic suspension system
FFT	fast fourier transform
FLEMS	floating electromechanical system
FNA	fuming nitric acid
HAR	high aspect ratio
ICP	inductively coupled plasma
IFOG	interferometric fiber-optic gyroscope

IMU	inertia measurement unit
IPA	isopropyl alcohol
LIGA	the German acronym for X-ray lithography (X-ray Lithographie), electro-deposition (Galvanoformung), and molding (Abformtechnik)
LPF	low pass filter
LTO	low temperature oxide
MEMS	microelectromechanical system
MOEMS	micro-opto-electromechanical system
NASA	national aeronautics and space administration
NTF	noise transfer function
PCB	printed circuit board
PSD	power spectral density
RIE	reactive ion etching
RLG	ring laser gyro
RPM	revolution per minute
SBM	sacrificial bulk micromachining
sccm	standard cubic centimetre per minute
SDM	sigma delta modulator
SNR	signal to noise ratio
SOG	silicon on glass
SOI	silicon on insulator
SQNR	signal to quantisation noise ratio
STF	signal transfer function
STS	silicon technology systems
UV	ultraviolet

List of Symbols

A	area of a rotor
A_{fb}	total area of feedback electrodes
α	Coriolis acceleration
b	damping coefficient
B	angular squeeze film damping coefficient
BS	output bitstream
b_{slide}	slide film damping coefficient
BW	signal bandwidth
C_E	nominal capacitance formed between an excitation electrode and a rotor
C_f	feedback capacitance
C_{fb}	nominal capacitance formed between a feedback electrode and a rotor
C_r	nominal capacitance formed between a rotation electrode and a rotor
C_s	nominal capacitance formed between a sense electrode and a rotor
C_s	transfer function of a phase compensator
C_{sw}	nominal capacitance formed between a sidewall electrode and a rotor
d_0	nominal separation gap between a rotor and a sidewall electrode
Δf	signal bandwidth
dx	displacement of the rotor along the x axis
dy	displacement of the rotor along the y axis
ε	dielectric constant of a material (= 8.854×10^{-12} F/m for air)
ϕ	angular displacement of a rotor about the x axis with respect to a substrate
f_c	cutoff frequency
F_{cor}	Coriolis force
F_d	driving force

$F_{e,z}$	vertical levitation force
f_{in}	input signal frequency
F_n	force generated by Brownian noise
F_{net}	resultant electrostatic force acting to a rotor
f_s	sampling frequency
F_{z0}	net vertical levitation force per unit length
g	acceleration due to gravity (9.8 m/s^2)
G_{ina}	gain of an in-amp circuit
g_n	mechanical noise floor (µg/Hz$^{1/2}$)
γ_z	geometry factor
h	rotor thickness
I	moments of inertia of a rotor
k	electrode geometry
k	spring constant
K	angular squeeze film stiffness
k_B	Boltzmann’s constant (1.38×10^{-23} N·m/K)
k_c	capacitance-to-voltage sensitivity of a front-end circuit
k_F	feedback gain
k_{fb}	feedback gain
k_{po}	front-end gain
k_Q	quantiser gain
m	mass of a sensing element
μ_{eff}	effective viscosity
M_{motor}	motive torque
M_n	mechanical noise introduced by Brownian motion of a rotor
M_x	precession torque
p	pole frequency in radian per second
P_o	ambient pressure
Q	quality factor

θ	angular displacement of a rotor about the y axis with respect to a substrate
θ_0	maximum amplitude of a driving angular displacement
θ_1	angle of a fin of a rotor
θ_2	angle of a hole of a rotor
$\theta_{overlap}$	overlap angle (in degree unit) between a rotor and a stator electrode
ρ	density of a rotor material
R_{di}	inner radius of a rotation control electrodes
R_{di}	inner radius of a rotation control electrode
R_{do}	outer radius of a rotation control electrodes
R_{do}	outer radius of a rotation control electrode
R_{Eo}	outer radius of an excitation electrode
R_f	feedback resistance
R_{fbi}	inner radius of a feedback electrode
R_{fbo}	outer radius of a feedback electrode
R_i	inner radius of a rotor
R_m	intermediate radius of a rotor
R_o	output radius of a rotor
R_{rotor}	radius of a rotor
R_{si}	inner radius of a sense electrode
$R_{sidewall}$	radius of inner sidewall electrodes
R_{so}	outer radius of a sense electrode
σ	squeeze number
σ	centrifugal stress of a material
S	static mechanical sensitivity
T	absolute temperature
τ_d	viscous drag torque
U	potential energy stored in a capacitor
v_{AC}	AC component of a $V_{feedback}$ signal
V_B	DC bias voltage

V_{bias}	DC bias voltage
V_{ca}	output signal of a charge amplifier
V_{DC}	DC component of a $V_{feedback}$ signal
V_{dm}	output signal of a demodulation circuit
V_{drive}	applied drive voltage to a stator electrode
V_{ex}	excitation voltage
V_{fb}	voltage applied to a feedback electrode
v_{fb}	feedback control voltage
$V_{feedback}$	feedback voltage
$V_{lev,\mathrm{min}}$	minimum levitation voltage
V_n	input referred op-amp noise ($\mathrm{nV/Hz^{1/2}}$)
V_{out}	output voltage of a front-end circuit
V_r	net potential of a levitating rotor
v_x	velocity of a sensing element along the x axis
ω	resonant frequency
ω_d	driving frequency
Ω_{MNE}	minimum detectable input rotation rate ($\mathrm{deg/hr/Hz^{1/2}}$)
Ω_n	mechanical-thermal noise equivalent angular rate
$\Omega_{\mathrm{x,y}}$	input rate of rotation
ω_y	rate of rotation to be measured
Ω_y	input rate of rotation
Ω_z	rotation rate about the z axis
Ω_z	spin speed of the rotor
z	zero frequency in radians per second
z	levitation height
z_0	maximum levitation height
z_o	nominal capacitive gap between a rotor and upper and lower electrodes

DECLARATION OF AUTHORSHIP

I, BADIN DAMRONGSAK declare that the thesis entitled DEVELOPMENT OF A MICROMACHINED ELECTROSTATICALLY SUSPENDED GYROSCOPE and the work presented in the thesis are both my own, and have been generated by me as the result of my own original research. I confirm that:

- this work was done wholly or mainly while in candidature for a research degree at this University;
- where any part of this thesis has previously been submitted for a degree or any other qualification at this University or any other institution, this has been clearly stated;
- where I have consulted the published work of others, this is always clearly attributed;
- where I have quoted from the work of others, the source is always given. With the exception of such quotations, this thesis is entirely my own work;
- I have acknowledged all main sources of help;
- where the thesis is based on work done by myself jointly with others, I have made clear exactly what was done by others and what I have contributed myself;
- ~~none of this work has been published before submission,~~ ~~**or**~~ ~~[delete as appropriate~~] parts of this work have been published as: ~~[please list references]~~

Refereed Journal Publications

1. B. Damrongsak, M. Kraft, S. Rajgopal and M. Mehregany, “Design and fabrication of a micromachined electrostatically suspended gyroscope,” *Proc. IMechE Part C: Journal of Mechanical Engineering Science.*, vol. 222, no. 1, pp. 53–63, 2008..

Conference Proceedings

1. B. Damrongsak and M. Kraft, “Electrostatic suspension control for micromachined inertial sensors employing a levitated-disk proof mass,” in Proc. MME 2005 Conference, pp. 240-243, Sweden, September 2005.

2. B. Damrongsak and M. Kraft, **“**A micromachined electrostatically suspended gyroscope with digital for feedback,” in Proc. IEEE Sensors, pp. 401-404, Irvine, CA, USA, October 2005.

3. B. Damrongsak and M. Kraft, “Design and simulation of a micromachined electrostatically suspended gyroscope,” in Proc. IET Seminar on MEMS Sensors and Actuators, pp. 267-272, London, UK, May 2006.

4. B. Damrongsak and M. Kraft, “Performance Analysis of a Micromachined Electrostatically Suspended Gyroscope employing a Sigma-Delta Force Feedback,” in Proc. of MME 2007 Conference, pp. 269–272, Portugal, September 2007.

Signed: …………………………………..…………………..

Date:…………………………………………………………….

Acknowledgements

The completion of this thesis has been a long journey of learning. It could not have been finished without the help and support of many people. First and foremost I would like to thank my supervisor, Prof. Michael Kraft for his invaluable guidance throughout my study. Michael always gives me positive encouragement and support to my research work. It is hard to imagine my Ph.D. life without him.

Secondly, I would like to acknowledge Prof. Mehran Mehregany from the Case Western Reserve University. Without his help and support, this research work could have not been completed. In addition, I wish to thank all members in MINO Lab, Hari Rajgopal, Grant McCallum, Noppasit Laotaveerungrueng, Dr. Li Chen and Dan Zula, for making my life in the states much more enjoyable.

Also, I would like to express gratitude to all my colleagues in the NSI group with special thank to Dr. Zakaria Moktadir, Dr. Liudi Jiang, Dr. Ruth Houlihan, Dr. Mircea Gindila, Dr. Carsten Gollasch, Dr. Yufeng Dong, Gareth N. Lewis, Kian S. Kiang, Christopher L. Cardwell, Ioannis Karakonstantinos, Dr. Ibrahim Sari, Dr. Prasanna Srinivasan, Dr. Jen Luo, Dr. Sun Tao, Sun Kai and Haitao Ding, who offered assistance and made an office a fun place to do research.

I am deeply grateful to the Royal Thai government for financial support during my study at the University of Southampton. Also, I must thank to the School of Electronics and Computer Science for financial support for conferences and research visits to the Case Western Reserve University and the University of Michigan.

Lastly, but the most important, I must thank to my wife, Pat Kittidachachan, my parent and my brother for their love and mentally support during my study in Southampton. No words can express my feelings for them.

Chapter 1

Introduction

1.1 BACKGROUND AND MOTIVATION

Gyroscopes are generally used to provide measurement of rate and angle of rotation. Numerous types of gyroscopes have been developed since 1850s when Léon Foucault demonstrated the rotation of the Earth by his invented Foucault pendulum. Macro-scale gyroscopes, for example conventional rotating wheel gyroscopes, ring laser gyroscopes and fibre optic gyroscopes, are found mainly in navigation and guidance applications. However, they are far too bulky and too expensive for use in mass market applications.

With current microfabrication technology, it is possible to develop a gyroscope several orders of magnitude smaller and significantly reduce the cost of fabrication. This will open up a wide range of applications [**1**]. Micromachined gyroscopes have a large volume demand in automotive applications where they can be used in smart airbag deployment, braking systems, active suspension and roll-over detection. They can also be exploited in consumer applications, including image stabilisers for video cameras, virtual reality handsets, novel pointing devices and robotics applications. Recently, high performance micromachined gyroscopes have become interesting for use in military and space applications, such as unmanned aerial vehicles, micro/pico satellites, missiles, etc.

Almost all micromachined gyroscopes reported to date are a vibratory type gyroscope, which relies on sensing the Coriolis acceleration of a vibrating proof mass [**2–4**]. Such a gyro requires matching of drive and sense mode resonant frequencies to increase its performance; hence, making it very sensitive to fabrication imperfections. Vibrating micromachined gyroscopes also suffer from the so-called quadrature error, which is resulted from a coupling of a drive mode into a sense signal. These issues are two major problems in the development of MEMS gyroscopes with navigation-grade or inertial-grade performance.

The figures of merit used to evaluate the performance of MEMS gyroscopes are device resolution[1] and angular bias stability[2]. The resolution of the sensor is limited by white noise and is generally defined by the noise level of the sensor. This can be expressed as a noise density in deg/s/Hz$^{1/2}$ or deg/hr/Hz$^{1/2}$, which describes the output noise as a function of the bandwidth of the sensor. Sometimes the term “angle random walk” (ARW[3]) in deg/hr$^{1/2}$ is used instead. The ARW describes the average angular displacement error that will occur when the signal is integrated over time. Gyro bias stability is the other important parameter, which represents changes in the long-term average of the collected data. For navigation use, it requires a gyroscope with the ARW less than 0.001 deg/hr$^{1/2}$ and the bias drift less than 0.01 deg/hr [**2**].

Table 1.1 shows the performance requirements for different classes of gyroscopes. Rate-grade and tactile-grade gyroscopes are typically used to measure relatively short term angular rates. The ARW is the dominating random error that limits their performance. On the other hand, inertial grade gyroscopes are used to maintain a fixed long-term heading in an inertial reference frame. The bias drift tends to dominate for long-term performance.

Table 1.1: Performance requirements for gyroscopes [**2**].

Parameters	**Rate grade**	**Tactical grade**	**Inertial grade**
Angle random walk (deg/hr$^{1/2}$)	>0.5	0.5 – 0.05	<0.001
Bias stability (deg/hr)	10-1000	0.1-10	<0.01
Scale factor accuracy (%)	0.1-1	0.01-0.1	<0.001
Full scale range (deg/s)	50-1000	>500	>400
Max. shock in 1ms (g)	1000	1000-10000	1000
Bandwidth (Hz)	>70	~100	~100

---

[1] The resolution is the smallest change of the input signal (rate of rotation) the gyro can detect.

[2] The bias stability, also referred to as the bias drift, is the minimum change in rotation rate over the time which the measurements are integrated.

[3] ARW in deg/hr$^{1/2}$ can be converted into deg/s/Hz$^{1/2}$ by dividing by 60.

While many research groups and companies worldwide have done research on MEMS gyroscopes, none of them has yet to achieve inertial-grade performance. Several focus on development of automotive/rate-grade performance MEMS gyroscopes. Only a few groups achieve tactile-grade performance. The Charles Stark Darper Laboratory has achieved a tactile-grade performance MEMS gyroscope [**5**]. The Darper gyroscope based on a tuning fork design has demonstrated 30 deg/hr bias stability and 5-10 deg/hr/Hz$^{1/2}$ noise floor. With temperature control and compensation, its bias stability can be reduced to 1 deg/hr. The other tactile-grade vibratory gyroscope was reported by the MEMS technology group at Jet Propulsion Laboratory (JPL) [**6**]. Its bias stability of 1 deg/hr was demonstrated under environmental lab conditions [**7**]. More details on the development of vibratory MEMS gyroscopes can be found in chapter 2.

To enhance the performance of MEMS gyroscopes, alternative approaches to vibratory type gyroscopes are of interest [**8, 9**]. Those with proven navigation-grade capability at the macro scale are worth investigating. This work aims to develop a small-scale electrostatically suspended gyroscope (ESG) using microfabrication technology. The ESG has commonly been employed for naval use. A similar gyroscope with electrostatic suspension has intensively been developed in the Gravity Probe B space mission and proven to be the current world's highest precision gyroscope [**10**].

A micromachined ESG has several advantages over a vibratory MEMS gyroscope. Its proof mass is electrostatically supported without physical contact with a substrate. This will isolate the proof mass from unwanted inputs such as friction, wear and stress; hence, improving the long-term stability of the sensor. The micromachined ESG can also be used as a tri-axial accelerometer [**11, 12**] and concurrently be able to measure rotation rate about two axes if the levitated proof mass was spun at high speed [**13, 14**]. The high spin speed of the rotor can produce angular momentum larger than that of a vibrating-type gyro, hence making it possible to achieve higher gyro sensitivity. More details can be found in chapter 3.

The micromachined ESG is unable to operate in open-loop mode. To control a position of the proof mass, an electrostatic suspension system is required. Generally, an electrostatic suspension system for the ESG is based on analogue feedback control, both at the macro and micro scale [**15, 16**]. A micromachined levitated spinning gyroscope with analogue servo control was successfully demonstrated by Tokimec, Inc. (Japan) [**16, 17**]. It revealed a potential to measure multi-axis acceleration and angular velocity simultaneously. However, analogue feedback control has some disadvantages, such as a nonlinear feedback relationship and the so-called *latch-up* problem for large deflections of the proof mass [**18**]. To avoid such problems, a digital closed-loop system based on an electromechanical sigma delta modulation (ΣΔM) is considered to be exploited in an electrostatic suspension system of the micromachined ESG. With ΣΔM force feedback, at one given point in time, only electrodes away from the proof mass are energised to force the proof mass back to its nominal position and thus the latch-up problem can be avoided. The ΣΔM control system also provides a pulse-density modulated bitstream that can be directly interfaced to a digital signal processing (DSP) without the requirement of an analogue-to-digital converter (ADC).

1.2 RESEARCH OBJECTIVES AND CONTRIBUTIONS

The aim of this thesis is to explore the feasibility in development of an electrostatically suspension gyroscope using microfabrication technologies. The research project is divided into three main tasks.

The first task is to design and analysis the micromachined ESG. A system level model is developed in Matlab/Simulink to investigate the dynamic behaviour of the micromachined ESG and the stability of the closed-loop control system. The developed Simulink model is employed to investigate the influence of the sensor performance in the presence of mechanical and electronic noise sources as well as non-idealities of electronic interface. The findings of this study have been published in references [**19–21**].

The second task is to design and develop an electronic front-end interface. The front-end circuit is used to measure a change in capacitance due to the displacement of the proof mass in the presence of rotation or acceleration. An OrCAD/PSPICE model is developed to study the performance of the front-end interface. The designed front-end circuit is also implemented on a printed circuit board (PCB). Measurements are carried out to verify results obtained from analytical calculations and OrCAD/PSPICE simulations.

The final task is to develop a suitable microfabrication process for the micromachined ESG. The fabrication process is based on a glass/silicon/glass sandwich structure, which combines a high-aspect-ratio DRIE process and triple-wafer stack anodic bonding. The development of these fabrication procedures is published in reference [**14**].

The prototype sensors suffer from the so-called stiction problem where a fabricated rotor is stuck inside a device cavity. The problem could not be resolved because the entire Southampton University cleanroom facilities were destroyed by a fire. Thus, the micromachined ESG cannot be tested with the designed closed-loop ΣΔM system during the course of this research project. Alternatively, the exploitation of sidewall electrodes to provide electrostatic levitation is investigated. The analysis of this approach is carried out in an ANSYS software package.

1.3 THESIS OUTLINE

This thesis is divided into eight chapters describing the theory, design and development of a micromachined electrostatically suspended gyroscope. Chapter 2 discusses the state-of-the-art attained on MEMS gyroscopes. The basic principle of conventional vibrating MEMS gyroscopes with due considerations to the design for performance improvement is presented. Alternative approaches to vibrating MEMS gyroscopes are also presented with emphasise on spinning type gyroscopes.

Chapter 3 discusses the operating principle of the micromachined ESG. Advantages of the micromachined ESG over conventional MEMS gyroscopes are also discussed. The last section of chapter 3 focuses on the major design issues for the development of the micromachined ESG. In particular, this involves the design of a levitated proof mass and the design of the sense and control electrodes.

In chapter 4, a capacitive front-end interface used to measure the linear and angular displacement of the rotor due to inertial forces/moments is described.

Chapter 5 presents a closed-loop electrostatic suspension system based on a digital ΣΔM feedback loop. The closed-loop system is required to levitate the mechanically unsupported micromachined rotor. Simulations at system and electronic level of the closed-loop micromachined ESG are used to evaluate the overall system performance and its stability.

Device fabrication of a micromachined ESG is detailed in chapter 6. Fabrication results are presented and also relevant issues are addressed.

In chapter 7, an alternative approach was explored to realise a micromachined levitated disc gyroscope. Sidewall electrodes of the device were used to provide electrostatic forces in order to levitate the rotor. System level simulations including preliminarily experimental results are described.

Chapter 8 is conclusion and gives an outlook on further work.

Chapter 2

High Performance MEMS Gyroscopes: Comprehensive Review

2.1 INTRODUCTION

The market value of MEMS gyroscopes is forecasted to reach $800M (approximately £400M) in 2010 [**22**]. This is because applications of MEMS gyros are very board with high growth potential from low-end automotive and consumer markets to defence and space applications. This motivates researchers worldwide to explore actively on the development of MEMS gyroscopes.

The vast majority of all reported MEMS gyroscopes are a vibratory type gyroscope, which detects the rotation-induced Coriolis acceleration of a vibrating proof mass to measure the rate of rotation of the reference frame [**2–4**]. Although various MEMS gyroscopes have been extensively researched worldwide for decades, achieving a sensor with tactical and inertial-grade performances has proven to be very challenging. Many companies (for example, Analog Devices [**23**], Silicon Sensing Systems which is a collaboration of BAE Systems and Sumitomo [**24**] and Samsung [**25**]) have commercialised automotive or rate-grade performance MEMS gyroscopes. Only two companies, i.e. Honeywell/Draper [**26, 27**] and Systron Donner/BEI [**28**] are producing tactical-grade performance MEMS gyroscopes. Section 2.2 discusses the principle of vibrating MEMS gyroscopes with due considerations to the design for performance improvement. Recent work to improve performance of conventional vibrating MEMS gyroscopes is presented in section 2.3.

Vibrating MEMS gyroscopes have yet to achieve inertial-grade performance to date. Such gyroscopes suffer from manufacturing tolerances and a mechanical cross-talk between drive and sense modes (the so-called quadrature error). Therefore, MEMS designers recently become interested in alternative approaches in order to improve the sensor performance. Among them, an electrostatically suspended gyroscope (ESG), which was mainly developed for navigation applications [**29**], is one of the most promising concepts. A review on this topic is presented in section 2.4.

2.2 PRINCIPLE OF CONVENTIONAL MEMS GYROSCOPES

Due to the difficulty in making a friction-less rotational element using current microfabrication technology, conventional MEMS gyroscopes are based on a principle called Coriolis effect [**2**]. The Coriolis force F_{cor} of a moving mass m in a rotating system is expressed as:

$$\vec{F}_{cor} = -2m\vec{\Omega} \times \vec{v} \tag{2.1}$$

where v is the velocity of the moving mass and Ω is angular rate of the rotating system. The equation implies that the Coriolis force will cause the moving mass to displace in the direction perpendicular to the direction of the velocity of the moving mass and the rotating frame.

Vibratory micromachined gyroscopes are typically comprised of a mass suspended on elastic flexures that are anchored to the substrate. They can be modelled with a two degree-of-freedom mass-spring-damper system as shown in Figure 2.1. In this discussion, x-axis is defined to be the drive axis, y-axis is the sense axis and z-axis is the axis of rotation. The dynamic equations of motion of vibratory MEMS gyroscopes can then be described as [**30**]:

$$m\ddot{x} + b_x\dot{x} + k_x x = F_x + 2m\Omega_z\dot{y} \tag{2.2}$$

$$m\ddot{y} + b_y\dot{y} + k_y y = F_y - 2m\Omega_z\dot{x} \tag{2.3}$$

where

m = mass of a sensing element,
x,y,z = subscripts that indicate x (drive), y (sense) and z (rotation) axes,
b = damping coefficient,
k = spring constant,
F = external force acting on a proof mass, and
Ω = rotation rate of the rotating frame.

F_x is the driving force applied to vibrate the proof mass and F_y is zero if the device is operated in open-loop mode. Equations (2.2) and (2.3) can then be simplified to:

$$m\ddot{x} + b_x\dot{x} + k_x x - 2m\Omega_z\dot{y} = F_x \tag{2.4}$$

$$m\ddot{y} + b_y\dot{y} + k_y y + 2m\Omega_z\dot{x} = 0 \tag{2.5}$$

Equation (2.4) represents the dynamic equation of the mechanical structure for the *drive* axis; whereas the equation of motion in the *sense* axis is defined by equation (2.5). The terms $2m\Omega_z\dot{y}$ and $2m\Omega_z\dot{x}$ are the Coriolis-induced forces resulted from the rotation of the reference frame.

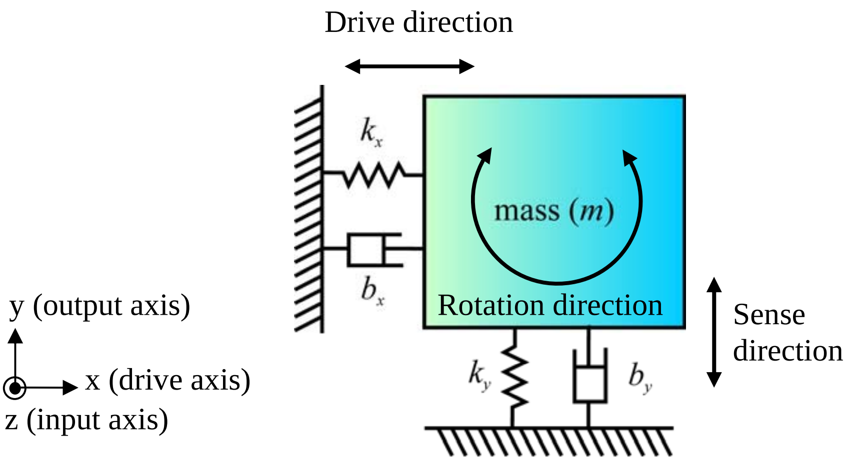

Figure 2.1 Mass-spring-damper model for a micromachined vibrating gyroscope.

For the sake of simplicity, assume that there is no Coriolis force induced into the drive axis ($2m\Omega_z\dot{y} = 0$). Rearranging equations (2.4) and (2.5) yields:

$$\ddot{x} + \frac{\omega_x}{Q_x}\dot{x} + \omega_x^2 x = \frac{F_x}{m} \tag{2.6}$$

$$\ddot{y} + \frac{\omega_y}{Q_y}\dot{y} + \omega_y^2 y = 2\Omega_z\dot{x} \tag{2.7}$$

where

F_x = sinusoidal driving force = $F_d \sin\omega_d t$,

F_d = amplitude of the driving force,

ω_d = frequency of the driving force,

x,y,z = subscripts that indicate x (drive), y (sense) and z (rotation) axes,

ω = resonant frequency ($\omega = \sqrt{k/m}$) and

Q = quality factor ($Q = m\omega/b$).

The steady state solutions of equations (2.6) and (2.7) can be expressed as:

$$x_d = \frac{F_d/m}{\omega_x^2\sqrt{\left(1-\frac{\omega_d^2}{\omega_x^2}\right)^2 + \left(\frac{1}{Q_x}\frac{\omega_d}{\omega_x}\right)^2}} \tag{2.8}$$

$$y_{cor} = \frac{2\Omega_z\dot{x}}{\omega_y^2\sqrt{\left(1-\frac{\omega_d^2}{\omega_y^2}\right)^2 + \left(\frac{1}{Q_y}\frac{\omega_d}{\omega_y}\right)^2}} \tag{2.9}$$

Assuming $x = x_d \sin \omega_d t$ yields $\dot{x} = x_d \omega_d \cos \omega_d t$. Then, equation (2.9) can be rewritten as:

$$y_{cor} = \frac{2\Omega_z \omega_d x_d}{\omega_y^2 \sqrt{\left(1 - \frac{\omega_d^2}{\omega_y^2}\right)^2 + \left(\frac{1}{Q_y}\frac{\omega_d}{\omega_y}\right)^2}} \tag{2.10}$$

Equations (2.8) and (2.10) are two basic equations employed in the design of vibratory MEMS gyroscopes. The former represents the motion of the mechanical structure in the drive mode. The latter equation determines the motion of the vibrating structure in the sense mode. It can be seen that the maximum sensitivity of the vibratory gyroscope can be obtained by matching the resonant frequencies of the drive and sense mode. Also, the driving frequency must be equal to the resonant frequency of the structure in the drive mode. Thus, equation (2.10) can be simplified to:

$$y_{cor,\max} = \frac{2\Omega_z Q_y x_d}{\omega_y} \tag{2.11}$$

In the open-loop operation, the rate of rotation can then be determined by measuring the amplitude of the sensing motion.

To give some idea about the magnitude of the Coriolis force, let's put some numbers into equation (2.11). Assuming the drive mode vibration amplitude is 2 μm, the drive mode resonant frequency is 40 kHz and the quality factor is 15,000, the maximum Coriolis displacement for the input rotation rate of 1 deg/sec is only 4.2 nm. It is obvious that the Coriolis motion is relatively weak.

It should be noted that the resolution of the vibratory gyroscopes is fundamentally limited by the noise source in the mechanical structure of the sense mode. Typically, the mechanical noise is generated from thermal vibration of air molecules causing Brownian motion of the proof mass. From Nyquist's relation, the fluctuating force due to mechanical-thermal noise for a given bandwidth *BW* is [**31**]:

$$F_n = \sqrt{4k_B TbBW} \tag{2.12}$$

where

k_B = Boltzmann’s constant (1.38 ×10^{-23} J/K) and

T = absolute temperature.

Assuming F_n is equivalent to the Coriolis force, equation (2.12) can then be rewritten as:

$$2m\Omega_n \omega_d x_d = \sqrt{4k_B TbBW} \tag{2.13}$$

Substituting $b = m\omega_y / Q_y$ into equation (2.13) yields:

$$\Omega_n = \sqrt{\frac{k_B T\omega_y BW}{m\omega_d^2 x_d^2 Q_y}} \tag{2.14}$$

The parameter Ω_n is called the mechanical-thermal noise equivalent angular rate, which represents the fundamental limiting noise component of vibratory MEMS gyroscopes.

In summary, the need for a high performance gyroscope requires:

- large drive amplitude,
- frequency matching between the drive and sense modes,
- high mechanical quality factor (by operating the gyroscope at very low pressure),
- low resonant frequency, but well above environmental noise level (>2 kHz) [**2**] and
- maximise mass per unit area.

2.3 DEVELOPMENT OF VIBRATORY MEMS GYROSCOPES

A conventional micromachined gyroscope typically consists of a vibratory proof mass mechanically supported above a substrate via elastic beams. The proof mass is driven into linear or rotary oscillation at its resonant frequency. External rotation applied to the substrate induces a second oscillation of the proof mass due to Coriolis forces. Typically, the sensing structure is arranged to be perpendicular to the drive axis. The displacement of the proof mass in the sense direction can be used to estimate the angular motion of a base on which the MEMS gyro is attached. General speaking, the vibratory gyroscopes are composed of two MEMS devices – a large-amplitude high-Q resonator and a high sensitivity submicro-g accelerometer – that have to work together to sense angular velocity.

Various transduction mechanisms have been employed to drive and maintain oscillation of the vibrating element at its resonant frequency. The most common drive mechanisms are piezoelectric [**32**], electromagnetic [**33, 34**] and electrostatic [**35–37**]. Both piezoelectric and electromagnetic actuations are common methods used in macro-scale devices since they can provide relatively high energy density. However, they are relatively difficult to implement in silicon-based technology as both require non-standard materials. Hence, the most common actuation mechanism employed for vibratory MEMS gyroscopes is electrostatic, particularly using a comb structure.

Similar to actuation mechanisms, capacitive detection is most commonly used for MEMS gyroscopes, even though there are a variety of sensing mechanisms available. This is mainly because a capacitive sensing is relatively simple to fabricate and can be simultaneously used as the actuator. Moreover, no special material is required in the fabrication.

Vibrating micromachined gyroscopes can be implemented by various microfabrication technologies, including surface micromachining [**35**], bulk micromachining and wafer bonding [**38, 39**], electroplating and LIGA [**40, 41**], combined surface-bulk micromachining [**42**] and recent developed EFAB™ technology [**43**]. Surface micromachining is based on the deposition and etching of thin layers (~2 μm) on the top of the substrate. The benefit of surface micromachining is its compatibility with a conventional IC fabrication technology and thus allowing a sensor and integrated electronic interfaces to be fabricated on a single chip. However, the surface micromachined gyroscopes suffer from the *low-mass* problem, making them difficult to reach a low noise floor required for high-end navigation applications. As a consequence, the majority of MEMS gyroscopes is developed using high-aspect-ratio bulk microfabrication, for example Silicon on Glass (SOG), Silicon on Insulator (SOI) and LIGA technologies.

The designs of vibrating micromachined gyros are typically based on three basic configurations, including tuning forks [**26, 27, 32, 39**], vibrating plates [**35, 36**] and vibrating rings [**40**]. A comprehensive review and evolution of micromachined gyroscopes has already been discussed in references [**2–4, 44, 45**]. This section presents the state-of-the-art in this field.

The classic example of vibrating MEMS gyros is a tuning fork design developed by The Charles Stark Darper Laboratory [**26, 27**] (Figure 2.2). It contains a pair of proof masses coupled to each other via a mechanical suspension. These masses are vibrated in anti-phase with the same amplitude, but in opposite direction. When the device is in the presence of rotation, Coriolis force will cause both masses to vibrate out-of-phase to each other, perpendicular to the drive axis (see Figure 2.3). The deflection of the proof masses represents the measured rate of rotation. Typically, the device structure is designed to allow motion in two directions (the drive and sense axes), but the other axis will be relatively rigid (the axis sensitive to applied angular velocity). The advantage of the tuning fork design is that it has an ability to reject common mode inputs (linear acceleration, for instance). The Darper gyroscope has demonstrated tactile-grade performance (30 deg/hr bias stability and 5-10 deg/hr/Hz$^{1/2}$ noise floor). However, it was realised with considerable effort and difficulty [**5**]. Matching between sense and drive mode frequencies has been proven to be challenging. The sense and drive resonant frequencies generally depend on the width and thickness of the elastic beams. For the Darper gyroscope, typical beam widths are 10 µm. Obtaining ±2 % sense-drive frequency separation tolerances requires 0.2 µm absolute accuracy of the beam widths. This challenges the tolerance on photolithography and silicon etching processes. The other issue is *cross-coupling* signals, which is caused by fabrication imperfections and anisoelasticity in the mechanical suspension system. These coupling signals can manifest itself as an output signal of the gyroscope even in the absence of rotation.

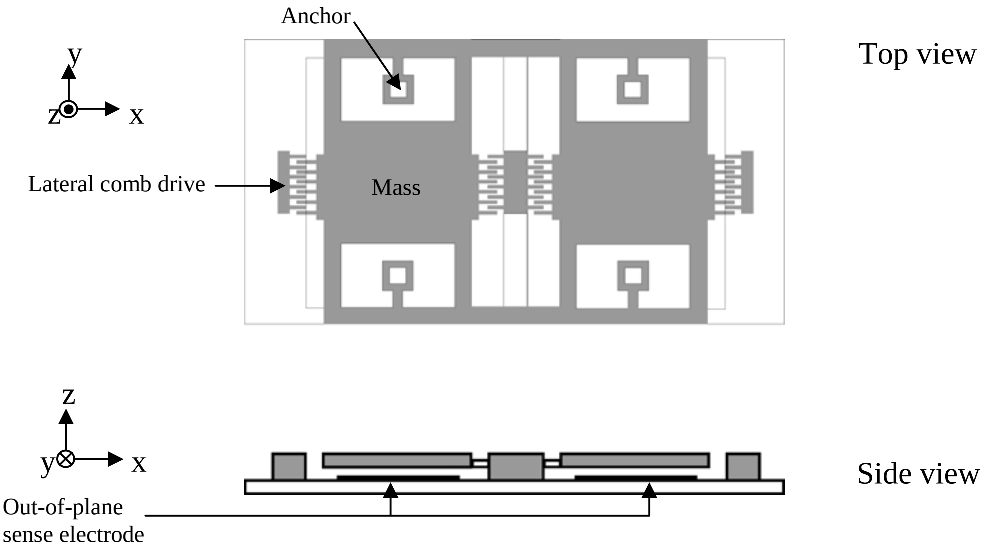

Figure 2.2 Configuration of a vibrating gyroscope based on a tuning fork design: (top) top view and (bottom) side view of the tuning fork vibrating gyroscope.

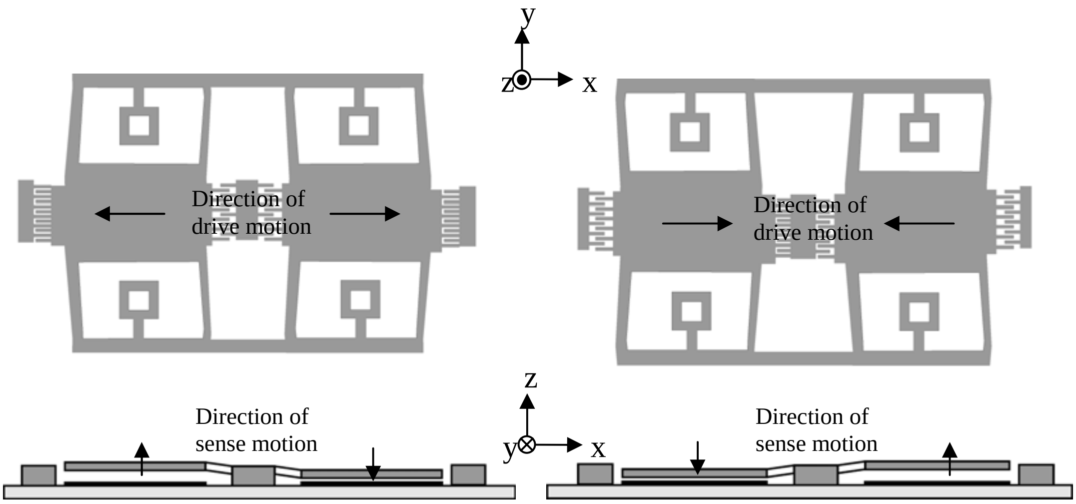

Figure 2.3 Operating principle of a tuning fork vibrating gyroscope. Top view shows the vibrating of a pair of proof masses with the same amplitude, but opposite direction. Bottom view shows the movement of the proof masses in the presence of rotation about the z axis.

The cross-coupling signal that arises from anisoelasticity and other asymmetry in the mechanical suspension system is called the *mechanical quadrature error*. The quadrature signal is in phase with the drive signal; but 90° phase different to the Coriolis force. This quadrature signal can easily dominate the output of a gyroscope due to the small magnitude of the Coriolis force. Nevertheless, the problem of quadrature signal can be alleviated by very careful micromachining and by applying electrostatic forces to null deflections resulting from quadrature error [**46**]. The use of adaptive control strategies and post signal processing are also proposed to cancel or minimise quadrature error [**47**]. However, mechanical quadrature over 50 rad/s is difficult to cancel out, due to the limited available feedback voltage. Quadrature error larger than 50 rad/s requires very precise mechanical trimming using laser ablation [**48**].

The other cross-coupling signal that originates from imperfections of the drive mode actuator is the most serious issue. For example, in the case of interdigitated-finger comb drive gyroscopes, fabrication imperfections can result in small geometric nonidealities of the comb fingers. This will generate additional electrostatic forces in the sense direction even if no rotation rate is applied to a gyroscope. This coupling signal causes a motion in the sense axis that has a 0° or 180° phase shift from the Coriolis signal [**5, 49**]. Thus, this signal cannot be rejected by means of electronic tuning.

To overcome these problems, several approaches have been investigated to provide frequency matching between drive and sense resonance modes and also to improve robustness against cross-coupling errors. Najafi *et al.* from the University of Michigan proposed a micromachined gyroscope based on a vibrating ring structure [**40**] as shown in Figure 2.4. The device is of symmetrical design providing two identical resonance modes with the same natural frequency. This will avoid unwanted cross-axis coupling and temperature stability problem. Akin *et al.* from Middle East Technical University (METU), Turkey have developed micromachined gyroscopes (Figure 2.5), which employs a symmetric design of the suspension beams as well as identical actuation and detection mechanisms [**50–53**]. The anchors of the structure are located in such a way that the drive and sense modes of the gyroscopes is mechanically decoupled from each other. The METU gyroscope demonstrated 7 deg/sec bias stability and 35 deg/hr/Hz$^{1/2}$ noise floor. Geiger *et al.*

from HSG-IMIT, Germany reported relatively high precision MEMS gyroscopes based on the patented decoupling principle, called DAVED (Decoupled Angular Velocity Detector) [**37, 54–55**]. Figure 2.6 shows conceptual drawings of decoupled MEMS gyroscopes. The prototype decoupled gyro fabricated by surface micromachining has a bias stability of 65 deg/hr and a noise floor of 0.14 deg/hr$^{1/2}$.

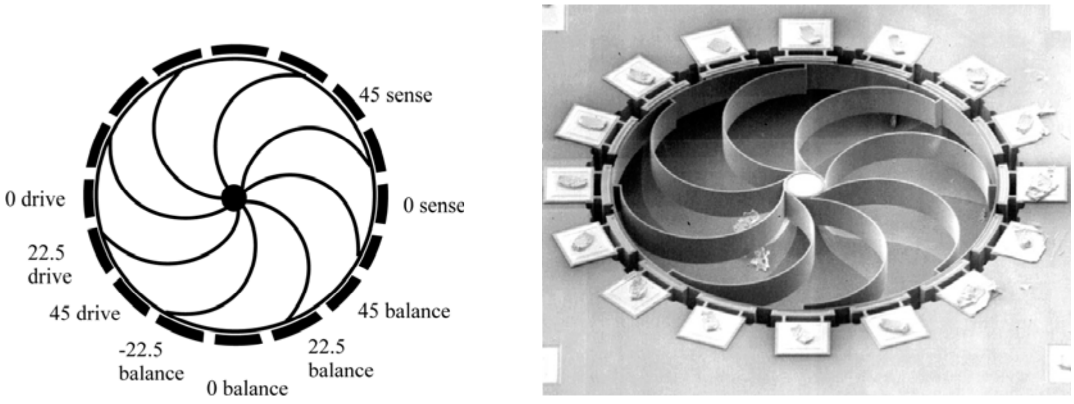

Figure 2.4 Micromachined vibrating ring-type gyroscope [**40**]: (left) conceptual drawing and (right) scanning electron micrograph (SEM) image.

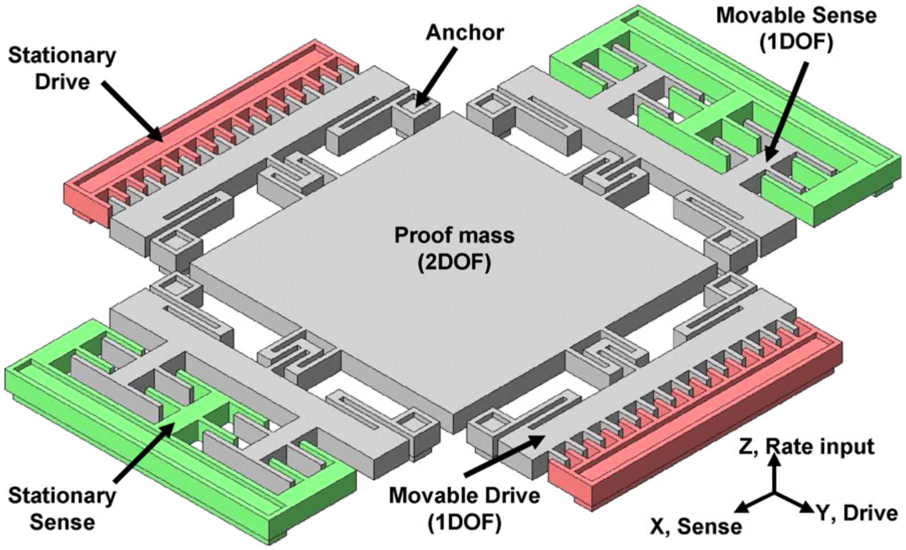

Figure 2.5 Conceptual drawing of the METU symmetrical and decoupled micromachined gyroscope [**53**].

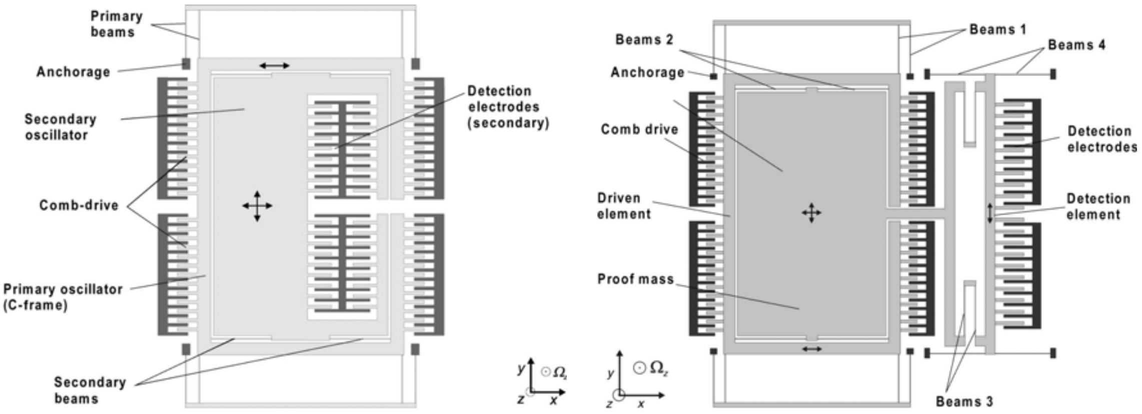

Figure 2.6 Conceptual drawing of decoupled MEMS gyroscopes developed at HSG-IMIT, Germany [**55**].

As mentioned earlier, the conventional MEMS gyroscopes are very sensitive to fabrication imperfections and tolerances. Therefore, recent work focuses on the development of vibratory micromachined gyroscopes that will provide inherent robustness against the variation of structural and thermal parameters [**3, 43, 56–62**]. Shkel *et al.* from the University of California, Irvine proposed novel structural designs to obtain a dynamical system with wide-bandwidth frequency response [**58–61**]. This can be achieved by: (1) increasing the degrees-of-freedom of the drive and sense mode vibrations (see Figure 2.7) and (2) utilizing multiple driven resonators with incremental resonant frequencies (see Figure 2.8). However, these designs trade off the increase in robustness with a decrease in device sensitivity. The other approach employs parametric resonance as a driving mechanism [**62**]. The prototype gyroscope developed by University of California, Santa Barbara showed large driving amplitude over a wide range of excitation frequencies.

Due to the weakness of Coriolis forces, mechanical Brownian noise and electronic noise limit device resolution. For surface micromachined gyroscopes, a noise level of about 1 deg/sec/$Hz^{1/2}$, which is accurate enough for automotive applications, has been achieved [**35**]. However, it suffers from the *low-mass* problem (high Brownian noise) which makes it unlikely to ever reach a level of 1 deg/hr/$Hz^{1/2}$ required for navigation and high-end military applications.

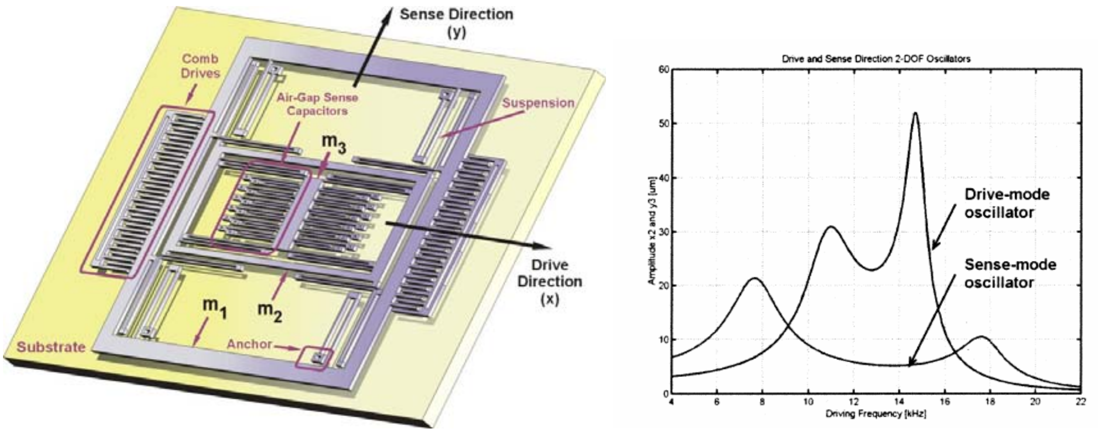

Figure 2.7 MEMS gyroscope developed at University of California, Irvine (USA) [**58**]: a conceptual illustration (left) and frequency responses of 2-DOF drive- and sense-mode oscillators, with overlap flat regions (right).

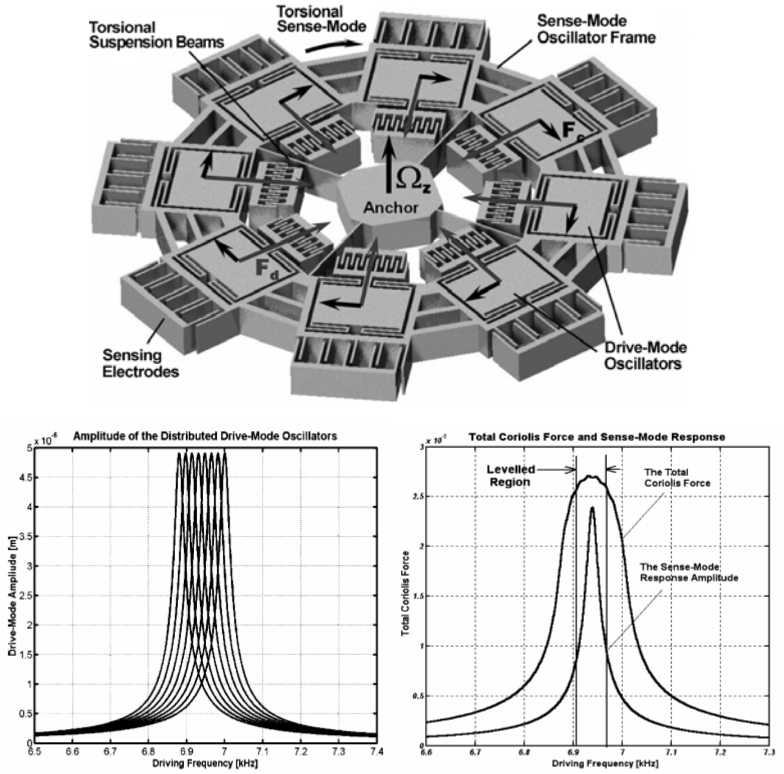

Figure 2.8 Distributed-mass MEMS gyroscope with eight drive oscillators developed at University of California, Irvine (USA) [**60**]: a conceptual drawing (top), a frequency response of distributed drive-mode oscillators (bottom, left) and a frequency spectrum of the total Coriolis forces generated by distributed drive-mode oscillators (bottom, right).

A variety of methods have therefore been investigated to reduce mechanical noise and also enhance the readout signal. In order to overcome the *mass* factor in surface micromachined gyroscopes and increase sense capacitances in capacitive devices, high-aspect-ratio (HAR) bulk micromachining techniques are of interest. Several companies like STS, Alcatel and Plasmatherm have developed the technology for deep and narrow trench etching in single-crystalline silicon. Deep etching with aspect ratio of 50:1 for hundreds of micron thick silicon can be achieved [**63, 64**].This technology greatly simplifies the design of high-performance gyroscopes by making the fabrication of high aspect ratio beams and proof mass possible. A matched-mode SOI tuning fork gyroscope developed by the Georgia Institute of Technology is an example of a HAR micromachined vibratory gyroscope with a reported resolution and bias stability of 0.05 deg/hr/Hz$^{1/2}$ and 0.96 deg/hr, respectively [**39, 65–66**]. Other examples of fabrication techniques to achieve high aspect-ratio MEMS gyroscopes are a HAR combined poly and single-crystal silicon MEMS technology developed by the University of Michigan [**38**], a post-release capacitance enhancement from the University of California, Irvine [**67**], a sacrificial bulk micromachining (SBM) process from Samsung [**68–70**] and EFAB™ process commercially available from Microfabrica [**43, 71**]

In summary, the performance of vibrating-type MEMS gyroscopes is limited by many factors, such as the weakness of the rotation-induced Coriolis force, the cross-coupling effect and the fabrication tolerances. Although, such gyroscopes have extensively been researched for decades, vibratory MEMS gyroscopes with navigation-grade performance have not yet been achieved to date. In order to realise a high performance MEMS gyroscope, it is worth investigating alternative approaches.

2.4 ALTERNATIVE APPROACHES TOWARDS HIGH PERFORMANCE MEMS GYROSCOPES

2.4.1 Introduction

The demand of high performance MEMS gyroscopes is steadily increasing; however, as mentioned previously, the performance of vibrating MEMS gyros with suspended mechanical structures is limited. To overcome those limitations, radically different design of MEMS gyroscopes with no mechanical suspension are of interest, especially those with proven inertial-grade capability on the macro scale. For example, a fluidic angular rate sensor which measures a change of fluid (air) velocity related to the applied rotation rate [**72–74**]. Other examples are micromachined gyroscopes based on the use of acoustic wave to measure angular rate of rotation [**75–78**], and a microfabricated nuclear magnetic resonant gyroscope developed by the University of California, Irvine [**79, 80**]. These approaches are currently in the initial state of development and have not achieved navigation-grade performance yet.

Macroscopic interferometric fiber-optic gyro (IFOG) and ring laser gyro (RLG) are the most widely used for navigation and guidance applications. They allow highly accurate measurement of rotation rates, with reported achievements of below 0.005 deg/hr$^{1/2}$ angle random walks, and attainment of below 0.015 deg/hr bias instability under laboratory simulated test conditions [**81**]. Both IFOG and RLG measure rotation based on the Sagnac effect, also called Sagnac interference. Basically, light is made to travel in opposite directions in a setup called ring interferometry, which comprises a long circular waveguide. When it is subjected to rotation, counter-rotation light beams will have different path lengths and thus exhibit a relative phase difference. The measured interference signal of the two beams provides a measure of angular velocity. The performance of optical gyroscopes scales directly with its optical path. This makes it relatively difficult to realise a small scale, high performance IFOG/RLG using the current microfabrication technology. There are very few examples in the literature reporting the development of micromachined optical gyroscopes; notable exceptions are an interferometric MOEMS gyroscope from the Air Force Institute of

Technology [**82**] and micro-ring optical gyros proposed by the University of Delaware [**83**]. Only realisation of the device and verification of the concept were performed; no device characterization has been reported so far.

One of the most promising alternative concepts is the electrostatically suspended gyroscope (ESG). A macro-scale ESG was developed mainly for guidance and space applications where high precision and robust sensors are crucial [**23, 84**]. It employs electrostatic forces to suspend a proof mass, which has no mechanical connection to the substrate. Electrostatic levitation isolates the proof mass from unwanted long term effects, such as mechanical friction, so that the long-term stability of the device is improved. A levitated proof mass is typically spun at high speed; then, the displacement of the proof mass resulted from the presence of rotation can be used to determine the angular velocity. Successful realisation of micromotors using microfabrication technology [**85, 86**] makes a micro-scale ESG even more interesting. The next section will discuss in detail on the evolution and development of spinning MEMS gyroscopes.

2.4.2 Spinning MEMS gyroscopes: a review

A micro-scale ESG employing a levitated proof mass has many advantages over conventional vibrating type gyros. It can be exploited as a tri-axial accelerometer and concurrently is able to measure the rate of rotation about two axes if the levitated proof mass is spinning. A micro-rotor with no mechanical connection to a substrate is levitated and spun by electrostatic forces. The absence of mechanical friction, wear and stress would result in the improvement of bias drift. It is also expected that a high speed rotation of the rotor can produce larger angular momentum compared with that of conventional vibrating type micromachined gyroscopes (see chapter 3 for more details). Hence, it is possible to design a high sensitivity and robustness MEMS gyro with this approach.

The operation of spinning MEMS gyroscopes is based on the conservation of angular momentum [**87**], which can be expressed using the following basic gyroscopic equation:

$$M_x = I_z \Omega_z \Omega_y \tag{2.15}$$

where

M_x = precession torque,

I_z = moment of inertia of the proof mass,

Ω_z = spin speed of the proof mass and

Ω_y = rate of rotation to be measured.

Basically, a proof mass, hereafter also called a rotor, is suspended and rotated by electromagnetic/electrostatic forces. The rotation rate can then be determined by detecting the torque-induced precession of the rotor.

Although an ESG has the potential to deliver navigation-grade performance, relatively little work has been done to realise an ESG using microfabrication techniques. Early development work of a micromachined rate gyroscope employing electrostatic suspension was reported using surface micromachining by SatCon Technology Co. (USA) [**88, 89**]. A micromotor-like silicon rotor with a diameter of 200 μm was patterned onto a 2.2 μm thick polysilicon layer. Analogue closed-loop system was used to control the orientation of the rotor. However, the sensor failed to operate due to charged induced adhesion [**89**]. Researchers at the Case Western Reserve University also developed a surface micromachined micromotor-based IMU as shown in Figure 2.9. Most of the published work in the literature focused on the sensing and control electronic interface for both suspension and rotation control [**90, 91**]. Recent work from the University of California at Berkeley also explores the use of surface micromachining process flow to fabricate a floating electromechanical system (FLEMS) gyroscope [**92**]. A micromotor-like rotor was made out of a thin film poly-$Si_{1-x}Ge_x$ layer. A 1 μm thick low temperature oxide (LTO) was used as a sacrificial layer. To avoid adhesion from wet-chemical release process, a HF vapour release process was used. However, it was found that more than half of the released device, the rotor was stuck to the electrodes.

Several literature sources [**93–97**] reported the use of electromagnetic induction in order to levitate and spin a rotor (Figure 2.10). The advantage of electromagnetic over electrostatic forces is that it is possible to produce both attractive and repulsive forces; hence, the levitation with great stability can be accomplished using electrodes on only one side of the rotor. Achievement of spinning a rotor was reported; however, no one yet reported a gyroscopic sensor with this approach. One major issue of an electromagnetically levitating gyroscope is relatively high currents are required during the operation which will make the stator reach 600°C temperature.

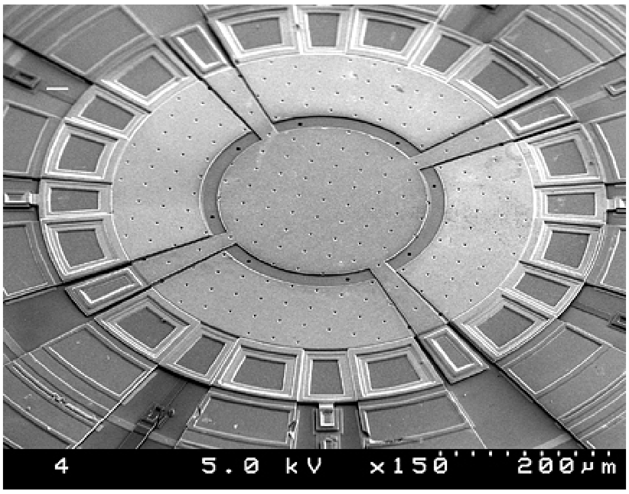

Figure 2.9 Surface micromachined micromotor-based IMU developed at the Case Western Reserve University (**private communication**).

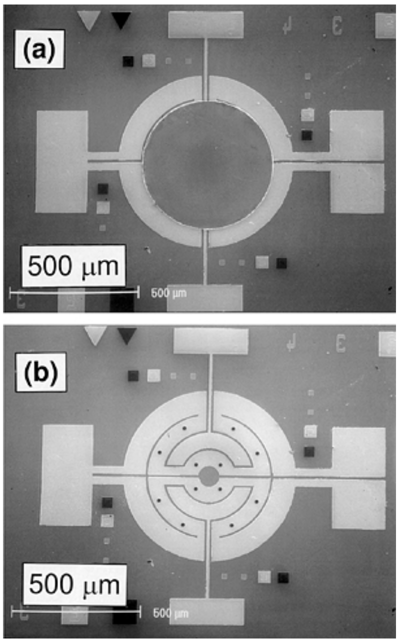

Figure 2.10 Electromagnetic induced rotational micromotor [**81**].

Recent developments from Tokimec, Inc. (Japan) have demonstrated the potential of a spinning gyro using a microfabricated, ring-shaped rotor, implemented into an analogue feedback control system [**17, 98–100**]. The Tokimec gyro was fabricated using bulk micromachining technique (Figure 2.11). Top and bottom electrodes were patterned on glass substrates and the ring rotor was fabricated on silicon or SOI wafers. Glass/Silicon/Glass substrates were assembled together by anodic bonding. The control system employed in the Tokimec gyro was based on an analogue frequency-multiplexing closed-loop system. A 6.5 mV/deg/s sensitivity, 0.05 deg/s resolution and 0.15 deg/hr$^{1/2}$ noise floor at a bandwidth of 10 Hz were reported.

Robert Bosch GmbH (Germany) patented a similar work to the Tokimec gyro with the difference in a design of sense and control electrodes [**101**]. Archangel System, Inc. (USA) also patented the on-going development of a motion sensor employing two spinning discs, rotating in opposite directions to detect a rate of rotation [**102**]. However, no literature about their results is publically released so far.

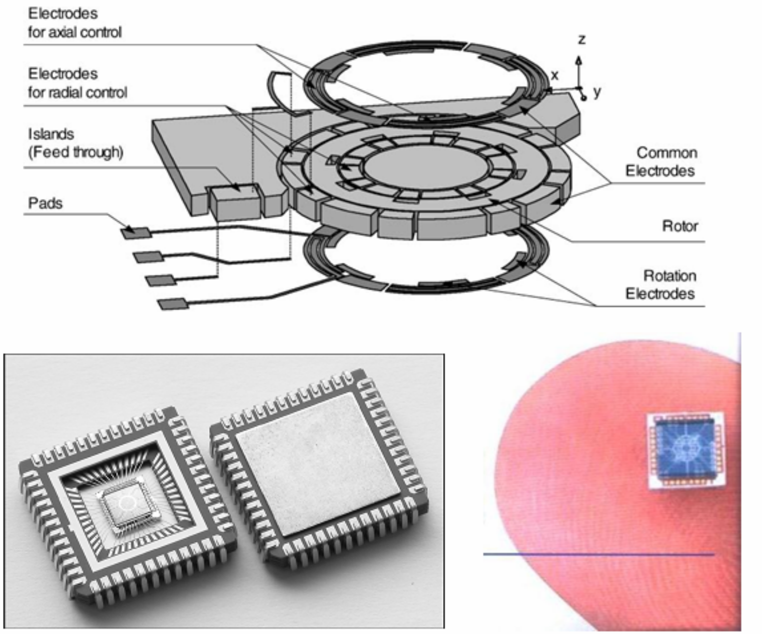

Figure 2.11 Tokimec spinning gyroscopes [**17**]

Almost all of spinning MEMS gyros reported to date employ analogue closed-loop system to control the rotor position. Such a control system has some disadvantages such as a nonlinear feedback relationship and stability problem for large deflections of a proof mass [**18**]. The instability issue is also known as the *electrostatic latch up* effect where a proof mass is attracted to one side of electrodes. To overcome the latch up problem, Kraft *et al.* proposed a digital control system based on sigma delta modulation (ΣΔM) for capacitive microsensors [**103–105**]. Basically, only electrodes on one side of the rotor are energised to maintain the position of the rotor at the nominal position, while the other side is grounded. This will prevent the latch up effect resulted from analogue feedback control. Kraft *et al.* [**11**] and Houlihan *et. al.* [**12, 106**] exploit the benefit of ΣΔ feedback control to realise a multi-axis microaccelerometer employing a levitated disc proof mass. Figure 2.12a shows a conceptual illustration of the micromachined sensor employing a levitated disc. Two fabrication processes were investigated, including nickel electroplating [**107, 108**] and DRIE process [**12**]. Figure 2.12b shows the fabricated prototype accelerometer employing a levitated proof mass.

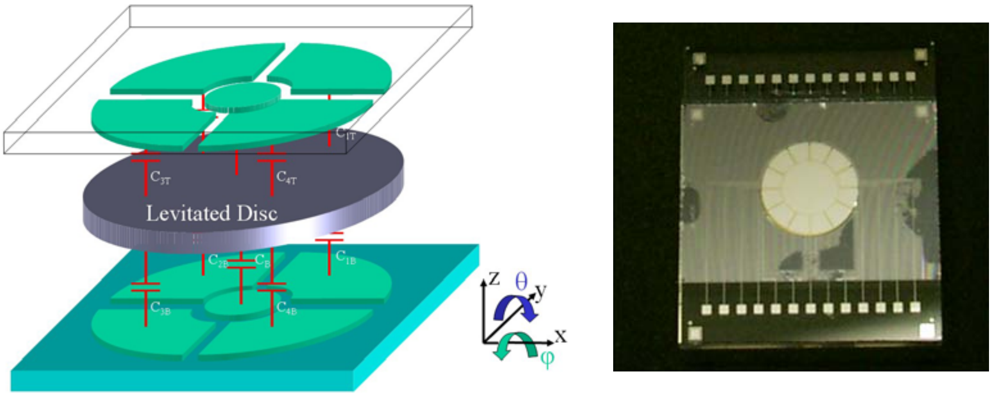

(a) (b)

Figure 2.12 Multi-axis microaccelerometer with an electrostatically levitated disc [**106**]: (a) conceptual illustration of the sensor and (b) the fabricated prototype sensor.

2.5 CONCLUSIONS

For decades vibrating-type gyroscopes have dominated the research work in the area of MEMS rotation-rate sensors. Numerous types of MEMS vibrating gyroscopes have been developed for a wide range of applications – from automotive and safety applications to consumer applications. However, they have a limit use in military and space applications, in which a high performance gyroscope is required. This is because vibration-type MEMS gyroscopes are extremely sensitive to defects and imperfections, which will result in a decrease in the gyro resolution and bias instability. In recent years, alternative approaches have intensively been investigated in order to achieve a high performance MEMS gyroscope.

One of the most promising alternative approaches is spinning MEMS gyroscopes, whose proof mass is suspended and spun using electrostatic forces. The proof mass has no mechanical connection to substrate, thereby unwanted long-term effects, such as friction and stress, are isolated. This will improve the gyro stability revealing a potential to deliver navigation-grade performance.

Spinning MEMS gyroscopes have been developed since 1990. However, relatively little work has been done to realise such gyroscopes due to the difficulty in microfabrication. At the present time the spinning MEMS gyroscopes are still in the initial phase of development using both surface and bulk micromachining techniques. One of the major issues in the development of spinning MEMS gyroscopes is that the released microstructure (the proof mass) is stuck to a substrate. This could be resulted from device fabrication itself and/or the so-called latch-up effect caused by an analogue control system.

In this research work, a new approach in development of a spinning MEMS gyroscope was investigated. A closed-loop control system based on a ΣΔM was employed in order to avoid the electrostatic latch-up effect. A bulk micromachining technique based on triple-stack wafer bonding was explored to realise a spinning MEMS gyroscope.

Chapter 3

Principle, Design and Analysis of the Micromachined ESG

3.1 INTRODUCTION

A spinning gyroscope, developed in this work, relies on the same principle as a macro-scale electrostatically suspended gyroscope (ESG); thus, it is called a micromachined ESG. The ESG is a two-axis gyro where the spinning levitated rotor is supported by electrostatic forces. The entire micromachined ESG system consists of a micromachined sensing element, and a closed-loop electrostatic suspension control system. This chapter discusses solely the sensing element. The closed-loop electrostatic levitation control system will be described in chapter 5.

In section 3.2 the operating principle of the prototype micromachined ESG is presented. It provides a brief overview of how the micromachined ESG works, followed by a comparison between the micromachined ESG and conventional vibrating MEMS gyros in section 3.3. Section 3.4 describes the dynamic response of the micromachined ESG when used as an accelerometer and a gyroscope. The design of the micromachined ESG is discussed thoroughly in section 3.5. The chapter ends with a summary in section 3.6.

3.2 THE MICROMACHINED ESG: PRINCIPLE OF OPERATION

An exploded view of the micromachined ESG is shown in Figure 3.1. The gyroscope consists of a disc-shaped rotor, surrounded by sets of sense, feedback and spin control electrodes. The electrodes located above and under the rotor are used to detect and control the position of the rotor in three degrees of freedom: the translation in the z-axis and the rotation about the x and y axes. They are also used to control a rotation of the rotor about the spin axis (the z-axis). The electrodes at the outer periphery of the rotor are for in-plane motion control along the x and y axes. Each of the surrounding control electrodes forms a capacitor with the levitated rotor.

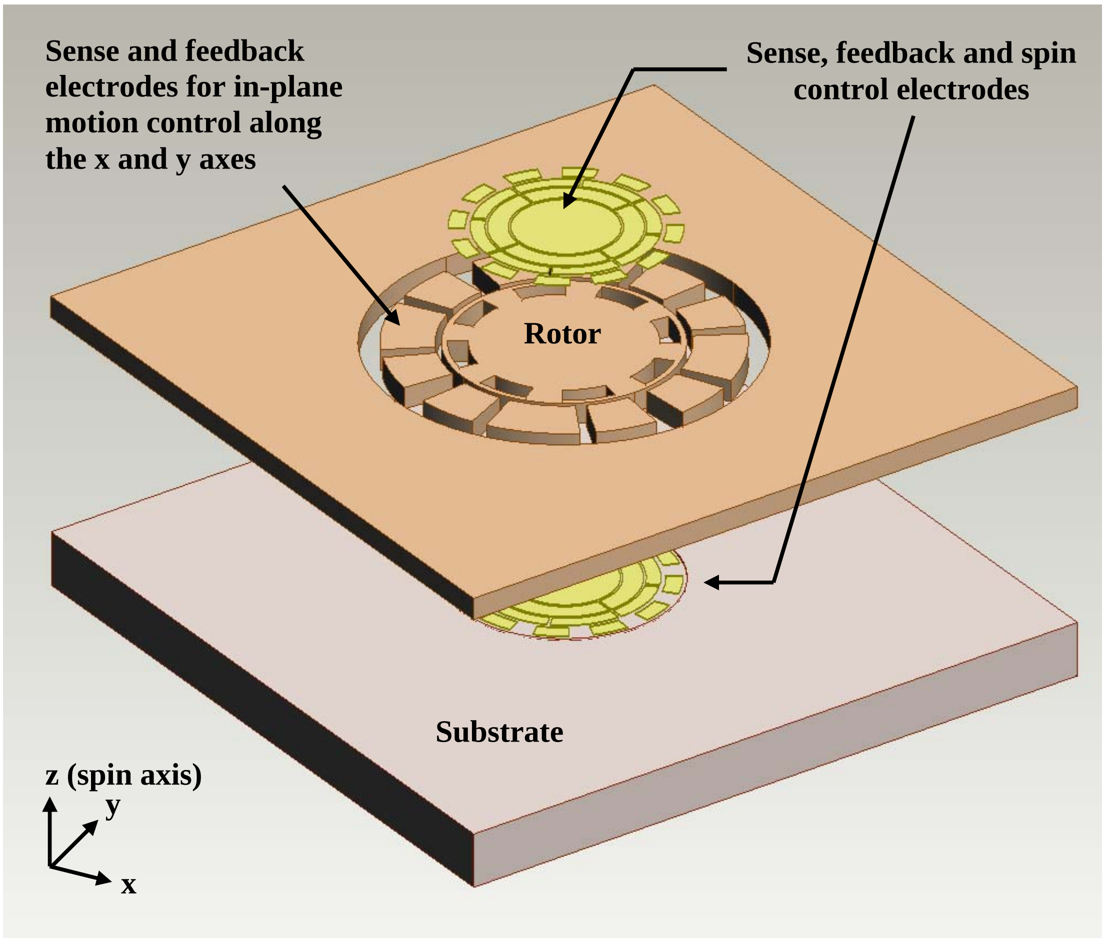

Figure 3.1 Exploded view of the prototype micromachined ESG.

The rotor is levitated and rotated using electrostatic forces produced by applying voltages on sets of control electrodes. When the gyro experiences, for example, a rotation about the y axis, the rotor will displace away from its nominal position about the x axis, which is perpendicular to the spin and input axes (see Figure 3.2b). This can be expressed using the following basic gyroscopic equation [**87**]:

$$M_x = \Omega_y \times I_z \Omega_z \tag{3.1}$$

where M_x is the precession torque, I_z is the moment of inertia of the rotor, Ω_z is the spin speed of the rotor and Ω_y is the input rate of rotation.

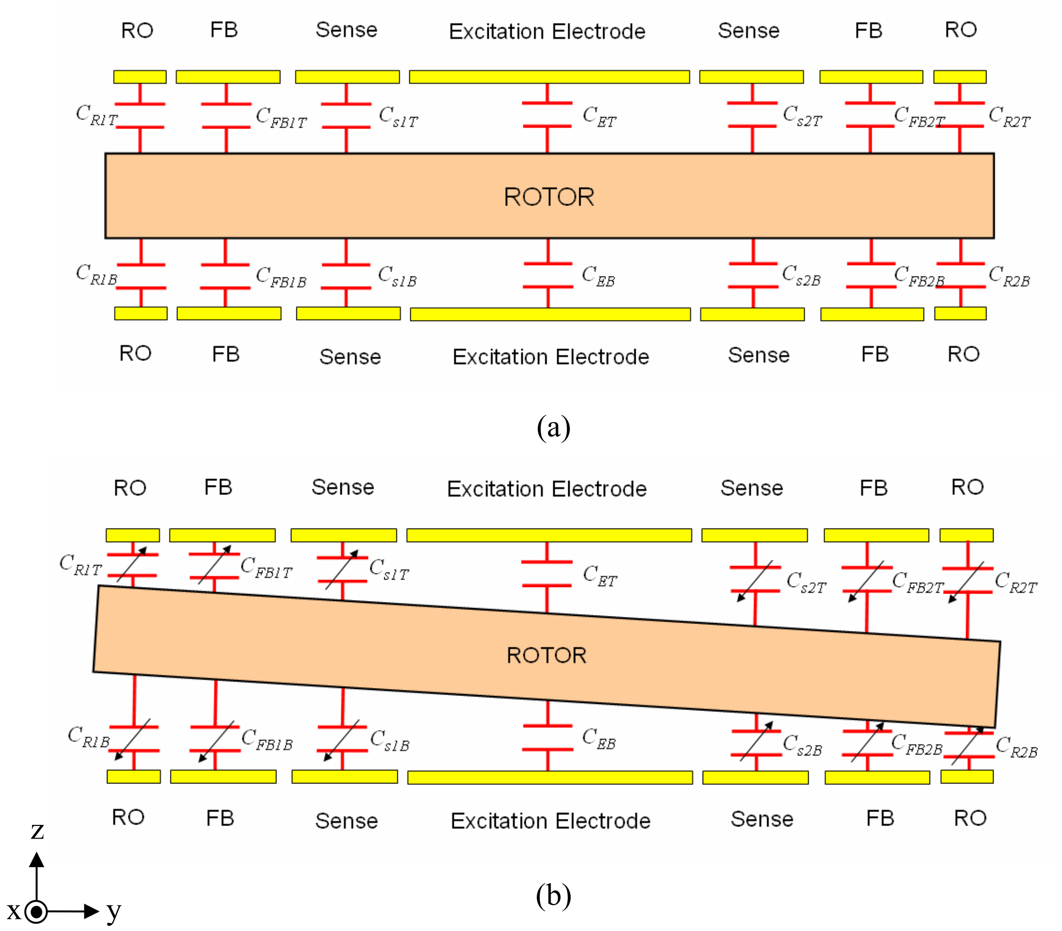

(a)

(b)

Figure 3.2 Illustrations showing the gyro rotor (a) when it is levitated at the nominal position and (b) when it displaces if a rotation about the y axis was applied.

Figure 3.2a shows the rotor at a nominal position where it is maintained at the middle between the top and bottom electrodes. At this nominal position, each capacitor pair has the same capacitance value. For example, sense capacitors, C_{s1T} and C_{s1B}, have the same capacitance value; and also capacitors, C_{s2T} and C_{s2B}, have the same capacitance value. The precession of the rotor results in a capacitance imbalance in each of the capacitor pairs (see Figure 3.2b). The capacitance of the capacitor C_{s1T} becomes greater than that of the capacitor C_{s1B}; and capacitor C_{s2T} has a lower capacitance than that of the capacitor C_{s2B}.

The capacitance imbalance is differentially sensed by a closed-loop electrostatic suspension control system. The system, in turn, produces electrostatic feedback forces to counteract the movement of the rotor, nulling it back to the nominal position. Due to the servo feedback principle, these feedback forces are related to the precession torque and, thus, provide a measure of the rotation rate (assuming the rotor spins at a constant velocity).

3.3 ADVANTAGES OF THE MICROMACHINED ESG

The micromachined ESG has several advantages compared with conventional MEMS vibratory gyroscopes. Inherently, the micromachined ESG has no quadrature error[1], which is one of the major issues in the development of MEMS vibratory gyroscopes. There is also no need to tune the drive and sense resonance frequencies; hence, the micromachined ESG is less sensitive to fabrication tolerances. Since the levitated spinning rotor is free to move in any degree of freedom, the micromachined ESG can be used to measure linear acceleration along the three axes simultaneously. More details of this topic are discussed later in section 3.4.

In the following, an initial calculation is performed to compare the sensitivity of the micromachined ESG to a MEMS vibratory gyroscope. A rotational vibration type gyroscope is considered in this comparison as its basic operating principle is similar to that of the micromachined ESG. More details regarding the rotational vibrating gyroscope can be found in references [**109**]. Figure 3.3a shows a conceptual drawing of the rotation vibration type

---

[1] See chapter 2 for more details on quadrature error.

MEMS gyroscope. Basically, the gyro is driven to vibrate about the z axis, the tilting oscillation about the x and y axes are used to detect rate of rotation. The prototype of the rotational MEMS gyroscope is shown in Figure 3.3b. Ideally, the x and y axes are identical due to its symmetric design. Therefore, it is sufficient to consider only one sensing axis (the x axis).

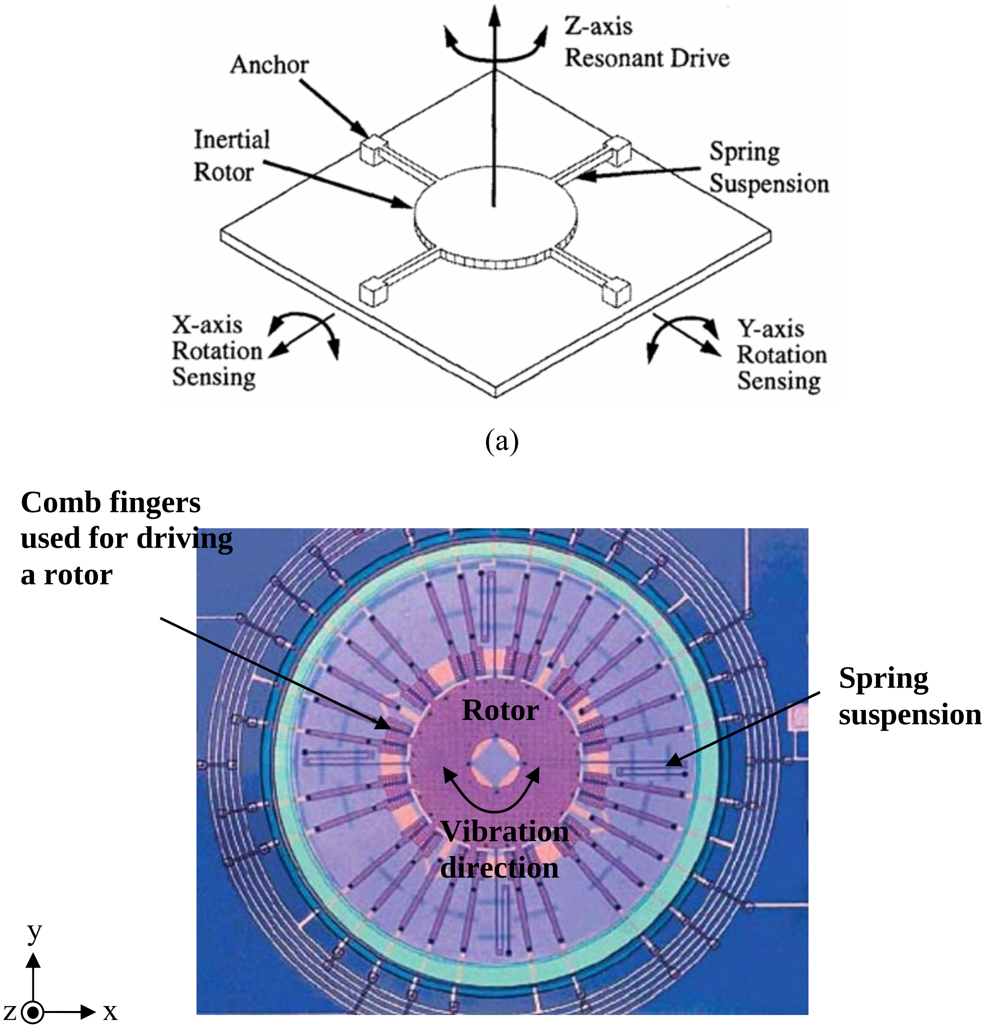

(a)

(b)

Figure 3.3 Rotation vibrating-type MEMS gyroscope: (a) conceptual sketch of the gyro and (b) scanning electron micrograph of the gyro [**109**].

The equation of motion of a rotation vibrating-type MEMS gyroscope is described in Equation (3.2), assuming there is no damping and stiffness coefficients:

$$I_x \alpha_x = I_z \Omega_y \dot{\theta}_z \tag{3.2}$$

where

α_x = Coriolis acceleration in the x axis,

Ω_y = input rotation rate to be measured, and

$\dot{\theta}_z$ = resonant drive angular rate.

For the gyro with a disc shape structure, the moment of inertia about the z axis I_z is two times greater than the moment of inertia about the x and y axis $I_{x,y}$ (i.e. $I_z = \frac{1}{2} mR^2$ and $I_{x,y} = \frac{1}{4} mR^2$ where m is the mass of the thin disc and R is the disc radius [**110**]). Equation (3.2) can then be re-written as:

$$\alpha_x = 2 \cdot \Omega_y \dot{\theta}_z \tag{3.3}$$

Assuming $\theta_z = \theta_0 \sin \omega_z t$, the mechanical sensitivity for the x axis can then be expressed as:

$$\frac{\alpha_x}{\Omega_y} = 2 \cdot \dot{\theta}_z = 2 \cdot \theta_0 \cdot \omega_z \cos \omega_z t \tag{3.4}$$

where

θ_0 = maximum amplitude of a driving angular displacement and

ω_z = driving angular frequency.

Equation (3.4) can then be compared to the mechanical sensitivity of the micromachined ESG.

From equation (3.1), the mechanical sensitivity of the micromachined ESG is:

$$\frac{\alpha_x}{\Omega_y} = \frac{I_z}{I_x} \cdot \Omega_z = 2 \cdot \Omega_z \tag{3.5}$$

where $M_x = I_x \alpha_x$. Replacing equation (3.5) into equation (3.4) results in:

$$\Omega_z = \theta_0 \cdot \omega_z \cos \omega_z t \tag{3.6}$$

This equation is the rotor spin speed Ω_z of the micromachined ESG that is required to achieve the same sensitivity as the rotational vibration MEMS gyroscope.

To give some idea about the magnitude of the required spin speed, let's put some numbers into equation (3.6). The rotational vibration MEMS gyroscope and the micromachined ESG are assumed to have the same size and material properties. The rotational vibration MEMS gyro is driven at a frequency of 4.4 kHz and a maximum angular displacement of 6 degrees [**109**]. Then, the spin speed required to obtain the same sensitivity as the rotational vibrating gyro can be calculated as shown below:

$$\begin{aligned}\Omega_z &= \theta_0 \cdot \omega_z = \left(\frac{6 \times 2\pi}{360}\right) \times 2\pi \times 4.4 \times 10^3 = 2.9 \times 10^3 \,\frac{\text{rad}}{\text{sec}} \\ &= 2.9 \times 10^3 \times 9.549 \text{ RPM} = 27645 \text{ RPM} \\ &= \frac{27645}{60} \text{ Hz} \approx 460 \text{ Hz}\end{aligned}$$

This means the micromachined ESG employing the levitated rotor, which spins at 27,645 RPM, will have the same sensitivity as the rotational vibration MEMS gyroscope mentioned above. To date, spin speeds greater than 75,000 RPM have been demonstrated [**17**]. Thus, such a micromachined ESG has the potential to achieve higher sensitivity than that of vibrating-type gyroscopes.

It is also interesting to note that the spinning of the rotor will cause an unavoidable wobble due to imbalance of the rotor. This will manifest itself at the rotation frequency. In case of the above example, the frequency of the wobble will be at the spin speed of the rotor, which is equal to 460 Hz. This frequency is about five times higher than the required frequency bandwidth of the navigation grade gyroscope (100 Hz). By spinning the rotor at higher spin speed, these two frequencies will be several of magnitude apart and hence easy to separate electronically.

3.4 DYNAMIC RESPONSE OF THE MICROMACHINED ESG

3.4.1 The micromachined ESG as a three-axis accelerometer

The micromachined ESG, when it is used to measure acceleration, can be modelled using a mechanical mass-spring-damper system. The levitated rotor is modelled as a mass mechanically attached to a rigid frame via an elastic spring and a damper as shown in Figure 3.4. Note that only one degree of freedom, the z-direction, is considered here in order to illustrate its principle.

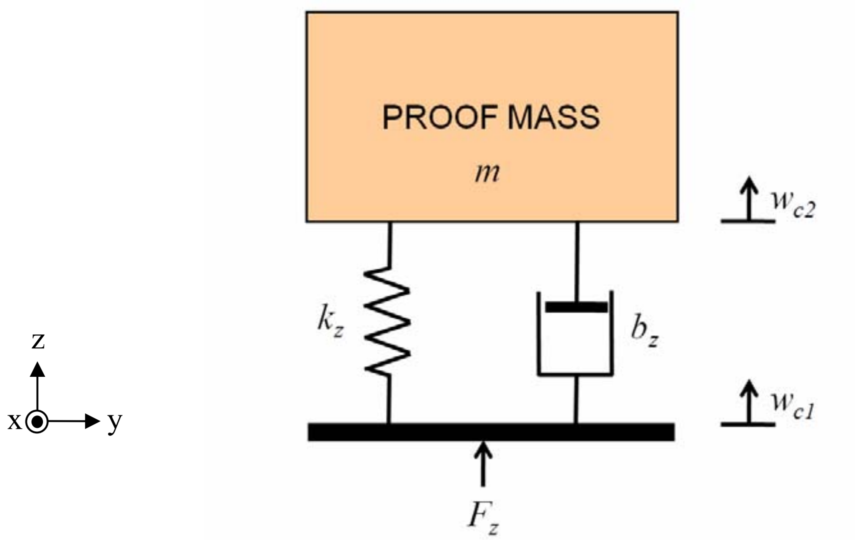

Figure 3.4 Mechanical lumped parameter model of the micromachined ESG when used as an accelerometer along the z axis.

Although the rotor has no actual mechanical spring and damper connecting it to the substrate, the existence of virtual stiffness and viscous damping of the system is due to the so-called squeezed-film and slide-film effects. This is caused by gas molecules in a micron-sized air gap between the rotor and substrate. These effects will be discussed in more details in section 3.5.1.2.

The working principle of the micromachined ESG as an accelerometer is based on Newton's law of motion. When the mass-spring-damper system is subjected to an acceleration in the z axis, a force F_z, equal to the product of the mass of the rotor m and the input acceleration a_z, is generated acting on the system. The basic equation that describes the translational movement of the mass is:

$$m\ddot{z} + b_z\dot{z} + k_z z = F_z \tag{3.7}$$

where b_z is the linear damping coefficient in the z-direction and k_z are the linear spring constant in the z-direction, $z = w_{c2} - w_{c1}$ is the relative displacement of the mass.

The static mechanical sensitivity S_z of the accelerometer is defined as a ratio between the relative mass displacement and the input acceleration. It can be expressed as:

$$S_z = \frac{z}{a_z} = \frac{m}{k_z}. \tag{3.8}$$

And its resonance frequency ω_z is:

$$\omega_z = \frac{1}{\sqrt{S_z}} = \sqrt{\frac{k_z}{m}}. \tag{3.9}$$

The bandwidth of the accelerometer, when it is operated open-loop, is determined by the resonant frequency of the sensor. The sensor bandwidth can be increased by reducing the mass of the rotor and increasing the stiffness constant. However, this will result in lower sensor sensitivity.

Taking the Laplace transform of equation (3.7) and replacing $F_z = ma_z$, the transfer function for the accelerometer can be expressed as:

$$H_z(s) = \frac{z(s)}{a_z(s)} = \frac{1}{s^2 + \frac{b_z}{m}s + \frac{k_z}{m}} = \frac{1}{s^2 + \frac{\omega_z}{Q_z}s + \omega_z^2}, \tag{3.10}$$

where $Q_z = \frac{\sqrt{mk_z}}{b_z}$ is the quality factor.

Equation (3.10) can be used to predict the behaviour of the micromachined ESG when it is employed to measure a linear acceleration in the z-direction. The same approach can also be used to analyse the operation of the micromachined ESG for sensing linear accelerations in the other directions. Their transfer functions in the x and y directions can be described respectively as:

$$H_x(s) = \frac{x(s)}{a_x(s)} = \frac{1}{s^2 + \frac{b_x}{m}s + \frac{k_x}{m}} = \frac{1}{s^2 + \frac{\omega_x}{Q_x}s + \omega_x^2}, \tag{3.11}$$

$$H_y(s) = \frac{y(s)}{a_y(s)} = \frac{1}{s^2 + \frac{b_y}{m}s + \frac{k_y}{m}} = \frac{1}{s^2 + \frac{\omega_y}{Q_y}s + \omega_y^2}. \tag{3.12}$$

3.4.2 The micromachined ESG as a dual-axis gyroscope

The micromachined ESG when used as a rotation rate sensor is described in this subsection. Note that the z axis is defined as the spin axis of the micromachined ESG (see Figure 3.5). In general, the dynamics of the gyroscope is complicated, involving both nonlinear and coupled terms. However, it can be simplified by assuming that the angular motion of the rotor due to precession is relatively small compared to the gap and also the rotor spins at a constant speed, which is higher than the measured angular velocity. Thus, the equations of motion of the micromachined ESG, which is the key to dual-axis operation for the angular motion about the x and y axes, can be expressed as [**87**]:

$$I_x\ddot{\phi} + B_x\dot{\phi} + K_x\phi = I_z\Omega_z\Omega_y \tag{3.13}$$

$$I_y\ddot{\theta} + B_y\dot{\theta} + K_y\theta = -I_z\Omega_z\Omega_x \tag{3.14}$$

where

x,y,z = subscripts that indicate x, y and z (spin) axes, respectively,

I = moments of inertia of the rotor,

B = angular squeeze film damping coefficient,

K = angular squeeze film stiffness,

$\Omega_{x,y}$ = input rate of rotation,

Ω_z = spin speed of the rotor and

ϕ,θ = angular displacement of the rotor about the x and y axes with respect to the substrate, respectively.

When the spinning rotor is experienced angular motion perpendicular to its spin axis, for example, about the y axis with rate of rotation Ω_y, a precession torque about the x axis will be induced, which in turn causes the rotor tilting about the x axis. Due to the symmetrical design of the micromachined ESG in two orthogonal axes, the rotor will tilt about the y axis when it is subjected to rotation motion about the y axis with rotation rate Ω_x.

The mechanical sensitivity of the micromachined ESG, which relates to a precession-induced displacement of the rotor to the substrate rotation rate, can be derived from equations (3.13) and (3.14), which are:

$$\frac{\phi(s)}{\Omega_y(s)} = \frac{I_z\Omega_z}{I_x s^2 + B_x s + K_x}, \tag{3.15}$$

$$\frac{\theta(s)}{\Omega_x(s)} = \frac{-I_z\Omega_z}{I_y s^2 + B_y s + K_y}. \tag{3.16}$$

The term $I_z\Omega_z$ is the sensitivity gain. The faster the rotor spins, the higher the sensitivity. In theory, the maximum spin speed of the rotor is limited by a mechanical centrifugal stress. For silicon, the ultimate physical limit of the rotation speed is about 10^7 RPM [**111**]. In practice, a micromachined motor with a spin speed of 100,000 RPM has been demonstrated so far [**112**]. The rotation speed of the motor was limited by the viscosity of surrounded air, friction and wear.

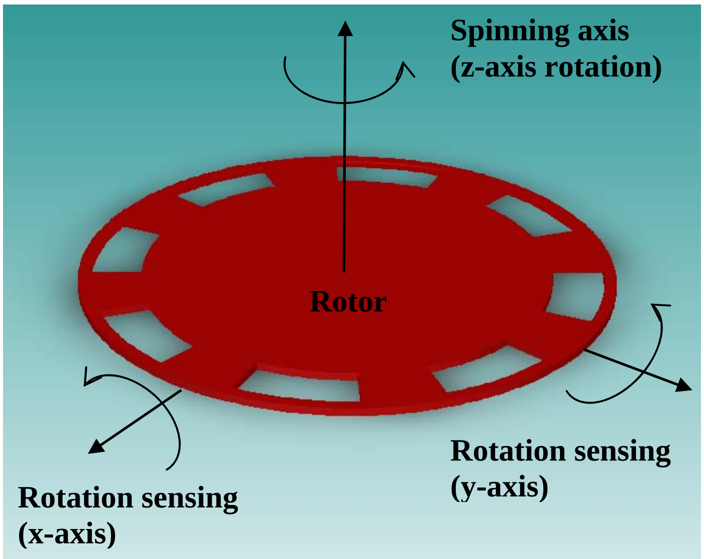

Figure 3.5 Coordinates used to define a rotor position with respect to the substrate.

3.5 DESIGN CONSIDERATIONS FOR THE MICROMACHINED ESG

This section describes the major design issues for the development of the micromachined ESG. In particular, this involves the design of a levitated proof mass and the design of the sense and control electrodes. Firstly, the design of the sensing element, the levitated rotor, is described, followed by a numerical estimation of its spring and damping components. Secondly, the design of the sense and control electrodes is discussed with regard to capacitive position sensing, electrostatic levitation, spinning actuation and lateral position sensing and control.

3.5.1 Design of the levitated spinning rotor

3.5.1.1 Rotor geometry

A macro-scale ESG typically employs a spherical solid rotor coated with highly conductive materials [**113**]. The sphere-shaped proof mass has a high degree of symmetry, offering a symmetric sensitivity in any direction. It is however difficult to make a sphere with current microfabrication technologies [**114, 115**]; hence, the development of micromachined spinning gyroscopes typically uses a disc-shaped [**12, 16, 93**] or ring-shaped proof mass [**99, 100**] as a rotor.

A ring rotor offers good suspension control in lateral directions, i.e. low suspension voltages and high sensitivity in the in-plane x and y axes. This is because electrodes for lateral positioning control can be placed both inside and outside the ring rotor, resulting in large sense and feedback capacitances. However, this is traded off for lower mass and moment of inertia of the proof mass as well as smaller sense capacitances in the gyro sensitive axes. Thus, in the design of the micromachined ESG developed in this work, the rotor was designed in disc shape. It has a higher mass and moment of inertia, and also offers larger sense capacitances for measuring the rotation rate.

For the prototype micromachined ESG, the configuration of the rotor is illustrated in Figure 3.6. The openings in the rotor are used for spinning the proof mass using the principle of electrostatic motors [**116**]. This section only deals with the mechanical design of the rotor. Details of rotor spinning are given in section 3.5.2.3.

The mass m of the rotor and the moments of inertia I_x I_y and I_z can be calculated by:

$$m = \rho \pi R_o^2 h - 8\left(\frac{\theta_2}{2}\rho h\left(R_m^2 - R_i^2\right)\right) \tag{3.17}$$

$$I_z = \frac{1}{2} m R_o^2 \tag{3.18}$$

$$I_{x,y} = \frac{1}{4} m R_o^2 + \frac{1}{12} m h^2 \tag{3.19}$$

where

h = thickness of the rotor

R_o = radius of the rotor and

ρ = material density of the rotor; in case of silicon, $\rho = 2330$ kg/m^3.

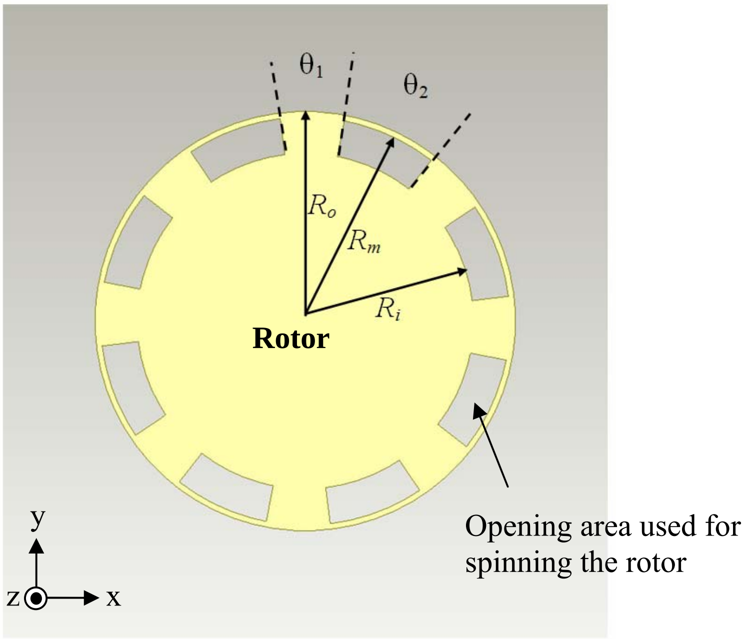

Figure 3.6 Conceptual drawing of the rotor employed in the design of the micromachined ESG.

The first prototype of the micromachined ESG was designed with device dimensions shown in Table 3.1. The rotor dimensions and the distance between the rotor and electrodes were chosen in such a way that a sense capacitance was greater than 1 pF (see section 3.5.2.1 for the design of sense capacitors); and a voltage required to levitate the rotor was low, less than 15 V (more detail about electrostatic levitation, see section 3.5.2.2). The design and dimension of opening areas used for spinning the rotor was discussed in section 3.5.2.3. From the given numbers, the mass and moment of inertias of the rotor can be calculated using Equations (3.17) – (3.19), which yield $m = 3.73$ mg, $I_x = I_y = 3.75\times10^{-12}$ kg m^2 and $I_z = 7.47\times10^{-12}$ kg m^2, respectively.

Table 3.1: Geometrical dimensions of the rotor in the prototype micromachined ESG.

Device dimensions	**Value**	**Unit**
Inner radius, R_i	1550	μm
Intermediate radius, R_m	1900	μm
Outer radius, R_o	2000	μm
Thickness, h	200	μm
Angle of the fin, θ_1	18	deg (°)
Angle of the hole, θ_2	27	deg (°)
Capacitive gap when the rotor is at the middle position between upper and lower electrodes, z_o	3	μm

3.5.1.2 Estimation of stiffness and damping coefficients

Equivalent spring and damping forces are present in the system of the micromachined ESG, even though there is no actual mechanical suspension connecting the rotor to the substrate. This is due to the so-called squeeze film and slide film effects. The slide action refers to the slipping of the moving rotor in a gas ambient causing a surface friction (see Figure 3.7a). This will produce a damping force at the interface between the surface of the rotor and the surrounding air molecules. In contrast, the squeeze action refers to compressing the gas molecules between the rotor and the substrate (see Figure 3.7b). When the rotor rapidly fluctuates about its nominal position, the gas molecules are squeezed to the substrate. The molecules, which cannot escape fast enough from a gap between the rotor and the substrate, are trapped. Thus, a pressure is built up in the central region of the gap, producing resisting forces, which is equivalent to air-spring and damping forces. Accurate modelling of the gas flow through the narrow air gap is important for precise estimation of the stiffness and damping coefficients due to the slide-film and squeeze-film effect [**117, 118**]. However, constructing such models requires an in-depth knowledge of fluidic dynamics, which is beyond the scope of this work. Instead, simpler estimation was employed to approximate these stiffness and damping constants.

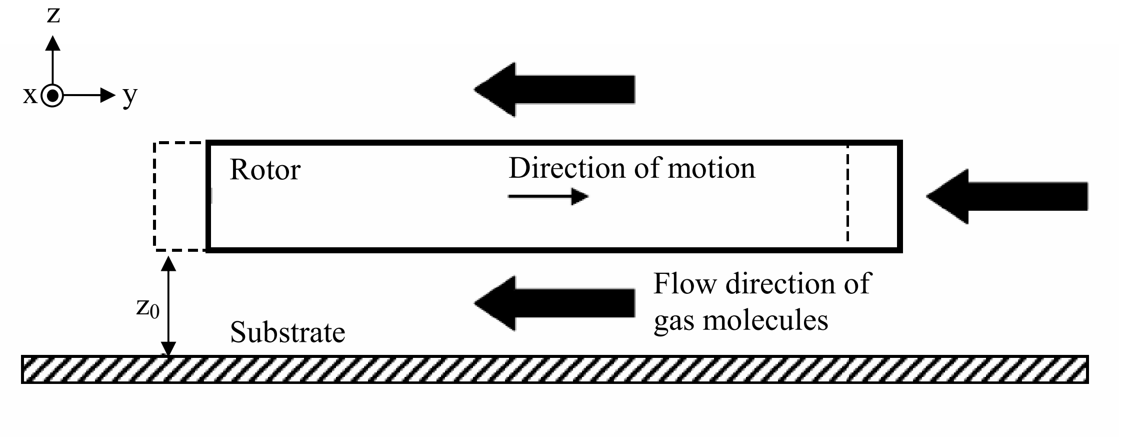

(a)

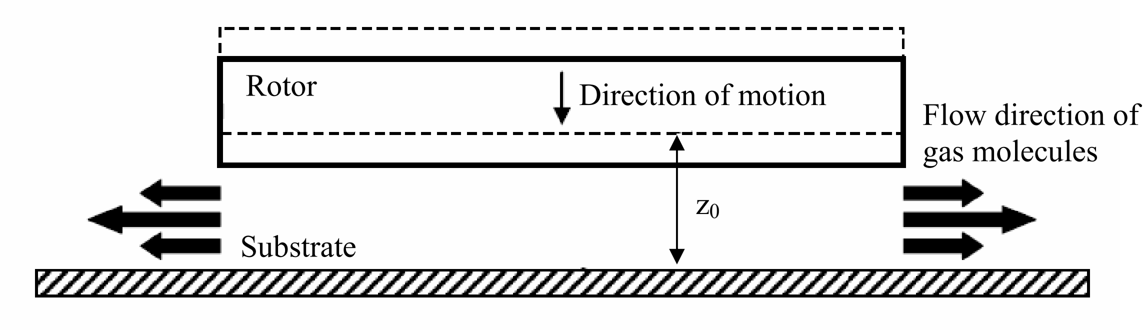

(b)

Figure 3.7 Conceptual illustrations of (a) the slide film effect and (b) the squeeze film effect.

For the micromachined ESG, the slide film effect influences the in-plane motions of the rotor along the x and y axes. Slide film damping, assuming the flow of gas molecules in the space between the rotor and the substrate is Couette flow[2], can be expressed by [**30**]:

$$b_{slide} = \frac{\mu_{eff} A}{z_o} \tag{3.20}$$

where

A = area of the rotor,

z_o = static gap between the rotor and the substrate,

---

[2] Couette flow refers to the flow of the viscous fluid with a constant velocity gradient across the gap.

μ_{eff} = effective viscosity $= \dfrac{\mu}{1+9.638\left(\dfrac{\lambda P_o}{p_o z_o}\right)^{1.159}}$,

P_o = ambient pressure (= 1.013×10^5 Pa),

λ = mean free path at the operating pressure p_o and

μ = viscosity of air (=18.27×10^{-6} Pa s).

On the other hand, the transverse motion of the rotor along the z axis and the out-of-plane motions about the x and y axes are dominated by the squeeze-film damping effect. The analytical solutions for the damping and stiffness coefficients for circular plates moving normal to a fixed substrate (see Figure 3.6) are given by [**119**]:

$$b(\omega) = -\sqrt{\frac{2}{\sigma}}\cdot\left[A_c\left(\mathrm{ber}_1\sqrt{\sigma}-\mathrm{bei}_1\sqrt{\sigma}\right)+B_c\left(\mathrm{ber}_1\sqrt{\sigma}+\mathrm{bei}_1\sqrt{\sigma}\right)\right]\cdot\frac{p_o A}{z_o\omega}, \qquad (3.21)$$

$$k(\omega) = 1+\sqrt{\frac{2}{\sigma}}\cdot\left[A_c\left(\mathrm{ber}_1\sqrt{\sigma}+\mathrm{bei}_1\sqrt{\sigma}\right)+B_c\left(\mathrm{ber}_1\sqrt{\sigma}-\mathrm{bei}_1\sqrt{\sigma}\right)\right]\cdot\frac{p_o A}{z_o}, \qquad (3.22)$$

where ω is the frequency of the rotor fluctuating about its nominal position,

$$A_c = \frac{\mathrm{bei}_0\sqrt{\sigma}}{\left(\mathrm{ber}_0^2\sqrt{\sigma}+\mathrm{bei}_0^2\sqrt{\sigma}\right)},$$

$$B_c = -\frac{\mathrm{ber}_0\sqrt{\sigma}}{\left(\mathrm{ber}_0^2\sqrt{\sigma}+\mathrm{bei}_0^2\sqrt{\sigma}\right)},$$

$\sigma = \dfrac{12\mu_{eff}R_o^2\omega}{p_o z_o^2}$ is the squeeze number for a circular plate with a outer radius R_o. The so-called squeeze number is a dimensionless factor, which provides a measure of the pressure built-up in the central plate area.

Equations (3.21) and (3.22) assume a small displacement of the circular plate and involve Kelvin functions $\mathrm{ber_n}(x)$ and $\mathrm{bei_n}(x)$, which are defined by an infinite series as [**120**]:

$$\mathrm{ber_n}(x)=\left(\frac{1}{2}x\right)^n\sum_{k=0}^{\infty}\frac{\cos\left[\left(\frac{3}{4}n+\frac{1}{2}k\right)\pi\right]}{k!(n+k)!}\left(\frac{1}{4}x^2\right)^k ,$$

$$\mathrm{bei_n}(x)=\left(\frac{1}{2}x\right)^n\sum_{k=0}^{\infty}\frac{\sin\left[\left(\frac{3}{4}n+\frac{1}{2}k\right)\pi\right]}{k!(n+k)!}\left(\frac{1}{4}x^2\right)^k .$$

As obvious from the above equations, the squeeze-film spring and damping coefficients for the disc-shaped rotor have very complex solutions. Yet there is no published literature reporting a general solution for the squeeze-film spring and damping coefficients of a circular plate tilting about its in-plane axes. It is even more difficult to find a solution in case of the micromachined ESG which employs the rotor with open areas. Rather, in this study, alternative approach using finite element simulations in ANSYS was performed to estimate the squeeze film stiffness and damping coefficients. This method assumes small deflections of a microstructure, which is a valid assumption for the micromachined ESG employing a closed-loop control system. Therefore, spring and damping coefficients can be assumed as a constant value.

In ANSYS simulations, a two-dimensional harmonic thermal analysis was performed in an analogous way to determine the squeeze film effect. The simulations were carried out by assuming that there is no fluid resistance across the openings in the rotor since the size of the openings is larger than the depth of the openings. A uniform heat generation rate was applied to the rotor to emulate the oscillating rotor. The resulting temperature distribution analogously represents a normalised pressure distribution across the rotor. Summing the pressure over the surface area of the rotor yields the net resultant force. The net force can then be divided into a velocity and a displacement term to obtain the squeeze-film damping and stiffness coefficients. In-depth discussions on this methodology can be found in reference [**121**].

An example result of the ANSYS simulations is shown in Figure 3.8 for the case of the rotor fluctuating about its nominal position at a frequency of 32 kHz under atmospheric pressure. Figure 3.8a shows the temperature distribution (analogous to the pressure distribution) of the rotor oscillating normal to the fixed substrate. The transverse squeeze film damping and spring constants for motion of the rotor along the z axis can then be extracted by summing the pressure over the surface area of the rotor. Similarly, the pressure distribution of the rotor tilting about the y-axis, obtained from ANSYS simulations, is shown in Figure 3.8b. This simulation was performed to obtain the rotational squeeze-film stiffness and damping coefficients about the y axis.

In general, the squeeze-film stiffness and damping constants depend mainly on two physical parameters, i.e. the oscillation frequency and operating pressure. In the following, ANSYS simulations were carried out to obtain the stiffness and damping coefficients of the micromachined ESG at varying operating pressure and oscillation frequencies. Figure 3.9 and 3.10 show the squeeze-film damping and spring coefficients for transverse motion along the z axis and rotation motion about the y axis, respectively, for ambient pressure ranging from 1 kPa to atmospheric pressure (~100 kPa). The red lines show corresponding damping coefficients with regard to oscillation frequencies. The blue lines represent squeeze-film spring constants corresponding to oscillation frequencies.

As can be seen from Figures 3.9 and 3.10, squeeze-film damping coefficients dominate the mechanical behaviour of the micromachined ESG at relatively low oscillation frequencies. The squeeze-film damping coefficients are relatively high and remain almost constant in a certain frequency range. In contrast, the squeeze-film spring constants are relatively low and become larger with higher frequencies. Beyond certain frequency, the squeeze-film spring constants become dominant as the damping constants drop rapidly with increasing frequencies. This implies that at low frequencies, the squeezed gas film behaves similar to a damper, whereas it acts like a mechanical spring when the rotor oscillating at higher frequencies.

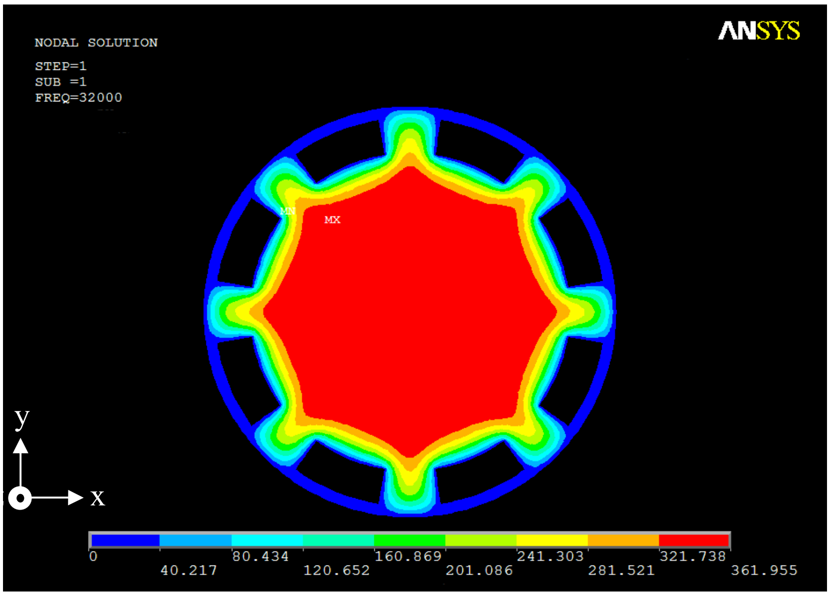

(a)

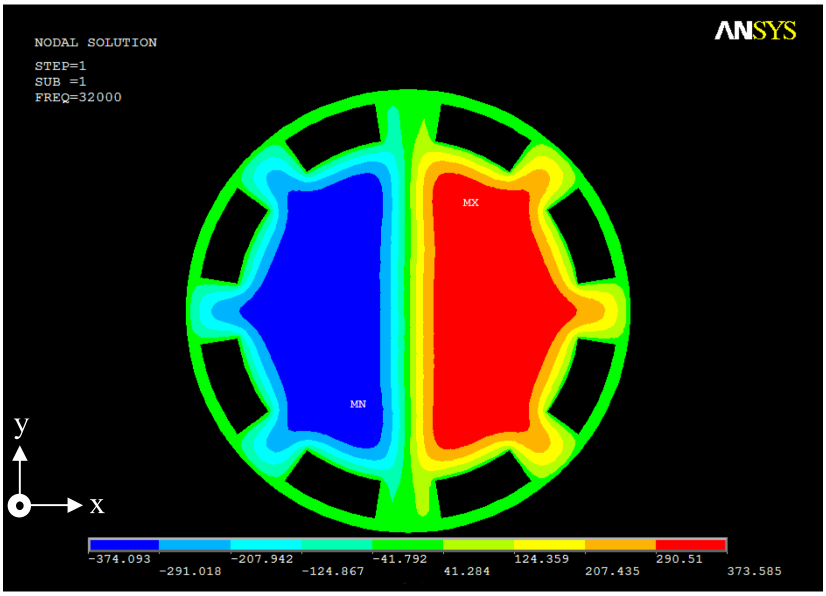

(b)

Figure 3.8 Temperature distribution, analogous to the pressure distribution, across the rotor when it is oscillating at a frequency of 32 kHz under atmospheric pressure: (a) the rotor is moving along the z axis and (b) the rotor is tilting about the y axis. The results were obtained from ANSYS simulations and a 2D thermal analogy. A red colour area is where the built-up pressure is high, while a blue colour area is where the built-up pressure is low.

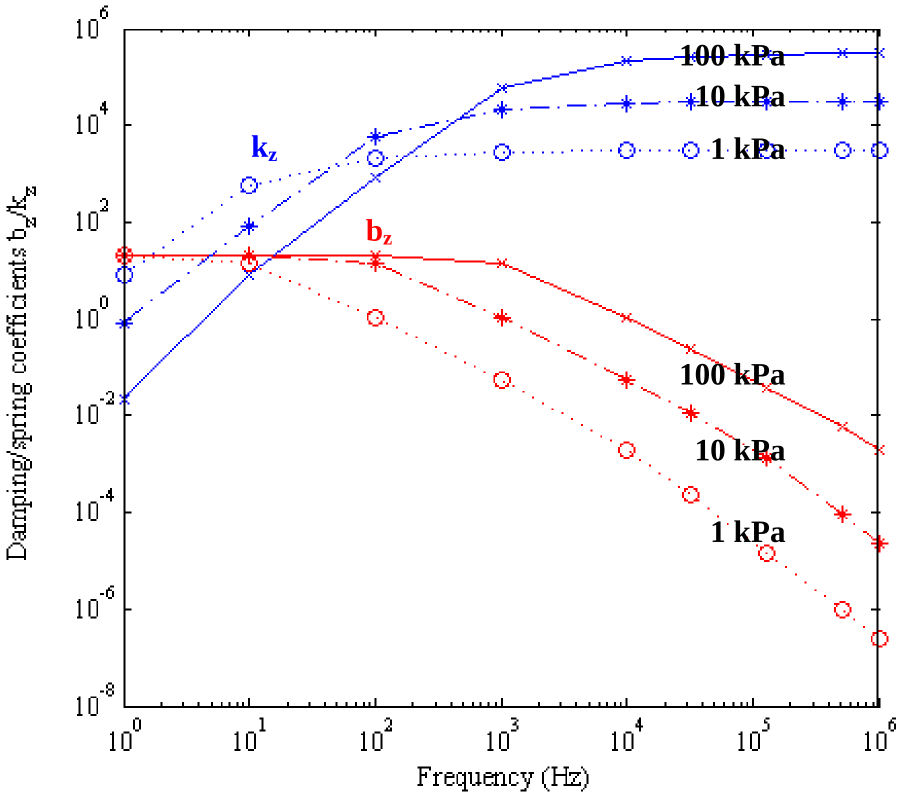

Figure 3.9 Transverse squeeze-film stiffness (blue) and damping constants (red) for different oscillation frequencies for the rotor with a diameter of 4 mm oscillating normal to the substrate. The space gap between the rotor and the substrate is 3 µm. The results were obtained from ANSYS simulations and a 2D thermal analogy.

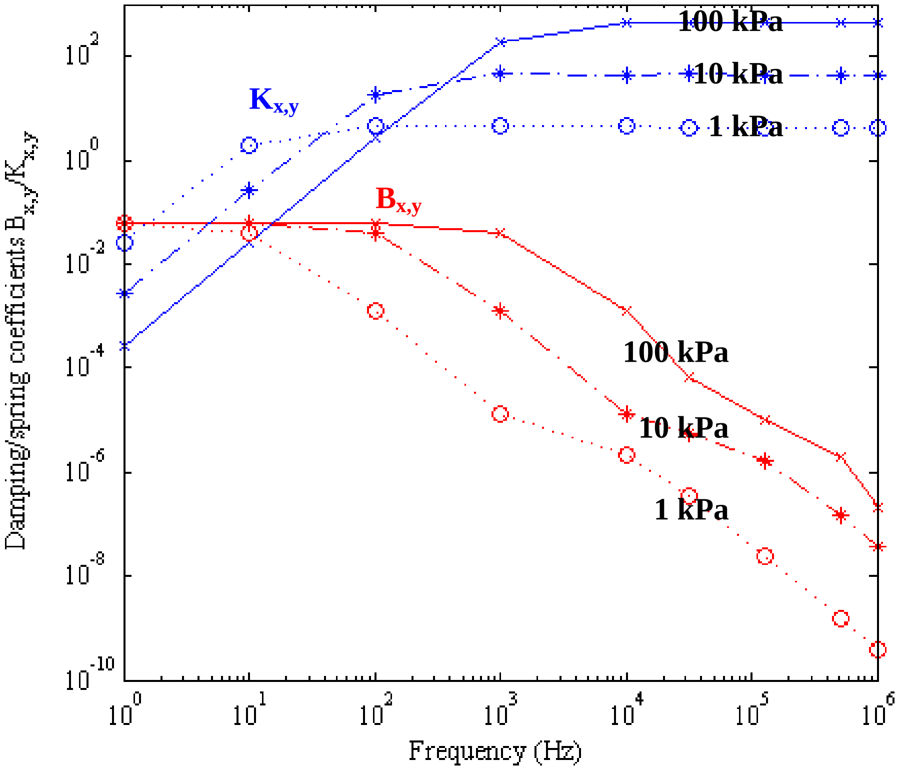

Figure 3.10 Rotational squeeze-film stiffness (blue) and damping constants (red) for the rotor with a diameter of 4mm tilting about the y axis, for different oscillation frequencies. The space gap between the rotor and the substrate is 3 μm. The results were obtained from ANSYS simulations and a 2D thermal analogy.

The relationship between the ambient pressure and the squeeze-film stiffness and damping coefficients is shown in Figures 3.11 and 3.12, for transverse motion along the z axis and rotation motion about the y axis, respectively. For the micromachined ESG, which is implemented with a ΣΔM force feedback loop, the rotor typically fluctuates about its nominal position at a high frequency (for more details see chapter 5). Therefore, in this study the ANSYS simulations were carried out with the assumption that the rotor is oscillating at the following frequencies: 32 kHz, 128 kHz and 512 kHz. As obvious from Figures 3.11 and 3.12, the squeeze-film damping and spring coefficients decrease rapidly as ambient pressure is reduced. This is because at lower pressure there is a small amount of gas molecules inside the gap between the rotor and the substrate. Thus, gas molecules have more chance to escape away from the gap, which consequently reduces the pressure built-up.

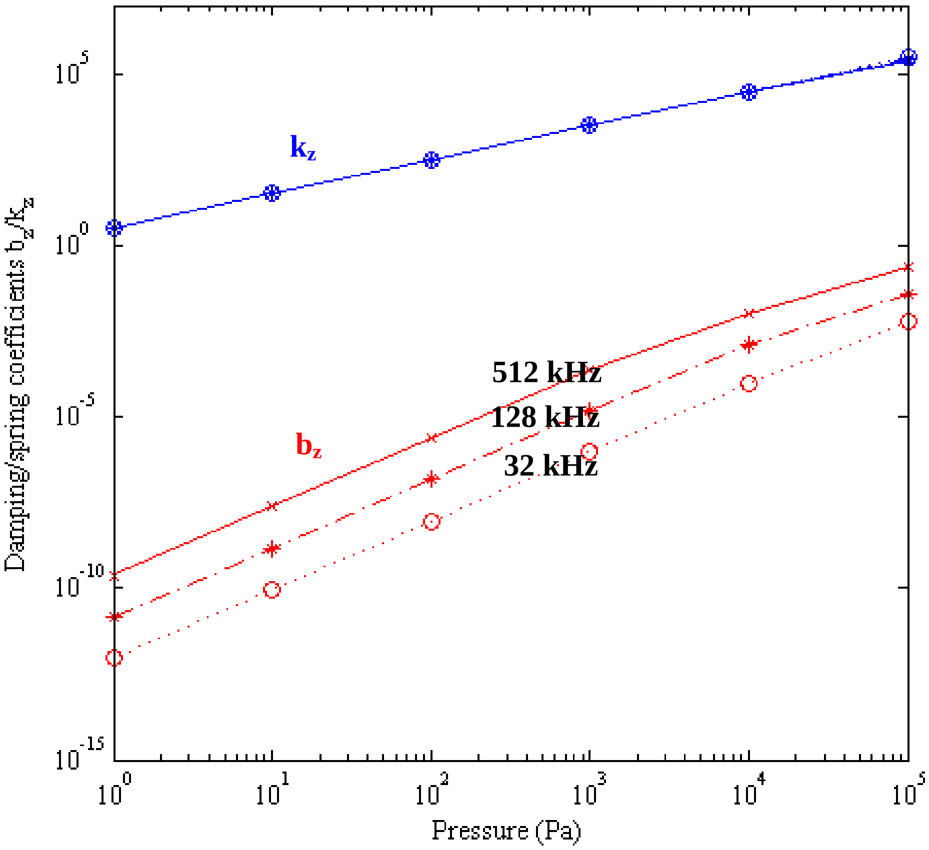

Figure 3.11 Squeeze-film stiffness (blue) and damping constants (red) for the rotor with a diameter of 4mm oscillating along the z axis, for different values of ambient pressure. The space gap between the rotor and the substrate is 3 µm. The results were obtained from ANSYS simulations and a 2D thermal analogy.

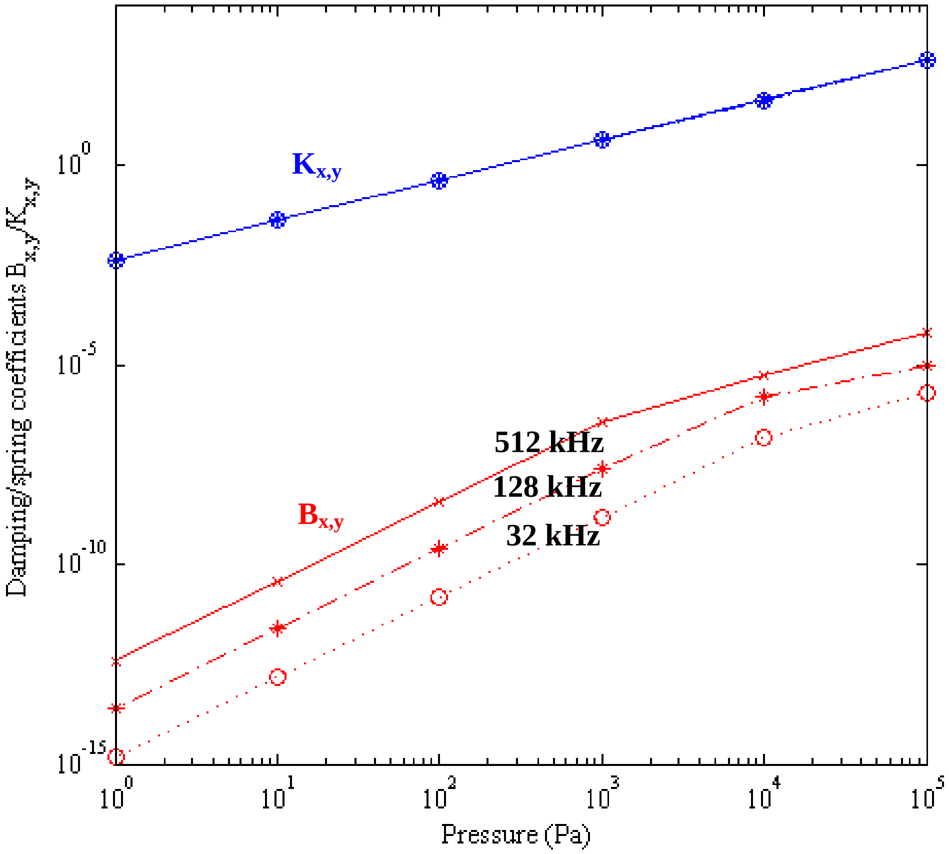

Figure 3.12 Rotation squeeze-film stiffness (blue) and damping constants (red) for the rotor with a diameter of 4mm tilting about the y axis, for different values of ambient pressure. The space gap between the rotor and the substrate is 3 μm. The results were obtained from ANSYS simulations and a 2D thermal analogy.

3.5.2 Electrodes Design

Capacitive sensing and electrostatic actuation, employed in the prototype micromachined ESG, are based on a parallel-plate capacitor. Basically, a capacitor is formed between two conductive surfaces: a fixed electrode and the rotor. Capacitive sensing and electrostatic actuation techniques offer high sensitivity, low drift, low temperature sensitivity and good noise performance, in addition to the ease of fabrication and integration with the micromachining technology [**122**].

The configuration of the electrodes positioned on the top and bottom Pyrex substrates is shown in Figure 3.13. The twelve outermost electrodes are used for rotor spin control. These electrodes are called *rotation control* electrodes. The other electrodes are divided into four quadrants as illustrated in the figure. Each quadrant comprises of three electrodes: one sense electrode and two feedback electrodes. The centre circular-shape electrode is called common *excitation* electrode. It is used to couple an electrical excitation signal, which is required for capacitive position measurement. The four sets of the sense and feedback electrodes, together with the excitation electrode, are used to control the displacement of the rotor in three degrees of freedom, i.e. translation along the z direction and rotation about the x and y axes.

It should be noted that the electrodes that are used for the position measurement, i.e. the excitation and sense electrodes, are placed close to the centre. This is to ensure that all sense capacitors (formed between the sense electrodes and the rotor) have the same capacitance even if the top and bottom electrodes are misaligned to each other due to fabrication tolerances. The actuation electrodes including feedback and rotation control electrodes are located further outside so that a high moment can be produced. Figure 3.14 shows the electrode arrangement for the rotor position control along the x and y directions. The electrodes are positioned at the rotor periphery and also divided into four quadrants. Each set consists of one sense and two feedback electrodes. According to the figure, the top and bottom sets of electrodes are used for rotor position control along the y axis, whereas the left and right ones are employed for translation control along the x direction.

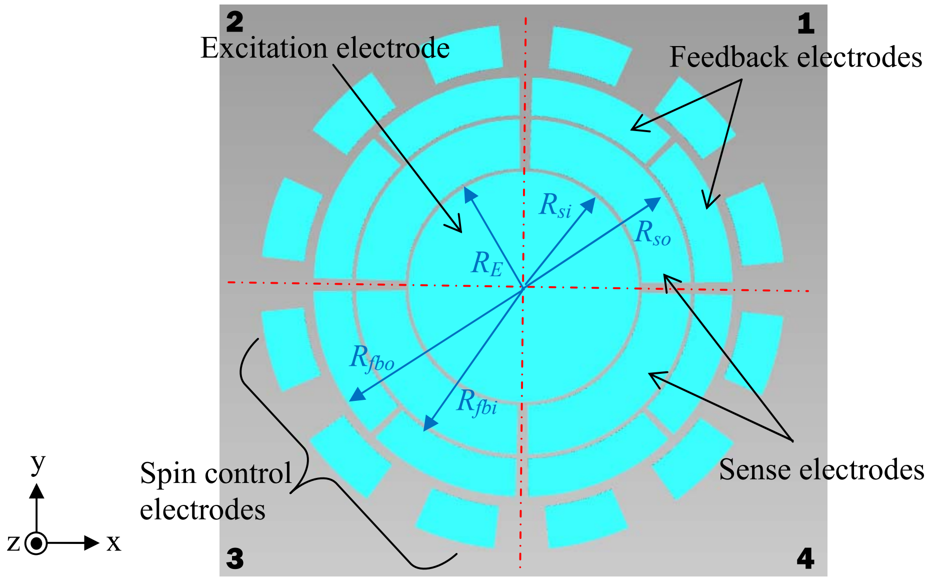

Figure 3.13 Conceptual drawing showing the configuration of the sense and control electrodes which are located on the top and bottom glass wafers. The numbers indicate the quadrant.

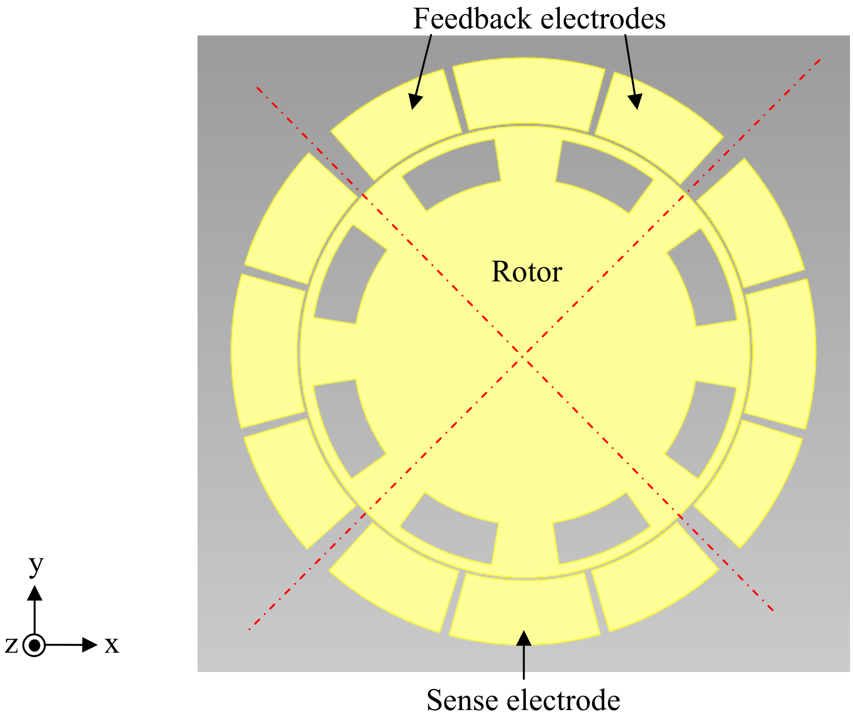

Figure 3.14 Conceptual drawing of the sense and feedback electrodes for lateral control along the x and y axes.

In the following, design and analysis of the capacitive sensing for the motion along the z axis and the rotation about the x and y axes are presented, followed by analysis of the electrostatic feedback and levitation. Then, design, simulation and analysis of the spin control electrodes are discussed in details. At last, the electrode design for the lateral control along the x and y directions are described.

3.5.2.1 Capacitive sensing for the motion along the z axis and the rotation about the x and y axes

As mentioned previously, the electrodes shown in Figure 3.13 are used to control the position of the rotor for motion along the z direction and rotation about the x and y axes. These electrodes are located above and underneath the rotor. The air gap between each of the pie-shaped electrodes and the rotor forms a capacitor (see Figure 3.15). Its capacitance is given by the general equation [**106**]:

$$C = \varepsilon \int_{\alpha_1}^{\alpha_2} \int_{R_i}^{R_o} \frac{r}{Z + r\theta\cos\alpha - r\phi\sin\alpha} dr d\alpha , \tag{3.23}$$

where

ε = dielectric constant (= 8.854×10^{-12} F/m, for air),

Z = distance between the rotor and the electrodes ($Z = z_o - z$ for the top electrodes and $Z = z_o + z$ for the bottom electrodes),

R_i, R_o = inner and outer radii of the electrode, respectively and

α_1, α_2 = angular position of the electrode.

Considering only the first quadrant, the sense capacitance formed between the rotor and the top electrode plate C_{1sT}, where and R_{so} are the inner and outer radii of the sense electrode, respectively, can be expressed as:

$$C_{1sT} = \varepsilon \int_0^{\frac{\pi}{2}} \int_{R_{si}}^{R_{so}} \frac{r}{z_o - z + r\theta\cos\alpha - r\phi\sin\alpha} dr d\alpha , \tag{3.24}$$

By integrating equation (3.24) and using a Taylor series approximation, C_{1sT} with respect to z, ϕ and θ can be estimated as:

$$C_{1sT}(z,\phi,\theta) \cong \varepsilon\left\{\frac{\pi}{4}\cdot\frac{\left(R_{so}^2-R_{si}^2\right)}{z_o-z}+\frac{\left(R_{so}^3-R_{si}^3\right)\cdot(\phi-\theta)}{3(z_o-z)^2}+\frac{\left(R_{so}^4-R_{si}^4\right)\cdot\left(\pi\phi^2+\pi\theta^2-4\phi\theta\right)}{16(z_o-z)^3}\right.$$
$$\left.+\frac{\left(R_{so}^5-R_{si}^5\right)\cdot\left(\phi\left(2\phi^2+3\theta^2\right)-\theta\left(3\phi^2+2\theta^2\right)\right)}{15(z_o-z)^4}+\ldots\right\} \tag{3.25}$$

The capacitances for the capacitors formed between the rotor and the other sense electrodes can be approximated using the same analysis as above. A detailed analysis can be found in reference [**123**].

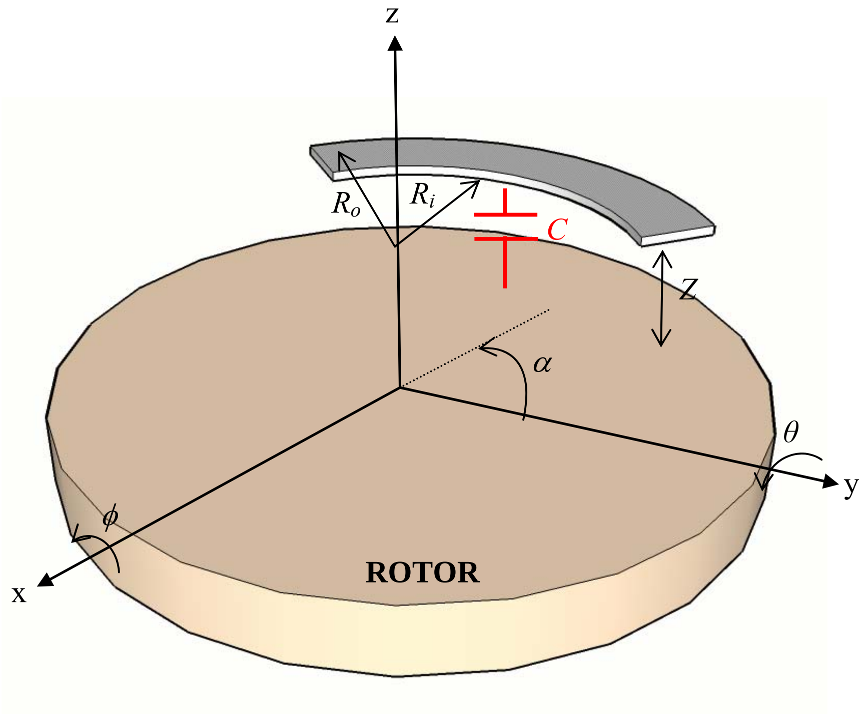

Figure 3.15 Conceptual drawing showing a capacitor formed between the rotor and an electrode above. Its capacitance is a function of the rotor displacement (Z) along the z axis and the tilt of the rotor (ϕ, θ) about the in-plane axes.

For the micromachined ESG, the detection of the rotor displacement is achieved by measuring a differential capacitance between two capacitors (a top and bottom sense capacitors). These two capacitors are designed in such a way that both have the same value of capacitance when the rotor is levitated at the middle between the top and bottom electrodes. The displacement of the rotor away from its nominal position will result in an imbalance between the top and bottom capacitances. For example, if the rotor moves toward the top electrode, the capacitance of the top sense capacitor will be higher than that of the bottom capacitor.

Generally, there are two basic schemes used for differential capacitance measurement. The first one is called a *half bridge* type which is configured for single-ended output. The excitation signals (positive and negative AC signals) are fed into the ends of the capacitive bridge and the output is taken from the centre node (see Figure 3.16a). For multiple sensing nodes, such as in the case of the micromachined ESG, several excitation sources with a different frequency are required as shown in Figure 3.16b. As a result, the output signal at the centre node contains multiple frequencies. The major issue using half-bridge capacitive sensing is the output stability. In order to obtain high output stability, very precise generation of the positive and negative AC signals is required independent of temperature and power supply fluctuation [**124**].

The other capacitive sensing scheme is configured for differential output [**125**] as shown in Figure 3.17. Differential output is achieved by reversing the roles of the centre node and the end terminals. The excitation signal is applied to the centre nodes with the ends providing the differential output signal. With this configuration it is possible to measure multiple sets of sense capacitors in different axes by using only single excitation source. Thus, it was employed in the capacitive position measurement of the prototype micromachined ESG.

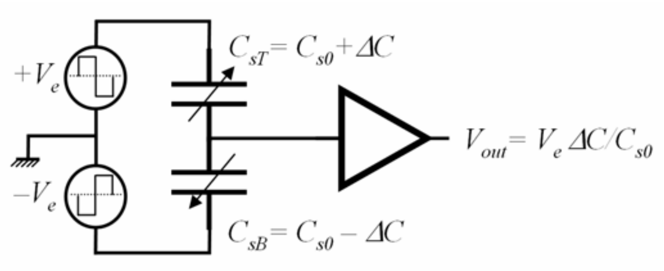

(a)

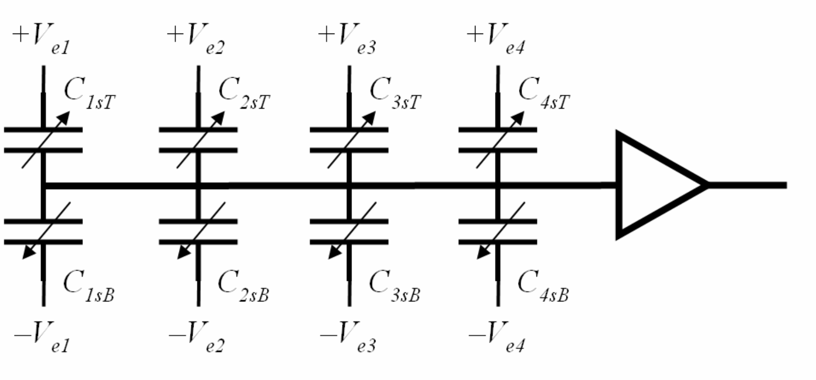

(b)

Figure 3.16 Half-bridge configuration of the differential capacitive sensing: (a) single channel sensing. (b) multi-channel sensing.

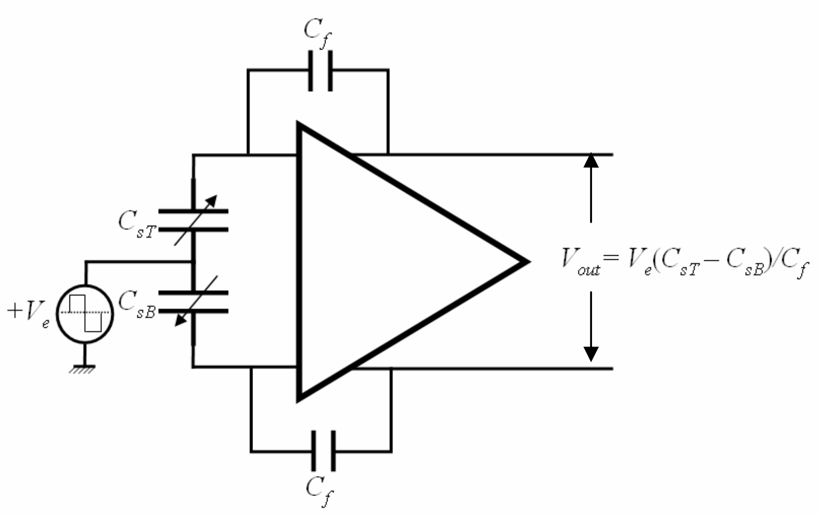

Figure 3.17 Half bridge capacitive sensing configured for differential output.

Since there is no direct electrical contact connecting the rotor to the substrate, the supplementary electrodes are necessary to couple the AC excitation signal through the rotor. This electrode pair is called the excitation electrodes (see Figure 3.13), which are located on the top and bottom glass substrate. The schematic diagram of the differential capacitance measurement for the micromachined ESG is shown in Figure 3.18. Note that only a single channel (one quadrant) of the control electrodes is illustrated.

The equivalent electronic model of the capacitive sensing for multi-channels is presented in Figure 3.19. During the sensing phase, the excitation voltage V_{ac} is applied to the top and bottom excitation electrodes. All feedback and rotation control electrodes are tied to ground and pairs of top and bottom sense electrodes are connected to high input impedance pick-off amplifiers. The pick-off amplifier is modelled as a high impedance resistor connected to ground. The pick-off currents i_{nsT} and i_{nsB} flowing through each top and bottom sense capacitor are given as a function of the capacitances in Equation (3.26).

$$i_{nsT(B)} = \frac{dV_{ac}}{dt} C_{nsT(B)} \frac{C_{ET} + C_{EB}}{C_{ET} + C_{EB} + \sum_{n=1}^{4} C_{nsT} + \sum_{n=1}^{4} C_{nsB} + \sum C_{FB} + \sum C_{R}} \tag{3.26}$$

where

T,B = subscripts that indicate the top and bottom capacitance, repectively,

C_E = capacitances of the excitation capacitors,

C_s = capacitances of the sense capacitors,

$\sum C_{FB}$ = total feedback capacitance and

$\sum C_R$ = total rotation control.

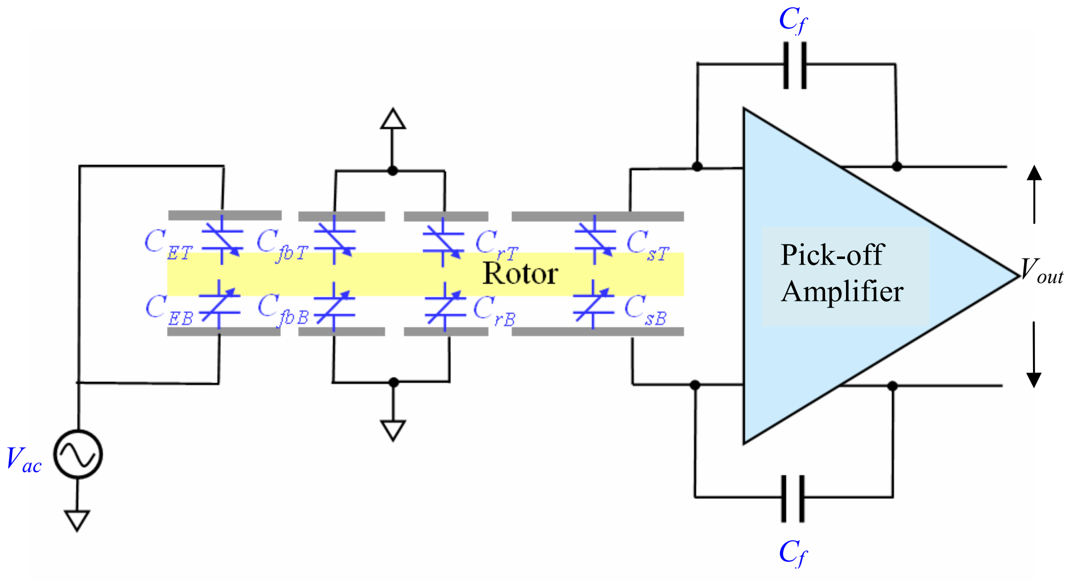

Figure 3.18 Schematic diagram of the capacitive position measurement employed in the prototype micromachined ESG. Only one channel is shown here. The AC excitation signal is applied to the top and bottom excitation electrodes. The excitation signal is then coupled through the rotor to the sense electrodes. During the sensing phase, feedback and rotation control electrodes are grounded.

According to equation (3.26), the magnitude of the pick-off current is proportional to the excitation and sense capacitances, which are related to the geometry of the excitation and sense electrodes. It is interesting to note that the dimension of these electrodes is related to each other ($R_E \approx R_{si}$). Therefore, the optimisation of the electrode design was carried out in order to obtain the maximum pick-off current as a function of the electrode geometry $k = R_{si}/R_{so}$.

Consider the case in which the rotor levitates at nominal mid-position between the top and bottom electrodes. Assuming no feedback and rotation control capacitance, the pick-off current $i_{nsT(B)}$ can then be re-written as a function of the term k as:

$$i_{nsT(B)}(k) = \frac{dV_{ac}}{dt}\frac{\varepsilon \pi R_{so}^2}{z_o}k^2\left(1-k^2\right) \qquad (3.27)$$

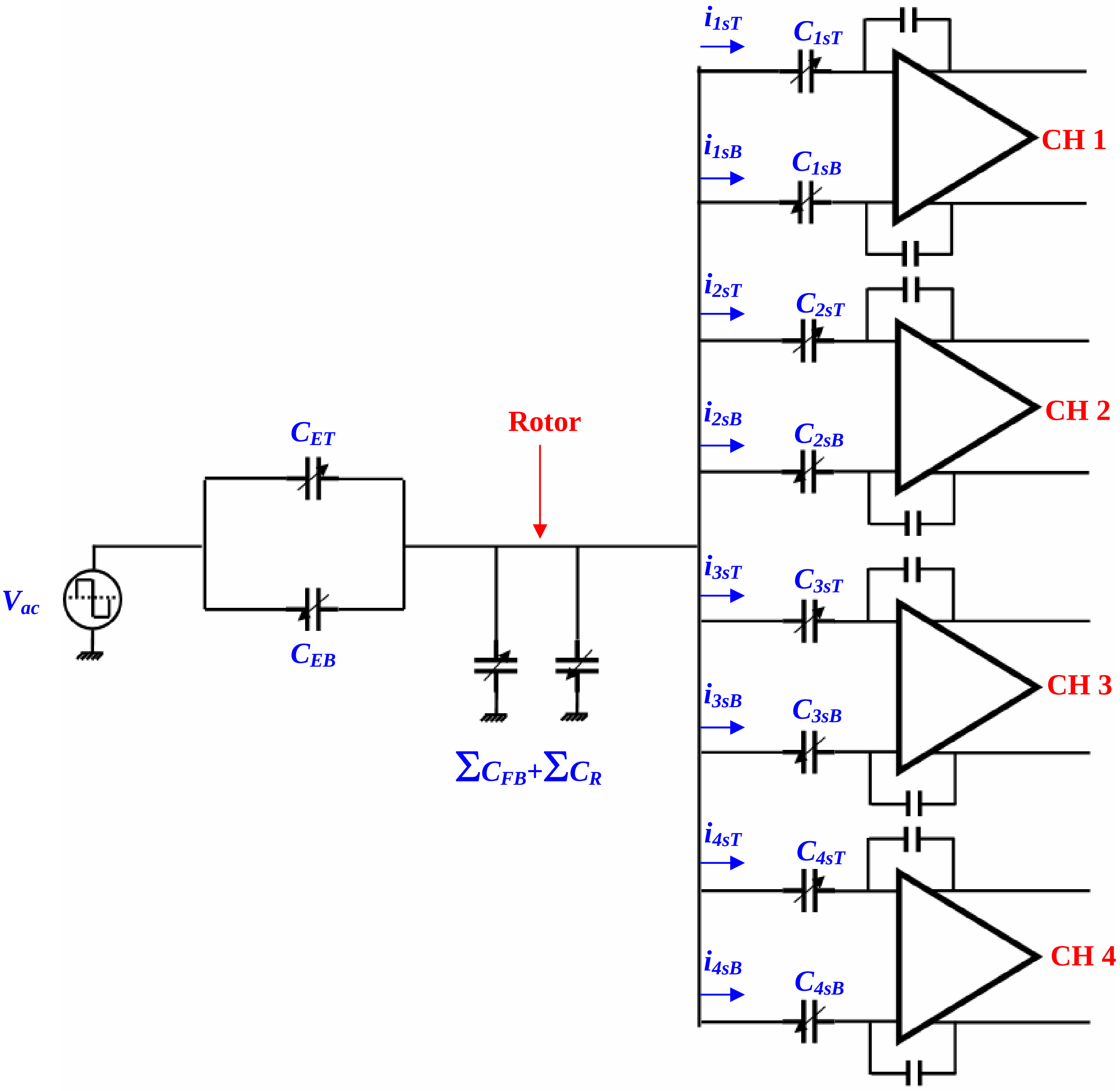

Figure 3.19 Schematic diagram of the multi-channel pick-off circuit employed in the prototype micromachined ESG. The AC excitation signal is applied to the top and bottom excitation electrodes. The excitation signal V_{ac} is applied to the upper and lower excitation electrodes. The pick-off amplifiers have high input impedance. During the sensing phase, feedback and rotation control electrodes are grounded.

Figure 3.20 shows the variation of the pick-off current with respect to the electrode geometry *k*. The maximum pick-off current can be derived from equation (3.27) and also from the plot shown in Figure 3.20. It was found that the optimised readout current occurs when $k = 1/\sqrt{2}$.

3.5.2.2 Electrostatic levitation and force/moment feedback

Stable electrostatic suspension can be ensured by the sets of feedback electrodes surrounding the rotor (see Figure 3.1). Each set is formed by two pairs of feedback electrodes: one pair is positioned on one side of the rotor and the other pair is located on the opposite side. In order to illustrate the concept of electrostatic levitation, let’s consider a simple example for motion of the rotor along only one direction (the z axis). Figure 3.21 illustrates the configuration of a floating rotor and feedback electrodes used in the following analysis. Note that only one set of feedback electrodes is considered here. One pair of feedback electrodes, called *top pair*, is located above the floating rotor; the other, called *bottom pair*, is positioned below.

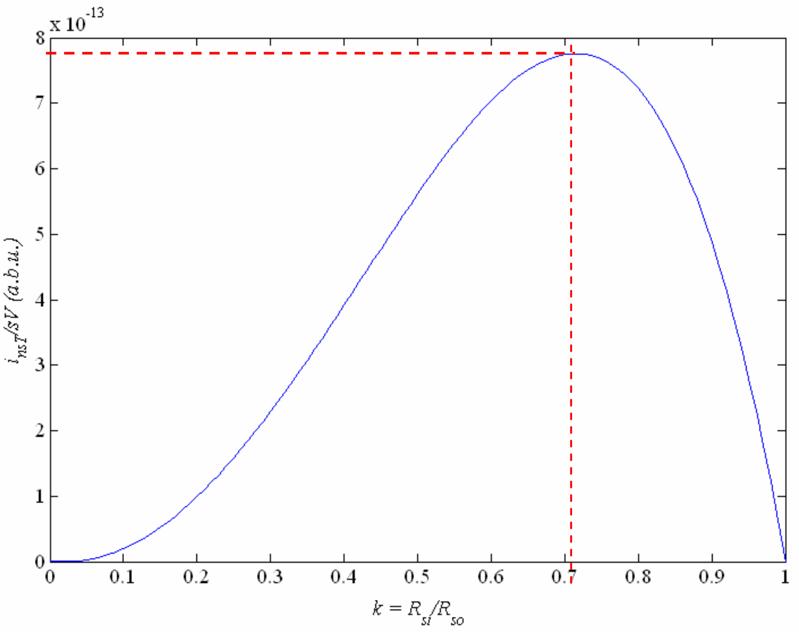

Figure 3.20 Variation of the pick-off current corresponding to the ratio between the inner and outer sense radii *k*. The pick-off current is optimised when $k = 1/\sqrt{2}$, that is, R_{si} = 0.707R_{so}.

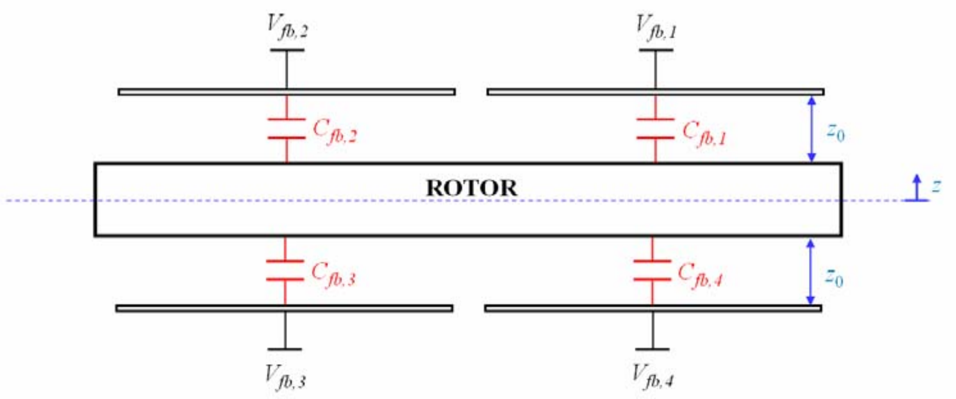

Figure 3.21 Rotor and feedback electrodes configuration employed to illustrate the concept of electrostatic levitation for motion of the rotor along the z axis. Equivalent capacitors (shown in red) are formed between the rotor and feedback electrodes.

Capacitances formed between the rotor and the feedback electrodes with regard to the displacement z can be expressed in the most general form as:

$$C_{fb} = \frac{\varepsilon A}{z_0 \mp z} \tag{3.28}$$

where A is the overlap area between the rotor and the feedback electrode and z_0 is the nominal gap between the rotor and the feedback electrode when the rotor is levitated in the middle position between the top and bottom electrodes. All feedback electrodes are assumed having the same overlap area; thus, all feedback capacitors will have the same value of capacitance when the rotor is levitated at its nominal position ($z = 0$):

$$C_{fb,1} = C_{fb,2} = C_{fb,3} = C_{fb,4} = \frac{\varepsilon A}{z_0}. \tag{3.29}$$

When the rotor is displaced away from its nominal position towards the top pair electrodes, the capacitances of the feedback capacitors will be:

$$\left.\begin{aligned} C_{fb,1} = C_{fb,2} = \frac{\varepsilon A}{z_0 - z} \\ C_{fb,3} = C_{fb,4} = \frac{\varepsilon A}{z_0 + z} \end{aligned}\right\} \tag{3.30}$$

By applying voltages to these feedback electrodes, electrostatic forces are generated. The net electrostatic force F_z acting on the rotor along the z direction can be derived as:

$$\begin{aligned} F_z = \frac{1}{2}\Bigg\{ & \frac{\partial C_{fb,1}}{\partial z}\left(V_{fb,1} - V_r\right)^2 + \frac{\partial C_{fb,2}}{\partial z}\left(V_{fb,2} - V_r\right)^2 - \frac{\partial C_{fb,3}}{\partial z}\left(V_{fb,3} - V_r\right)^2 \\ & - \frac{\partial C_{fb,4}}{\partial z}\left(V_{fb,4} - V_r\right)^2 \Bigg\} \end{aligned} \tag{3.31}$$

where the subscripts 1 – 4 denote the number of electrodes, V_{fb} is the voltage applied to the feedback electrode and V_r is the net potential of the levitating rotor, which can be derived from [**126, 127**]:

$$V_r = \frac{\sum_{n=1}^{4} C_{fb,n} V_{fb,n}}{\sum_{i=1}^{4} C_{fb,n}} \tag{3.32}$$

Assume that the rotor is a conductor and it is maintained at the nominal position. When a positive voltage is applied to the top pair electrode and a negative voltage with the same magnitude is applied to the bottom pair, charges will move within the rotor until the interior field becomes zero. The positive voltage on the upper electrodes draws negative charges to the top surface of the rotor. On the other hand, the negative voltage applied to the bottom-pair electrodes forces positive charges moving to the bottom surface of the rotor. Figure 3.22 illustrates the charge induced on the rotor. From solving equations (3.31) and (3.32), it can be seen that the net electrostatic force acting on the rotor is zero and the rotor potential is maintained at ground potential.

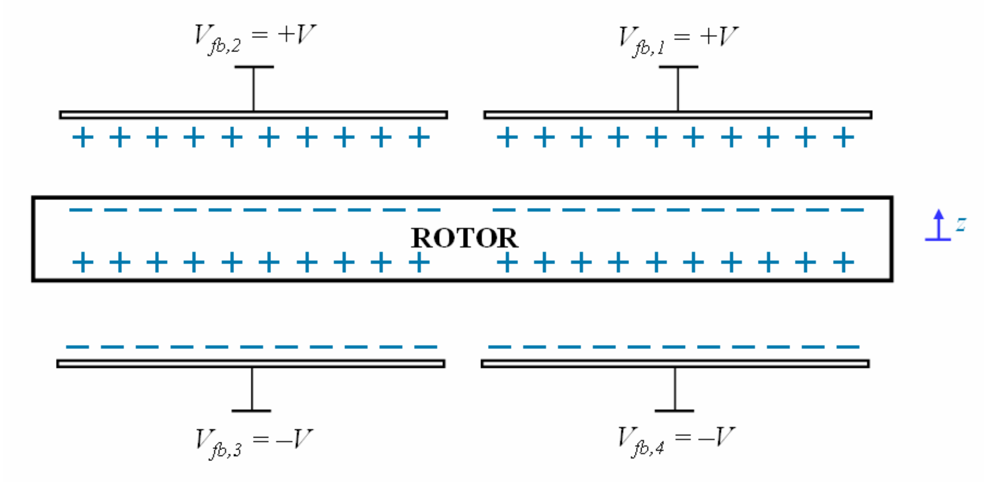

Figure 3.22 Charge distributions in the rotor when a positive voltage is applied to the upper electrodes and a negative voltage is applied to the lower electrodes.

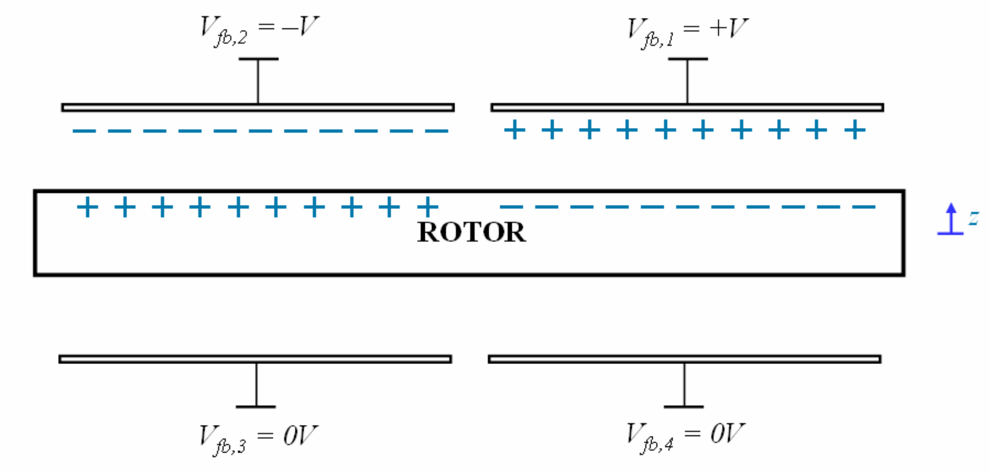

Figure 3.23 Charge distributions in the rotor when a positive voltage is applied to one of the upper electrodes and a negative voltage is applied to the other upper electrodes. The lower electrodes are connected to ground potential.

Alternatively, electrostatic levitation can be achieved by applying positive and negative voltages with the same magnitude to one pair of the electrodes and grounding the electrodes on the opposite side (see Figure 3.23). The applied voltages will draw positive and negative charges to the top surface of the rotor. With this setup, there is no force pulling the rotor toward the bottom-pair electrodes. Only electrostatic force attracting the floating rotor toward the upper electrodes occurs, giving rise to electrostatic levitation. Let's consider the setup in Figure 3.23. Assume that the top pair electrodes are connected to positive and negative voltage sources, which have the same magnitude but opposite polarity, $V_{fb,1} = +V$ and $V_{fb,2} = -V$, and the bottom pair is grounded ($V_{fb,3} = V_{fb,4} = 0$). The resultant electrostatic force F_{net} acting to the rotor along the z direction can be calculated from equation (3.31), yielding:

$$F_{net} = \frac{1}{2}\left\{ \frac{\partial C_{fb,1}}{\partial z}(+V)^2 + \frac{\partial C_{fb,2}}{\partial z}(-V)^2 \right\} \tag{3.33}$$

In order to levitate the rotor, the resultant electrostatic force must be large enough to counteract the sum of the forces acting on the rotor. These forces includes the force of gravity, the damping force on the rotor, the spring force on the rotor, the externally applied inertial force and the pull-off force emerging during the start-up phase where the rotor sits on the bottom substrate. Consider only the simplest case in which only the gravity force acts on the rotor. The generated electrostatic force must then be greater than the force of gravity ($F_{net} > mg$). Thus, the minimum voltage required to levitate the rotor $V_{lev,\min}$ is given by:

$$V_{lev,\min} = \sqrt{\frac{mg(z_o - z)^2}{\varepsilon A}} \tag{3.34}$$

However, the levitation voltage applied to the feedback electrodes should be kept as low as possible to avoid electric discharge at the gap between the rotor and feedback electrodes. This can be achieved by reducing the nominal gap z_0. For micro-scaled devices, the minimum electric breakdown field occurring under atmospheric pressure is approximately 360 V at a gap of 6.6 μm (see the Paschen curve in references [**128**]). The breakdown voltage should rise with narrower or wider gap spacing. Chen *et. al.* have studied this phenomena for MEMS device with different micron separations [**129**]. When the gap distance approaches 5 μm, the minimum breakdown voltage occurs at the voltage of 340 V (for electrodes made of n-type silicon) and 375 V (for p-type silicon), respectively. The minimum breakdown voltage is 320 V at 2 μm separation for metal electrodes.

Two dimensional electrostatic simulations in ANSYS were carried out to verify the concept of electrostatic levitation. The configuration of the rotor and electrodes as shown in Figure 3.21 was modelled in the ANSYS simulations. The gap between the rotor and electrodes y_0 is 5 microns. Assume that the rotor is made of highly conductive silicon and it is floating at the middle between the top and bottom electrodes. Figure 3.24a shows the resulting potential distribution in the case that a positive voltage (+10 V) is applied to the upper electrodes and a negative voltage (–10 V) is connected to the lower electrodes. The extracted potential distribution along the path defined by A–A' is illustrated in Figure 3.24b. The potential of the rotor lies at 0 V and the voltage varies linearly across the gap. Consequently, the electric field is uniform and equal for both the upper and lower gaps. The resulting forces on the rotor are then equal in magnitude but act in opposite directions. This yields a net force on the rotor of zero.

Figure 3.25 shows the distribution of potential when a positive voltage of +10 V is connected to one of the upper electrodes and a negative voltage of –10 V is applied to the other one, while the lower electrodes are grounded. The potential of the rotor is close to the voltage applied to the lower electrodes (0 V). Thus, the electric field between the rotor and the lower electrodes is relatively small. On the other hand, the electric field between the rotor and the upper electrodes is significantly higher. This results in the net electrostatic force moving the rotor towards the upper electrode, giving a rise to electrostatic levitation. ANSYS simulations were carried out to investigate the net vertical force F_{z0} as a function of a vertical displacement z. The following device parameters were used in the simulations: the rotor diameter is 200 μm, the thickness of the rotor is 20 μm, a nominal capacitive gap is 5 μm and each electrode is 90 μm long. Note that the resulting electrostatic force calculated from 2D ANSYS simulations is the force per unit length. Figure 3.26 shows the relationship between the resulting electrostatic levitation force F_{z0} and the displacement of the rotor z along a vertical direction. It can be seen that the results obtained from ANSYS simulations agreed well with the analytical calculation (using equations (3.32) and (3.33)).

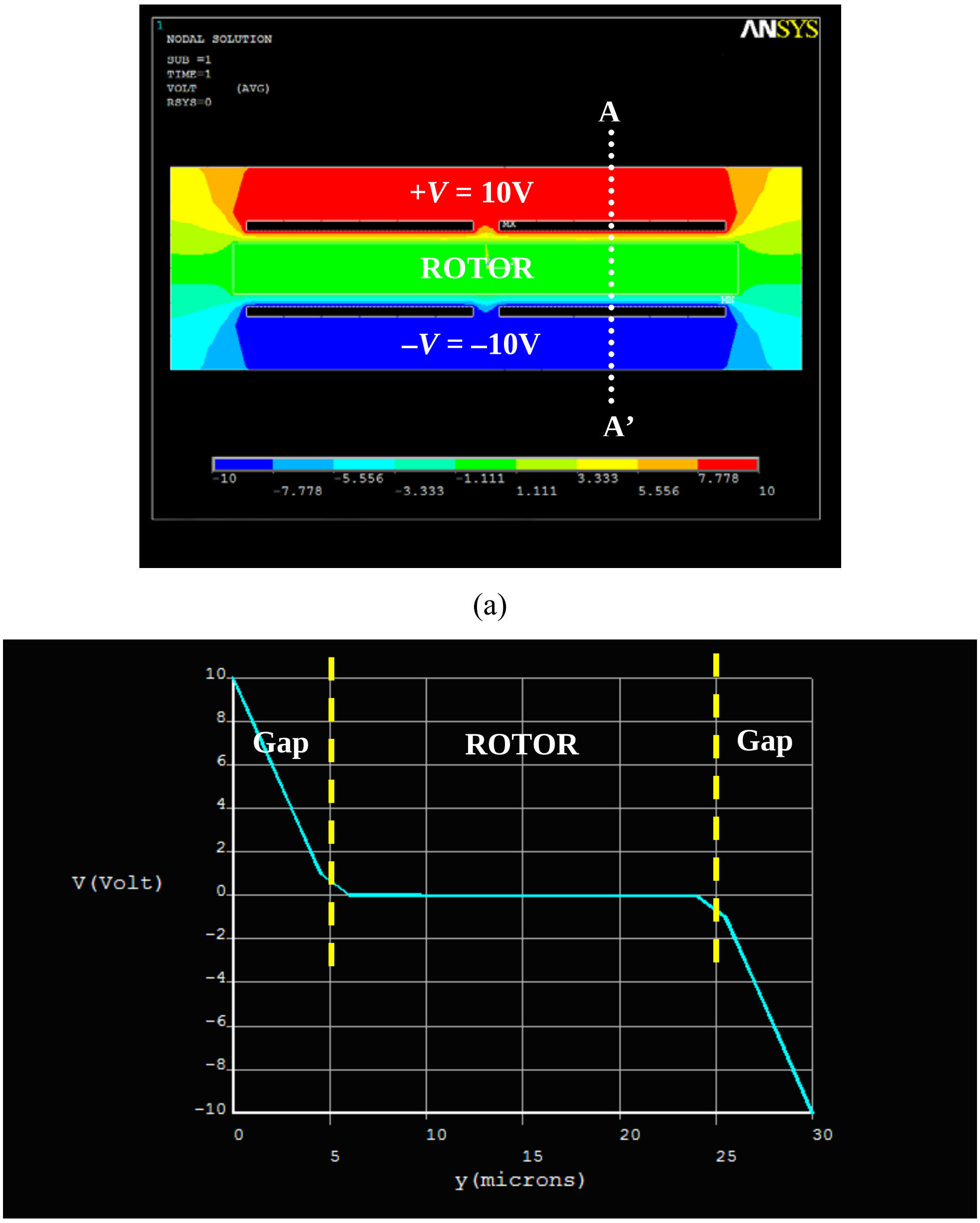

(a)

(b)

Figure 3.24 Simulation results obtained from 2D electrostatic analysis in ANSYS for the rotor levitating in the centre position between the upper and lower feedback electrodes: (a) The contour plot of the potential distribution when the upper electrodes are connected to a positive voltage of 10 V and the lower electrodes are connected to a negative voltage of –10 V. (b) The potential distribution along path A–A’.

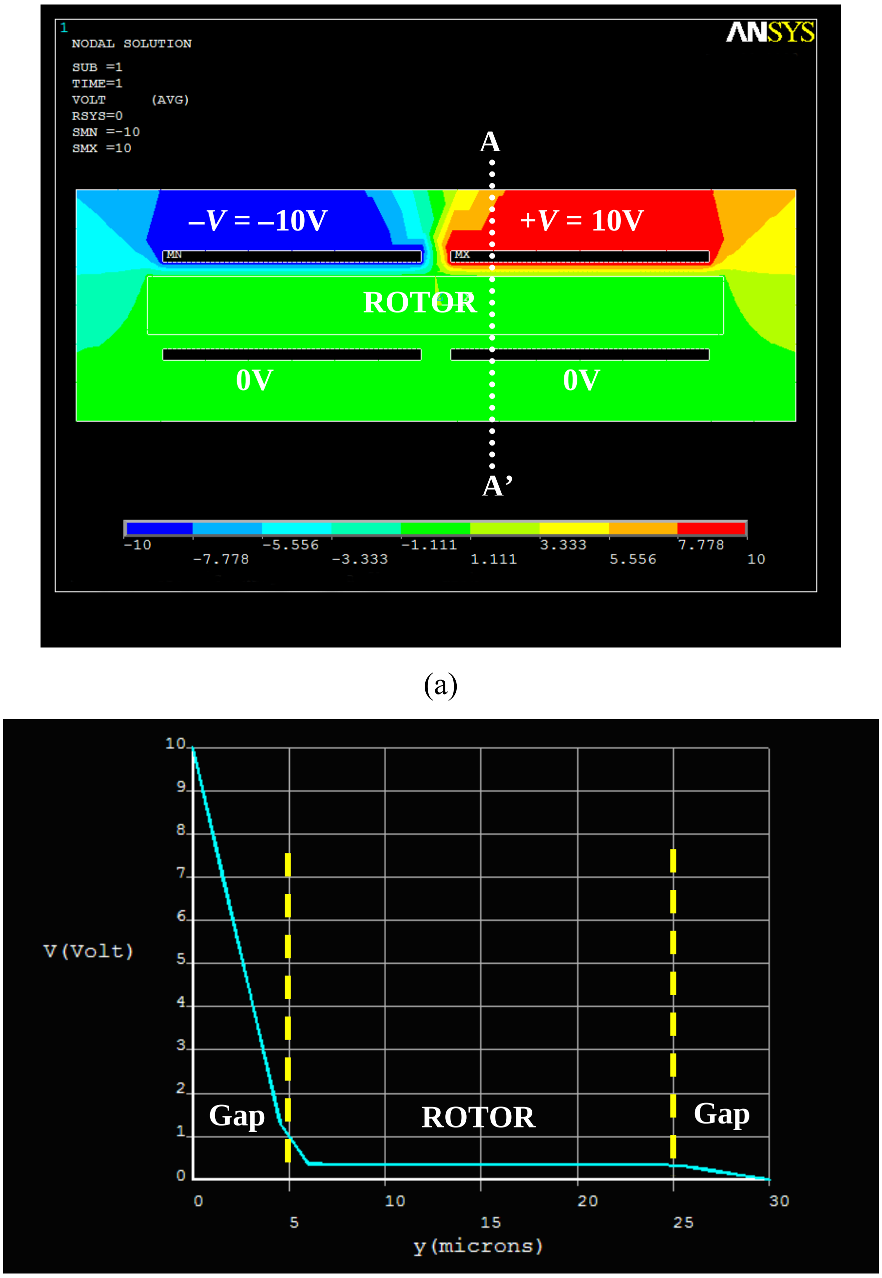

(a)

(b)

Figure 3.25 ANSYS simulation results for the rotor levitating in the centre position between the upper and lower feedback electrodes: (a) the contour plot of the potential distribution when 10 V is applied to the right upper electrode and –10 V is applied to the left upper electrodes while the lower electrodes are connected to ground (0 V). (b) The potential distribution along path A–A’.

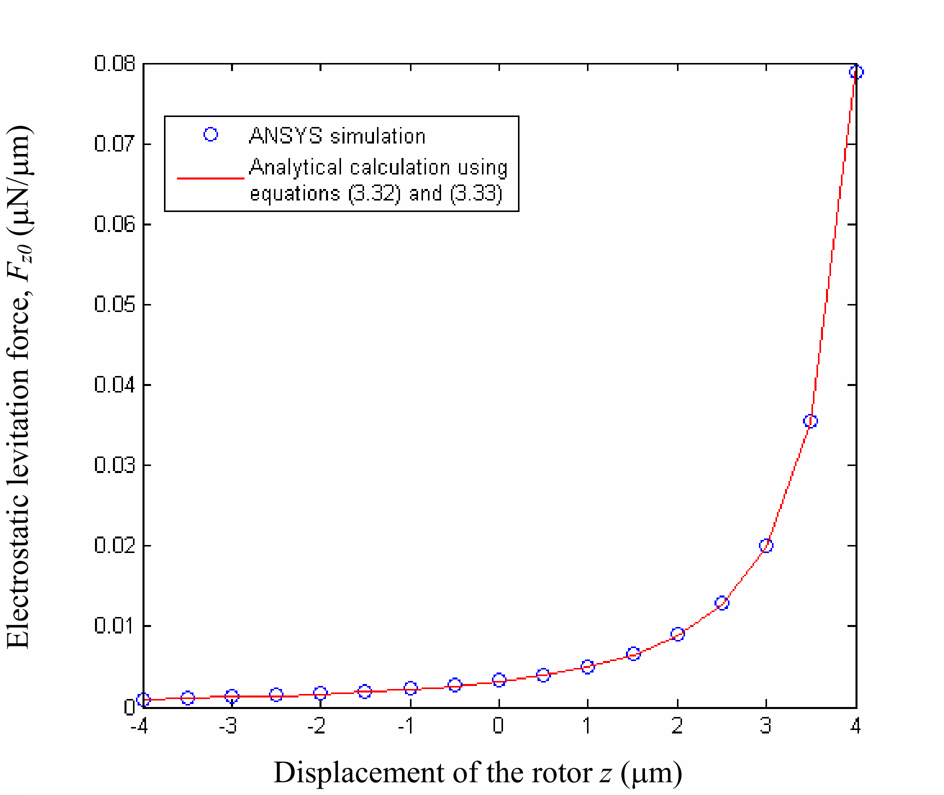

Figure 3.26 Plot of the electrostatic levitation forces per unit length F_{z0} as a function of a vertical displacement z with respect to the nominal position (the rotor is levitated at the middle position between the upper and lower electrodes).

For the electrode design of the micromachined ESG (see Figure 3.13), the capacitance formed between the rotor and the pie-shaped feedback electrodes can be derived using the same method as described in section 3.5.2.1. The capacitance of the upper feedback electrodes located in the first quadrant C_{1fbT} as a function of the displacement z and the angular displacements ϕ and θ can be estimated as:

$$
\begin{aligned}
C_{1fbT}(z,\phi,\theta) \cong \varepsilon \Bigg\{ & \frac{\pi}{4}\cdot\frac{\left(R_{fbo}^{2}-R_{fbi}^{2}\right)}{z_o-z}+\frac{\left(R_{fbo}^{3}-R_{fbi}^{3}\right)\cdot(\phi-\theta)}{3(z_o-z)^2} \\
& +\frac{\left(R_{fbo}^{4}-R_{fbi}^{4}\right)\cdot\left(\pi\phi^2+\pi\theta^2-4\phi\theta\right)}{16(z_o-z)^3} \\
& +\frac{\left(R_{fbo}^{5}-R_{fbi}^{5}\right)\cdot\left(\phi\left(2\phi^2+3\theta^2\right)-\theta\left(3\phi^2+2\theta^2\right)\right)}{15(z_o-z)^4}+\ldots\Bigg\}
\end{aligned}
\tag{3.35}
$$

The resulting electrostatic force F_{z1T} and moments M_{x1T} and M_{y1T} are calculated by differentiating equation (3.35) with respect to z, ϕ and θ, yielding:

$$
\begin{aligned}
F_{z1T} &= \frac{1}{2}V^2\frac{\partial C_{1fbT}}{\partial z} \\
&= \frac{1}{2}V^2\varepsilon\Bigg\{\frac{\pi}{4}\cdot\frac{\left(R_{fbo}^{2}-R_{fbi}^{2}\right)}{(z_o-z)^2}+\frac{2}{3}\frac{\left(R_{fbo}^{3}-R_{fbi}^{3}\right)\cdot(\phi-\theta)}{(z_o-z)^3} \\
&\quad +\frac{3}{16}\frac{\left(R_{fbo}^{4}-R_{fbi}^{4}\right)\cdot\left(\pi\phi^2+\pi\theta^2-4\phi\theta\right)}{(z_o-z)^4} \\
&\quad +\frac{4}{15}\frac{\left(R_{fbo}^{5}-R_{fbi}^{5}\right)\cdot\left(\phi\left(2\phi^2+3\theta^2\right)-\theta\left(3\phi^2+2\theta^2\right)\right)}{(z_o-z)^5}+\ldots\Bigg\}
\end{aligned}
, \tag{3.36}
$$

$$
\begin{aligned}
M_{x1T} &= \frac{1}{2}V^2\frac{\partial C_{1fbT}}{\partial \phi} \\
&= \frac{1}{2}V^2\varepsilon\Bigg\{\frac{\left(R_{fbo}^{3}-R_{fbi}^{3}\right)}{3(z_o-z)^2}+\frac{\left(R_{fbo}^{4}-R_{fbi}^{4}\right)\cdot(2\pi\phi-4\theta)}{16(z_o-z)^3} \\
&\quad +\frac{\left(R_{fbo}^{5}-R_{fbi}^{5}\right)\cdot\left(-6\phi\theta+6\phi^2+3\theta^2\right)}{15(z_o-z)^4}+\ldots\Bigg\}
\end{aligned}
, \tag{3.37}
$$

$$\begin{aligned} M_{y1T} &= \frac{1}{2}V^2\frac{\partial C_{1fbT}}{\partial \theta} \\ &= \frac{1}{2}V^2\varepsilon\left\{-\frac{\left(R_{fbo}^3-R_{fbi}^3\right)}{3(z_o-z)^2}+\frac{\left(R_{fbo}^4-R_{fbi}^4\right)\cdot(2\pi\theta-4\phi)}{16(z_o-z)^3}\right. \\ &\quad \left.+\frac{\left(R_{fbo}^5-R_{fbi}^5\right)\cdot\left(6\phi\theta-3\phi^2-6\theta^2\right)}{15(z_o-z)^4}+\ldots\right\} \end{aligned} \tag{3.38}$$

Equations (3.36) – (3.38) are used to calculate the feedback forces and moments generated when a voltage V is applied to the upper feedback electrode in the first quadrant. The other feedback capacitances and the resulting electrostatic forces and moments can also be approximated using the above method.

The net electrostatic force acting on the rotor along the z direction is the sum of electrostatic forces generated from all upper and lower feedback electrodes, which is:

$$F_z=\sum_{n=1}^{4}F_{znT}+\sum_{n=1}^{4}F_{znB}=F_{z1T}+F_{z2T}+F_{z3T}+F_{z4T}+F_{z1B}+F_{z2B}+F_{z3B}+F_{z4B} \tag{3.39}$$

The net electrostatic moments acting on the rotor for motions about the x and y axes are:

$$M_x=\sum_{n=1}^{4}M_{xnT}+\sum_{n=1}^{4}M_{xnB} \tag{3.40}$$

$$M_y=\sum_{n=1}^{4}M_{ynT}+\sum_{n=1}^{4}M_{ynB} \tag{3.41}$$

In order to lift the rotor up from its initial state where the rotor sits on the bottom substrate ($z = -z_{init}$), the net electrostatic force should be greater than the force of gravity. Positive and negative voltages are applied to the upper feedback electrodes and 0 V is connected to all lower electrodes. Then, the resultant electrostatic force F_z is:

$$F_z=\sum_{n=1}^{4}F_{znT}=4\times F_{z1T}>mg\ .$$

Thus, the minimum voltage required to levitate the rotor V_{lev} is:

$$V_{lev} = \sqrt{\begin{aligned} &\frac{mg}{2\varepsilon} \times \left\{ \frac{\pi}{4} \cdot \frac{\left(R_{fbo}^2 - R_{fbi}^2\right)}{\left(z_o + z_{init}\right)^2} + \frac{2}{3} \frac{\left(R_{fbo}^3 - R_{fbi}^3\right) \cdot (\phi - \theta)}{\left(z_o + z_{init}\right)^3} \right. \\ &\qquad + \frac{3}{16} \frac{\left(R_{fbo}^4 - R_{fbi}^4\right) \cdot \left(\pi\phi^2 + \pi\theta^2 - 4\phi\theta\right)}{\left(z_o + z_{init}\right)^4} \\ &\qquad \left. + \frac{4}{15} \frac{\left(R_{fbo}^5 - R_{fbi}^5\right) \cdot \left(\phi\left(2\phi^2 + 3\theta^2\right) - \theta\left(3\phi^2 + 2\theta^2\right)\right)}{\left(z_o + z_{init}\right)^5} + \ldots \right\}^{-1} \end{aligned}} \quad . \tag{3.42}$$

For the ideal case, the rotor, which has a circular shape, is parallel to all electrodes; hence $\phi = \theta = 0$. The levitation voltage can then be re-written in a simple form as:

$$\begin{aligned} V_{lev} &= \sqrt{\frac{\rho\pi R^2 hg}{2\varepsilon} \times \left(\frac{\pi}{4} \cdot \frac{\left(R_{fbo}^2 - R_{fbi}^2\right)}{\left(z_o + z_{init}\right)^2} \right)^{-1}} \\ &= \sqrt{\frac{2\rho\pi R^2 hg\left(z_o + z_{init}\right)^2}{\varepsilon\pi\left(R_{fbo}^2 - R_{fbi}^2\right)}} \end{aligned} \quad . \tag{3.43}$$

3.5.2.3 Electrostatic spin control

The variable capacitance principle used in axial drive electrostatic micromotors [**85, 86, 111**] is employed to control spinning of the levitated rotor. It is based on the storage of electrical energy in variable rotor-stator capacitances. The variation of the stored energy in the direction of motion will result in the output torque of the motor. The motive torque M_{motor} can be expressed as the rate of change of the potential energy U stored in the capacitor with respect to the rotor angular displacement θ as given by:

$$M_{motor} = \frac{\partial U}{\partial \theta} = \frac{1}{2} V_{drive}^2 \frac{\partial C_r(\theta)}{\partial \theta} \tag{3.44}$$

where

V_{drive} = applied drive voltage to the stator electrodes and

C_r = rotation control capacitance.

For the first prototype micromachined ESG, the configuration of spin control electrodes was taken from the design of the micromachined motor reported in references [**85, 86**]. It employs the configuration with a stator:rotor ratio of 3:2, which was reported that it provides a relatively high motive torque with minimum torque ripples. The spin control electrodes employed in the micromachined ESG is comprised of twelve stator poles and eight rotor poles as shown in Figure 3.27. The rotation control electrodes, called *stators,* are located above and below the silicon rotor. The length of a stator electrode is 300 μm and the width is 18 degrees with 12 degree separation between each stator electrode. The opening patterns on the rotor have a length of 400 μm, a width of 18 degrees and a pitch of 45 degrees. The length of the opening patterns was designed so that it is somewhat larger than that of the stator electrodes. This is to deal with misalignment in fabrication process. In addition, the value of the width and separation between each stator electrodes was chosen so that when one stator electrode aligns with a rotor pole, the other stator electrodes have an area overlapping with rotor poles. The capacitance formed between the rotor and the upper stator electrode can be expressed using the parallel-plate capacitor estimation, which yields:

$$C_r = \frac{\varepsilon\left(R_{do}^2 - R_{di}^2\right)\theta_{overlap}}{2(z_o - z)} \tag{3.45}$$

where

R_{do}, R_{di} = outer and inner radii of the rotation control electrodes and

$\theta_{overlap}$ = overlap angle (in degree unit) between the rotor and stator electrode.

Note that the so-called fringe field effect, in which the electric fields bow out at the edges, is neglected.

As illustrated in Figure 3.27, each set of the rotation control electrodes consists of three stator electrodes, termed *phase A*, *phase B* and *phase C* electrodes. The motive torque is produced by applying voltages to these stators in sequence. Assume that the rotor is levitated in the middle position between the upper and lower electrodes. Driving voltages are applied to only one phase of the stator electrodes at the time, the other phase stators are grounded. A positive voltage of $+V_{drive}$ is connected to the upper rotation control electrodes and a negative voltage of $-V_{drive}$ is connected to the lower electrodes. According to equations (3.31) and (3.32), the net electrostatic force in the z direction is zero and also the potential of the rotor is maintained at 0 V. Thus, only tangential forces act on the rotor providing motive torques. There is no electrostatic force acting on the rotor along the z axes.

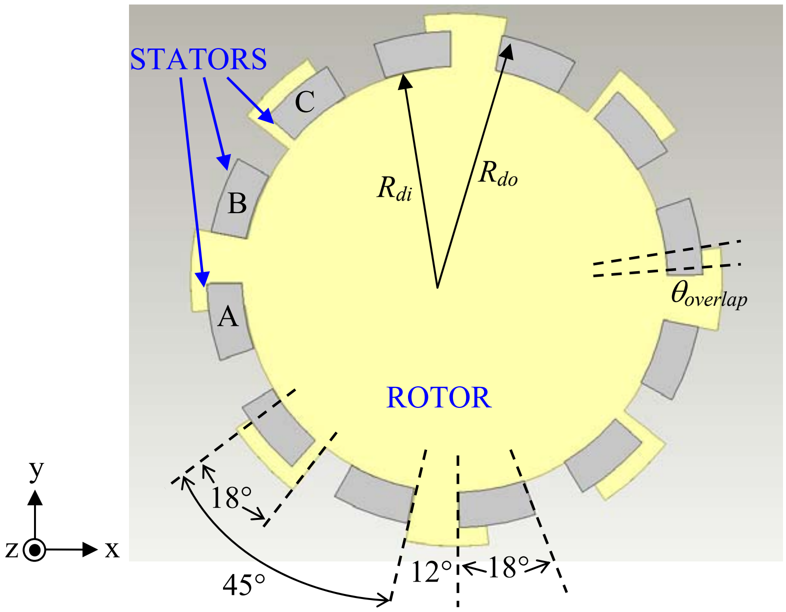

Figure 3.27 Configuration of spin control electrodes employed in the first prototype micromachined ESG.

The stator electrodes are designed in such a way as they are misaligned to the opening patterns on the rotor (see Figure 3.27). In order to generate the motive torque, driving voltages are applied to each phase of stator electrodes in sequence. For example, driving voltages $+V_{drive}$ and $-V_{drive}$ are applied to *phase A* stator electrodes, whereas 0 V is applied to the other phase stator electrodes. The rotor then rotates to align the rotor poles with the energised stators. Immediately after the rotor poles are aligned with the stators, the *phase B* stator electrodes are then energised and the stators in the other phases are grounded. This will cause the rotor continuously to rotate. When the rotor poles are aligned with the *phase B* stator electrodes, the driving voltages are applied to the *phase C* stator electrodes. By repeating the sequence, the rotor will keep spinning about the z axis. Figure 3.28 demonstrates the concept of the motor drive sequence employed in a side-drive electrostatic micromotor. This method is similar to the rotor spinning sequence mentioned above, except the rotor is driven by exciting electrodes located at its periphery.

Finite element simulations in ANSYS were performed to validate equations (3.44) and (3.45). As the design of the micromachined ESG is symmetrical, the simulations were carried out using only a quarter model of the rotor and stator electrodes as shown in Figure 3.29. However, the actual device geometry is relatively large, causing a problem in mesh generation. Therefore, in the following simulations, a gyro sensor with smaller device dimensions is modelled. Device parameters used in the ANSYS simulations are as follows: a rotor has a diameter of 2 mm and a thickness of 100 μm, a capacitive gap is 10 μm, and the length of the stator is 150 μm. The upper *phase B* stator electrode is connected to a driving voltage of +10 V and the lower *phase B* stator electrode is connected to –10 V. The other stator electrodes are connected to ground (0 V).

Figure 3.30 shows the capacitance formed between the rotor and the *phase B* electrode corresponding to the angular position of the rotor and also the resultant electrostatic torque acting on the rotor. The results show a good agreement between the analytical estimations and FEM simulations; except at the angular position where there is no overlap between the rotor and stator. This is due to the fringe field effect is excluded in the analytical equations.

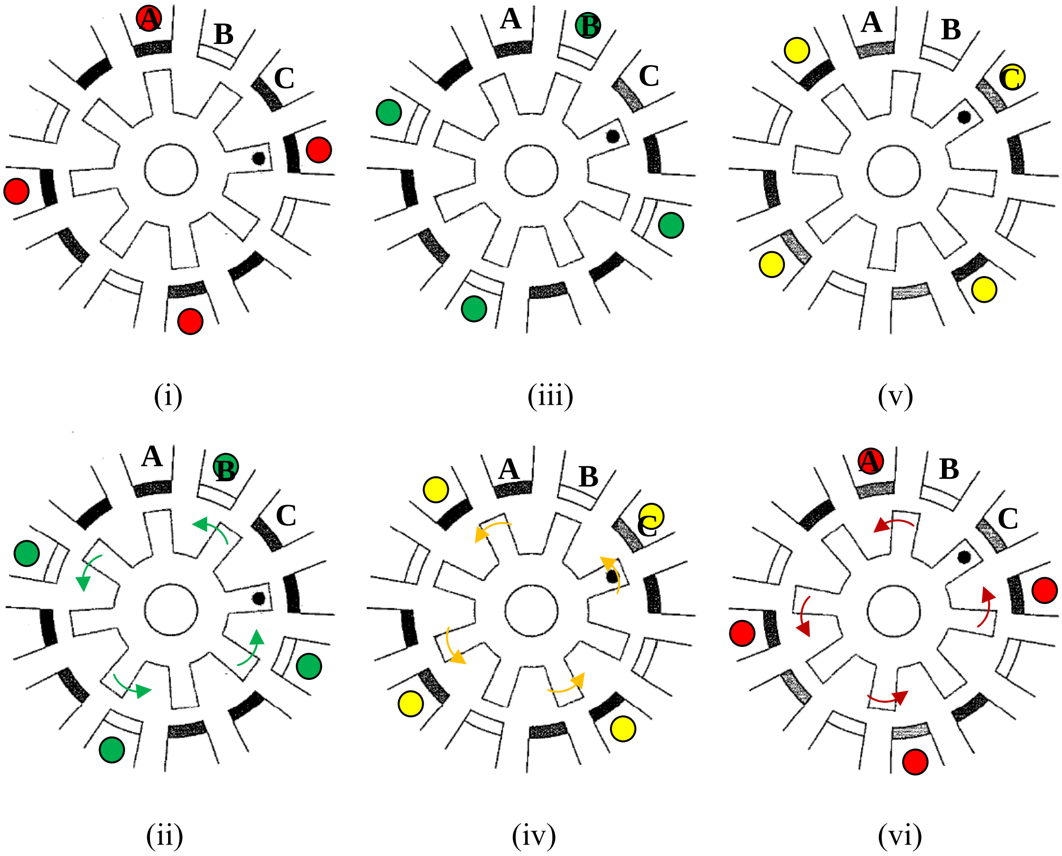

(i) (iii) (v)

(ii) (iv) (vi)

Figure 3.28 Drive sequence employed in a side-drive electrostatic micromotor: (i) *Phase A* stator electrodes are activated, the energised electrodes shown with red dots. (ii) *Phase B* stator electrodes are connected to driving voltages, forcing the rotor to rotate. (iii) The rotor is aligned to the energised stator electrodes (green dots). (iv) *Phase C* stator electrodes are then energised, forcing the rotor to spin. (v) The rotor is aligned to the active stator electrodes (yellow dots). (vi) The *phase A* stator electrodes are re-activated. The rotor will keep spinning by repeating steps (i) – (vi).

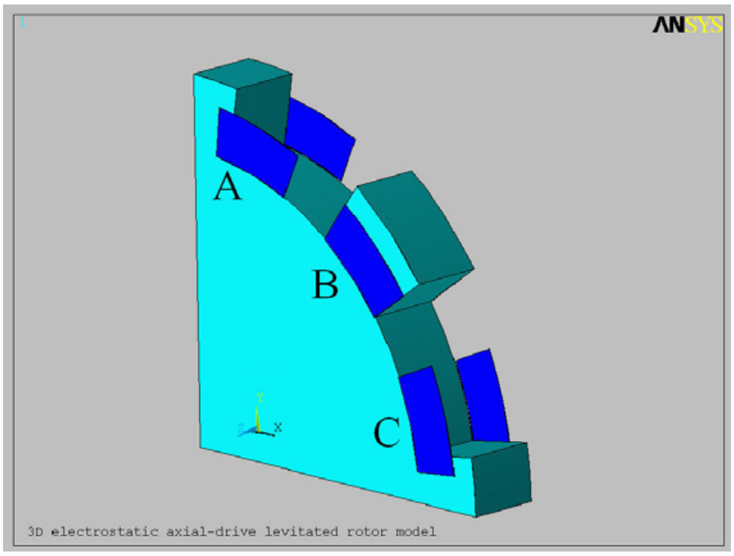

Figure 3.29 ANSYS quarter model of the rotor and stators employed to estimate the capacitance of the capacitor formed between the rotor and the *phase B* stator.

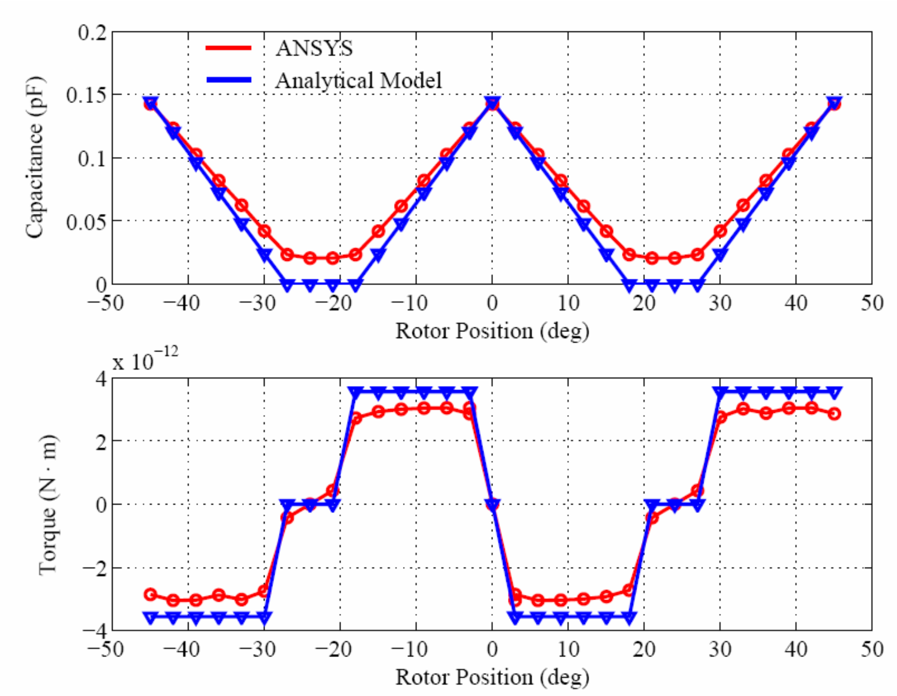

Figure 3.30 *Phase B* stator capacitance (top) and electrostatic torques (bottom) as a function of the rotor position, obtained from ANSYS simulations (red) and analytical calculations using equations (3.44) and (3.45) (blue).

The maximum achievable spin speed of the levitating rotor $\Omega_{z,max}$ is limited by the mechanical centrifugal stress in the rotor, which can be given as [**111**]:

$$\Omega_{\max}^2 = \frac{\sigma}{\rho \cdot R \cdot h} \tag{3.46}$$

where

σ = maximum centrifugal stress of silicon ($\cong 10^9$ N/m^2),

ρ = density of the silicon rotor (= 2330 kg/m^3),

R = radius of the rotor and

h = rotor thickness.

Therefore, for the prototype micromachined ESG, the ultimate spin speed is approximately 1.0358×10^6 rad/s or 9.8915×10^6 RPM.

In practice, the spin speed of the rotor is also limited by the viscosity of surrounding air. The viscous drag torque τ_d is calculated by multiplying the coefficient of viscous drag B_z by the spin speed of the rotor Ω_z:

$$\tau_d = B_z \Omega_z \tag{3.47}$$

The contribution to the viscous drag torque from each part of the micromachined ESG is calculated separately and the results are summed to obtain the total viscous drag torque. Assume that the rotor is levitated at its nominal position. The coefficients of viscous drag at the gaps between the rotor with the radius of R_{rotor} and the top and bottom substrate are given by [**118**]:

$$B_{z1T(B)} = \frac{\pi \mu_{eff} R_{rotor}^4}{2 z_o} \tag{3.48}$$

where

z_o = nominal gap between the rotor and the substrate,

μ_{eff} = effective viscosity of surrounding air.

The coefficient of viscous drag for a region between the rotor and side wall electrodes is given by [**130**]:

$$B_{z2} = \frac{2\pi\mu_{eff} h R_{rotor}^2 R_{sidewall}}{R_{sidewall} - R_{rotor}} \tag{3.49}$$

where

$R_{sidewall}$ = radius of the inner sidewall electrodes and

h = thickness of the rotor.

The total coefficient of viscous drag B_z is the sum of $B_{z1T(B)}$ and B_{z2}:

$$B_z = B_{z1T} + B_{z1B} + B_{z2} = \frac{\pi\mu_{eff} R_{rotor}^4}{z_o} + \frac{2\pi\mu_{eff} h R_{rotor}^2 R_{sidewall}}{R_{sidewall} - R_{rotor}} \tag{3.50}$$

Figure 3.31 shows the relationship between the total coefficient of viscous drag and the ambient pressure and also the maximum achievable spin speed of the rotor corresponding to the ambient pressure and driving voltages. The device parameters employed in this analytical calculation are as follows: the diameter of the rotor is 4 mm, its thickness is 200 μm, the capacitive gap between the rotor and the top/bottom substrate is 3 μm, and the capacitive gap between the rotor and the sidewall electrodes is 10 μm. The damping coefficient B_z drops dramatically as the ambient pressure is reduced, hence, higher rotor spin speed can be achieved. The rotor only spins at speeds of approximately 10 – 100 RPM under atmospheric pressure (~10^5 Pa). The spin speed can go up to 10^5 RPM by decreasing the operating pressure to 10^{-2} mtorr (~10 Pa).

3.5.2.4 Lateral suspension control

As mentioned earlier in section 3.5.2, the electrodes for lateral control along the x and y axes divided into four quadrants. Each set consists of one sense and two feedback electrodes as shown in Figure 3.14. The width of the sense electrode is 30 degrees and the width of each feedback electrode is 27 degrees. A capacitive gap between the rotor and the sense/feedback electrodes located at the rotor periphery is 10 µm. The minimum size of the gap is limited by the aspect ratio of deep reactive ion etching (DRIE) process (for more details, see chapter 5).

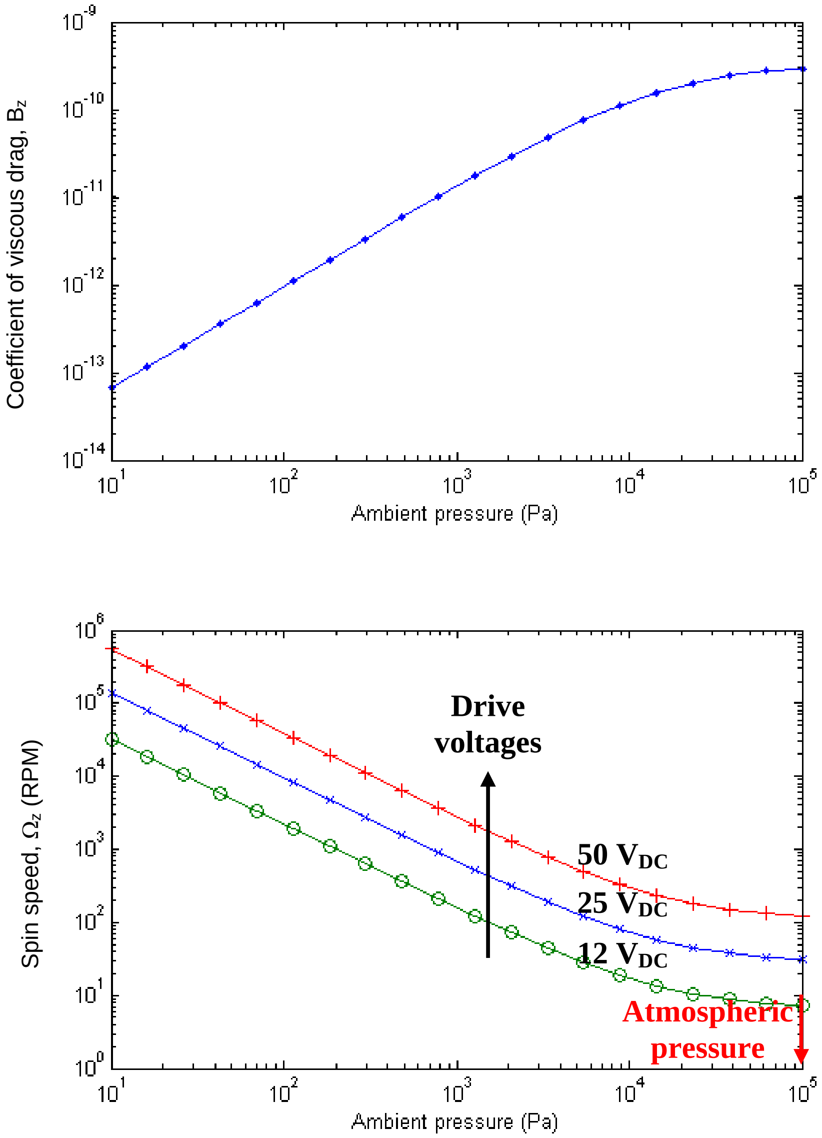

Figure 3.31 Viscous damping coefficients (top) and rotor spin speeds (bottom) corresponding to ambient pressures and driving voltages for the prototype micromachined ESG with the rotor diameter of 4 mm and the thickness of 200 µm. The capacitive gap between the rotor and the substrates is 3 µm and the gap between the rotor and the sidewall electrodes is 10 µm.

Figure 3.32 illustrates a diagram of the rotor and sidewall electrodes. The radius of the rotor is R_o, the radius of the electrode is R_s and the angular position of the electrode centre is θ. In this figure, the origin of the reference axis is fixed at the electrode centre. At nominal position, the centre of the levitated rotor is at the centre of the electrodes. The capacitance C_{sw} formed between each electrode and the rotor can be estimated using the parallel plate capacitor approximation, which is:

$$C_{sw} = \int_{\theta_1}^{\theta_2} \frac{\varepsilon R_s h}{d_0} d\theta \tag{3.51}$$

where d_0 is the nominal separation gap between the rotor and the sidewall electrode. Equation (3.51) is used for calculating a nominal capacitance of the sidewall sense and feedback electrodes.

Assume that the rotor is displaced away from its nominal position as shown in Figure 3.33. The distance between the centre of the rotor and the centre of the electrode is *dr*. To calculate the capacitance formed between each electrode and the rotor, the separation gap *d* between the electrode and the rotor as a function of the rotor displacement and the electrode position (θ) is needed. The distance *d* between the rotor and electrode at angle θ is given by:

$$d(\theta) = R_s - R(\theta) \tag{3.52}$$

When the rotor is centred as shown in Figure 3.32, $R(\theta) = R_o$ and thus the distance between the rotor and electrode is equal to d_0. Note that all symbols are defined in Figures 3.32 and 3.33.

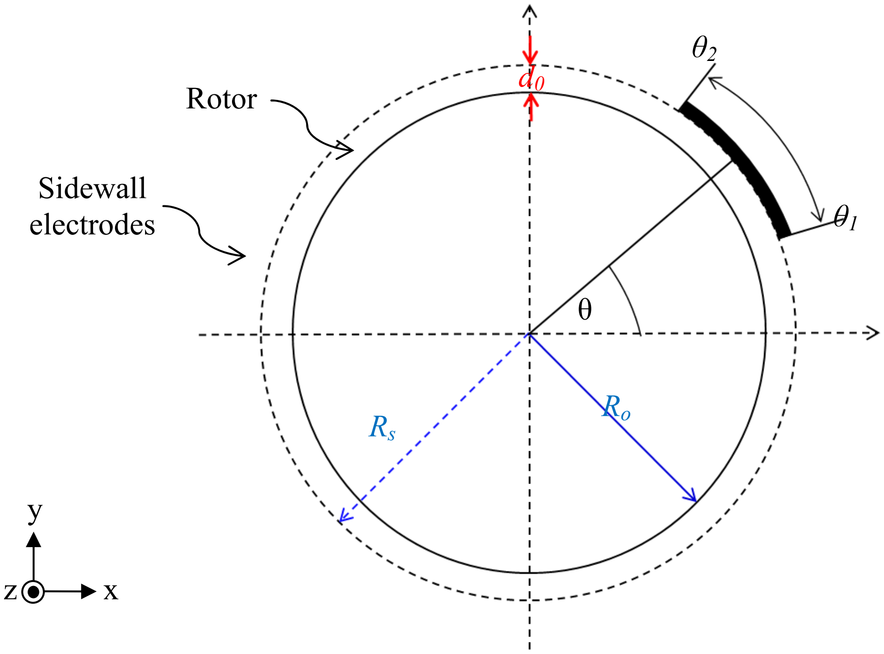

Figure 3.32 Diagram of the rotor and sidewall electrodes, showing radii, angles and the separation gap between the rotor and electrode when the rotor is at the nominal position.

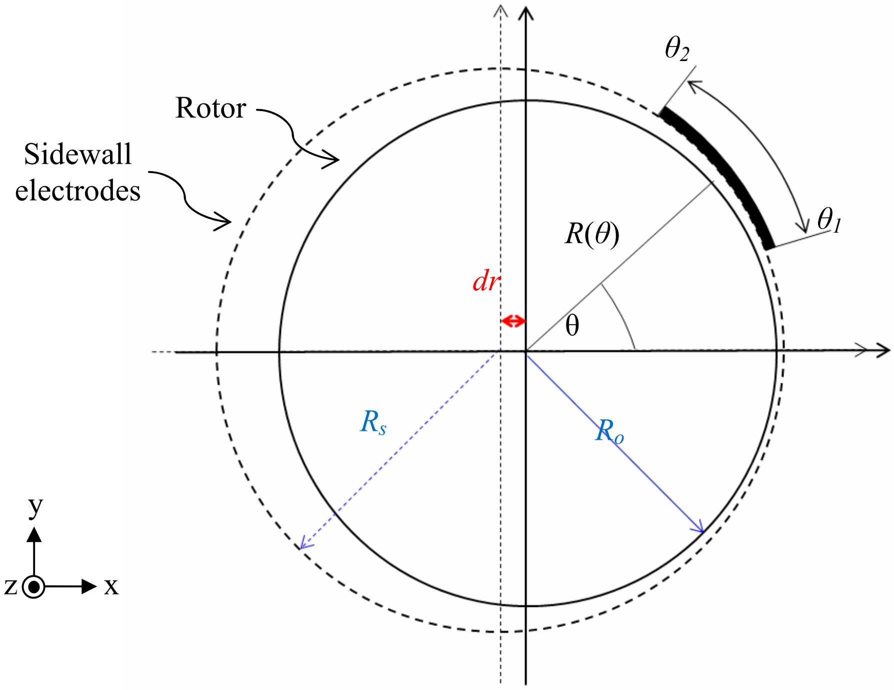

Figure 3.33 Diagram of the rotor and sidewall electrode, showing radii, angles and a displacement of the rotor away from the centre by *dr*.

Considering Figure 3.33 in the polar coordinate system, R as a function of θ can be written as [**131**]:

$$R(\theta) = R_o \sqrt{1 + \frac{dr^2}{R_o^2} - \frac{2dr}{R_o}\cos\theta} \tag{3.53}$$

Substituting equation (3.53) into (3.52) yields:

$$d(\theta) = R_s - R_o \sqrt{1 + \frac{dr^2}{R_o^2} - \frac{2dr}{R_o}\cos\theta} \tag{3.54}$$

Then, the capacitance formed by the rotor and sidewall electrodes is given as:

$$C_{sw} = \int_{\theta_1}^{\theta_2} \frac{\varepsilon R_s h}{d(\theta)} d\theta \tag{3.55}$$

However, a simple closed-form solution for equation (3.55) cannot be derived. Therefore, two parallel-plate capacitor approximation in equation (3.51) is used to model the capacitance changes between the rotor and sidewall electrodes in system level simulations (in chapters 5 and 7). The capacitances $C_{sw,x}$ and $C_{sw,y}$ in the x and y axis can then be estimated as:

$$C_{sw,x} = \frac{\varepsilon R_s h(\theta_2 - \theta_1)}{d_0 \mp dx} \tag{3.56}$$

$$C_{sw,y} = \frac{\varepsilon R_s h(\theta_2 - \theta_1)}{d_0 \mp dy} \tag{3.57}$$

where dx and dy are the displacement of the rotor along the x and y axes, respectively.

The feedback forces produced by the sidewall electrodes can be calculated as:

$$F_x = \frac{1}{2}\frac{\partial C_{sw,x}}{\partial x}V^2 = -\frac{1}{2}\frac{\varepsilon R_s h(\theta_2 - \theta_1)}{(d_0 \mp dx)^2}V^2 \tag{3.58}$$

$$F_y = \frac{1}{2}\frac{\partial C_{sw,y}}{\partial y}V^2 = -\frac{1}{2}\frac{\varepsilon R_s h(\theta_2 - \theta_1)}{(d_0 \mp dy)^2}V^2 \tag{3.59}$$

Thus, in system-level simulations presented in chapters 5 and 7, equations (3.56) and (3.57) are used to model the capacitance changes due to the rotor is displaced away from its nominal position; and feedback forces acting on the rotor can be modelled using equations (3.58) and (3.59).

3.6 SUMMARY

The micromachined ESG is composed of a mechanically unsuspended micro-rotor that is surrounded by sets of sense, feedback and spin control electrodes. These sets of electrodes are used to sense and control the rotor position in five degrees of freedom, i.e. the out-of-plane translation in the z-axis, the in-plane motion along the x and y axes and the out-of-plane rotation about the x and y axes. The operating principle of the sensor is discussed in detail in section 3.2, followed by design and analysis of the micromachined ESG. The prototype micromachined ESG has been designed according to all the aforementioned design considerations. The rotor and electrode dimensions are given in Table 3.1 and 3.2, respectively. The device parameters and expected properties are summarised and given in Table 3.3.

Table 3.2: Electrode dimensions of the first prototype micromachined ESG.

Electrode dimensions	**Value**	**Unit**
The outer radius of excitation electrode, R_{Eo}	820	μm
The inner radius of sense electrode, R_{si}	850	μm
The outer radius of sense electrode, R_{so}	1175	μm
The inner radius of feedback electrode, R_{fbi}	1200	μm
The outer radius of feedback electrode, R_{fbo}	1500	μm
The inner radius of rotation control electrode, R_{di}	1600	μm
The outer radius of rotation control electrode, R_{do}	1900	μm
The stator pole width	18	°
The separation displacement between each stator pole	12	°
The rotor pole width	18	°
The separation between each rotor pole	27	°

Table 3.3: Device parameters of the first prototype micromachined ESG.

Parameters	**Value**
Mass of the rotor, m (mg)	3.73
Moment of inertia about the spin axis, I_z (kg·m^2)	7.47×10^{-12}
Moment of inertia about the x and y axes, $I_{x,y}$ (kg·m^2)	3.75×10^{-12}
Spring constant along the z direction, k_z (N/m)	16
Damping coefficient along the z direction, b_z (N·s/m)	4.66×10^{-9}
Damping coefficient along the x and y directions, $b_{x,y}$ (N·s/m)	8.42×10^{-7}
Out-of-plane spring constant, $K_{x,y}$ (kg·m^2/rad)	7.17×10^{-4}
Out-of-plane damping coefficient, $B_{x,y}$ (kg·m^2·s/rad)	6.34×10^{-13}
Nominal capacitance of excitation electrodes, C_E (pF)	6.25
Nominal capacitance of sense electrodes, C_{ns} (pF)	1.54
Nominal capacitance of feedback electrodes, C_{nfb} (pF)	1.88
Nominal capacitance of sidewall sense electrodes, $C_{ns(sw)}$ (pF)	0.186
Nominal capacitance of sidewall feedback electrodes, $C_{nfb(sw)}$ (pF)	0.168

Chapter 4

Front-end Interface Design for the Micromachined ESG

4.1 INTRODUCTION

The prototype micromachined ESG employs a differential capacitive measurement to sense the displacement of the rotor. The capacitive sensing is based on the capacitance half-bridge configured for differential output as discussed in chapter 3. This chapter presents the design and analysis of a front-end circuit for the differential capacitance sensing.

Section 4.2 discusses design considerations of the prototype front-end circuit, which is based on commercial off-the-shelf components. It is then followed by simulations at electronic-level using OrCAD/PSPICE, which were carried out to evaluate the circuit operation. In section 4.3, a printed-circuit-board (PCB) prototype of the front-end circuit was built and experiments were carried out to compare the results obtained from the measurement with simulation results.

4.2 DESIGN AND SIMULATION OF THE FRONT-END INTERFACE

The measurement of a sensor capacitance, in practice, has to deal with stray and parasitic capacitances [**132**]. These undesired strays typically arise from the parasitic capacitances of the sensing electronics connected to the sensor and also the stray capacitances between the electrodes (including the leads to the sensing circuit) and the grounded electrodes. Figure 4.1 shows a simplified model of a sense capacitor with stray capacitors C_{stray} at its terminals.

The value of these stray capacitances is often in the same order of magnitude as the nominal sensor capacitance[1]. Thus, a front-end circuit should be immune to stray capacitances and provides the output voltage which is only dependent on the sensor capacitance. Several capacitance measuring circuits have been reported [**132, 133**], including oscillation methods, charge measurement circuits and switched-capacitor interfaces

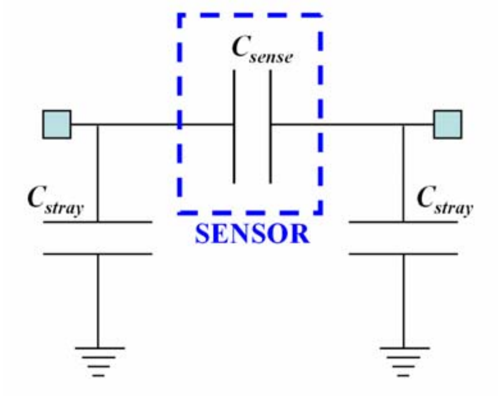

Figure 4.1 Sense capacitance with stray capacitances at its terminals.

The basic circuit of the front-end interface is shown in Figure 4.2. The front-end circuit is completely symmetrical providing a relatively high common-mode rejection ratio. It consists of charge amplifiers, diode demodulators and an instrumentation amplifier. The charge amplifier, also called a *pick-off* amplifier, detects and converts the variation of the sense capacitance into voltage. The output voltage of the charge amplifier is in a form of amplitude modulation (AM), in which a high-frequency excitation signal acts as a signal carrier. The diode demodulator is employed to extract a data signal (the variation of the sense capacitance) from the modulated signal. At last, the instrumentation amplifier converts the differential output into the single-ended output and rejects common mode signals. More detail about the front-end circuit is given in the following sections.

---

[1] The nominal sense capacitance is the capacitance formed between a sense electrode and the rotor when the rotor is positioned at a centre between the upper and lower electrodes.

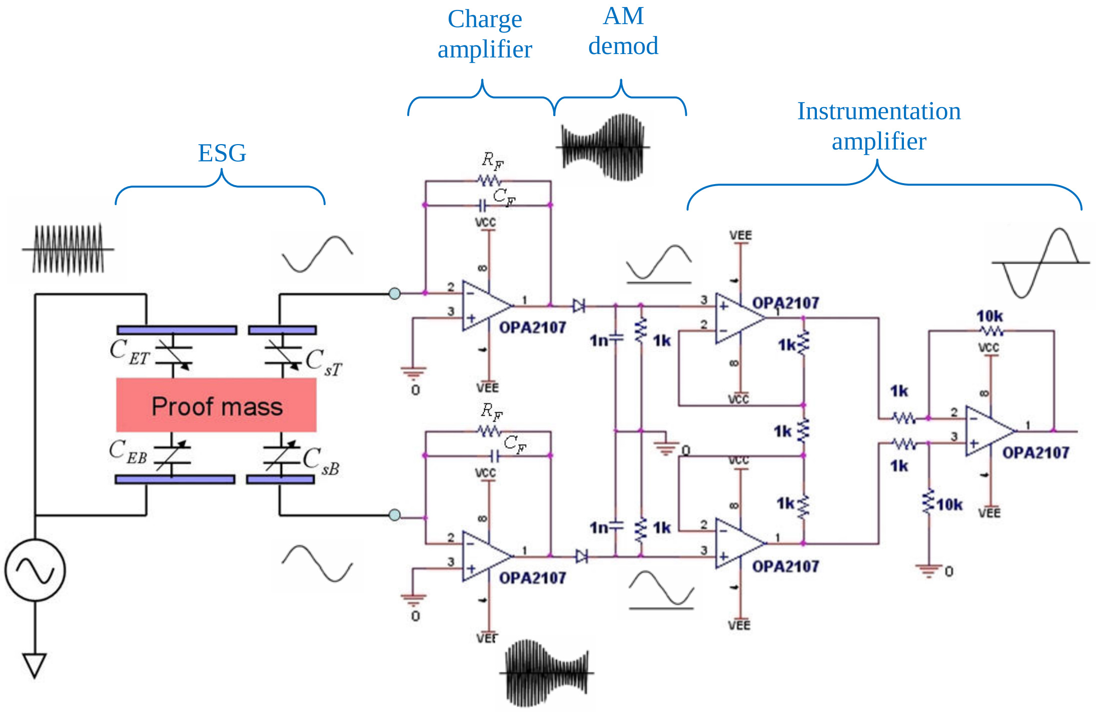

Figure 4.2 Basic circuit of the front-end interface employed to convert the differential capacitance to a voltage signal.

4.2.1 Excitation Signal

In order to convert the capacitance to voltage, the front-end circuit needs to be driven by a high frequency voltage source, hereafter called the *excitation* signal. This excitation signal can create electrostatic forces which disturbs the displacement of the rotor. The electrostatic forces can be expressed as shown below:

$$F_{ET(EB)} = \frac{1}{2}\frac{\partial C_{ET(EB)}}{\partial z}V_{ex}^{2} \tag{4.1}$$

Therefore, the frequency of the excitation signal must be far above the resonance frequency of the rotor and the magnitude of the excitation voltage should be sufficiently small so that the position disturbance can be negligible. Accurate measurement also requires the use of very short pulses in such a way as the measurement is completed before the rotor can change position.

As discussed in chapter 3, the micromachined ESG has no direct electrical contact to the rotor. The excitation signal is coupled to the rotor via capacitive coupling. The potential at the levitated rotor V_{rotor} can be calculated using equation (4.2).

$$V_{rotor} = \frac{C_{ET} + C_{EB}}{C_{ET} + C_{EB} + \sum C_s + \sum C_{fb} + \sum C_r} \cdot V_{ex} \cos \omega_{ex} t \tag{4.2}$$

The high-frequency excitation voltage V_{ex} is divided by coupling capacitors. In order to maximise V_{rotor} the excitation capacitances should be greater than the sum of all sense, feedback and rotation capacitances. Refer to chapter 3 for a detailed discussion about the optimisation of these capacitances.

4.2.2 Charge Amplifier

The schematic diagram of the op-amp charge amplifier is shown in Figure 4.3. C_s represents the variable sense capacitance of the micromachined ESG. The output of the charge amplifier V_{ca} is:

$$V_{ca} = -\frac{j\omega R_f C_s}{1 + j\omega R_f C_f} \cdot V_{rotor} \tag{4.3}$$

The feedback resistor R_f provides DC bias current to the op-amp input so that the DC value at the inverting input is clamped at zero. The feedback resistor together with the feedback capacitor C_f also acts as a high-pass filter with a cut-off frequency of $\frac{1}{2\pi R_f C_f}$. The value of R_f was chosen in such a way that the resulting cut-off frequency is much lower than the frequency of the excitation signal.

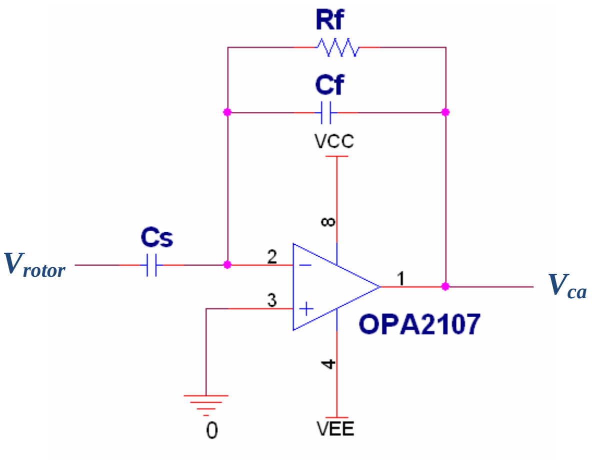

Figure 4.3 Schematic diagram of a charge amplifier. C_s is a sense capacitor; R_f and C_f are a feedback resistor and capacitor, respectively. VCC and VEE are the positive and negative supply voltage, respectively.

For the ΣΔM micromachined ESG, the sinusoidal signal with a high frequency (between 500 kHz to 2 MHz) is chosen as the excitation signal. Thus, the term $\omega R_f C_f$ is generally larger than unity. Then the output signal of the charge amplifier can be approximated in a frequency independent form as:

$$V_{ca} \approx -\frac{C_s}{C_f} \cdot V_{rotor} \tag{4.4}$$

Generally, the variation of C_s due to external rotation rates and/or accelerations is at low frequency ω_{signal}. The capacitance change can be expressed as:

$$C_s = C_{s0} + \Delta C_s \cdot \cos \omega_{signal} t \tag{4.5}$$

where

C_{s0} = nominal sense capacitance[2] and

ΔC_s = variations of C_s due to external rotation rates and/or accelerations.

---

[2] A nominal sense capacitance is the capacitance value of the sense capacitor when the rotor is at the middle position between the upper and lower sense electrodes.

Substituting equations (4.2) and (4.5) into equation (4.4) yields:

$$V_{ca} \approx -\frac{C_{s0} + \Delta C_s \cdot \cos\omega_{signal} t}{C_f} \cdot \left(\frac{C_{ET} + C_{EB}}{C_{ET} + C_{EB} + \sum C_s + \sum C_{fb} + \sum C_r} \right) \cdot V_{ex} \cos\omega_{ex} t \tag{4.6}$$

The output signal of the charge amplifier is then proportional to the variations of C_s. In general, when no rotation rate or acceleration is applied C_f is chosen such that its value equals to:

$$C_f = C_{s0} \cdot \left(\frac{C_{ET} + C_{EB}}{C_{ET} + C_{EB} + \sum C_s + \sum C_{fb} + \sum C_r} \right) \tag{4.7}$$

Consequently, the transfer function from V_{ex} to V_{ca} will be –1. Then in the presence of rotation rates and/or accelerations, the output voltage of the charge amplifier will show small variations around –1 due to the small value of $\Delta C_s / C_{s0}$.

In addition, the output of the charge amplifier is in a form of amplitude modulation (AM). By rearranging equation (4.6), it can be expressed in a simple equivalent form as:

$$V_{ca} = A \cdot \cos\omega_{ex} t + \frac{B}{2}\left(\cos\left(\left(\omega_{ex} - \omega_{signal}\right)t\right) + \cos\left(\left(\omega_{ex} + \omega_{signal}\right)t\right)\right) \tag{4.8}$$

where

$$A = -\frac{C_{s0}}{C_f} \cdot \left(\frac{C_{ET} + C_{EB}}{C_{ET} + C_{EB} + \sum C_s + \sum C_{fb} + \sum C_r} \right) \cdot V_{ex} \quad \text{and}$$

$$B = -\frac{\Delta C_s}{C_f} \cdot \left(\frac{C_{ET} + C_{EB}}{C_{ET} + C_{EB} + \sum C_s + \sum C_{fb} + \sum C_r} \right) \cdot V_{ex} .$$

It can be seen that the output is composed of three frequency components at the high frequency excitation signal ω_{ex}, $\omega_{ex} + \omega_{signal}$ and $\omega_{ex} - \omega_{signal}$. The circuit modulates the low-frequency input signal to higher frequency range where there is low 1/*f* noise. As a result, this will suppress low-frequency amplifier 1/*f* noise and drift in the signal band.

4.2.3 AM Demodulator

A simple diode demodulation circuit, illustrated in Figure 4.4, is employed to extract the modulated amplitude. The circuit consists of one diode and an RC low-pass filter circuit with resistor R_D and capacitor C_D. The R_DC_D time constant of the demodulator was selected in such a way that the input frequency f_{ex} is eliminated and the sensor signal can be transferred unaffectedly. In a case of the sensor with a ΣΔM feedback loop, the RC low-pass filter is designed to cover the sampling frequency f_s of a ΣΔ modulator. After demodulation, the output signal of the demodulation circuit V_{dm} becomes:

$$V_{dm} = -\frac{C_{s0} + \Delta C_s \cdot \cos\omega_{signal} t}{C_f} \cdot \left(\frac{C_{ET} + C_{EB}}{C_{ET} + C_{EB} + \sum C_s + \sum C_{fb} + \sum C_r} \right) \cdot V_{ex} - V_D \quad (4.9)$$

where V_D is the voltage dropped across the diode.

As can be seen from equation (4.9), the output signal of the charge amplifier is decreased by the amount of voltage dropped across the demodulation diode. Therefore, the diode with fast switching time and low turn-on voltage is preferable.

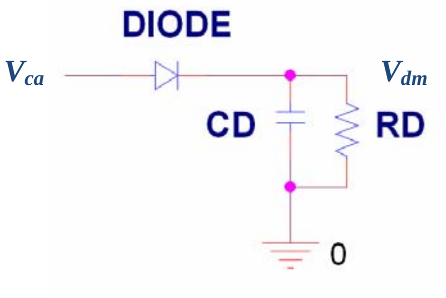

Figure 4.4 Synchronous AM demodulation circuit

4.2.4 Instrumentation Amplifier

The instrumentation amplifier, also called *in-amp*, is employed to amplify the differential output signal obtained from upper and lower sense capacitances. The in-amp circuit is illustrated in Figure 4.5. The gain of the circuit G_{ina} is given as:

$$G_{ina} = \left(1 + \frac{2R_1}{R_2}\right)\frac{R_4}{R_3} \tag{4.10}$$

The output voltage of the front-end circuit can then be expressed as:

$$V_{out} = -G_{ina}\left(\frac{C_{s0,1} + \Delta C_{s,1}\cdot\cos\omega_{signal}t}{C_{f,1}} - \frac{C_{s0,2} + \Delta C_{s,2}\cdot\cos\omega_{signal}t}{C_{f,2}} - V_{D,1} + V_{D,2}\right)\cdot V_{rotor} \tag{4.11}$$

Assume that the circuit is symmetrical, $C_{f,1} = C_{f,2} = C_f$, $C_{s,1} = C_{s,2} = C_s$, $\Delta C_{s,1} = \Delta C_{s,2} = \Delta C_s$ and $V_{D,1} = V_{D,2}$. Equation (4.11) can be simplified to:

$$V_{out} = -G_{ina}\left(\frac{2\Delta C_s\cdot\cos\omega_{signal}t}{C_f}\right)\times\left(\frac{C_{ET} + C_{EB}}{C_{ET} + C_{EB} + \sum C_s + \sum C_{fb} + \sum C_r}\right)\cdot V_{ex} \tag{4.12}$$

It can be seen that the output signal of the front-end circuit is proportional to the variations of C_s and thus the displacement of the rotor. In the absence of external accelerations and/or rotation rates, $\Delta C_s = 0$. Hence, the output voltage of the front-end circuit remains zero ($V_{out} = 0$). When rotation rates and/or accelerations are applied, the output voltage of the front-end circuit will be varied about zero, assuming the ideal case where amplifiers have no DC offset.

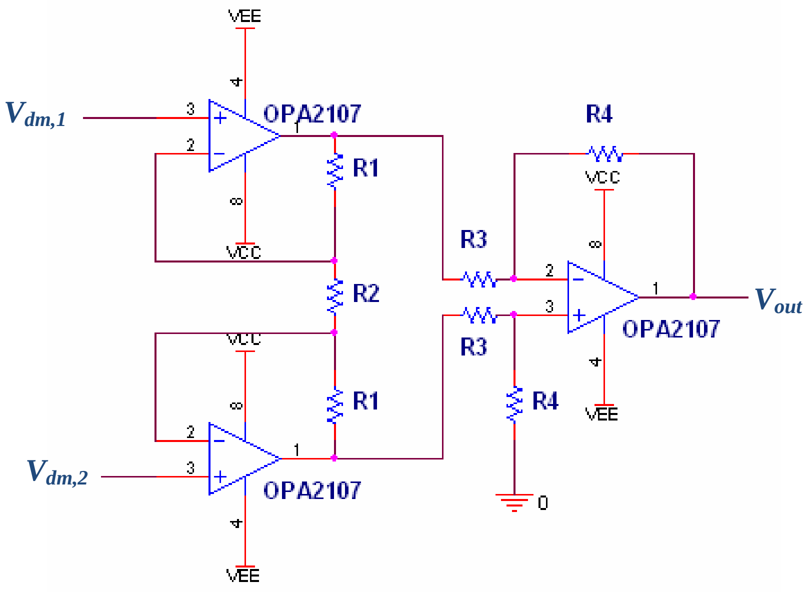

Figure 4.5 Schematic diagram of the instrumentation amplifier. The amplifier consists of three op-amps. Two op-amps act as a buffer providing high input impedance. The third op-amp acts as a differential amplifier.

4.2.5 Simulation of the front-end interface

OrCAD/PSPICE simulation was carried out to evaluate the operational behaviour of the front-end circuit. A variable capacitance was modelled in PSPICE as a voltage controlled variable admittance (YX) [**18, 134**]. Figure 4.6 illustrates the PSPICE model for the variable capacitances of the excitation and sense capacitors. Note that only one channel was investigated in the simulation. The variable admittances X1 and X2 model the excitation capacitors with a nominal capacitance of 6.25 pF, and the admittances X3 and X4 are the upper and lower sense capacitors with a nominal capacitance of 1.54 pF. The AC voltage source V_{ex} is the excitation voltage. The time-variable signal *dC_signal* and two function blocks emulate the capacitance variations. A high value resistor *Rdummy* is required to prevent a floating point error in OrCAD/PSPICE simulations.

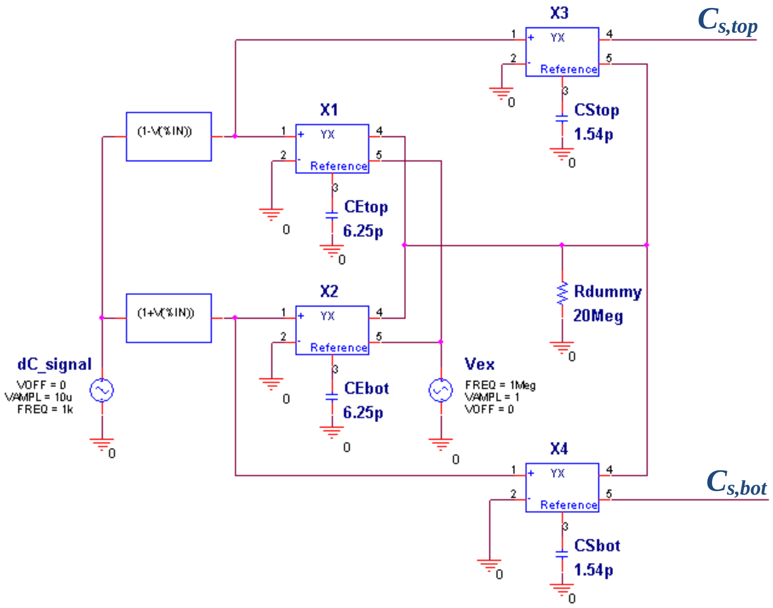

Figure 4.6 PSPICE model for the upper/lower excitation and sense capacitors.

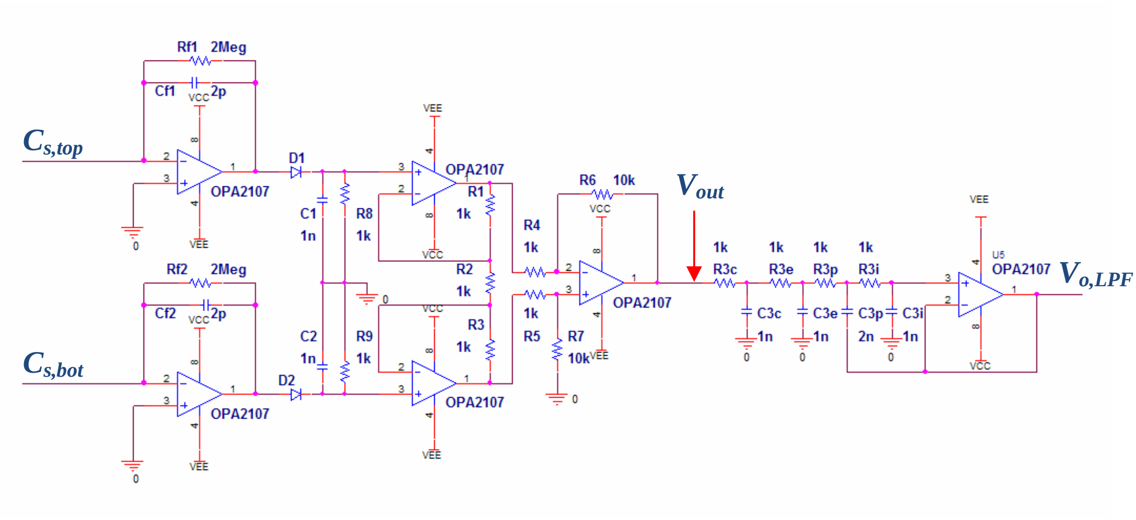

Figure 4.7 Front-end circuit for one channel of the micromachined ESG.

Figure 4.7 shows the front-end circuit in OrCAD/PSPICE simulations. Low-noise and high-gain-bandwidth-product amplifiers are required in the front-end circuit due to a low value of the sense capacitances and a high frequency of the carrier signal. Thus, precision *Difet* operational amplifiers, OPA2107 [**135**], were used because they provide low noise (8 nV/Hz$^{1/2}$ at 1 kHz), low bias current (10 pA maximum), and relatively high gain bandwidth product (4.5 MHz at ±12 V supply voltage).

Figure 4.8 shows simulation results of the front-end circuit. The simulation was carried out to evaluate the sensitivity of the front-end circuit. The input signal was a sinusoidal wave, which emulates 10 ppm capacitance variation. The sinusoidal signal with a peak magnitude of 1 V and a frequency of 1 MHz was used as the excitation signal. The orange waveform is a differential signal between the outputs of the charge amplifiers. The waveform is amplitude modulated signal which is composed of two components, i.e. 1 MHz excitation signal and the capacitance variations at a frequency of 1 kHz. The pink waveform represents the differential output signal of the diode demodulation circuit. As expected, some high-frequency ripple signal still present. This is because the filter in the demodulation circuit is merely a simple first-order low-pass filter. The shape of the roll-off or transition band is too wide to filter out some high frequency components. This ripple signal was brought through to the output signal of the in-amp (as shown in the red waveform). To filter out this high-frequency ripple signal, an additional low pass filter circuit is required. The forth-order low-pass filter, including a second-order passive filter and a second-order Sallen-Key filter [**136**], was then employed here. It was designed to cut off the frequency components above 5×f_s, which approximately 625 kHz. The output signal of the filter is illustrated in the blue waveform.

The results reveal that the front-end circuit can cope with the capacitance variation in the order of 10 ppm of the nominal sense capacitance (1.54 pF). This corresponds to a capacitance change of 15.4 aF. The corresponding output voltage of the front-end circuit is 150 μV approximately. This can imply that the capacitance-to-voltage sensitivity of the front-end circuit is about 9.74 V/pF. However, the phase lag and offset are inherent to the output signal of the front-end interface. Thus, care must be taken during the design of the closed-loop system.

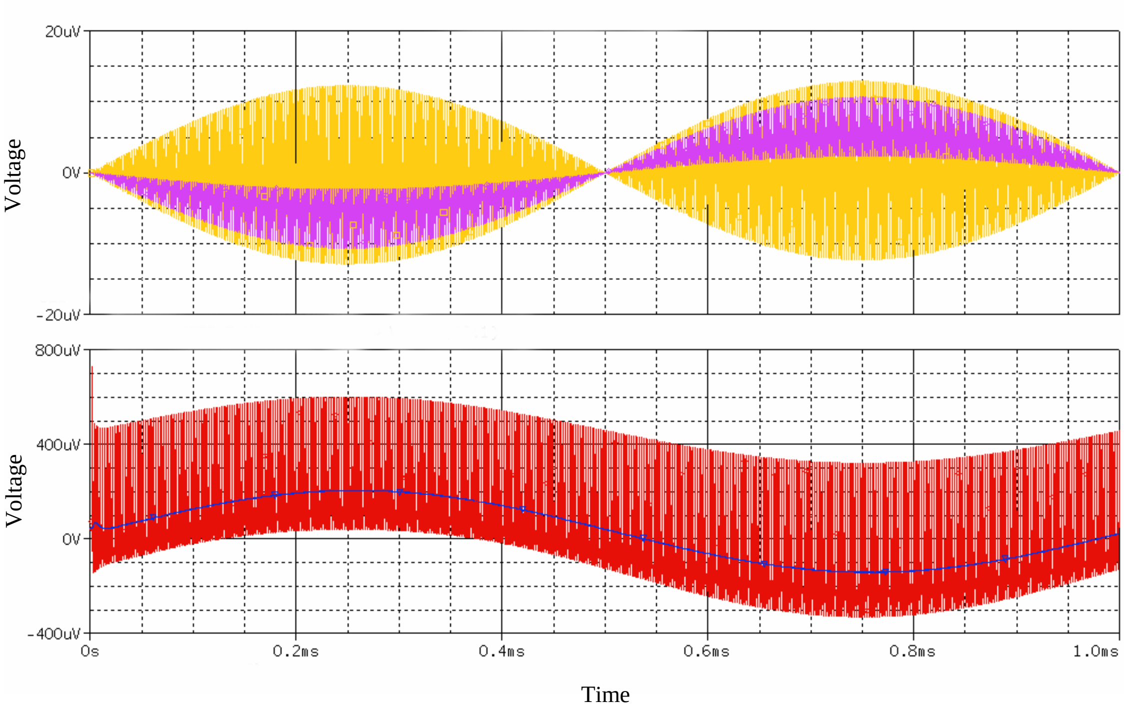

Figure 4.8 OrCAD/PSPICE simulation results of the front-end circuit for the capacitance variations of 10 ppm at a frequency of 1 kHz. The upper trace shows response waveforms of differential outputs of the charge amplifiers (yellow) and the demodulation circuits (pink). The bottom trace shows response waveforms of the output signals of the in-amp (red) and the low-pass filter (blue).

4.3 MEASUREMENT RESULTS

4.3.1 Hardware implementation

The hardware implementation was realised using the circuit diagram shown in Figure 4.7. All components are surface mount devices. The charge amplifiers were designed with R_f = 5 MΩ and C_f is adjustable between 0.167 – 0.5 pF. The feedback capacitance was tuned so that the charge amplifier has a gain of 2. The domodulation diodes were Schottky diodes with forward voltage V_D of 0.4 V. For the initial tests, only fixed capacitors were used instead of the sensor capacitances.

4.3.2 Transfer function of the charge amplifier on the excitation frequency

The first test was carried out to evaluate the operation of the charge amplifier. Two fixed capacitors with a capacitance of 1 pF were used to emulate the nominal sense capacitors. A sinusoidal excitation signal generated from a signal generator, Agilent 33220A, was directly connected to the common node between these two fixed capacitors. The frequency response of the charge amplifier was investigated by varying the excitation frequency f_{ex} from 500 Hz up to 5 MHz while the excitation amplitude was kept constant at 2.31 V. A digital oscilloscope, Agilent DSO032A, was used to measure the input and output signals of the charge amplifier. The resulting transfer function from the excitation voltage to the output voltage of the charge amplifier is illustrated in Figure 4.9.

As mentioned in section 4.2.2, the expected cut-off frequency was found at a frequency $1/R_fC_f$. At low frequencies, the measurement result agreed well with both OrCAD/PSPICE simulation and the analytical calculation from equation (4.3). However, a decrease in the gain at high frequencies was found in measurement and OrCAD/PSPICE simulation. This is due to the limited gain bandwidth product of the amplifier [**137**]. For an operational amplifier, OPA2107, its gain bandwidth product is 4.5 MHz at ±12 V supply voltage [**135**]. For the amplifier with a gain of 2, its bandwidth drops to about 2 MHz (see the dotted line in Figure 4.9). However, for the case of measurement results (the circles shown in Figure 4.9), it showed somewhat higher gain, but narrower bandwidth. This could be resulted from experimental error due to parasitic capacitances from lead wires, which connect fixed capacitors on a breadboard to the charge amplifier.

According to Figure 4.9, it can be concluded that the operating range of the charge amplifier is about 100 kHz to 1 MHz. Therefore, the front-end circuit should be operated with the excitation frequency within this operating range.

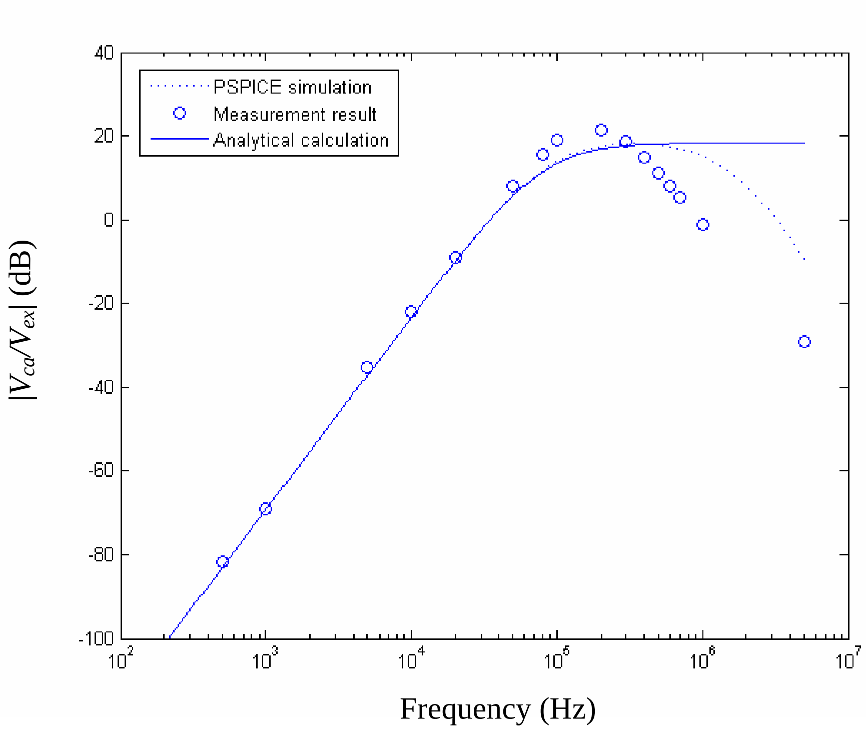

Figure 4.9 Bode plot of the transfer function V_{ca}/V_{ex}: the circles are data taken from the measurement, the solid line is obtained from equation (4.3) and the dotted line is the results from OrCAD/PSPICE simulations.

4.3.3 Linearity of the capacitance-to-voltage front-end circuit

In this section, the linearity of the conversion of capacitance to voltage was experimentally tested. Fixed capacitors were used to emulate the nominal sense capacitors and the change in capacitance was implemented using smaller fixed capacitors connecting in parallel to one of the nominal sense capacitors.

With a closed-loop control system, the displacement of the rotor is maintained within about 1% of the nominal capacitive gap (see chapter 5). The maximum ΔC to be measured is 20 fF for the sensor with a nominal sense capacitance of 1 pF. The value of ΔC is, however, too small to realise experimentally. Therefore, the fixed capacitors with a value of 10 nF were used as the nominal sense capacitors. The excitation frequency f_{ex} was then decreased to 100 Hz so that the impedance of the sensing element remains constant. The excitation signal with amplitude of 100 mV was applied to the common node of the nominal sense capacitors.

The symmetry of the two charge amplifiers is also critical. Thus, care must be taken in the selection of components used in the front-end circuit. For the prototype front-end circuit, all components are packaged in dual units. In addition, prior to the experiment, the charge amplifiers were tuned (by trimming feedback capacitance) in such a way that its output signal was well matched to each other.

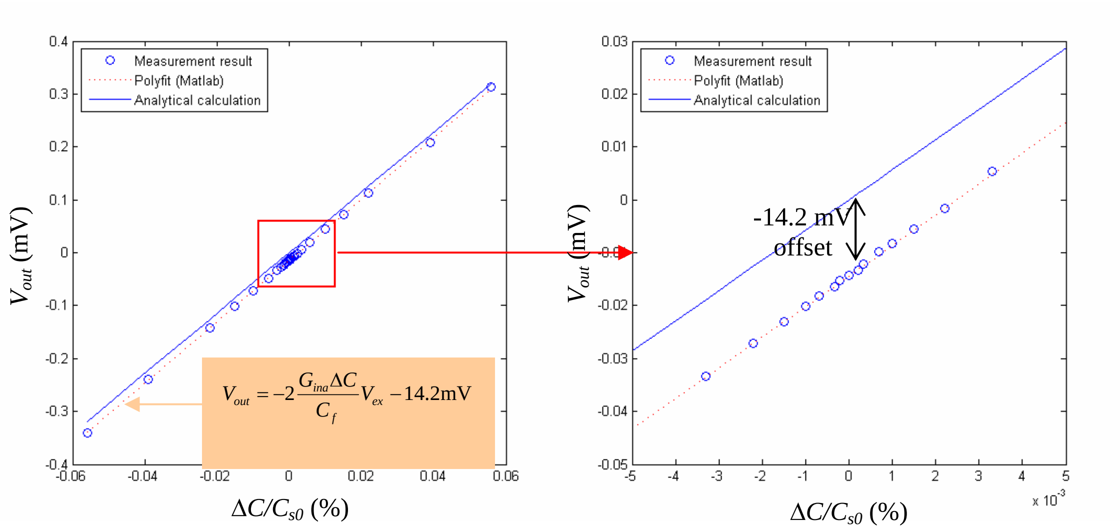

(a) (b)

Figure 4.10 Output voltage of the front-end circuit corresponding to a change in capacitance: the circles are data taken from the measurement, the dot line is the results from curve fitting using *polyfit* function in Matlab and the solid line is calculated from equation (4.12).

The measurement was carried out by varying Δ*C* from 560 pF down to 2.2 pF (using a fixed capacitor connecting in parallel to one of the nominal sense capacitors). The variation of Δ*C* is equivalent to the displacement of the rotor between 3% and 0.01% of the nominal capacitive gap (3 µm). The measurement results are shown in Figure 4.10. Figure 4.10a shows the output voltage due to capacitance variations Δ*C* from 560 pF down to 2.2 pF. Figure 4.10b shows the output voltage corresponding to small variations of capacitance. It can be seen that a small offset (–14.2 mV) is present in the measured output voltage of the front-end circuit. This DC offset can come from any operation amplifiers or mismatch between two charge amplifiers. This nevertheless can be compensated electronically. The expected theoretical output voltage can be calculated using equation (4.12) and is represented by the solid lines in Figure 4.10. The red dot lines are the result from data fitting using *polyfit* function in Matlab. The results show that the conversion of capacitance to voltage is linear within the operating range of interest. The measurement results also show a good correspondence with the theoretical values.

4.4 CONCLUSIONS

This chapter discusses the front-end circuit to be used in the prototype micromachined ESG. The circuit is completely symmetrical and it is used to measure a differential capacitance and convert it to voltage. The design and analysis of the prototype front-end circuit are described in detail.

The printed-circuit-board (PCB) prototype of the front-end circuit was built and experiments were carried out to evaluate the measurement results with that obtained from theoretical calculation and OrCAD/PSPICE simulation. It was found that the operating bandwidth of the charge amplifier is in the range between 100 kHz and 1 MHz. The initial test also shows that the front-end circuit can convert capacitance to voltage linearly for the capacitance variations ΔC, which are equivalent to the displacement of the rotor between 3% and 0.01% of the nominal capacitive gap. All measurement results agreed well to theoretical calculation and OrCAD/PSPICE simulation.

Note that the front-end circuit described in this chapter is also employed in chapter 7, which investigates a use of sidewall electrodes to levitate the mechanically unsuspended rotor.

Chapter 5

Electrostatic Suspension System Based on Sigma Delta Modulation

5.1 INTRODUCTION

The micromachined ESG requires a closed-loop electrostatic suspension system in order to levitate the mechanically unsupported micromachined rotor at the nominal position between the upper and lower electrodes. The closed-loop suspension system capacitively senses the displacement of the rotor. When the rotor is away from its nominal position, the suspension system will apply corresponding voltages to feedback electrodes in order to re-balance the rotor. The resulting electrostatic forces can then be used to measure the motion of the levitating rotor.

Typically, electrostatic control systems based on analogue force feedback is employed to suspend the levitating gyro rotor [**15–17, 89**]. Figure 5.1 shows the diagram of a basic levitating gyroscope with analogue feedback using electrostatic forces. For the sake of simplicity, only one degree of freedom along the z-axis is considered here. Assume that the rotor is levitated at the middle position between the upper and lower electrodes.

The electrostatic force is non-linear. It is proportional to the square of the voltage and inversely quadratically dependent on the distance between the rotor and the electrode. Therefore, to achieve linear electrostatic force feedback, the common approach is to apply the feedback voltage v_{fb} together with a DC bias voltage V_B to the feedback electrodes [**136, 138**]. A positive bias voltage is applied to one of the feedback electrode (say, the upper electrode), whereas a negative DC voltage with the same magnitude is applied to the lower electrode. The net electrostatic force F_{fb} on the rotor then becomes:

$$F_{fb} = \frac{1}{2}\varepsilon A_{fb}\left[\frac{(v_{fb}-V_B)^2}{(z_o-z)^2} - \frac{(v_{fb}+V_B)^2}{(z_o+z)^2}\right] \tag{5.1}$$

where

ε = dielectric constant of the air gap,

A_{fb} = total area of feedback electrodes and

z_o = nominal capacitive gap.

For a closed-loop system, small displacements of the rotor, z → 0, can be assumed. The quadratic terms cancel and the net electrostatic force can then simplify as shown in equation (5.2) where C_{fb} represents the feedback capacitance formed between the top and bottom electrodes and the rotor.

$$F_{fb} = -2C_{fb}\frac{v_{fb}V_B}{z_o} \tag{5.2}$$

However, in practice, the linearity of the analogue force feedback is also limited by the accuracy in matching $C_{fb,top}$ and $C_{fb,bottom}$.

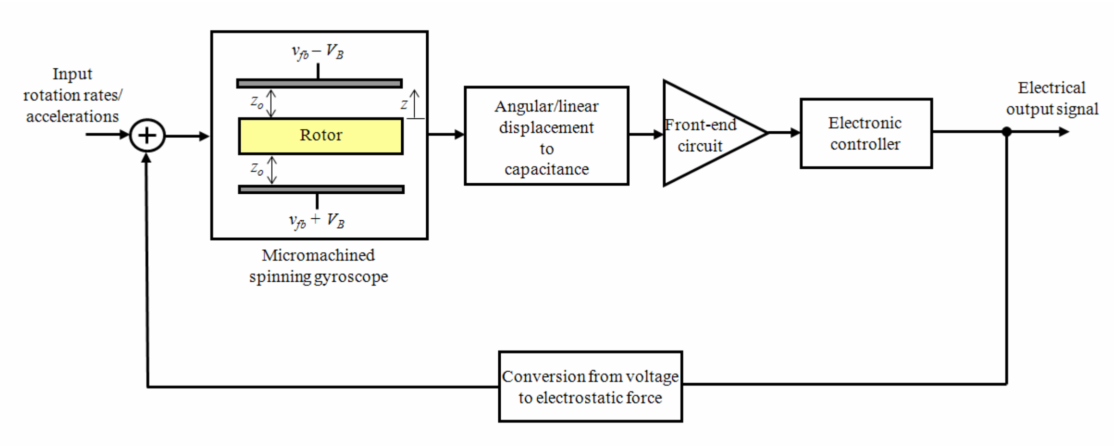

Figure 5.1 Block diagram of a closed-loop, analogue force-feedback micromachined levitating gyroscope.

The feedback voltage v_{fb} is generally derived from the output voltage of the front-end position measurement circuit. For larger displacements, the front-end circuit gain becomes non-linear [**139**]. This non-linearity will also affect the force feedback loop. For even larger deflections, e.g., the rotor is subjected to a shock or at the start-up phase where the rotor sits on the bottom substrate, the feedback force will change its polarity and drives the rotor towards the electrodes, resulting in the *latch-up* effect[1] [**18**]. This can lead to instability of the sensor system.

Due to these disadvantages, a digital force feedback system based on ΣΔM architectures is employed in the design of the micromachined ESG. This aims to improve the overall system stability compared with an analogue force feedback system. In this chapter, the concept of ΣΔM force feedback is discussed. Simulations of the micromachined ESG implemented into a ΣΔM force feedback loop were carried out to investigate the system behaviour and to evaluate the overall system performance. Two simulation tools were employed: one is OrCAD/PSPICE, which was used to perform simulations at electronic component level; the other tool is Matlab/Simulink with which simulations of the micromachined ESG at system level were carried out.

5.2 THE MICROMACHINED ESG WITH ΣΔM DIGITAL FORCE FEEDBACK

The micromachined ESG considered in this work employs a closed-loop electrostatic suspension system (ESS) based on electro-mechanical ΣΔM force feedback. The role of the ESS is to electrostatically levitate the rotor and maintain it at the middle position between the upper and lower control electrodes. Furthermore, the output of the ESS can be employed to measure both angular and linear displacements of the levitated rotor, which are related to input rates of rotation and accelerations. The basic block diagram of the micromachined

---

[1] The latch-up occurs when the rotor is stuck to one side of the electrodes. This is a non-recoverable situation requiring a sensor power shut down.

ESG implemented with a ΣΔM ESS is shown in Figure 5.2. The ESS contains four channels of the ΣΔM force feedback loop. These four channels are used to control the movement of the levitating rotor in the in-plane translation along the z directions and the out-of-plane tilting about the x and y axes. The ESS also comprises of the other two channels of the ΣΔM loop for a control of rotor motion along two in-plane axes (the x and y directions). Each channel of the ΣΔM feedback loops works independently.

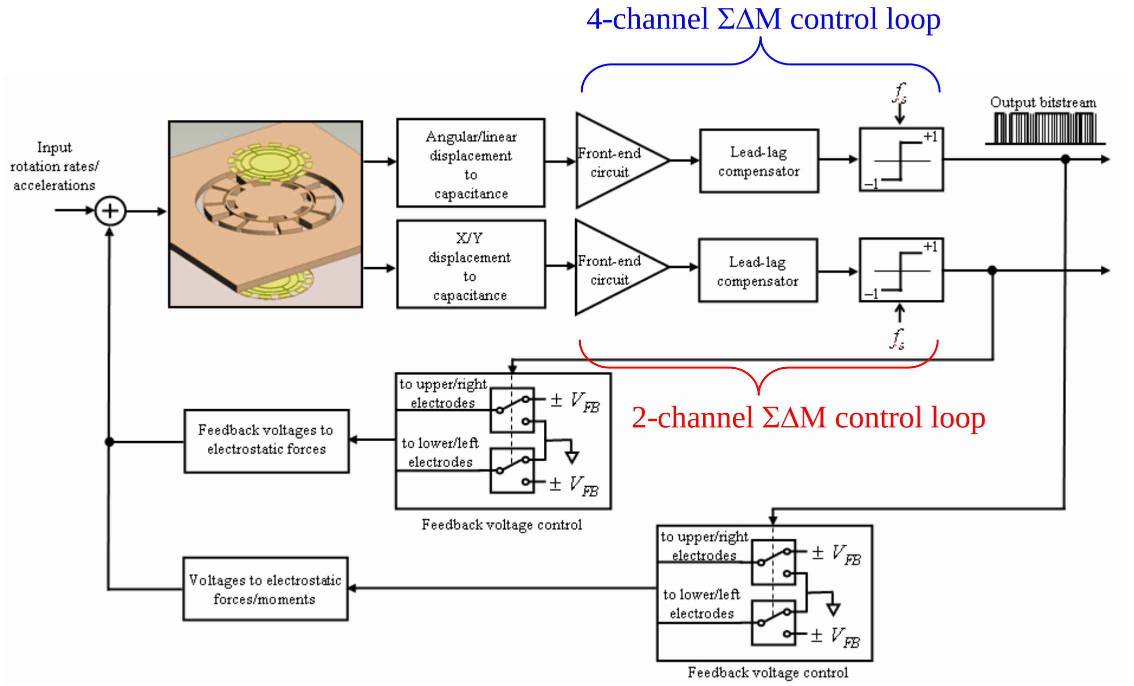

Figure 5.2 Block diagram of the micromachined ESG implemented with a closed loop electrostatic suspension system based on ΣΔM.

5.2.1 Principle of operation

The basic principle of the ΣΔM ESS is similar to that of purely electronic ΣΔM low-pass analogue to digital converters (ADC) [**140**]. In general a ΣΔM ADC evaluates the input signal by measuring the difference between the input and the output, integrating it and then compensating for that error at a frequency considerably higher than the sensing bandwidth. This is an intrinsic property of a ΣΔM, thus, sometimes it is referred to as an oversampling system. Typically, a basic ΣΔM ADC consists of three important components: (1) a loop transfer function, (2) a clocked quantiser and (3) a digital-to-analogue converter (DAC). A loop transfer function in a general ΣΔM ADC is built from integrators. Thus, noise is shaped away from frequencies near DC [**141**]. Such a ΣΔM low pass ADC is then normally used for low frequency applications. Thus, the ESS based on ΣΔM is well suited for navigation grade gyroscopes, where a signal bandwidth is about 100 Hz.

The basic principle of operation for each channel can be described as follows (see Figure 5.2): the sensing element itself acts as a double integrator for frequencies beyond its resonance frequency. In the presence of external forces and rotations, the rotor will move away from the middle position between the upper and the lower electrodes (i.e. the nominal position). The displacement of the rotor is then sensed by a front-end circuit which converts the differential change in capacitance into a voltage signal (for more details, see chapter 4). The signal is passed on to an electronic compensator in order to ensure system stability by adding some phase lead-lag to the control loop. The voltage signal is then followed by a clocked comparator with a sampling frequency f_s, which is higher than the frequency bandwidth of the ESG (100 Hz). In the feedback path, the digital output signal of the comparator is then amplified and fed to the feedback electrodes. The sign of the output signal of the comparator is used to determine to which electrodes feedback voltages are applied to. For example, the output signal of the comparator is +1 when the rotor moves away from its nominal position towards the upper electrode and its output is –1 if the rotor displaces from its nominal position towards the lower electrode. Then, if the output of the comparator is +1, the lower feedback electrodes are activated and vice versa. Generally speaking, only feedback electrodes that the rotor is further away from are applied with positive and negative fixed feedback voltages $\pm V_{fb}$, while the feedback electrodes closer to the rotor are grounded. This generates electrostatic forces pulling the rotor back to its nominal position. By assuming there is negligible movement of the rotor during one sampling period, the net electrostatic forces are approximately constant. This assumption is valid by the short duration of a clock cycle compared to the dynamics of the micromachined ESG. Thus, normally the electromechanical ΣΔM control loop is designed to use a sampling frequency far higher than the bandwidth of the sensing element.

5.2.2 Linear model of the micromachined ESG with ΣΔM force feedback

A ΣΔM control system consists of a non-linear component (i.e. a comparator/quantiser) that cannot be linearised easily. This makes it complicated and difficult to analyse. For the purposes of analysis, such a comparator is normally replaced by an arbitrary gain element with added quantisation noise, which is white. Thus, the micromachined ESG under consideration (Figure 5.2) can be modelled as a linear block diagram shown in Figure 5.3. The transfer functions of the sensing element are defined in section 3.4. In the presence of the input rotation rates and inertial forces, the rotor will be displaced away from its nominal position. The displacement of the rotor is sensed and, in turn, converted to a voltage signal by the front-end interface with a gain constant k_{po}. The gain constant k_{po} can be expressed as: $k_{po} = k_x k_c$ where k_x is the gain constant relating the displacement variation of the rotor to the differential change in capacitance as defined in equation (3.25). k_c is the capacitance-to-voltage sensitivity of the front-end circuit as expressed in Equation (4.10). The simulation results in OrCAD/PSPICE shows that the gain k_c is 9.74 V/pF (see section 4.3). The feedback gain k_F is given by equations (3.36) – (3.38).

The compensator provides some phase lead to compensate for the phase lag introduced by the micromachined ESG. The transfer function of the compensator can be expressed in the Laplace’s domain as:

$$C_s = \frac{s+z}{s+p} \tag{5.3}$$

where z and p are the zero and pole frequencies in radians per second. To provide phase lead in the correct frequency range (i.e., between the resonant peak of the micromachined ESG and the sampling frequency), the pole and zero frequencies are chosen so that $p > 2\pi f_s > z$. The comparator is linearlised and modelled as a quantiser gain k_Q with the introduced quantisation noise N_Q.

Each channel of the ΣΔM control loops individually provides one-bit output stream tracking the input rotations rates and/or accelerations. In order to retrieve the input signals (i.e., ma_z,

ω_x and ω_y) the digital output bitstreams (*BS*) from the four-channel ΣΔM are summed as expressed in equations (5.4) – (5.6)

$$BS_z = BS_1 + BS_2 + BS_3 + BS_4 \propto ma_z, \tag{5.4}$$

$$BS_{wx} = BS_1 + BS_2 - BS_3 - BS_4 \propto \omega_x\left(M_y\right), \tag{5.5}$$

$$BS_{wy} = -BS_1 + BS_2 + BS_3 - BS_4 \propto \omega_y\left(M_x\right), \tag{5.6}$$

where subscript 1 – 4 denote the channel of the ΣΔM control loops. The input signals ma_x and ma_y can be retrieved by BS_x and BS_y, respectively.

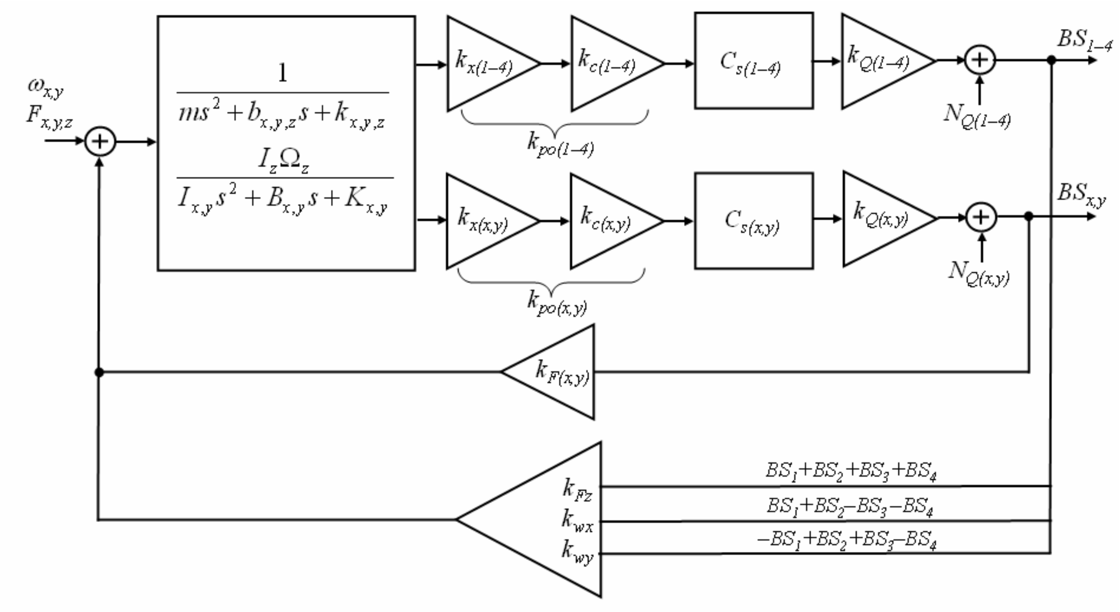

Figure 5.3 Linear model of the micromachined ESG implemented with a closed loop electrostatic suspension system based on ΣΔM.

The outputs (i.e., BS_x, BS_y, BS_z, BS_{wx} and BS_{wy}) can now be written in terms of the inputs (i.e., ma_x, ma_y, ma_z, ω_x and ω_y) and noise introduced by the quantisers as follows:

a) in the case of BS_x:

$$BS_x = N_{Qx} + \left(ma_x - BS_x k_{Fx}\right)\left(\frac{1}{m_x s^2 + b_x s + k_x}\right) k_{pox} k_{Qx} C_{sx} \tag{5.7}$$

Equation (5.7) can then be reworked as:

$$BS_x = \left(\frac{m_x s^2 + b_x s + k_x}{m_x s^2 + b_x s + \left(k_x - k_{Fx} k_{pox} k_{Qx} C_{sx}\right)}\right) N_{Qx} + \left(\frac{k_{pox} k_{Qx} C_{sx}}{m_x s^2 + b_x s + \left(k_x - k_{Fx} k_{pox} k_{Qx} C_{sx}\right)}\right) ma_x \tag{5.8}$$

The term $\left(\frac{m_x s^2 + b_x s + k_x}{m_x s^2 + b_x s + \left(k_x - k_{Fx} k_{pox} k_{Qx} C_{sx}\right)}\right)$ is defined as a noise transfer function (*NTF*) relating the output signal to the quantisation noise (in the absence of the input inertial force) and the term $\left(\frac{k_{pox} k_{Qx} C_{sx}}{m_x s^2 + b_x s + \left(k_x - k_{Fx} k_{pox} k_{Qx} C_{sx}\right)}\right)$ is defined as a signal transfer function (*STF*) relating the output signal to the input inertial force when no quantisation noise.

b) in the case of BS_y:

The relationship between the output and the two inputs ma_y and N_{Qy} is similar to the case of BS_x:

$$BS_y = \left(\frac{m_y s^2 + b_y s + k_y}{m_y s^2 + b_y s + \left(k_y - k_{Fy} k_{poy} k_{Qy} C_{sy}\right)}\right) N_{Qy} + \left(\frac{k_{poy} k_{Qy} C_{sy}}{m_y s^2 + b_y s + \left(k_y - k_{Fy} k_{poy} k_{Qy} C_{sy}\right)}\right) ma_y \tag{5.9}$$

and

$$NTF_{BS_y} = \left(\frac{m_y s^2 + b_y s + k_y}{m_y s^2 + b_y s + \left(k_y - k_{Fy} k_{poy} k_{Qy} C_{sy} \right)} \right),$$

$$STF_{BS_y} = \left(\frac{k_{poy} k_{Qy} C_{sy}}{m_y s^2 + b_y s + \left(k_y - k_{Fy} k_{poy} k_{Qy} C_{sy} \right)} \right).$$

c) in case of *BS*:

$$BS_z = \sum_{n=1}^{4} N_{Qn} + \left(ma_z - BS_z k_{Fz} \right) \left(\frac{1}{m_z s^2 + b_z s + k_z} \right) \sum_{n=1}^{4} k_{pon} k_{Qn} C_{sn} \tag{5.10}$$

Equation (5.10) can then be reworked as:

$$BS_z = NTF_{BS_z} \sum_{n=1}^{4} N_{Qn} + STF_{BS_z} ma_z \tag{5.11}$$

where

$$NTF_{BS_z} = \left(\frac{m_z s^2 + b_z s + k_z}{m_z s^2 + b_z s + \left(k_z - k_{Fz} \sum_{n=1}^{4} k_{pon} k_{Qn} C_{sn} \right)} \right) \text{ and}$$

$$STF_{BS_z} = \left(\frac{\sum_{n=1}^{4} k_{pon} k_{Qn} C_{sn}}{m_z s^2 + b_z s + \left(k_z - k_{Fz} \sum_{n=1}^{4} k_{pon} k_{Qn} C_{sn} \right)} \right).$$

c) in case of BS_{wx} and BS_{wy}:

$$BS_{wx} = \sum_{n=1}^{4} N_{Qn} + \left(\omega_x - BS_{wx} k_{Fwx}\right)\left(\frac{I_z \Omega_z}{I_y s^2 + B_y s + K_y}\right)\sum_{n=1}^{4} k_{pon} k_{Qn} C_{sn} \tag{5.12}$$

$$BS_{wy} = \sum_{n=1}^{4} N_{Qn} + \left(\omega_y - BS_{wy} k_{Fwy}\right)\left(\frac{I_z \Omega_z}{I_x s^2 + B_x s + K_x}\right)\sum_{n=1}^{4} k_{pon} k_{Qn} C_{sn} \tag{5.13}$$

Rework these two equations yields:

$$BS_{wx} = NTF_{BS_{wx}} \sum_{n=1}^{4} N_{Qn} + STF_{BS_{wx}} \omega_x \tag{5.14}$$

$$BS_{wy} = NTF_{BS_{wy}} \sum_{n=1}^{4} N_{Qn} + STF_{BS_{wy}} \omega_y \tag{5.15}$$

where

$$NTF_{BS_{wx}} = \left(\frac{I_y s^2 + B_y s + K_y}{I_y s^2 + B_y s + \left(K_y - k_{Fwx} I_z \Omega_z \sum_{n=1}^{4} k_{pon} k_{Qn} C_{sn}\right)}\right),$$

$$STF_{BS_{wx}} = \left(\frac{I_z \Omega_z \sum_{n=1}^{4} k_{pon} k_{Qn} C_{sn}}{I_y s^2 + B_y s + \left(K_y - k_{Fwx} I_z \Omega_z \sum_{n=1}^{4} k_{pon} k_{Qn} C_{sn}\right)}\right),$$

$$NTF_{BS_{wy}} = \left(\frac{I_x s^2 + B_x s + K_x}{I_x s^2 + B_x s + \left(K_x - k_{Fwy} I_z \Omega_z \sum_{n=1}^{4} k_{pon} k_{Qn} C_{sn}\right)}\right) \text{and}$$

$$STF_{BS_{wy}} = \left(\frac{I_z \Omega_z \sum_{n=1}^{4} k_{pon} k_{Qn} C_{sn}}{I_x s^2 + B_x s + \left(K_x - k_{Fwy} I_z \Omega_z \sum_{n=1}^{4} k_{pon} k_{Qn} C_{sn} \right)} \right).$$

Equations (5.9), (5.10), (5.11), (5.14) and (5.15) present the characteristics of the output bitstreams BS_x, BS_y, BS_z, BS_{wx} and BS_{wy} in terms of the signal and noise transfer functions. However, a numerical evaluation of the above equations is problematic since it is difficult to estimate the quantiser gain k_Q. The general approach is to simulate the system using Matlab/Simulink model, which is described in the next section.

5.3 SIMULATION OF THE ELECTROMECHANICAL ΣΔM MICROMACHINED ESG

This section presents simulations of the micromachined ESG with the ΣΔM electrostatic suspended system. The purpose of the simulations at system level is to analyse the behaviour and performance of the system. More importantly, the simulations are performed in order to investigate the stability of the closed-loop sensor with digital ΣΔM force feedback because a linear analysis is not suitable for predicting the stability of the ΣΔM system [**139**].

In this thesis, two simulation software packages, i.e. Matlab/Simulink and OrCAD/PSPICE, are used to model the micromachined ESG with the ΣΔM closed-loop control system. Matlab/Simulink is a simple, yet powerful tool to study the behaviour of the whole system at system level. It allows the integration of sensor dynamics together with a mixed-signal electronic interface by using mathematical models. It is mainly used to perform simulations for system analysis in this chapter. The other tool employed in this study is OrCAD/PSPICE which is used to simulate the device system at electronic-level. The OrCAD/PSPICE model provides more realistic insight into the system behaviour and performance as it takes into account of various effects, such as non-idealities of electronic components, saturation effects and electrical feedback signals coupling to a sensing circuit. However, the drawback of OrCAD/PSPICE simulations is simulation time. Therefore, the OrCAD/PSPICE model was developed only just to simulate the stability of the micromachined ESG with ΣΔM feedback, in particular, at the “start-up” phase. This was carried out to ensure that the closed loop ESS is able to levitate the rotor when it sits on stoppers at the bottom substrate and maintain the rotor at the mid-position between the upper and lower electrodes. Furthermore, the OrCAD/PSPICE model was performed to compare results to the Matlab/Simulink model, which has much faster simulation time.

5.3.1 Matlab/Simulink model

This section presents Matlab/Simulink models of the micromachined ESG with the digital ΣΔM ESS. Two models were developed. The first model (Figure 5.4) was implemented by considering only the behaviour of the micromachined ESG for the motion along the z axis (levitation direction), thus hereafter also called the “concise” model. It was developed for a purpose: to predict the stability and behaviour of the device system at the start-up phase. The simulation results were also compared to those obtained from the OrCAD/PSPICE model (discussed in section 5.3.2). This model assumes that only one channel of a ΣΔM control loop is implemented to control the position of the rotor along the z axis.

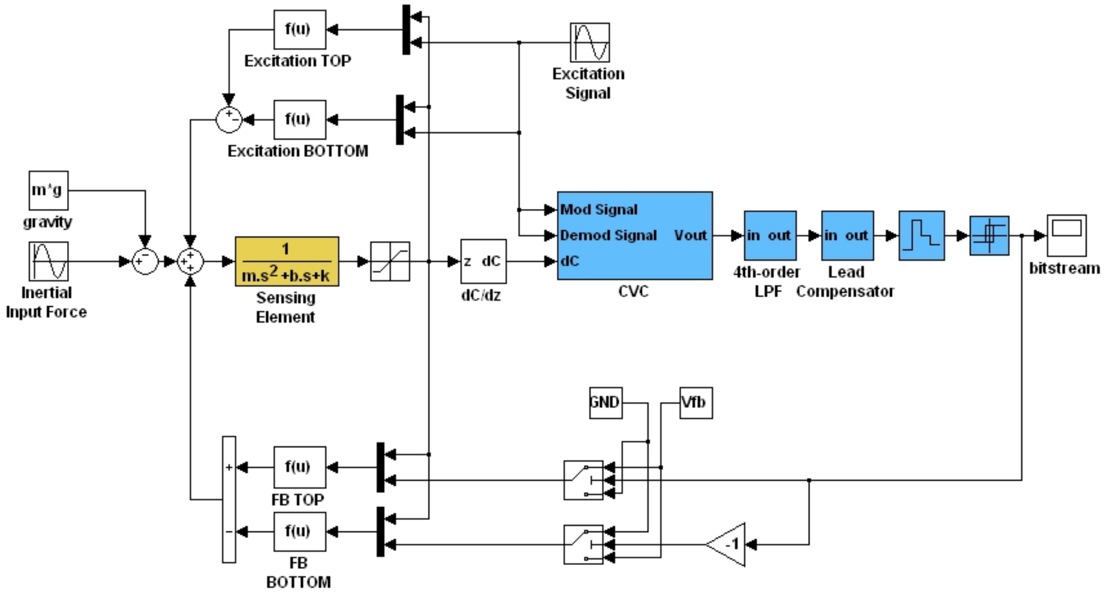

Figure 5.4 Matlab/Simulink model of the micromachined ESG with a closed loop ESS based on ΣΔM.

The concise Matlab/Simulink model contains several building blocks as follows: the model of the micromachined ESG for the motion along the z direction is shown in a yellow building block. It is a second-order mass-spring-damper model (see chapter 3) including an over-range displacement stoppers[2]. The displacement of the rotor is then converted into the differential capacitance using a building block *dC/dz*. The model of the electronic interface is shown in light-blue building blocks, including a front end circuit, a lead-lag compensator and a clocked comparator. The clocked comparator was modelled using a zero-order hold building block, which represents a sample and hold clocked at the sampling frequency, and an ordinary comparator building block. The output of the comparator controls switches that decide the sign of the feedback force; in other words, whether the rotor is pulled up or down. The concise model also includes major internal disturbances; for example, the gravity force (*mg*), electrostatic forces generated from the excitation voltages required for the position measurement circuit and the op-amp non-idealities (i.e. saturation voltage, bandwidth and finite gain).

The second Matlab/Simulink model shown in Figure 5.5 was developed to simulate the full system of the micromachined ESG, hereafter also called the *full* model. The model takes into account of motions in five degrees of freedom, i.e. the translation of the rotor along the x, y and z axes and the rotation of the rotor about the x and y axes. The dynamics of the sensing element is shown in a yellow-colour building block. The dynamics of the rotor spinning about its main axis (the z-axis) is neglected. The rotor is assumed to spin at a constant speed. Light-blue building blocks represent the front-end capacitive readout circuit and electronic interface. As discussed earlier, clocked comparators were modelled using a zero-order hold building block connecting in series with an ordinary comparator. The output of the comparator in each channel controls switches that decide whether the feedback voltages are applied to the upper or lower feedback electrodes. The conversion of the feedback voltages to electrostatic forces and moments is modelled by a white building block.

5.3.2 OrCAD/PSPICE model

---

[2] Separate mechanical stoppers were designed to prevent the rotor touching the electrodes which will lead to a short circuit problem.

The model of the micromachined ESG incorporating into a ΣΔM feedback control system at electronic level was implemented in OrCAD/PSPICE. Due to the simulation time issue as mentioned in the beginning, just only the behaviour of the micromachined ESG in the z direction was considered. This OrCAD/PSPICE model was developed to investigate the behaviour of the device in the z axis (the levitation direction) and, in particular, to ensure the stability of the sensor when it is operated from the start-up.

Figure 5.6 shows the OrCAD/PSPICE model of the sensing element, which was implemented using the analogue behavioural modelling library [**134, 142**]. The model is the second-order mass-spring-damper representing the rotor motion along the z axis. The variable sense and feedback capacitors were modelled by the use of two OrCAD/PSPICE components, i.e. function blocks and time-variable admittances [**143**], as illustrated in Figure 5.7. Two function blocks convert the displacement of the rotor into the signal which represents the imbalance in capacitance. The variable admittances X1 and X2 represent the top and bottom excitation capacitors, respectively. The admittances X3 and X4 are the top and bottom sense capacitors. The top and bottom feedback capacitors were included into the OrCAD/PSPICE model using the admittances X5–X7. These feedback capacitors were modelled to examine whether or not the feedback signals are coupled into the pick-off circuit. This may influence to the system stability. The sinusoidal carrier signal *Vcarrier* with a frequency of 1 MHz was used as the excitation voltage source. A high value resistor *Rdummy* was required to prevent a floating point error.

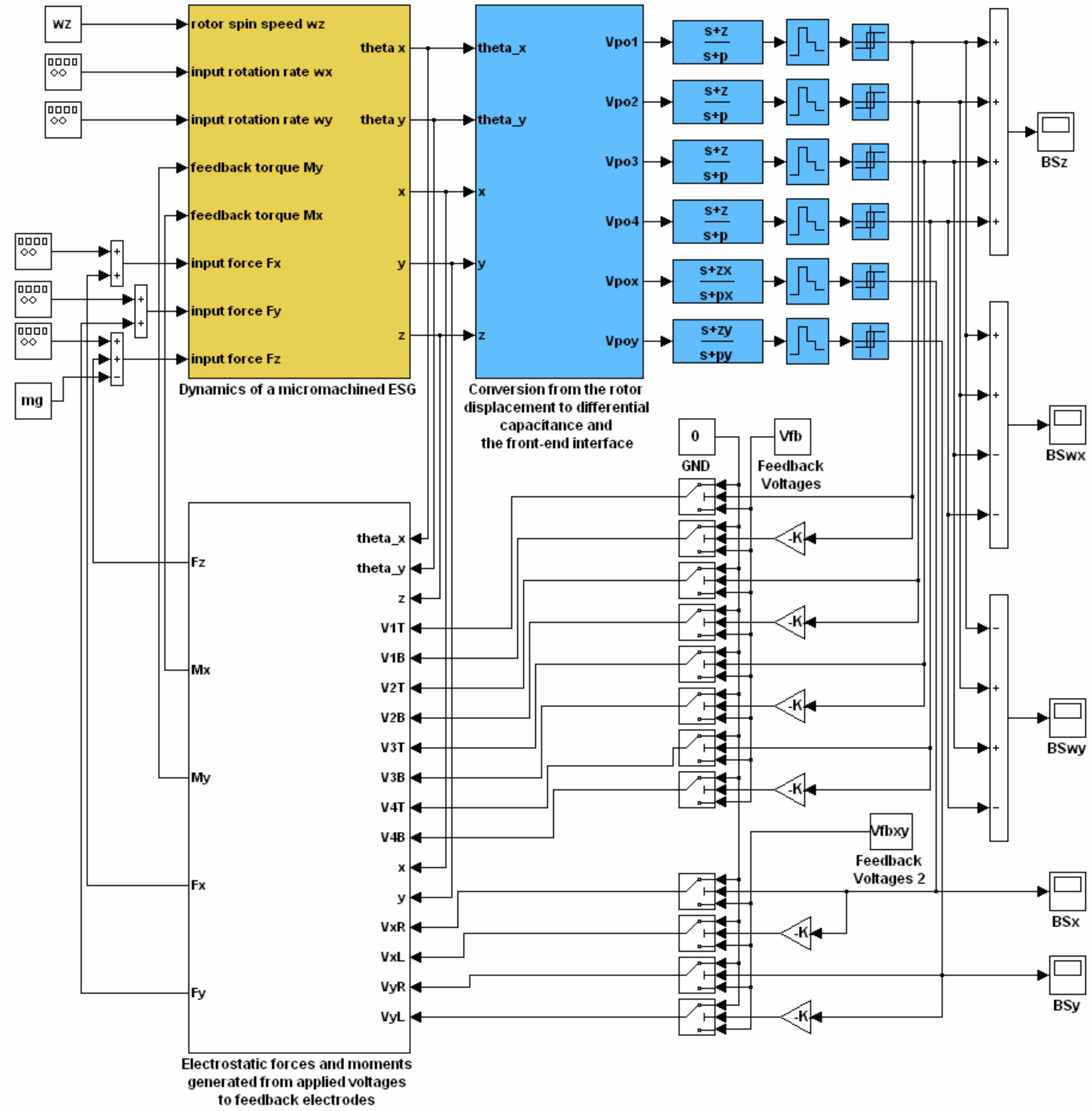

Figure 5.5 Matlab/Simulink model of the micromachined ESG implemented into the multi-channel ΣΔM electrostatic suspension system.

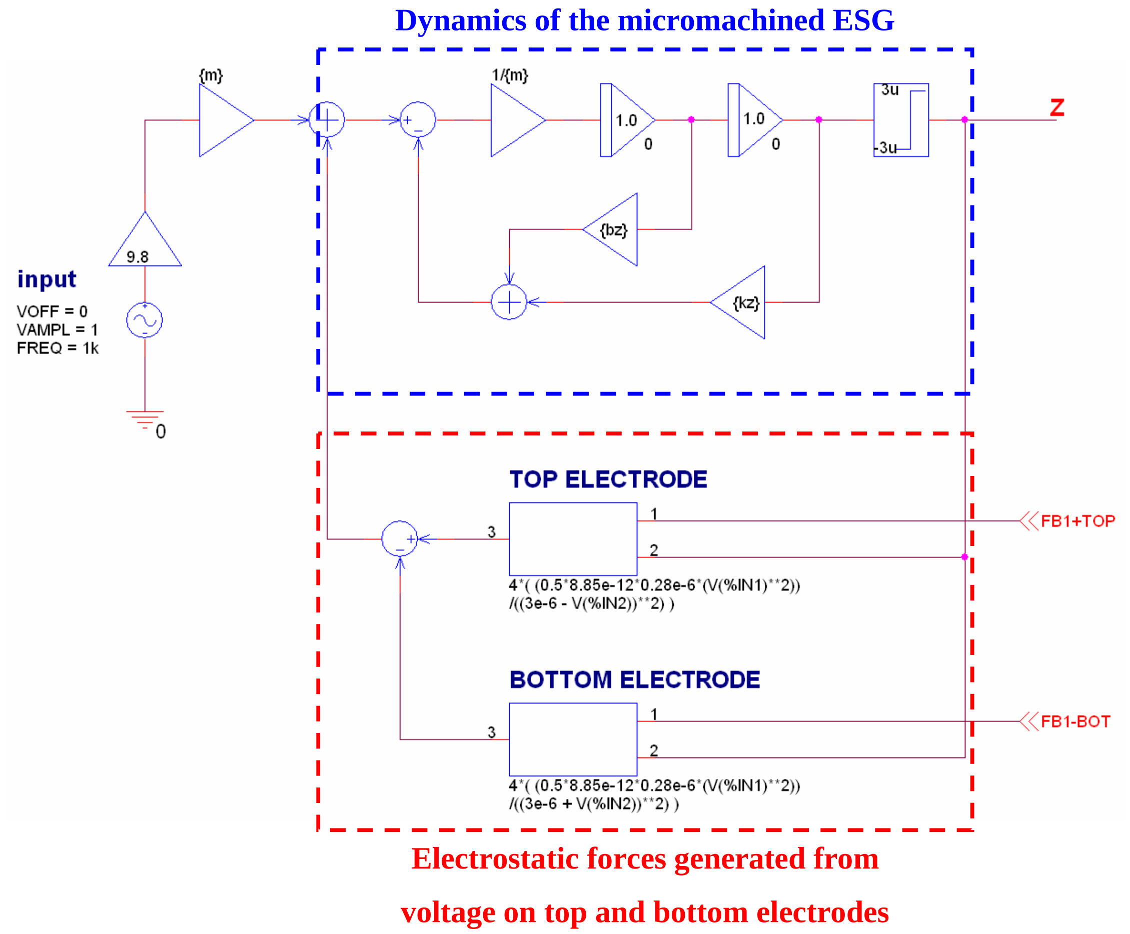

Figure 5.6 OrCAD/PSPICE model of the sensing element for the motion along the z axis and function blocks representing electrostatic forces generated from voltage applied to top and bottom electrodes.

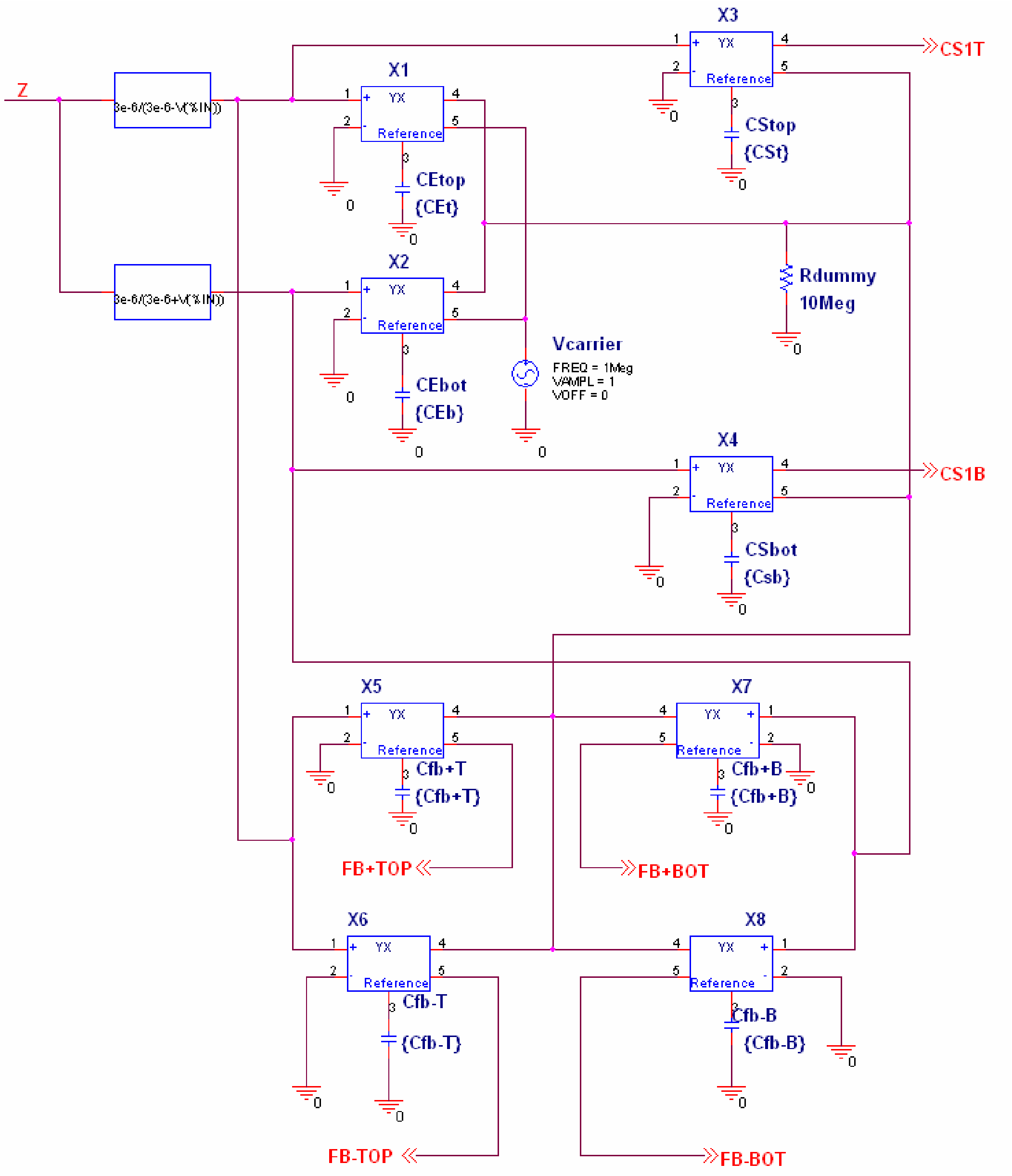

Figure 5.7 OrCAD/PSPICE model of variable capacitors formed between top/bottom electrodes and the rotor.

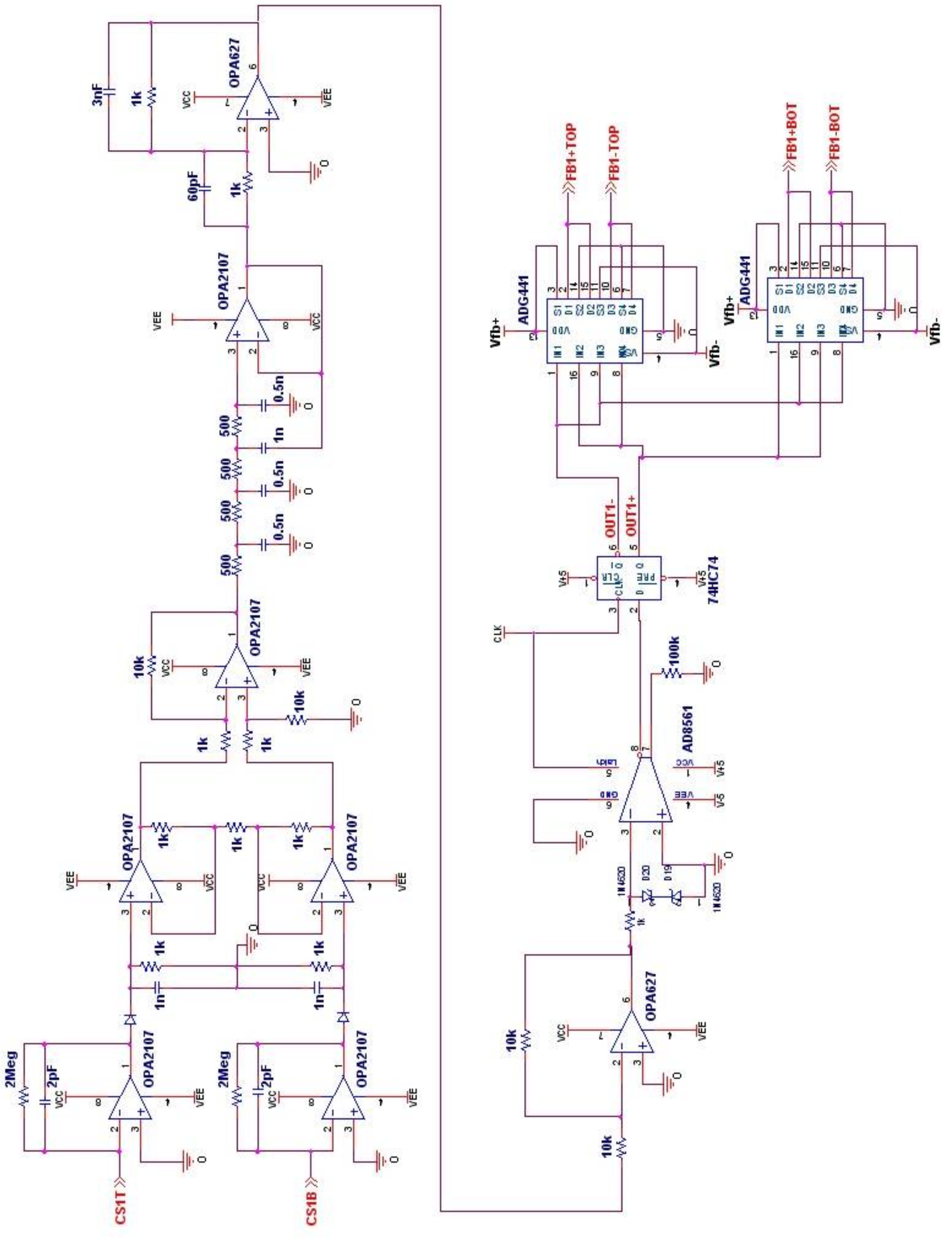

Figure 5.8 OrCAD/PSPICE model of the front-end interface and a ΣΔM feedback loop for the micromachined ESG.

The front-end interface and a ΣΔM control circuit are shown in Figure 5.8. The front-end interface converts the differential capacitance to the single-end output voltage. Its principle of operation is discussed in chapter 4. A phase compensator is added into the loop in order to compensate phase lag resulted from the double integration characteristics of the sensing element and phase delay in electronic components. The output is then digitised by a clocked comparator, which is implemented in OrCAD/PSPICE by a comparator AD8561 and a D-type flip flop. The electrode-selection switches were modelled by a SPICE model of a commercial discrete component, ADG441 [**144**]. Conversion of the output feedback voltages to electrostatic forces is done by two function blocks as illustrated in Figure 5.6.

5.3.3 Stability analysis

In this section, the stability analysis of the closed-loop micromachined ESG under two circumstances was investigated. The first simulation was carried out to examine the stability of the system at the start-up phase. As mentioned earlier in chapter 3, the rotor has no mechanical connection to a substrate and thus during the start-up it does not stay in the middle position between the upper and lower electrodes, rather it sits on the bottom electrodes. As the distance of the rotor with respect to the middle position is relatively large, it can result in a nonlinear effect in the force feedback process, which may lead to system instability. Therefore, the simulation was carried out to ensure that the closed-loop ESS is able to levitate the rotor from the bottom substrate and keep it floating at the centre between the upper and lower electrodes (i.e. the so-called nominal position). The second simulation carried out in this section is to evaluate the stability and performance of the closed-loop micromachined ESG when it experienced the input acceleration only along the levitation axis (the z-axis).

The simulations considered in this section were performed using OrCAD/PSPICE model and the concise Matlab/Simulink model. The micromachined ESG having the following parameters is used: m = 3.73 mg, b_z = 4.66 nNm/s, k_z = 16 Nm, $C_{E(T,B)}$ = 6.25 pF, $C_{s(T,B)}$ = 4 × 1.54 pF and $C_{fb(T,B)}$ = 4 × 1.88 pF. For the sensing element with a closed-loop control system, the damping coefficient b_z can be assumed as a constant value. The parameters related to the closed-loop ΣΔM control system are given in Table 5.1.

At the start-up, assume that the rotor sits on stoppers at the bottom substrate and thus the initial distance of the rotor is 1 μm below the nominal position. Figure 5.9 shows the simulation results which present the system behaviour of the micromachined ESG at the start-up phase. The upper trace shows the displacement of the rotor along the z axis, the middle trace showing the feedback force and the bottom trace showing the output bitstream. It can be seen that at the start-up phase the feedback force shows a non-linear behaviour and its magnitude is not constant. However, it is apparent that the control system can cope with this large displacement. After transient-state behaviour, the control system captures the rotor and ensures that the rotor is maintained at the middle position between the electrodes. When the rotor reaches steady state (i.e. the rotor levitating at the nominal position), the waveform of the output bitstream indicates a limit cycle frequency changing between $f_s/4$ and $f_s/6$ (see 5.9b). This is the expected behaviour of the second-order ΣΔM system [**125**]. From Figure 5.9a and 5.9b, both OrCAD/PSPICE and Matlab/Simulink simulations show similar results and have a good agreement to each other.

Table 5.1: System parameters of the closed-loop ESS which are employed in the system stability analysis.

Parameters	**Value**
Sampling frequency, f_s (kHz)	128
Signal bandwidth, BW (Hz)	1024
Excitation frequency, f_{ex} (Hz)	1×10^6
Feedback voltage, V_{fb} (V)	±15

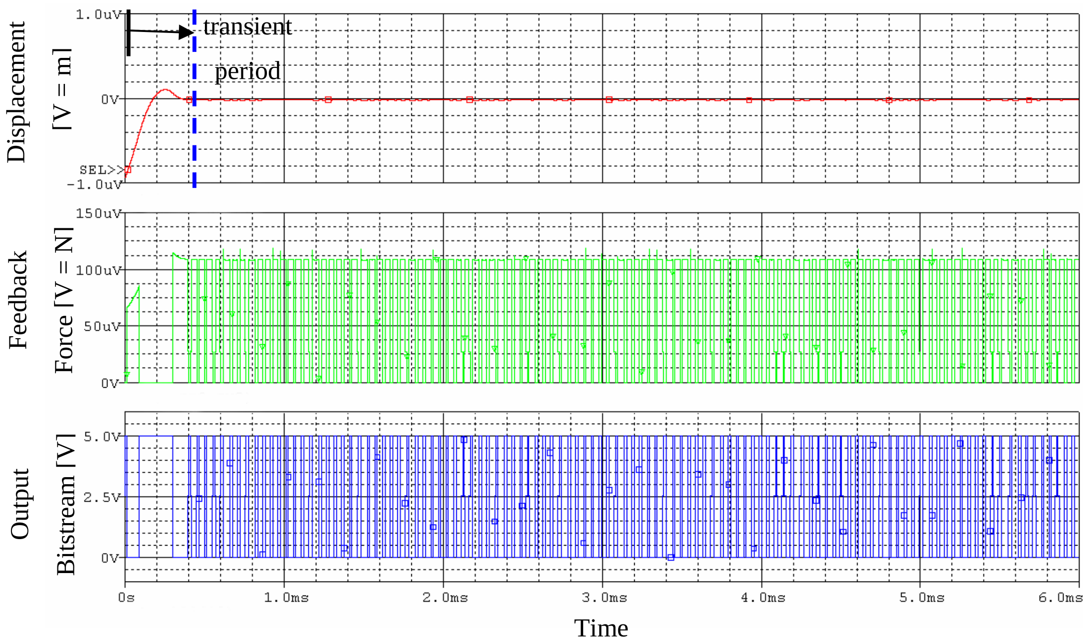

(a) OrCAD/PSPICE

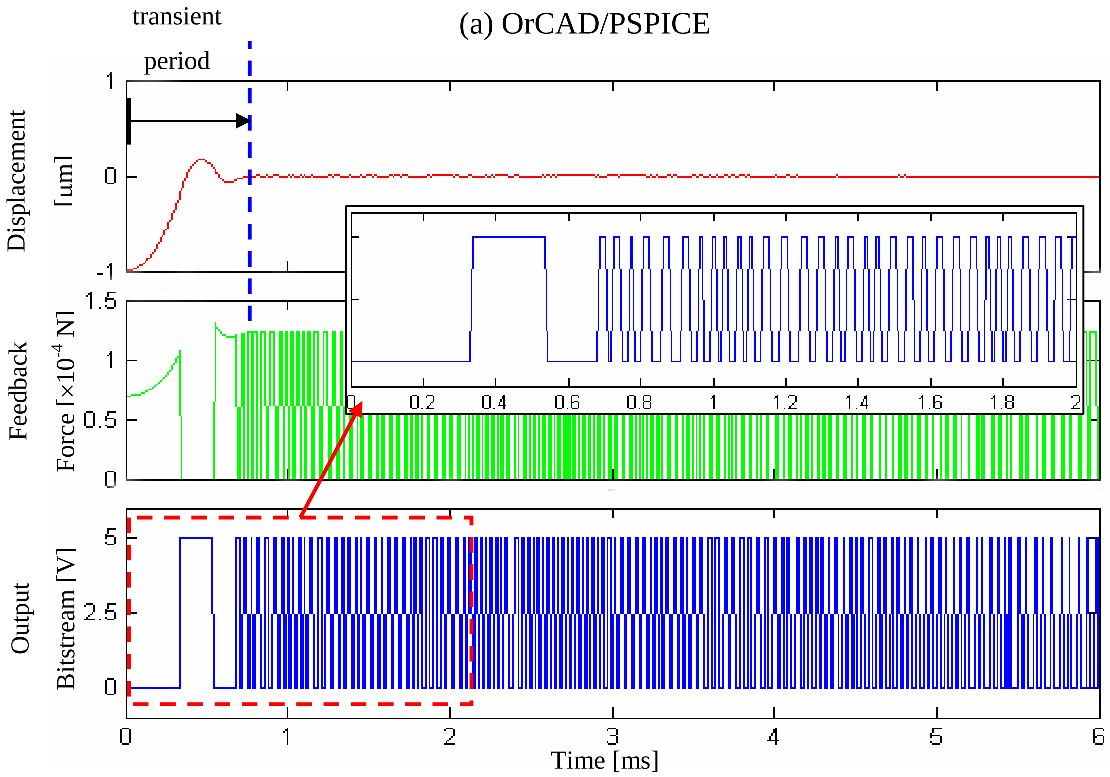

(b) Matlab/Simulink

Figure 5.9 System response at the start-up phase, assuming the rotor sits on the stoppers at the bottom substrate (1 μm below the nominal position). The top trace shows the displacement of the rotor, middle trace showing the feedback forces and bottom trace is the digital output bitstreams.

Figure 5.10 shows the system response when the micromachined ESG experiences acceleration along the z direction. The acceleration is a sinusoidal signal and has a peak magnitude of 1 g (1 g = 9.8 m/s^2) and a frequency of 1 kHz. The upper trace shows the input force due to the applied acceleration, the middle trace the displacement of the rotor in the z axis direction and the bottom trace the pulse-modulated output bitstreams. The simulations were carried out by assuming the rotor is already levitated in the middle position between the upper and lower electrodes. It was found that the rotor displaces up and down about 5 nm below the centre position between the upper and lower electrodes. The maximum displacement of the rotor was ±5 nm as a result of the input acceleration. The offset displacement of 5 nm was resulted from the constant force of gravity (*mg*). Figure 5.11 shows the power spectral densities (PSD) of the output bitstream in the above simulation. A peak value was found at the input frequency (1 kHz). This indicates that the output bitstream can be employed to track the input acceleration. Furthermore, the spectra showed the expected noise-shaping characteristics of the second-order ΣΔM control system. Both OrCAD/PSPICE and Matlab/Simulink simulations showed results that have a good agreement to each other, although the OrCAD/PSPICE simulation yields a lower signal to quantisation noise ratio[3] (SQNR) than that of Matlab/Simulink simulation (SQNR = 50 dB). However, these simulations revealed the potential of the designed electrostatic suspension system for being used to levitate and suspend the rotor. A good agreement between OrCAD/PSPICE and Matlab/Simulink simulations indicates that the Matlab/Simulink tool can be employed to investigate the behaviour of the micromachined ESG and also to evaluate its performance.

---

[3] SQNR is the ratio of the signal present to the noise generated by the ΣΔM control system.

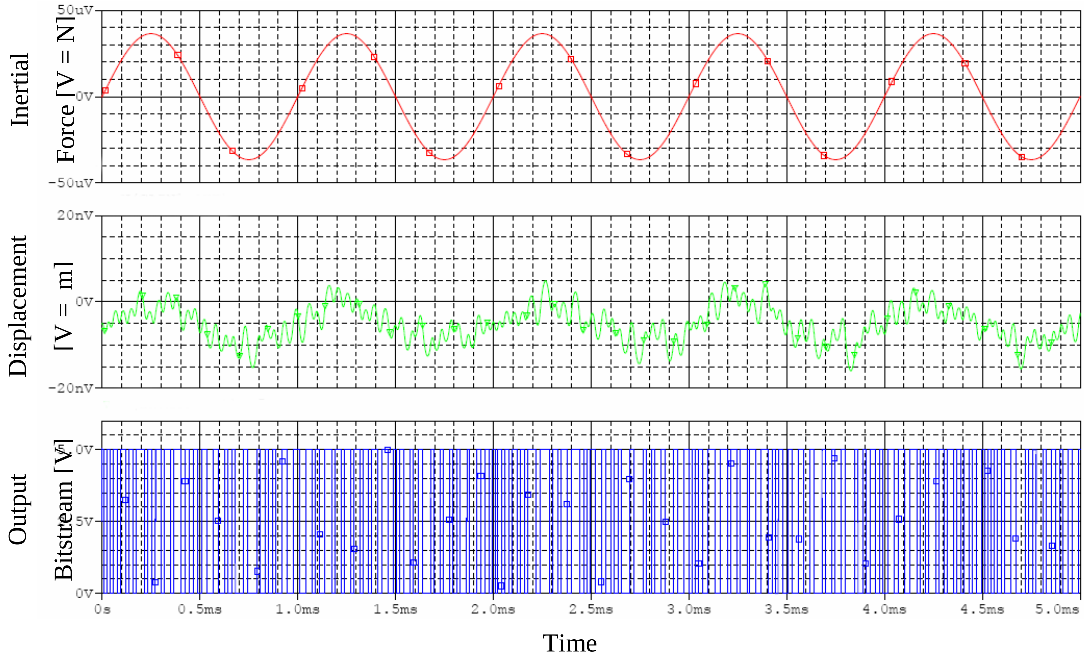

(a) OrCAD/PSPICE

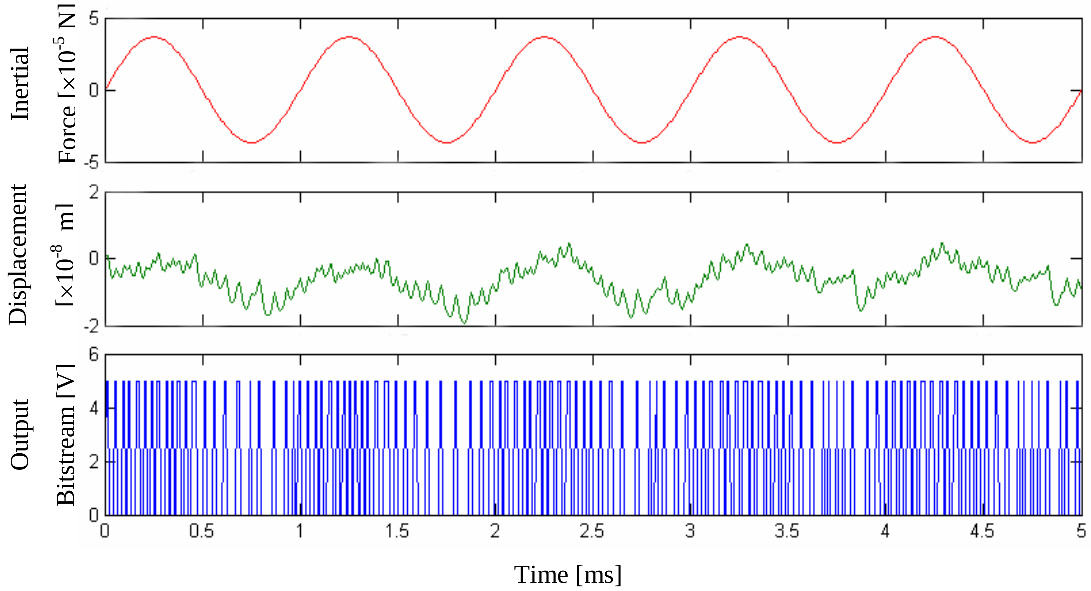

(b) Matlab/Simulink

Figure 5.10 Device response when ±1 g sinusoidal acceleration with a frequency of 1 kHz is applied. The top trace shows the input acceleration, middle trace showing the displacement of the rotor and bottom trace is the digital output bitstreams.

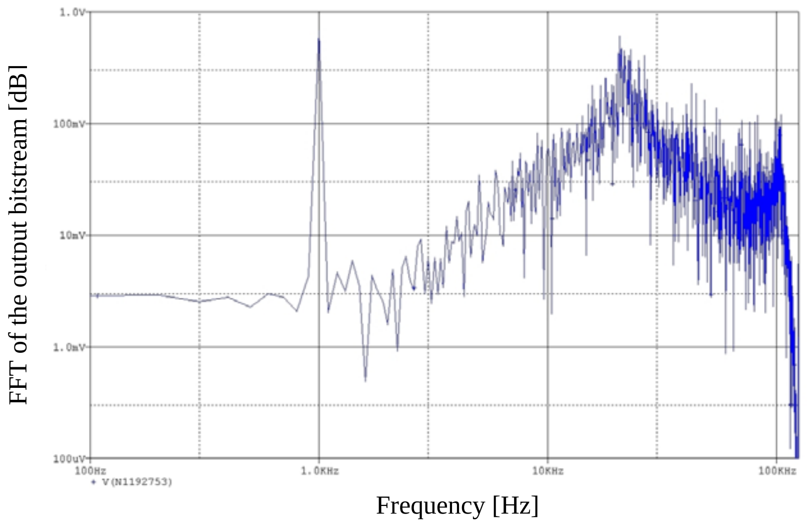

(a) OrCAD/PSPICE

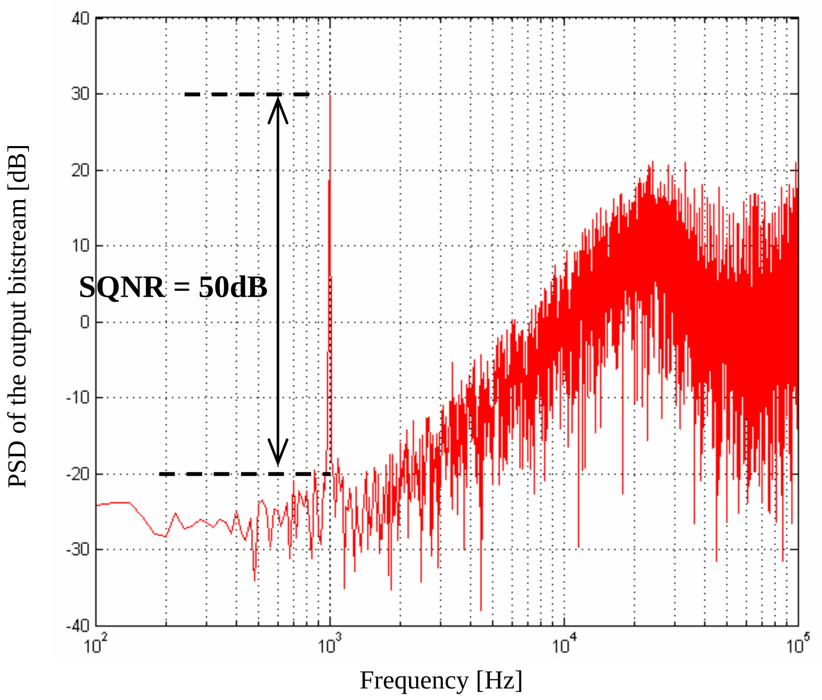

(b) Matlab/Simulink

Figure 5.11 Power spectral densities of the output bitstreams when ±1 g sinusoidal acceleration with a frequency of 1 kHz is applied

5.3.4 Simulink simulations of the multi-axis micromachined ESG

Simulations of the full model of the micromachined ESG with digital ΣΔM force feedback (see Figure 5.5) were carried out at system level using Matlab/Simulink. The purpose of the simulations was to investigate the system behaviour and also to evaluate the performance of the sensor. The sensor parameters given in Table 3.3 were used in the following simulations.

5.3.4.1 *Cross coupling issue*

As mentioned in chapter 2, the so-called quadrature error coupling between drive and sense modes has been the major problem in the design of conventional vibration-type micromachined gyroscopes. However, the quadrature error is inherently ruled out with the design of the micromachined ESG. Rather, in the micromachined ESG a precession torque from one gyro axis can be coupled into the other gyro axis due to its operating principle (see equations (3.13) and (3.14)). This may decrease the performance of the sensor. In order to investigate the effect of the cross coupling, the gyro model was developed as shown in Figure 5.12. The model includes the aforementioned cross coupling issue.

The parameters related to the closed-loop ΣΔM control system are given in Table 5.2. Assume that the micromachined ESG experienced the rotation about the x axis only. The input rotation rate is a sinusoidal signal having a magnitude of ±10 rad/s and a frequency of 48 Hz. The output bitstreams from four channels were summed according to equations (5.4) – (5.6) to extract ω_x, ω_y and F_z. Figure 5.13 shows the power spectrum densities of the summed output bitstreams. As can be seen from the figure, only the ω_x signal was observed at the M_y output bitstream; there was no peak signal at 48 Hz induced into the other axis, hence no cross coupling can be observed. A SQNR was calculated from the PSD of the M_y output bitstream, yielding 72 dB.

Table 5.2: System parameters of the closed-loop ESS which are used in the full-model Simulink simulations.

Parameters	Value
Sampling frequency, f_s (kHz)	512
Signal bandwidth, BW (Hz)	128
Excitation frequency, f_{ex} (Hz)	1×10^6
Feedback voltage, V_{fb} (V)	±15

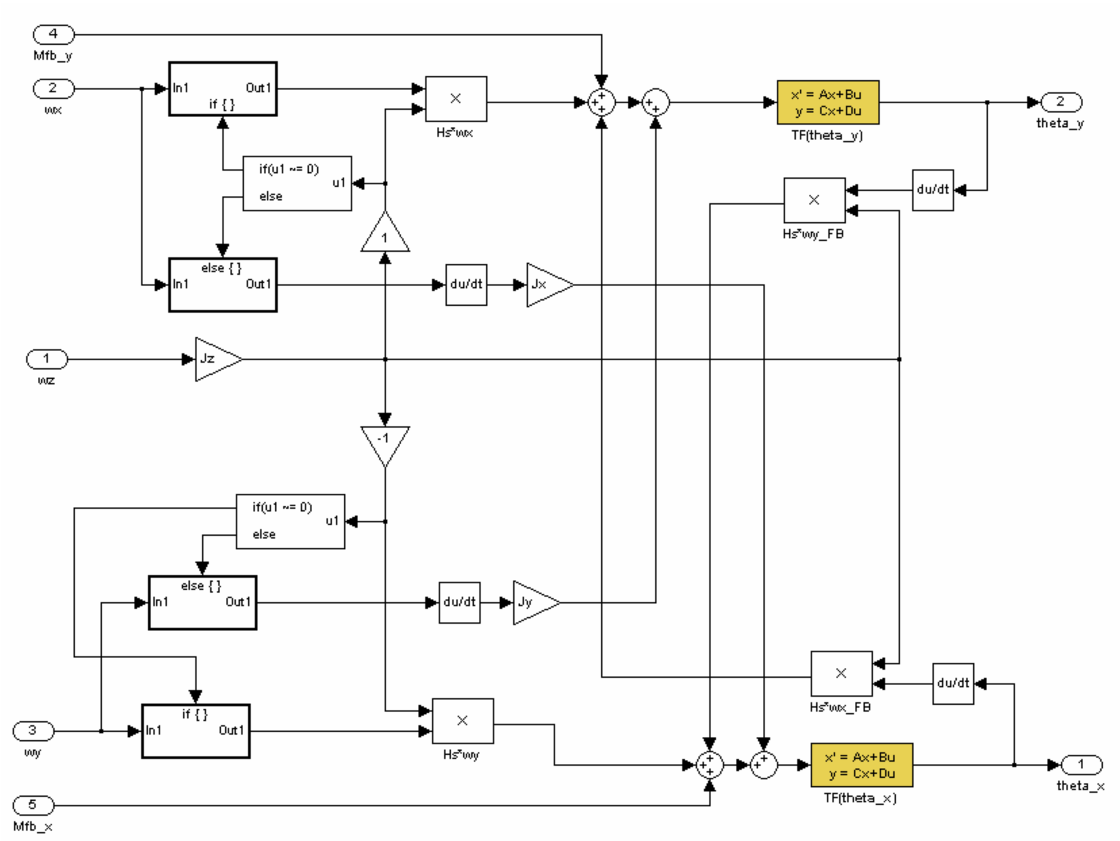

Figure 5.12 the gyro model implemented in Matlab/Simulink simulations.

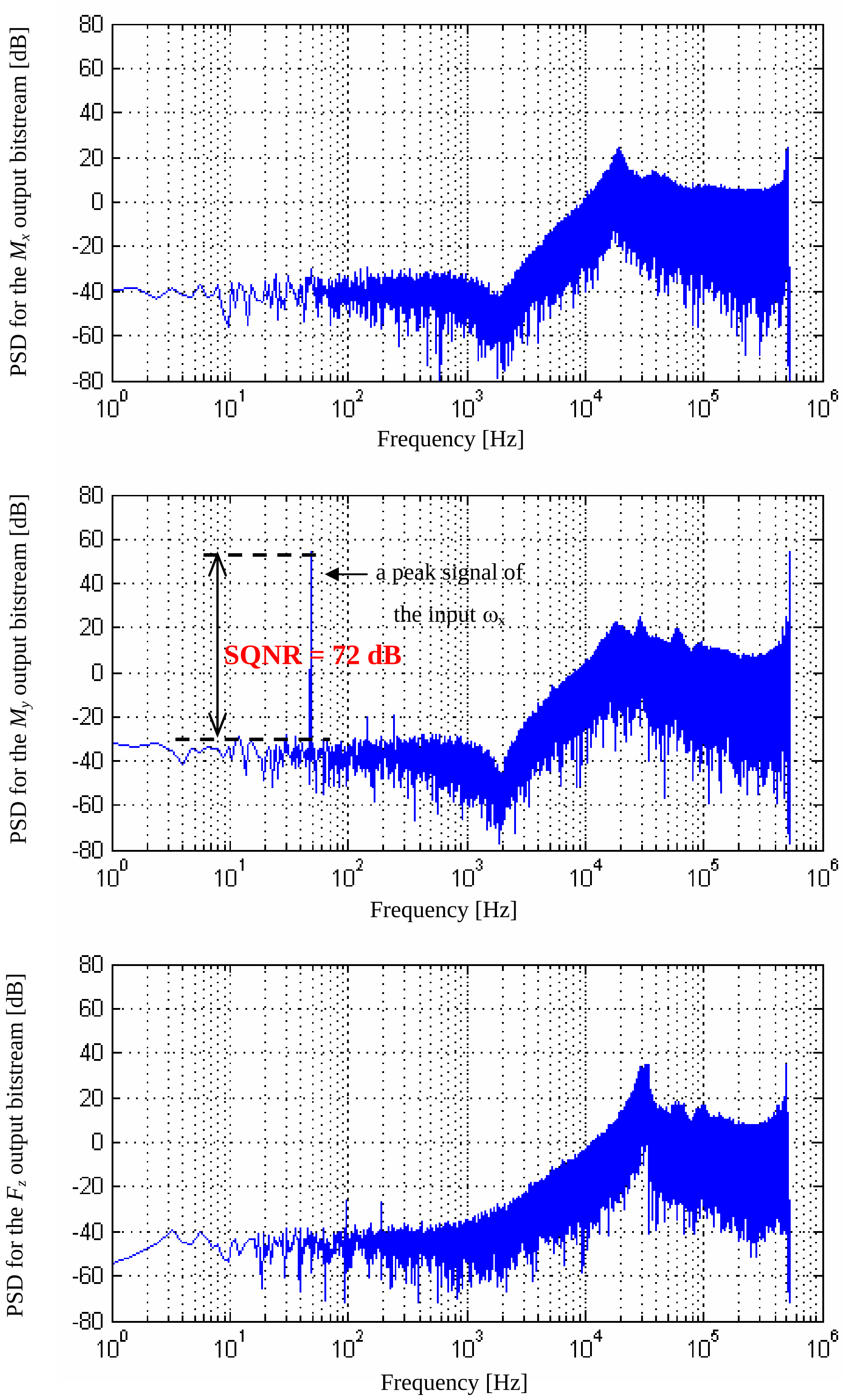

Figure 5.13 Device responses when only rotation about the x axis was applied. The input is a sinusoidal signal with the rotation rate of ± 10 rad/s and a frequency of 48 Hz.

5.3.4.2 *Multi-axis sensing*

A Simulink simulation in this section was carried out to evaluate a multi-axis sensing capability of the micromachined ESG. Assume that three sinusoidal signals were simultaneously applied to the micromachined ESG: the rotation rate about the x axis ω_x having a magnitude of ±10 rad/s and a frequency of 16 Hz, the rotation rate about the y axis ω_y having a magnitude of ±10 rad/s and a frequency of 48 Hz and the acceleration along the z axis a_z with a ±1 g magnitude and a frequency of 4 Hz.

The parameters related to the closed-loop ΣΔM control system are given in Table 5.2. Figure 5.14 shows the power spectrum densities of the summed output bitstreams. The result revealed that the full system micromachined ESG has the ability to measure rotation rates and acceleration simultaneously. The M_x output bitstream represents the ω_y signal, the M_y output bitstream represents the ω_x signal and the F_z output bitstream is related to the a_z input signal. The SQNR of these three output bitstreams are 64 dB for the M_x, M_y bitstreams and 69 dB for the F_z bitstream. Compared to Figure 5.13, it can be seen that the SQNR of the M_y bitstream reduced from 72 dB to 64 dB, due to the level of the quantisation noise increased. The cross coupling between the M_x and M_y bitstreams can be observed; however its magnitude is the same level as the quantisation noise.

To evaluate the performance of the micromachined ESG with the designed ΣΔM control system, the SQNR with regard to the variation of the input signals applied to the device system was calculated. For example, the magnitude of the rotation rate about the x axis was varied. Then, only the SQNR of the M_y bitstreams was considered. The SQNR plot corresponding to various magnitudes of the rotation rate is shown in Figure 5.15. As can be seen from the figure, the micromachined ESG can be used to measure the rotation rate in the range of 0.01 – 10 rad/s. The input rate of rotation below 0.01 rad/s, the SQNR became dominated by the quantisation noise. It can also be seen that beyond 10 rad/s the SQNR dropped dramatically. This is because the magnitude of the electrostatic force generated from the feedback voltage ±15 V is not enough to counteract the input rotation.

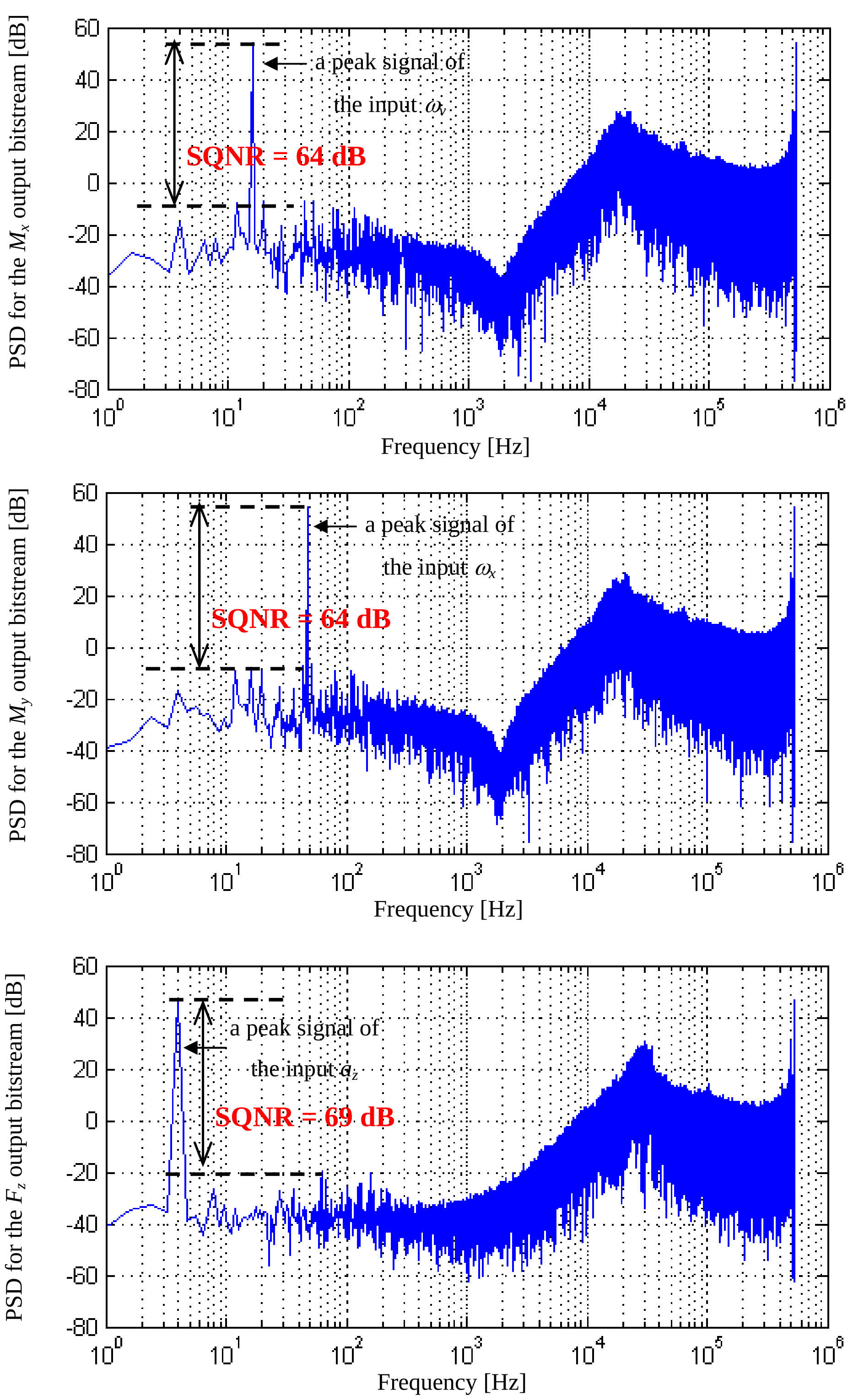

Figure 5.14 Power spectral densities of all three degrees of freedom assuming three input signals, ω_x, ω_y and F_z with three different frequencies, 48, 16 and 4 Hz, respectively, were applied to the device.

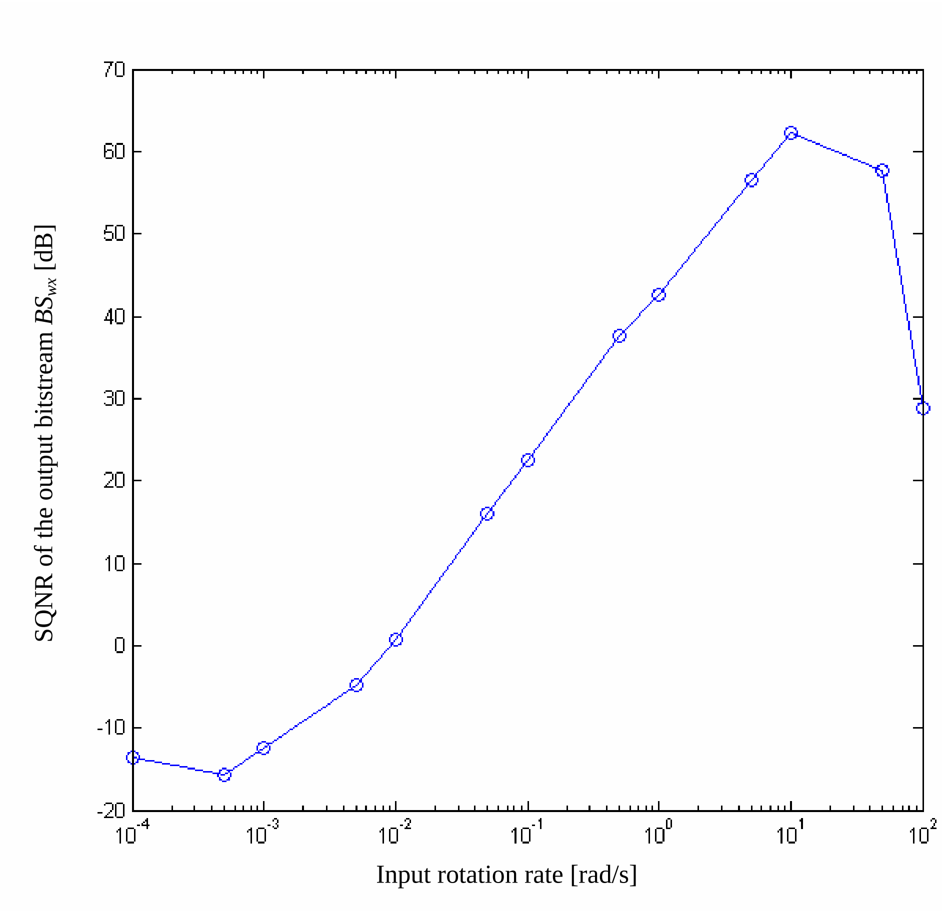

Figure 5.15 SQNR of the output bitstream BS_{wx} for various input rate of rotation about the x axis ω_x. Assume that the feedback voltage is ±15 V which is limited by the maximum supply voltage of a commercial available analogue switch, ADG441.

5.3.5 Noise analysis

Typically, there are three main noise sources limiting the performance of the micromachined ESG, i.e. mechanical, electronic and quantisation noises. These noise sources generally limit the minimum detectable rotation rate signal of the device. The mechanical noise M_n is introduced by Brownian motion of the rotor [**31**]. This can be calculated by equating the Brownian motion to the displacement caused by the precession torque for the minimum detectable input rotation rate, Ω_{MNE}:

$$M_n = I_z \Omega_z \Omega_{MNE} = \sqrt{4k_B T B_{x,y} BW} \tag{5.16}$$

Therefore, Ω_{MNE} of the micromachined ESG can be estimated as:

$$\Omega_{MNE} = \frac{\sqrt{4k_B T B_{x,y} BW}}{I_z \Omega_z} \tag{5.17}$$

where

k_B = Boltzmann constant = 1.38×10^{-23} J/K,

T = absolute temperature,

x,y = subscripts that incidate the x and y axes,

B = damping coefficient and

BW = signal bandwidth.

For the designed device dimension, assuming the rotor spins at 10,000 RPM, BW = 100 Hz and the device working at a room temperature (300 K), the thermo-mechanical noise equivalent rate signal will be approximately 0.027 deg/hr. Note that the mechanical noise can be reduced even further by increasing the moment of inertia and the spin speed of the rotor and also by reducing the damping coefficient.

An electronic interface circuit also introduces noise to a device system due to thermal noise sources in electronic devices. In a ΣΔM force feedback system, the so-called *quantisation noise* is present, which is introduced by the analogue to digital conversion process. The quantisation noise is less significant than the other two noise sources as it is relatively easy to push the quantisation noise floor to a level below any other intrinsic noise sources. This can be achieved by increasing the sampling frequency of the sigma-delta modulator and/or by the use of higher order electromechanical ΣΔM [**105, 145**].

Simulations in Matlab/Simulink were performed to evaluate the signal-to-noise ratio (SNR) and power spectral density (PSD) of the full system corresponding to mechanical and electronic noise. The block diagram of the micromachined ESG which includes all noise sources is shown in Figure 5.16. Brownian noise was added at the input of the device system. Electronic noise sources were also added at the input of all building blocks which are related to electronic interface. The most importance source is at the input of the front-end circuit.

Simulations were carried out using device and system parameters in Table 3.3 and 5.3, respectively. The external acceleration was applied to the z axis, which was assumed to be a sinusoidal ±1 g signal at a frequency of 100 Hz. Figure 5.17 shows comparisons of the PSD of the system with and without noise sources. The rotation rate about the y axis with ± 10 rad/s peak-to-peak amplitude at a frequency of 100 Hz was assumed as the external input. The corresponding PSD of a simulation with and without noise sources are shown in Figure 5.18. As obvious from those figures, the electronic noise is the most significant noise source reducing the SNR of the micromachined ESG. It was found that the SNR was decreased by approximately 20 dB (for acceleration measurement) and 10 dB (for rotation rate measurement).

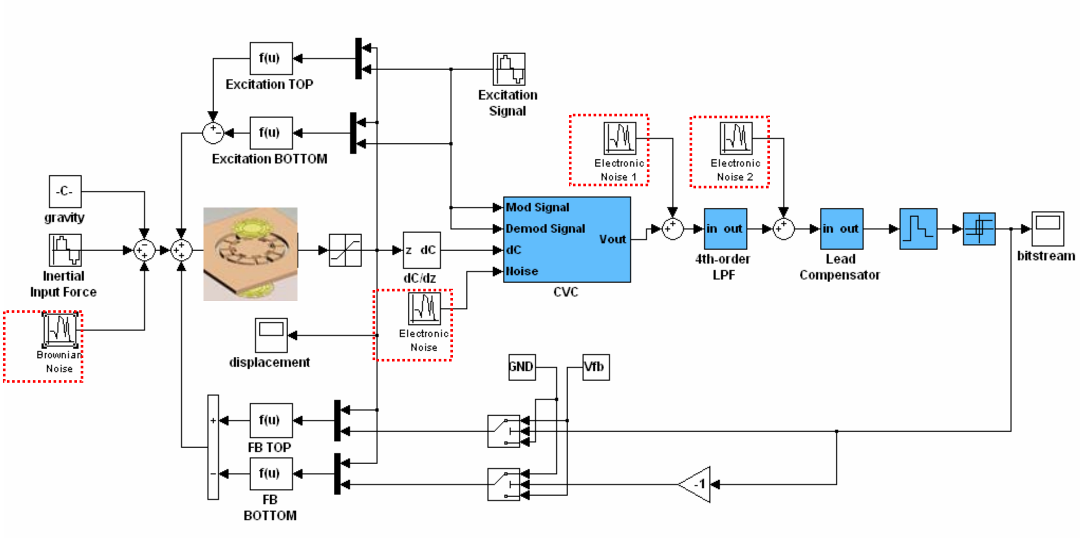

Figure 5.16 Simulink model of the micromachined ESG for noise analysis. A Brownian noise source is added to the input of the sensing element. Electronic noise sources are added to the input of the front-end circuit, low-pass filter and lead compensator circuits.

Table 5.3: Simulink parameters employed in the simulation for noise analysis.

Parameters	**Value**
Sampling frequency, f_s (kHz)	512
Signal bandwidth, BW (Hz)	128
Input signal frequency, f_{in} (Hz)	100
Excitation frequency, f_{ex} (Hz)	10^6
Feedback voltage, V_{fb} (V)	±15
Rotor spin speed, Ω_z (RPM)	10,000
Input referred op-amp noise, V_n (nV/√Hz)	20
Mechanical noise floor, g_n (μg/√Hz)	0.02
Minimum detectable input rotation rate, Ω_{MNE} (deg/hr/√Hz)	0.0027

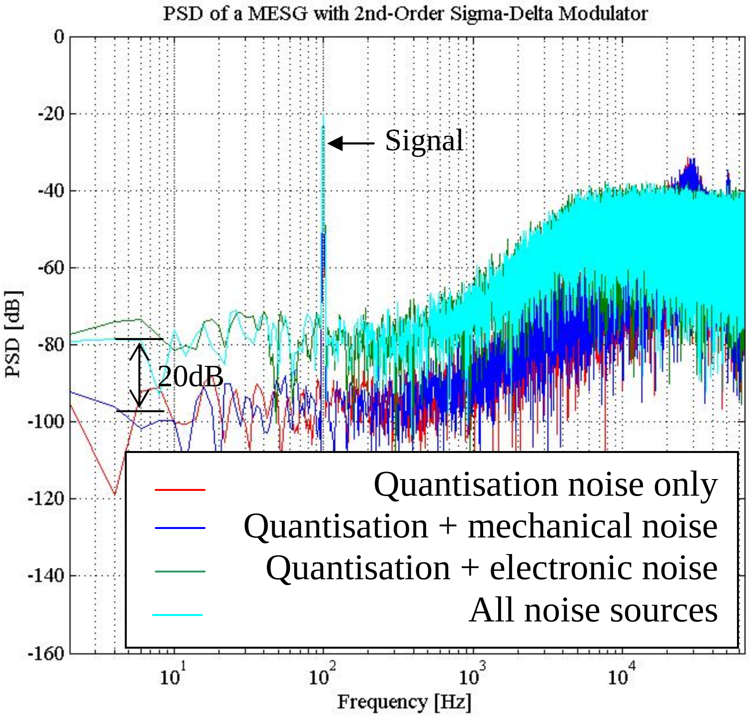

Figure 5.17 Power spectral densities of a simulation with noise sources. The input signal was a sinusoidal ±1 g at 100 Hz, applied to the z axis.

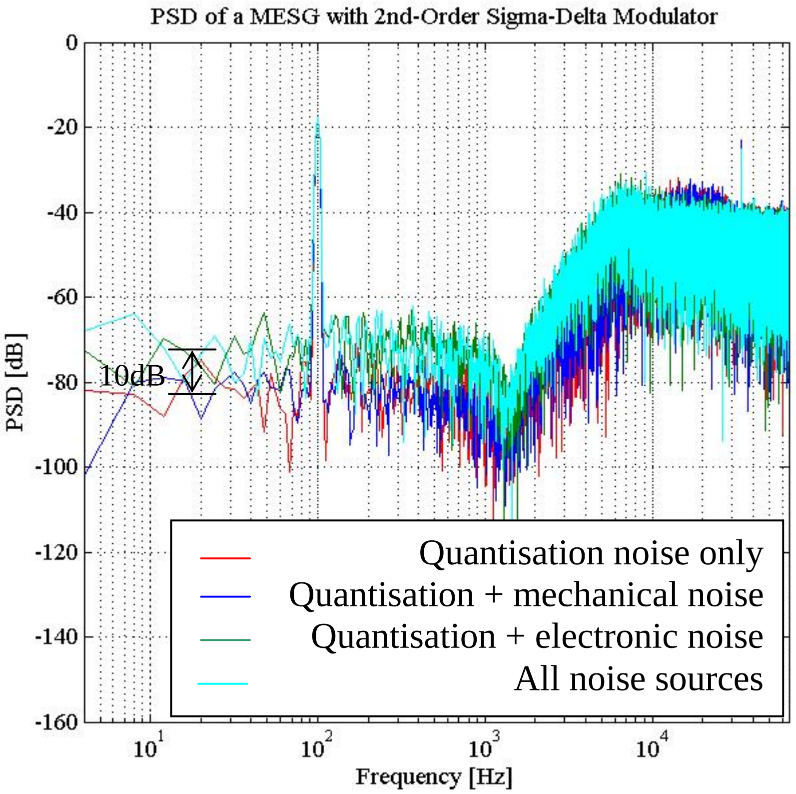

Figure 5.18 Comparisons of power spectral densities of the ΣΔM micromachined ESG with/without noise sources. The rotation rate about the y axis, with a sinusoidal ± 10 rad/s at 100 Hz, was assumed as the input signal.

5.4 CONCLUSIONS

This section presented the design and simulations of the closed-loop electrostatic suspension system to be implemented together with the micromachined ESG. The ESS was based on ΣΔM force feedback. It was employed to levitate and maintain the rotor at the mid-position between the upper and lower electrodes. The output bitstream of the ESS can also be used to measure the linear and angular displacements of the rotor and thus the input acceleration and rotation rates.

In order to investigate the stability of the device system, OrCAD/PSPICE and Matlab/Simulink models were developed. The simulations were carried out to ensure that whether or not the closed-loop ESS is able to levitate the rotor at the start-up phase where the rotor sits on stoppers at the bottom substrate. The result shows that the developed ESS can be levitate the rotor and maintain it at the mid-position between the upper and lower electrodes. Both simulation results obtained from OrCAD/PSPICE and Matlab/Simulink model gave similar results and agreed well with each other. The output bitstream showed the expected characteristic of a second-order ΣΔM. Its power spectrum density revealed the ΣΔM noise shaping. The results showed the potential of the developed ESS to be used together with the micromachined ESG.

The full system model was developed in Matlab/Simulink. This model was employed to evaluate the performance of the micromachined ESG implemented with a ΣΔM feedback control system. The first simulation was carried out to investigate the cross coupling issue when the device experienced the rotation rate about one input axis. As can be seen from the power spectrum densities of the summed output bitstream, no sign of cross coupling was found. When three input signals, i.e. rotation rate about the x and y axes and the acceleration along the z direction, were applied to the micromachined ESG, it was found that the level of the noise floor increased and thus the SQNR is reduced. The simulation also revealed that the micromachined ESG with the designed ESS can be measure the input rotation rate in the range between 0.01 – 10 rad/s.

In addition, two main noise sources, which limit the performance of the developed micromachined ESG, were analysed. The first one is a mechanical noise source generated from Brownian motion of air molecules under room temperature. The mechanical noise is proportional to the damping coefficient of the sensing element. Typically, the micromachined ESG is operated under vacuum pressure and thus the mechanical noise is relatively low compared to other noise sources. From noise analysis, it can be seen that the noise floor and SNR of the micromachined ESG were limited by intrinsic thermal noise generated from electronic components, especially noise at the input of the front end interface. This shows that special attention should be paid in the design and development of low-noise electronic interface.

Chapter 6

Device Fabrication

6.1 INTRODUCTION

With current microfabrication technology, the realisation of a frictionless microstructure having no mechanical connection to a substrate is considerably challenging. For the micromachined ESG, it must be ensured that a fabricated rotor is encaged within a cavity and can move freely in six degrees of freedom. Several microfabrication techniques, including surface micromachining [**86, 89, 92**], high-aspect-ratio electroplating [**107, 108**] and glass/silicon/glass bonding [**9, 16, 17**], have been investigated by several research groups to develop a micromachined rotor with no mechanical bearing. The fabrication based on surface micromachining suffers from the adhesion of the rotor and the substrate, also known as *stiction* problem. This is usually caused when a device is removed from aqueous solutions after wet etching of a sacrificial layer. Capillary forces originating from the dehydration of liquid residue pulls the rotor towards the substrate and thus the stiction occurs. However, this release-stiction can be alleviated by vapour-phase HF etching and CO_2 supercritical point drying. The other problem is in-use stiction which occurs during operation when the rotor came into contact to the substrate. This is due to the thickness of the surface-micromachined rotor is relatively thin, typically in the order of two to ten microns. When electrostatic forces are applied to some area of the rotor, it may be bent and bonded to the substrate. In order to alleviate the problem, the microfabrication based on bulk micromachining has gained more interest. Bulk micromachining generally involves multiple wafers, which are stacked together using bonding techniques [**16, 17, 102**]. At the University of Southampton, two fabrication processes have been investigated in the development of a micromachined accelerometer employing a levitating proof mass, including nickel electroplating [**107, 108**] and a combination with glass/silicon/glass bonding and DRIE processes [**12**]. The latter approach revealed promising results, i.e. simpler and batch fabricatable. Therefore, the fabrication process of the micromachined ESG was developed based on glass/silicon/glass bonding in a combination of a high-aspect-ratio DRIE process. This chapter presents in detail the fabrication process flow, followed by fabrication results and processing issues.

6.2 PROCESS FLOW FOR THE MICROMACHINED ESG

This section describes the developed fabrication process for the micromachined ESG. The fabrication process of the micromachined ESG was started with two different rotor dimensions: 2 mm and 4 mm diameters. The device was fabricated using one 4-inch silicon wafer and two 4-inch glass substrates. The silicon wafer is N-type (100), 200 µm thick, double-side polished with a resistivity of 0.001-0.005 Ω-cm. The glass wafers are 525 µm thick, double-side polished, borosilicate Pyrex 7740. The fabrication on glass wafers requires three photolithographic masks. The process sequence for top and bottom Pyrex wafers is the same, but with different mask designs. The process sequence for the silicon wafer consists of only one single mask, for high-aspect-ratio DRIE through the wafer. The complete fabrication process flow is shown in Figure 6.1. Full detail of the process flow is described in Appendix B.

Firstly, the glass wafers were cleaned to remove surface contaminations in a piranha solution, a 3:1 mixture of concentrated sulfuric acid (H_2SO_4) with hydrogen peroxide (H_2O_2). Then, the capacitor gap and stoppers were patterned and etched in two steps into the glass wafers by using standard photolithography and wet etching in hydrofluoric (HF) -based solution (Figure 6.1a and 6.1b). The first etch defined a 1 µm gap spacing between the rotor and stoppers. The second etch defined the capacitor gap (3 µm) and also the mechanical stoppers, which prevent the rotor making direct contact to the electrodes and therefore preventing a short circuit and stiction. After etching, 200 Å/500 Å/2500 Å thick Chrome/Platinum/Gold (Cr/Pt/Au) layers were evaporated and patterned using a lift off process to form control electrodes and wire bond pads (Figure 6.1c).

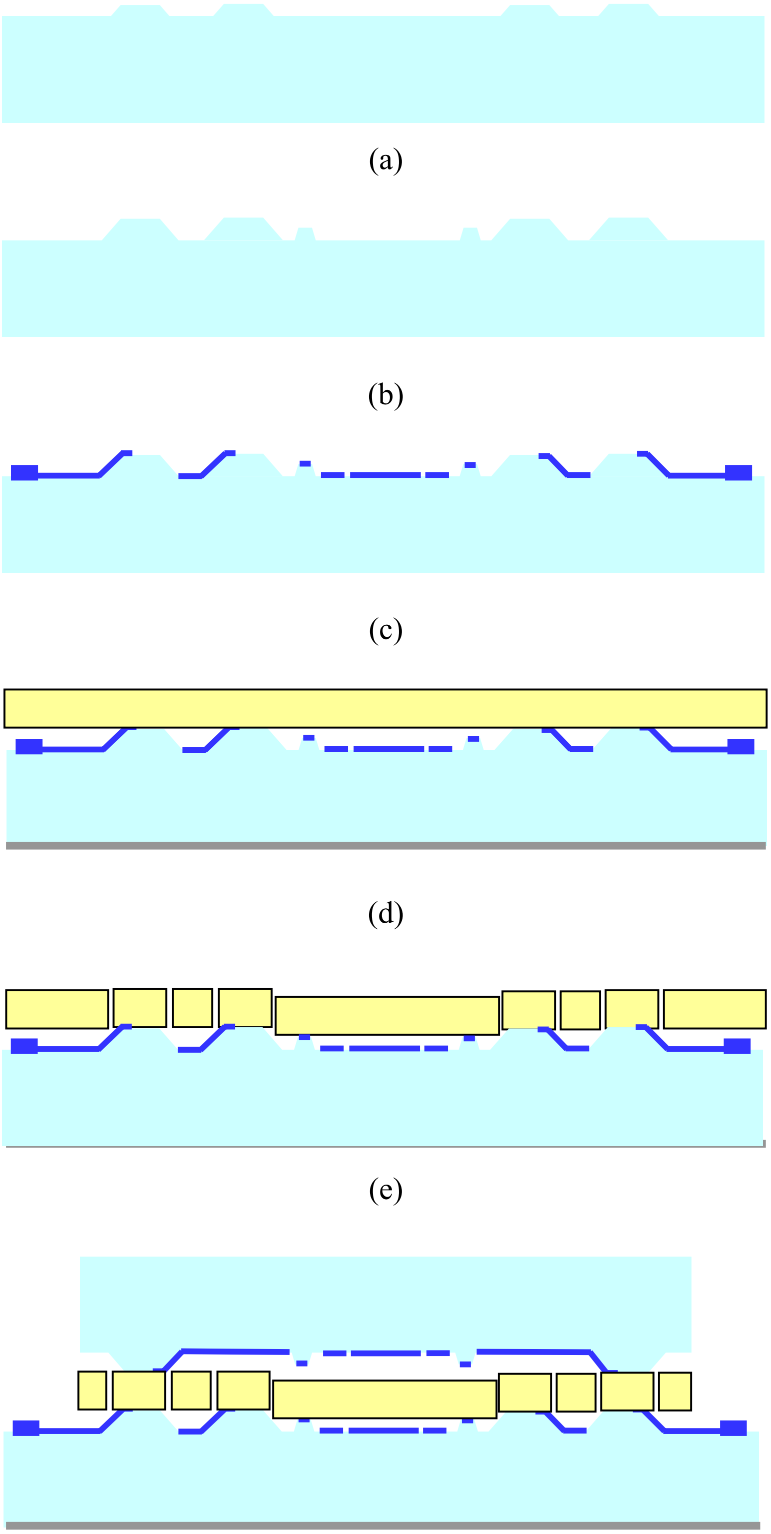

(a)

Glass wafer is cleaned and then etched to define a gap spacing between the rotor and stoppers.

(b)

A second wet etch is performed to define stoppers and a capacitive gap.

(c)

Cr/Pt/Au metal layers are deposited and patterned using Lift-off technique.

(d)

Silicon wafer is bonded to the bottom glass substrate and then aluminium layer is coated on the backside using sputtering.

(e)

Silicon wafer is etched through to release a rotor and also define sidewall electrodes

(f)

Anodically bond a top wafer to silicon/glass substrate. Then, the stack is diced into small chips.

Figure 6.1 Process flow of the developed micromachined ESG.

The bare silicon and bottom glass substrates were initially cleaned in solvent solutions (acetone, followed by IPA) to remove surface contaminations prior to anodic bonding. They were then electrostatically bonded together using a Karl Suss SB6e bonder (Figure 6.1d). Prior to the bonding operation, the two wafers were separated by spacers and the bonder chamber was pumped down to 1×10^{-5} torr. During the pump-down step, both wafers were heated up. When the temperature reached the pre-set value (350 °C), the two wafers were brought into contact and the spacers were pulled out. Anodic bonding was then carried out by applying a negative voltage to the glass substrate in multiple steps, starting from –250 V to –800 V, under a contact force of 400 N. With this procedure, the air trapped between the two wafers has enough time to escape towards the edges of the wafer, resulting in void-free and uniform bonding. After bonding, a 1000 Å thick aluminium layer was deposited on the back side of the glass substrate by sputtering. It needs to be ensured that the rims of both wafers are covered by the aluminium layer. This step forms the electrical contact between the two wafers, which is necessary for triple-wafer stack bonding.

10 μm thick AZ9260 photoresist was spun on the front surface of the silicon wafer as the mask for DRIE. The photoresist layer was then exposed to a UV radiation and developed in a 1:3 mixture of commercial developer AZ400K and DI water. Before etching, the device wafer was mounted to a handle wafer using thermal cool grease (AI Technology, Inc.). The DRIE process step etched the silicon wafer all the way through (Figure 6.1e) and not only released the rotor, but also defines a capacitor gap between the rotor and the sidewall electrodes. After the rotor was freed, the AZ9260 mask was stripped off using oxygen plasma etching and the handle wafer was removed using isopropyl alcohol.

The top glass wafer was cleaned in solvents, followed by the triple-wafer stack bonding step. The wafers were aligned and anodically bonded by the Karl Suss MA6/SB6e. At this step, the top electrodes were electrically connected to the bottom bond pads via silicon pillars. The wafer was then diced to open the wire bond pads and also to separate the sensors into small chips (see Figure 6.1f). Finally, the sensor was wire bonded to a ceramic chip package for further testing.

Due to a fire, the entire Southampton University cleanroom facility was destroyed in October 2005, the fabrication of the micromachined ESG described above was carried out in two different places in the United States: the microfabrication laboratory (MFL) at the Case Western Reserve University and the Michigan nanofabrication facility[1] (MNF) at the University of Michigan. The prototype micromachined ESGs were fabricated, but, unfortunately, problems were found in all of the fabricated devices. It was found that none of them came out working due to the fabricated rotor was stuck inside the cavity. In the following section, the developed process flow is discussed in detail. Fabrication problems and issues are also addressed.

6.3 RESULTS AND DISCUSSION

This section describes in detail the developed processes for the fabrication of the micromachined ESG. The first section presents the glass etching and its results. Next, material selection and processing for the metal deposition are discussed. The detailed processing and recipe for the anodic bonding are then described, followed by the deep etching of silicon bonded on a glass substrate. Lastly, the triple-wafer stack bonding and its issues are presented. At last, the wafer dicing and associated problems are discussed.

6.3.1 Glass etching

A Corning Pyrex 7740 glass wafer is not a pure silicon dioxide, but also has other components, i.e. 80.6% SiO_2, 13% B_2O_3, 4% Na_2O, 2.3% Al_2O_3, etc. [**146**]. This makes glass etching difficult since each component has a different etch rate, resulting in an etched surface with considerable roughness. For the micromachined ESG, glass etching is important as it defines the capacitive gap between the rotor and the upper and lower control electrodes. Any variation of the gap spacing will affect the device sensitivity, hence potentially degrading the performance of the device. Therefore, the glass etching solution should provide a uniform and smooth etch surface. Two different HF-based solutions, 7:1 buffered oxide etch (BOE) and a mixture of hydrofluoric and nitric acid (7:3:10 $HF:HNO_3:H_2O$), were investigated in this study.

---

[1] The MNF is currently run under a new name, i.e. the Lurie Nanofabrication Facility (LNF).

For etching in BOE, a standard photoresist, Shipley S1800 series, was employed as the etch mask. The glass wafer with 2 μm thick S1813 photoresist was hard baked at 115 °C for 25 minutes in an oven prior etching. Note that it is necessary to apply a primer on a wafer before photoresist coating. This improves adhesion of the photoresist to the glass substrate. Glass wafers were etched in BOE; and then the etch depths were examined using an alpha step profilometer. It was found that the glass etching in BOE provides a uniform and smooth etched surface and sidewall, however, the etch rate is very slow. It took 1 hour to etch 1 μm of the glass wafer, corresponding to an etch rate of approximately 16 Å/min. This is due to the low concentration of HF in the BOE solution, which does not contain enough fluoride ions for etching. The slow etch rate, however, makes it possible to precisely control the etch depth. It was also observed that the glass substrate was etched both in the lateral and vertical direction with an etch ratio of approximately 20:1. This anisotropic behaviour of the etching physically creates a gradual slope from the bottom to the top surface, which is beneficial for the design of the micromachined ESG. The resulting step heights measured on a Dektak 3030 ST profilometer are shown in Figure 6.2. The distance between the stoppers and the rotor is 1 μm and the gap from the bottom to the rotor is 3 μm.

Glass etching in a HF/HNO_3 mixture was carried out aiming to improve the etch rate. As expected, the etch rate of the glass etching is significantly higher, approximately 1.5 μm/min, which is about 100 times faster than etching in BOE. The etched recess shows a uniform and smooth finish; and it was also observed that the etch ratio in the lateral and vertical direction was reduced from 20:1 to around 4:1 (see Figure 6.3). However, the relatively fast etch rate makes it difficult to define the etch depth accurately.

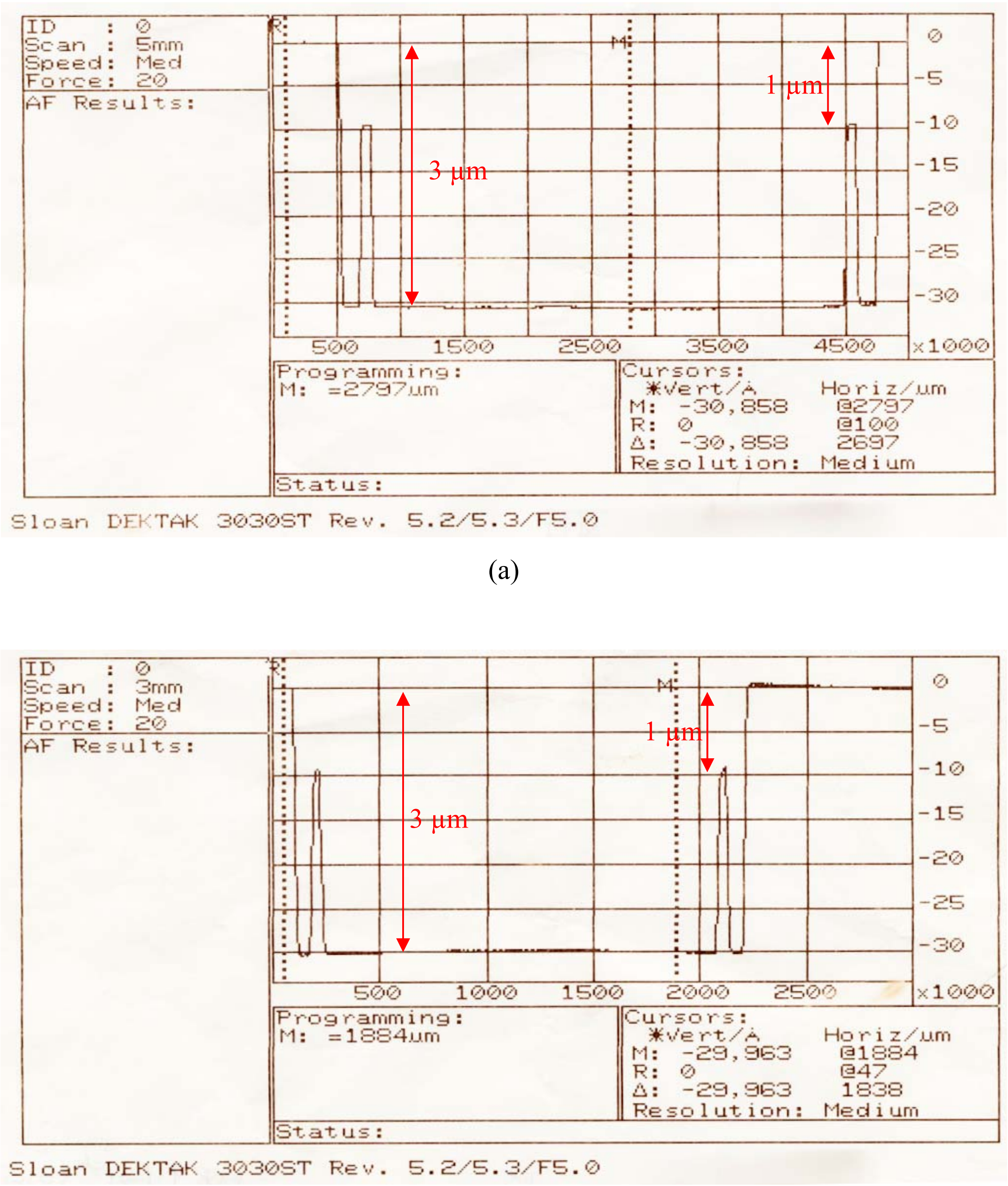

```
ID    : 0
Scan  : 5mm
Speed: Med
Force: 20
AF Results:

Programming:
M:  =2797um

Cursors:
 *Vert/Å      Horiz/um
M:  -30,858    @2797
R:  0          @100
Δ:  -30,858    2697
Resolution: Medium

Status:

Sloan DEKTAK 3030ST Rev. 5.2/5.3/F5.0
```

(a)

```
ID    : 0
Scan  : 3mm
Speed: Med
Force: 20
AF Results:

Programming:
M:  =1884um

Cursors:
 *Vert/Å      Horiz/um
M:  -29,963    @1884
R:  0          @47
Δ:  -29,963    1838
Resolution: Medium

Status:

Sloan DEKTAK 3030ST Rev. 5.2/5.3/F5.0
```

(b)

Figure 6.2 The measured step height of the etched glass wafer in 7:1 BOE: (a) for 4 mm diameter rotor and (b) for 2 mm diameter rotor.

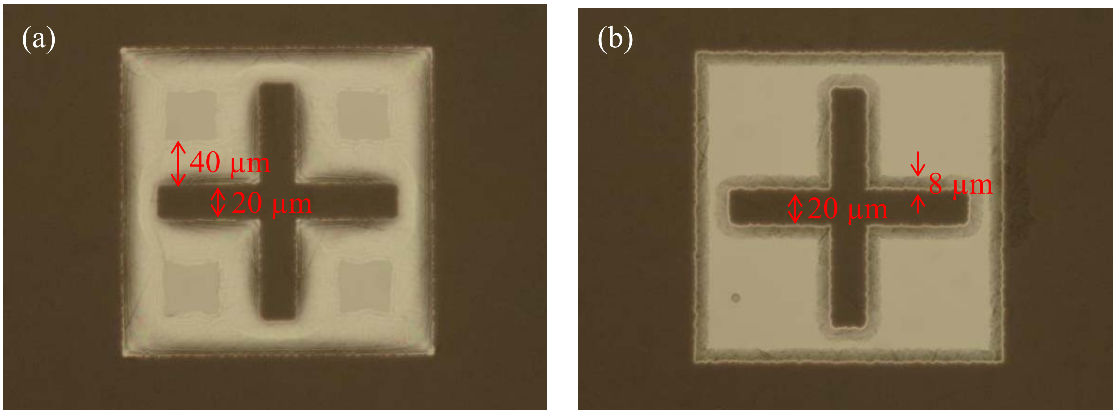

Figure 6.3 Optical image of the alignment key when a Pyrex wafer was etched to a depth of 2 µm in (a) 7:1 BOE and (b) 7:3:10 HF/HNO_3/H_2O mixture.

The other issue when etching glass wafers in a HF/HNO_3 mixture is the mask material. A photoresist is not suitable to be used as the mixture is too strong. The photoresist peeled off right after dipping wafers in the mixture for a few minutes. Therefore, a metal mask, i.e. Cr/Au layers, is required. This makes the process flow of the micromachined ESG more complicated; consequently, taking a total time from start to finish longer than glass etching in BOE. Therefore, glass etching in this study was carried out using 7:1 BOE solution.

6.3.2 Metallisation

The material used for electrodes and wire bond pads is generally aluminium or gold as both metals have very low resistivity. According to the design of the micromachined ESG, the sidewall silicon electrodes have to form the low-resistance contact to the metal wires located on the bottom glass wafers during the anodic bonding process. As aluminium can relatively easily become oxidised with oxygen from the air, resulting in high resistance at the interface, gold is preferable. Gold, however, has a poor adhesion to a glass substrate so that a chrome adhesive layer is necessary. It was also found that chrome diffused into the gold layer at high bonding temperatures (above 350 °C) and thus potentially degrading the gold conductivity. Higher resistivity of gold tracks can result in a higher voltage drop across lead lines, leading to a decrease in signal amplitude. This will result in lower device resolution. The inter-diffusion of chrome and gold layer can be alleviated by decreasing the bonding temperature to below 320 °C, however it resulted in a poor quality bond (bond strength is reduced and un-bonded areas can be observed). To overcome the diffusion problem, platinum was used as an intermediate layer preventing the diffusion of chrome into the gold layer.

Figure 6.4 shows optical images of the electrodes after the anodic bonding process. The images were taken from the backside through the Pyrex wafers. The electrodes shown in Figure 6.4a were made of a deposited Cr/Au layer. After anodic bonding, it was observed that the colour of the electrodes became yellow and there were dark dots in the electrodes area. These indicate inter-diffusion between the gold and chrome layers. For Cr/Pt/Au electrodes, there was no inter-diffusion problem after bonding. The colour of electrodes (seen from the backside of the Pyrex wafers) was still silver/chrome (see Figure 6.4b).

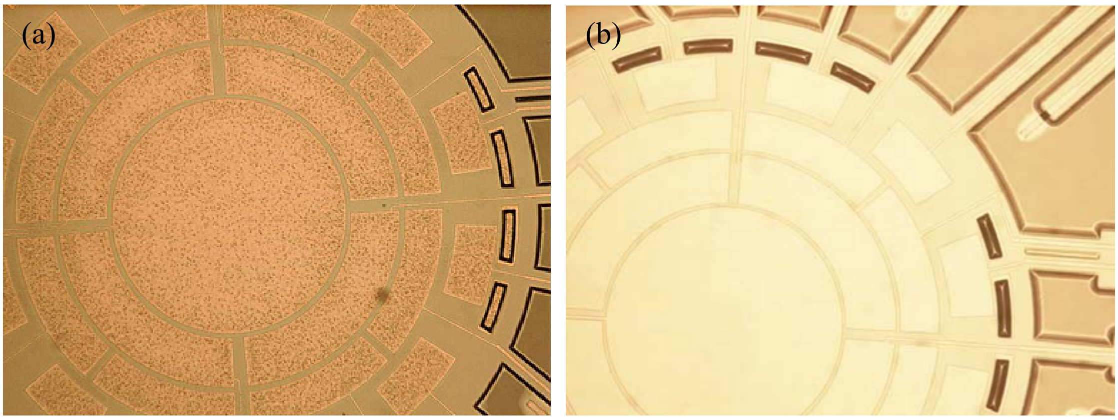

Figure 6.4 Optical images of metal electrodes after anodic bonding. (a) Electrodes were made of Cr/Au layers and (b) electrodes were made of Cr/Pt/Au layers.

6.3.3 Anodic Bonding

The process of anodic bonding is dependent on several parameters – flatness of silicon and glass wafers, bonding temperature, applied DC voltage across the wafers, and pressure. In this study, anodic bonding of silicon and glass wafers was done using a Karl Suss SB6e bonder at University of Michigan (see Figure 6.5). The setup configuration for anodic bonding is shown in Figure 6.6.

Double-side polished glass and silicon wafers with an average roughness of less than 8 Å are employed as the starting material. A silicon wafer sits on a hotplate, which provides heat to the two wafers. A Pyrex substrate is placed on top of the silicon wafer. A graphite plate located on top of the Pyrex wafer is an electrode. Generally, for anodic bonding, the hotplate is connected to ground while a negative voltage is applied to the graphite electrode. Above a temperature of 310 °C, a Pyrex substrate will behave like an electrolyte, containing two mobile ions – sodium ion (Na^+) and oxygen ion (O^{2-}). When applying a negative voltage to the glass substrate and positive voltage to the silicon wafer, oxygen ions in the Pyrex wafer will be driven towards the interface and migrate into the silicon, forming a permanent chemical bond at the interface of the two wafers.

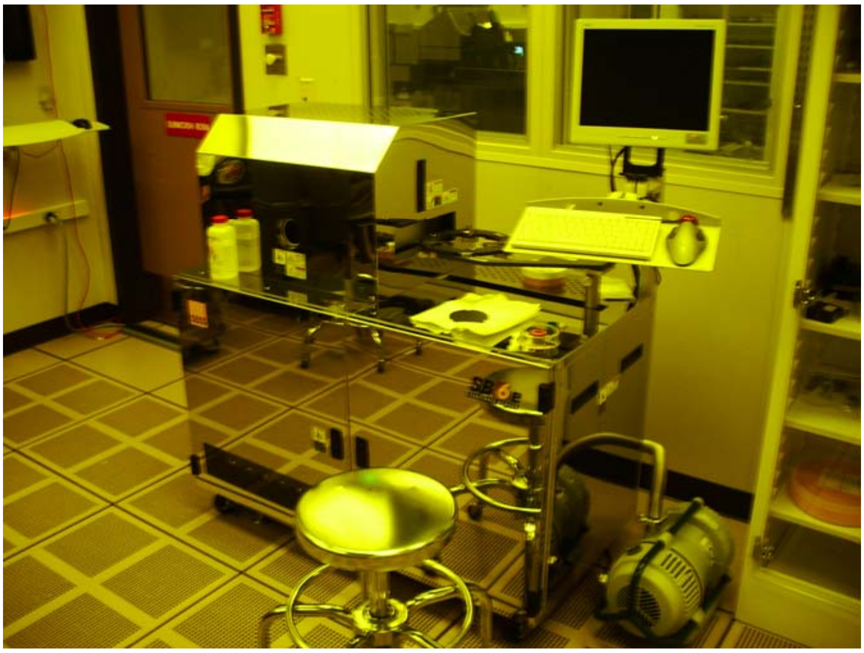

Figure 6.5 Karl Suss SB6e bonder in MNF at the University of Michigan.

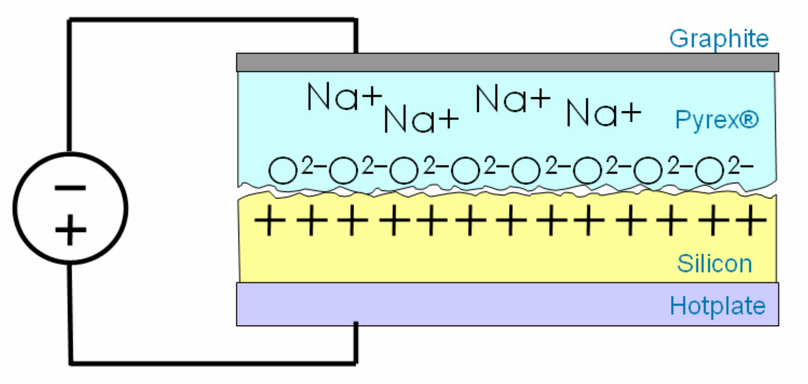

Figure 6.6 Setup configuration for anodic bonding of a Pyrex wafer to a silicon wafer. A high negative voltage is applied to a Pyrex wafer and ground is connected to a silicon substrate.

Achieving a good bond (uniform and void-free bonding) is important for fabrication of the micromachined ESG. Therefore, prior to bonding, both the silicon and glass wafers require proper cleaning in order to remove any contamination. This can be done using strong chemical acids, such as fuming nitric acid (FNA), or a combination of solvent solutions (acetone and IPA). Generally, solvent cleaning is preferred since it is much simpler and less dangerous compared with acid-based cleaning processes.

Care must be taken when bonding thin silicon to a glass substrate with recessed cavities. The voltage applied to the two wafers, normally around –1000 V, will introduce a high electric field across any air gaps between the silicon surface and the surface of the etched glass. When attempting to bond the wafers at atmospheric pressure, electric breakdown occurred since the height of etched cavity is very shallow (3 μm), resulting in damage on the electrodes and silicon surface. The applied voltage also generates electrostatic forces pulling together the surfaces of silicon and Pyrex substrates (see Figure 6.7). It was found that when an electric potential greater than –850 V was applied, silicon located above the 4 mm diameter cavity is pulled down and bonded to the etched glass surface.

Wafer bonding was performed at two different operating pressures – (1) atmospheric pressure and (2) low pressure, in the order of 10^{-3} mtorr. For bonding at atmospheric pressure, voids due to air trapped were found randomly at the interface. In addition, when the bonded wafers were DRIE etched in the next step, the wafers were found broken when opening the DRIE chamber. This is likely due to a pressure difference between the recess and the etching chamber. The difference between the pressure inside the recess (high pressure) and the DRIE chamber (low pressure) introduces a strong force on a thin silicon wafer (see Figure 6.8), leading to the wafer being broken.

In order to alleviate voids and to prevent the damage due to the pressure difference, anodic bonding process was performed at vacuum pressure. Basically, a pressure inside a bonding chamber is reduced prior the silicon wafer and the glass substrate are brought into contact. Then, heat is applied to the two wafers until the temperature of the wafers reaches 350 °C. Then, a high voltage of –850 V is applied to the glass substrate.

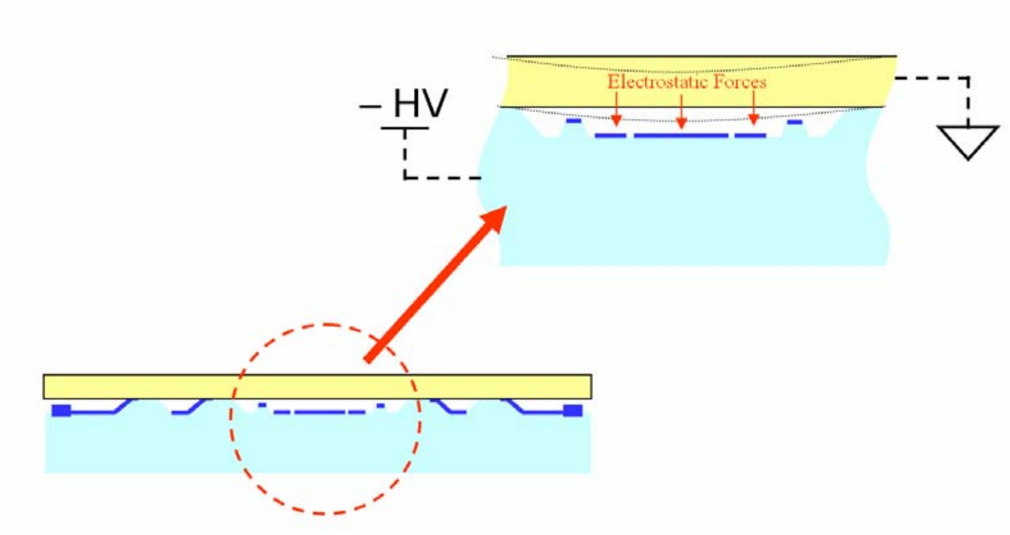

Figure 6.7 Pull-down effect in the anodic bonding of the silicon and glass wafers, which has shallow recesses between their interfaces. This is due to too high bonding voltages are applied to the two bonding wafer.

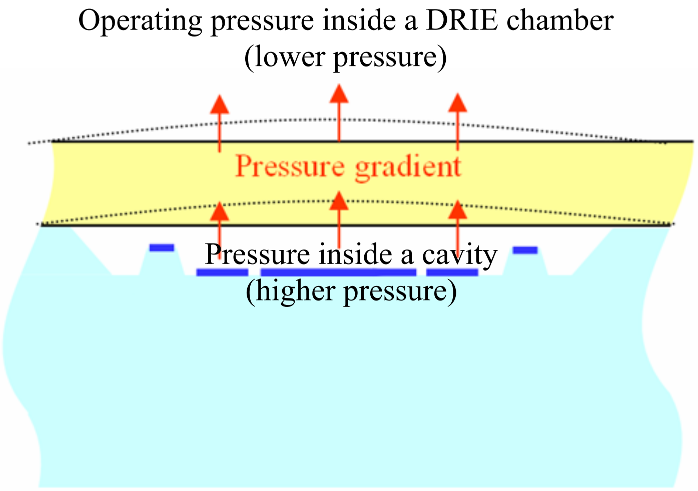

Figure 6.8 Pressure different between a device cavity (atmospheric pressure) and a DRIE chamber (vacuum pressure) resulting in the area of thin silicon above the cavity being damaged.

6.3.4 Deep reactive ion etching (DRIE)

High-aspect-ratio (HAR) dry etching plays an important role in the development of the micromachined ESG since it is not only used to release the rotor, but also to define the gap spacing between the rotor and the sidewall electrodes. The etching was carried out using the so-called Bosch process, which is widely used to produce deep and HAR features with almost vertical sidewalls. It is achieved by switching between passivation (C_4F_8) and etching (SF_6) cycles in sequence [**147, 148**]. There are a number of equipment manufacturers who have licensed the Bosch process, including Silicon Technology Systems (STS) and Oxford Instruments. In this study, the DRIE process was performed in a STS multiplex inductively coupled plasma (ICP) etcher (see Figure 6.9) in the MNF at the University of Michigan.

Figure 6.9 STS single chamber multiplex ICP etcher at the University of Michigan.

For the DRIE process, 10 µm thick positive photoresist, AZ9260, was used as the etch mask. It was spun on the front surface of the silicon wafer at a spin speed of 2100 RPM for 30 seconds. Photoresist coating was followed by a soft bake at 110 °C for 110 seconds on a hotplate. After exposure to UV radiation, the photoresist layer was developed in a 1:3 mixture of a commercial developer AZ400K and DI water. No hard baking is required prior to etching.

It is somewhat difficult to etch the silicon wafer that was bonded to a glass substrate. In general, Helium backside cooling is used in order to cool down the silicon wafer during etching of silicon in a STS ICP etcher. This will improve an etch selectivity between silicon and photoresist and also prevent photoresist burning. However, a glass substrate does not provide a good thermal contact between the silicon wafer being etched and Helium backside cooling. Hence, prior etching, the wafer was mounted to a handle wafer (a silicon wafer) using thermal cool grease (AI Technology, Inc.). After etching, the device wafer was separated from the handle wafer using a razor blade. The cool grease was cleaned by wiping with isopropyl alcohol using a lint free cloth.

In this study, the deep etch was performed using an etch recipe shown in Table 6.1. The recipe employs the technique called parameter ramping in order to achieve deep, high-aspect-ratio silicon etching. At the start of the process, a high pressure etching cycle is used. Under a high-pressure condition, a silicon etch rate is high, but removal of the passivating polymer film from the deep trench base is less efficient. Therefore, the process pressure is ramped down at the rate of 0.2 %/min throughout the etching process. Decreasing the pressure in the chamber increases the mean free path of F^+ ions. This allows F^+ ions to reach the deep trench base. However, the silicon etch rate is reduced [**149**]. The pressure inside a DRIE chamber is controlled by setting a parameter, which is called automatic pressure control (APC). The APC actually sets the valve, which is located between the main DRIE chamber and a vacuum turbo pump, to open up at certain percentage. The more the valve is opened up, the lower the pressure inside the DRIE chamber.

Table 6.1: Etching recipe used in a STS DRIE etch tool for etching through a 200 µm thick silicon wafer which is bonded to a glass substrate.

	Etch cycle	Passivation cycle
SF_6 flow rate (sccm)	130	-
O_2 flow rate (sccm)	13	-
C_4F_8 flow rate (sccm)	-	85
Time duration (s)	12	7
Coil power (W)	800	600
Platen power (W)	10.0	-
Automatic pressure control	65 % and ramped pressure down at 0.2%/min	65 % and ramped pressure down at 0.2%/min
Chiller temperature (°C)	5	5

The etch depth of different opening areas was inspected using a Zygo interferometer. It was found that the average silicon etch rate is around 1.8 µm/min (a gap between the rotor and sidewall electrodes) to 2.4 µm/min (the largest opened area). The smaller the exposed areas, the slower the etch rate. Therefore, the etching process was performed for 120 minutes to ensure that the rotors were released.

Device designs with different sized capacitive gaps between the rotor and the sidewall electrodes were pursued on the same wafer. Figure 6.10 shows optical images of three rotors with gap sizes of 10 μm (left), 15 μm (middle) and 20 μm (right), respectively. The images reveal that the front surface of the rotors with 15 and 20 μm gap sizes had an unacceptably high surface roughness, while that with a gap size of 10 μm was not visibly damaged. This can be explained by non-uniform etch rates for different gap sizes, which result in rotors with larger gap sizes being released first and rotors with smaller gap sizes still being etched, due to the so-called *RIE lag* effect. The released rotor has no thermal path to get rid of heat generated during etching; hence, the photoresist mask burnt out leading to top surface of some rotor damaged.

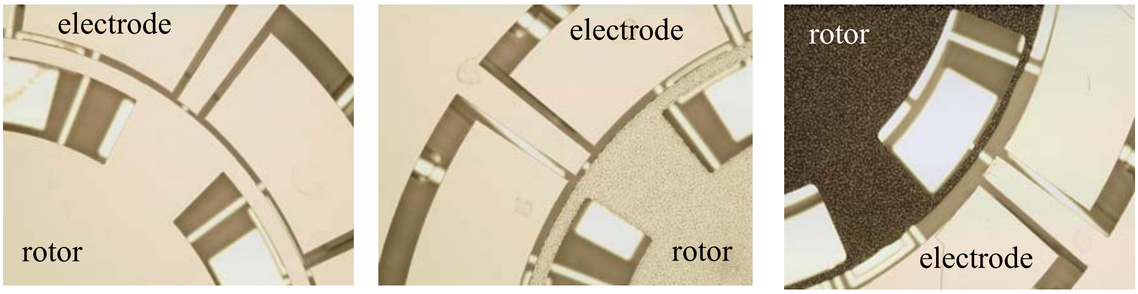

10 μm gap size 15 μm gap size 20 μm gap size

Figure 6.10 Optical images of fabricated rotors with various gap spaces(10, 15 and 20 μm) between the rotor and the sidewall electrodes. Images reveal the damage on the front surface of the fabricated rotor due to the RIE lag effect. The rotor with a gap size of 10 μm (left) was not damaged by the etching. It still has a shiny polished surface. The other rotors with gap sizes of 15 μm (middle) and 20 μm (right) were visibly damaged as their front surface became darker and not shiny. Their front surfaces were etched away by 1 to 2 μm (measured from a white interferometer).

Due to the design of the first prototype micromachined ESG, there are various opened areas on the same device, i.e. gap spacing and opened patterns for rotation control. Once the etching of the opened patterns (wider trench) is complete, plasma ions can reach the bottom glass substrate through the wide trench and get charged up on the bottom wafer. Plasma ions then can get underneath the rotor and etch the bottom side of the rotor. An optical image of the backside of the rotor is shown in Figure 6.11a. A Zygo interferometer was employed to inspect the damage on the backside of the rotor. It revealed that the surface of the rotor was etched to a depth between 0.2 to 0.4 μm (see Figure 6.11b). The etched shape looks more like metal electrodes located underneath the rotor. Thus, the damage of the rotor possibly came from plasma ion scattering from the metal surface bombarding the bottom side of the rotor.

The damage of the front and back sides of the rotor will contribute to the imbalance between the top and bottom sense capacitances, resulting in the undesirable output bias. This problem can be minimised by designing all the exposed areas in such a way that they all have similar geometry resulting in a uniform etch rate. Alternatively, the damage can be avoided by coating a metal layer on both top and bottom sides of the rotor. Practically, it can also be compensated using electronic trimming.

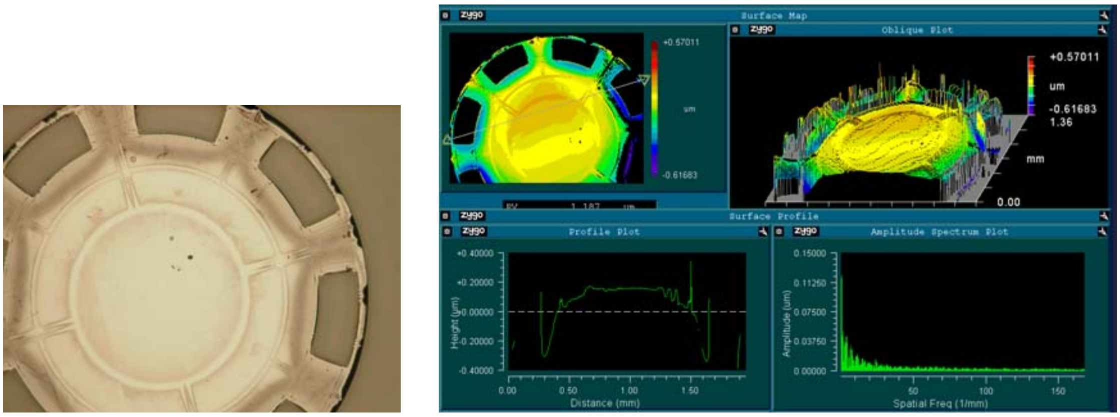

(a) (b)

Figure 6.11 Damage on the back side of rotors: (a) the optical image and (b) the measurement result from Zygo white interferometer.

The DRIE lag not only causes damage on the front and back side of the rotor, but also results in the so-called footing effect in some area; for instance, the pillars (see Figure 6.12), which are used as a feed through connecting between the top electrodes and the bond pads located on the bottom glass wafer. Inspection by an optical microscope revealed that an over etch resulted in about 35 μm undercut.

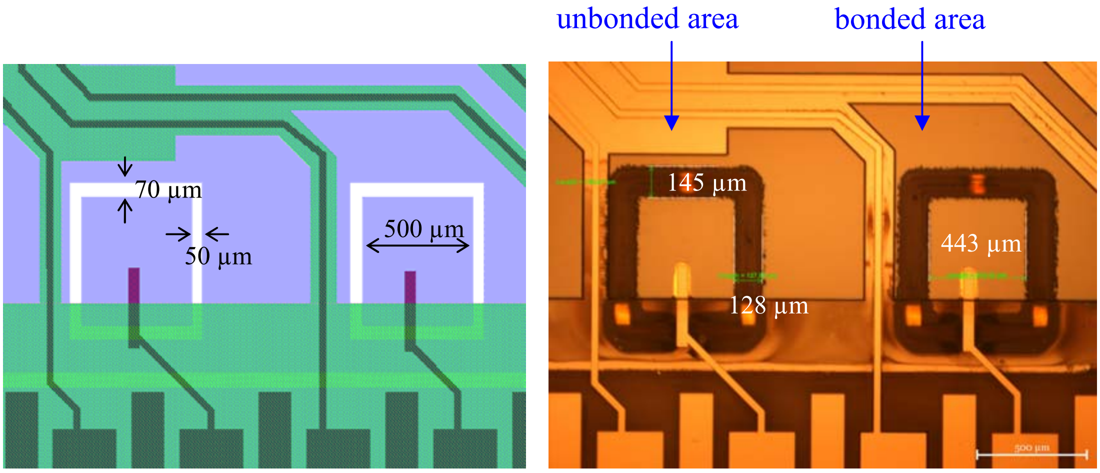

(a) (b)

Figure 6.12 Footing effect due to the RIE lag: (a) mask layout and (b) the optical image of the actual device after DRIE etch. The image was taken from the backside of the glass wafer. The image revealed that an over etch resulted in about 35 µm undercut.

After etching, the rotor was completely released and free to move. This makes photoresist removal and wafer cleaning relatively difficult; wet processing is therefore impossible. Immersing etched wafers into a removal solution will cause released rotors to float away. Thus, in the fabrication of micromachined ESGs, the removal of photoresist was carried out using dry oxygen plasma process. This photoresist ashing was done in Semi Group 1000 RIE using the following parameters: pressure = 300 mtorr, power = 200 W, O_2 flow rate = 100 sccm. It was carried out until the photoresist is clear.

Wafer cleaning of the etched wafer is also challenging. This was done by putting the wafer on a spinner and spraying acetone and IPA. Basically, the etched wafer was placed on a spinner and spun at the speed of 500 RPM. Then, acetone and IPA were gently sprayed onto the surface of the wafer. The proper spin speed is crucial to ensure that the whole surface of the etched wafer was soaked; however, it should not be too low so that the released rotor came off. Then, the spin speed was raised high up to 1500 RPM in order to dry the wafer.

6.3.5 Anodic bonding of a triple-wafer stack

Anodic bonding of a triple-wafer stack was carried out using a Karl Suss BA6/SB6e aligner/bonder. A Karl Suss BA6 was used to align a top Pyrex wafer to the so-called bottom wafer (i.e. a silicon wafer bonded to a bottom Pyrex wafer). The three wafers were then mechanically clamped before they were transferred to a Karl Suss SB6e to pursue anodic bonding.

As mentioned in section 6.3.3, the general method for anodic bonding of a glass substrate to a silicon wafer can be achieved by applying a voltage on the two wafers in such a way as that the voltage applied to the glass substrate is negative with respect to that of the silicon wafer. However, this general method cannot be used for the case of triple-wafer stack bonding. A bottom Pyrex wafer, which was already bonded to a silicon wafer, prevents a current from passing through. Thus, in order to provide an electrical connection to a silicon wafer, the backside of the bottom glass wafer was coated with an aluminium layer in advance before bonding. A sputtering method was preferred over metal evaporation to ensure that the rims of both wafers were covered by a metal layer. This aluminium layer provides an electrical connection between the silicon wafer and the graphite electrode.

A Karl Suss BA6 aligner was employed to align the top glass substrate with the bottom silicon/glass wafer. Firstly, the top glass substrate was loaded into the aligner, followed by the bottom silicon/glass substrate. When the wafers were aligned with each other, they were then clamped together on the aligner. The clamped wafer stack was then loaded into a Karl Suss SB6e bonder. According to loading mechanism of the SB6e bonder, the triple-wafer stack had to be flipped over before loaded into the bonder. The top glass substrate then sit on a bonding chuck as shown in Figure 6.13. The bonding chuck is normally connected to ground potential; thus, to perform anodic bonding of the wafer stack, a positive high voltage was applied to the bonded glass/silicon wafer.

The recipe for the triple-wafer stack bonding is as follows: temperature = 350 °C, ambient pressure = 4×10^{-2} mtorr and applied voltage = 700 V. Figure 6.14 shows the photograph of a bonded wafer.

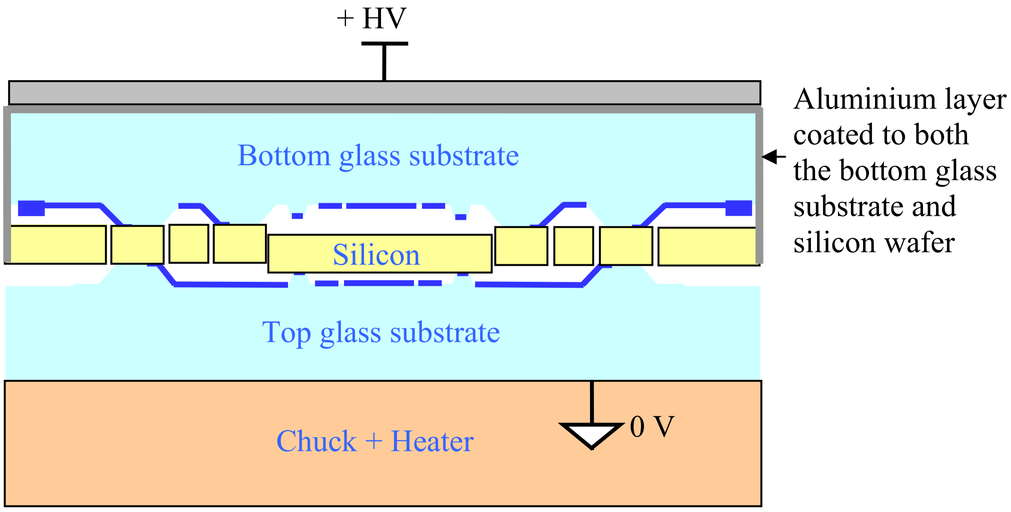

Figure 6.13 Schematic diagram showing the setup configuration for anodic bonding of the glass/silicon/glass wafer stack. The bonding was carried out using a Karl Suss SB6e.

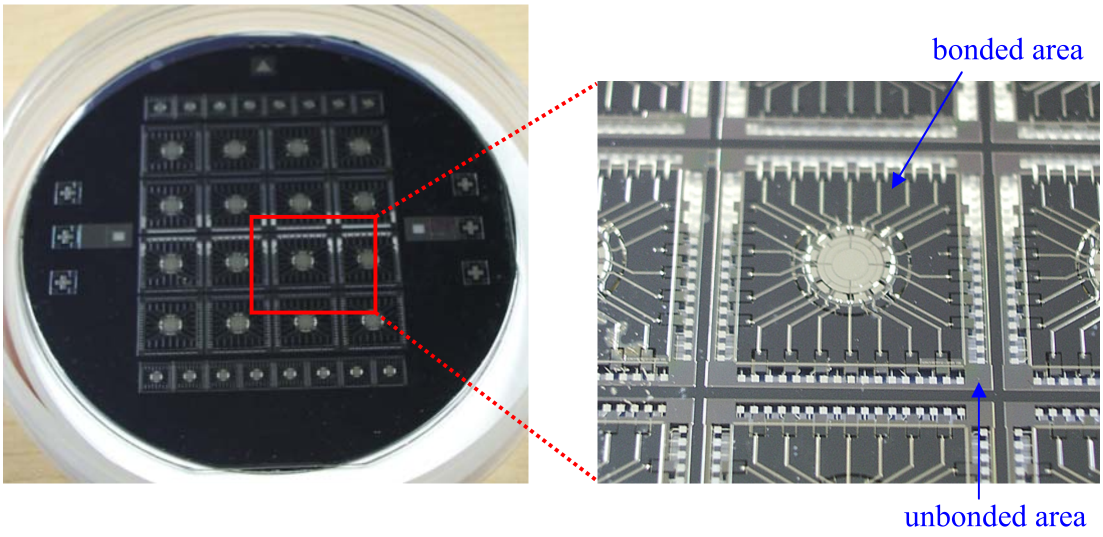

Figure 6.14 Top view of the bonded triple-wafer stack. The dark area is where the glass wafer is bonded to the silicon wafer.

6.3.6 Wafer dicing

A bonded wafer stack was separated into individual small chips using a wafer dicing tool, Micro Automation model 1006, as shown in Figure 6.15. The dicing blade was Glass blade 777 and it has a thickness of 250 μm. The blade was spun at a speed of 8500 RPM.

In order to prevent water and debris getting into a device cavity, the bonded wafer stack cannot be cut all the way through. The following procedure was employed to dice the wafer into small chips: firstly, a top glass substrate was diced to a depth of 475 μm. Next, a bottom glass substrate was diced to a depth of 475 μm. Then, the diced wafer was snapped into small pieces. However, it was found difficult to snap the wafer into pieces since the thickness of the silicon wafer is relatively thick, 200 μm. Therefore, to separate the stack into individual chips, the wafer stack was sawed all the way through the silicon wafer. Unsurprisingly, water was found inside a device cavity of the diced chips (see Figure 6.16).

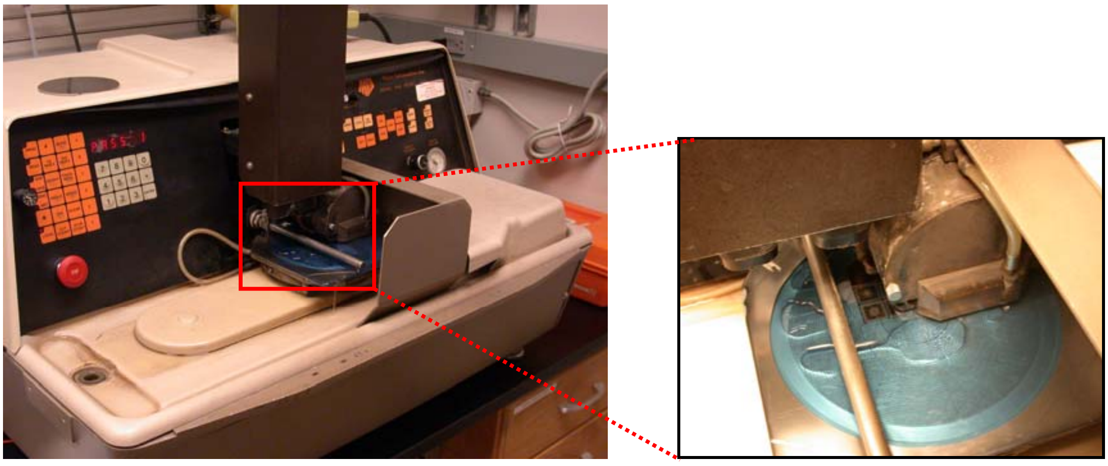

Figure 6.15 Wafer dicing tool, Micro Automation model 1006 at the University of Michigan.

The following method was performed to get rid of trapped water: the diced chips were soaked into Methanol for 10–20 minutes. Agitation was required to ensure that water is replaced by Methanol. Then, the diced chips were transferred into a super critical point dryer (CPD) as shown in Figure 6.17. Basically, Methanol is washed away by a high pressure liquid CO_2. Then, the CPD chamber is heated up until the pressure goes beyond the critical point of CO_2. At the end, the pressure is released making the CO_2 gas to escape from the device cavity. Figure 6.18 illustrates the prototype micromachined ESG after drying in a CPD and after the chip was wired bonded to a chip carrier.

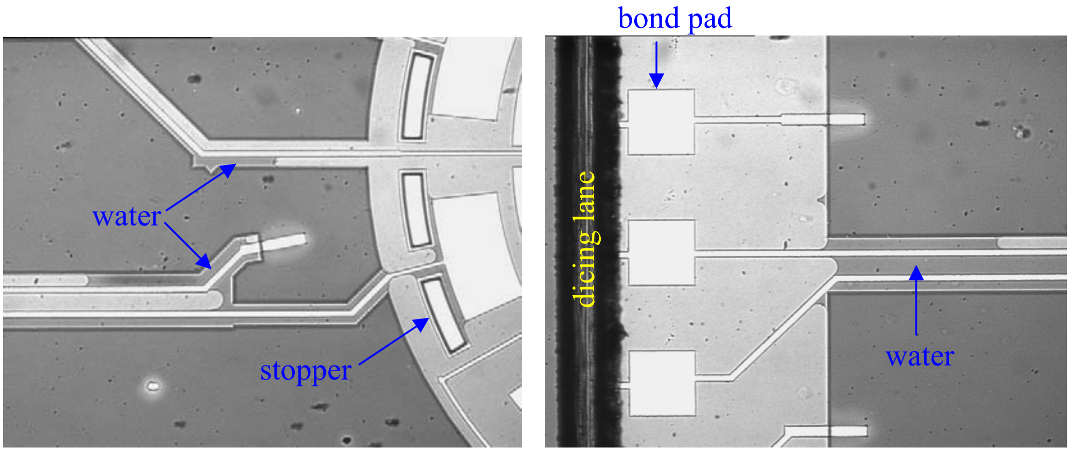

Figure 6.16 Water was found inside a device cavity after the water was diced to separate into individual chips.

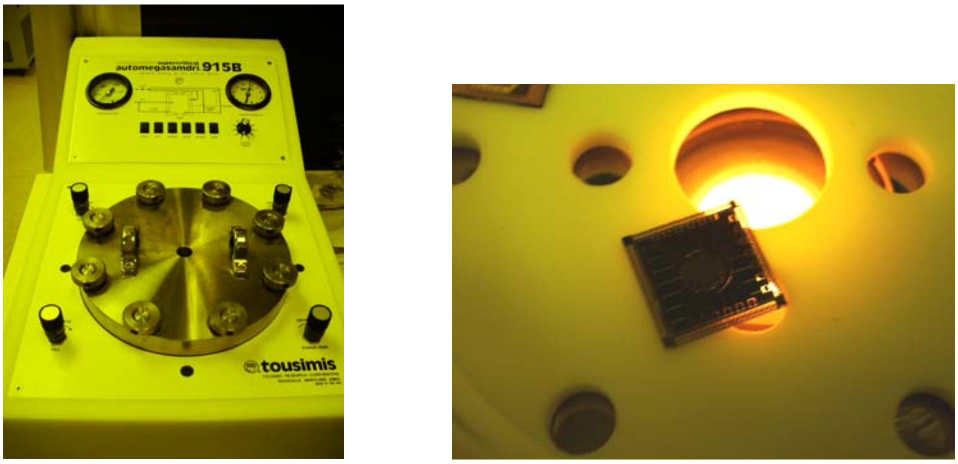

(a) (b)

Figure 6.17 (a) Tousimis 915B super critical point dryer at the University of Michigan. (b) A sample soaked with Methanol in the CPD chamber.

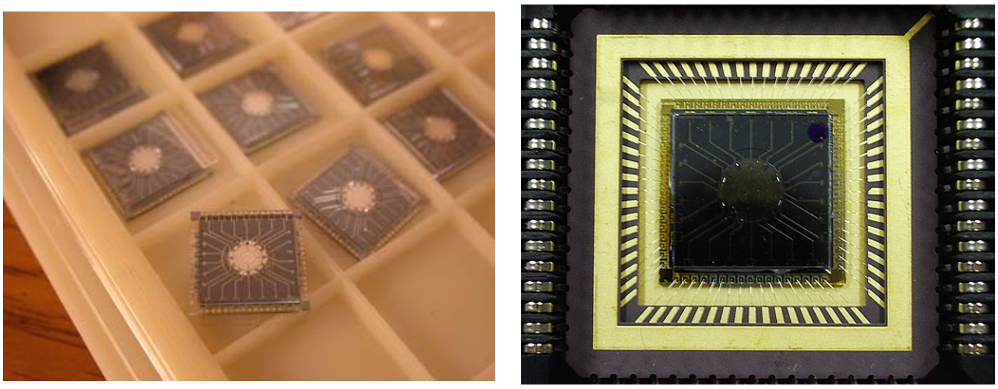

(a) (b)

Figure 6.18 Photograph of the prototype micromachined ESG: (a) after complete fabrication process flow and (b) after the prototype chip was mounted and wire-bonded to a chip carrier.

6.3.7 Discussion

There are two major issues found in the fabrication of the first prototype micromachined ESG. The first issue is the so-called RIE lag. In the first batch, devices were designed to have various gap sizes between the rotor and the sidewalls. As a consequence, when some rotor was already released, others were still being etched. The photoresist coated on the released rotors was then burnt out since heat cannot be dissipated from the rotors. This resulted in damage on the front surface of the rotors by plasma etching. In addition, the design of the first micromachined ESG has different opening areas (see Figure 3.1 and 3.6). The larger areas were etched faster and thus the area of the bottom glass substrate, which lies underneath the large areas, was exposed to plasma ions. As a result, the bottom surface of the rotors was damaged. This will cause an imbalance between the upper and lower sense and feedback capacitances. The RIE-lag issue can be sorted out by designing the micromachined ESG in such a way as that it has the same opening area. The other approach is by depositing a metal layer, for instance platinum, aluminium or chrome/gold, on both front and bottom rotor surfaces.

The second issue in the fabrication of the micromachined ESG is the so-called stiction problem where a rotor got stuck to substrates. It was found that all of the devices from the first batch have the stiction problem. There are several possibilities that can cause a released rotor getting stuck to a substrate. Water got into a device cavity after wafer dicing is one of them. Water used in the dicing tool is not ultrapure DI water, but just filtered city water. Particles in water itself and also dicing debris can make a rotor stuck and thus resulting in stiction.

Electrostatic bonding of a triple-wafer stack is the other possibility. As mentioned in section 6.3.5, during the operation of triple-wafer bonding a silicon wafer was connected to a positive high voltage, while a released rotor was electrically floated (since it has no direct contact to a silicon substrate). Assuming if the released rotor touched silicon sidewall electrodes, its potential will be the same as the silicon wafer (a positive high voltage). As the rotor already sit on the top glass substrate (see Figure 6.13), the rotor can be electrostatically bonded to the top glass wafer.

One issue needs to be pointed out here is the difficulty in cleaning a wafer after a DRIE process. It was found that the wafer cleaning using wet chemicals, for instance fuming nitric acid, acetone or IPA, was difficult since the rotors were already released. Although oxygen plasma etching was carried out to strip off photoresist, a very thin layer of photoresist sometimes remains on the surface of the silicon substrate. This remaining thin photoresist layer is unable to be inspected by an optical microscope. It was found this thin photoresist layer can be removed in fuming nitric acid or acetone. The photoresist residual can result in a failure in triple-wafer stack bonding and also the stiction. The etched wafer was cleaned by putting the wafer on a spinner and spraying acetone and IPA as discussed in section 6.3.4. However, this method is difficult to thoroughly clean the whole wafer, in particular the surface of the rotor. In the end, the individual released rotor was taken out of the cavity and was cleaned in acetone and IPA. After cleaning, it was then put back to the cavity.

6.4 CONCLUSIONS

The micromachined ESG has been developed using a microfabrication process, which combines high-aspect-ratio dry etching with triple-wafer stack bonding. The process sequence, fabrication results and issues were discussed in detail in this chapter. In brief, the fabrication of top and bottom glass wafers has the same process flow. Glass etching was carried out to define a capacitive gap and also stoppers. This was followed by metal deposition and wet chemical etching in order to pattern top and bottom electrodes. Then, a thin bare silicon wafer was anodically bonded to a bottom glass substrate. Silicon etching was carried out using a DRIE process to define sidewall electrodes as well as the rotor. Next, the fabricated top glass wafer was electrostatically bonded to the etched silicon wafer. Lastly, the triple-wafer stack was sawed into individual chips and a diced chip was wire bonded to a chip carrier.

The second part in this chapter describes results and issues regarding to the fabrication of the micromachined ESG. It was found that glass etching using 7:1 BOE is suitable for defining a capacitive gap. It provides a uniform and smooth etched surface. The etch rate is relatively slow; however, this makes it easy to control the etch depth accurately. Metal electrodes and bond pads were made of chrome/platinum/gold layers. The chrome layer acted as an adhesive layer; the platinum layer was deposited in-between chrome and gold layers in order to prevent the diffusion from chrome to gold and vice versa.

The anodic bonding was carried out to bond silicon and glass substrates. This was done under ambient vacuum pressure to minimise voids, which cause by air trapped at the interface between silicon and glass wafers. The bonding parameters, i.e. temperature and bonding voltage, were optimised. It was found that the magnitude of bonding voltage must be less than 850 °C to avoid silicon located above a shallow recess pulled down and bonded to the etched glass surface.

A DRIE process was used to releases the rotor and also define a gap between the rotor and the sidewall electrodes. The recipe of the DRIE process employs the parameter ramping technique. Ambient pressure was ramped down throughout the etching process in order to achieve deep, high-aspect-ratio silicon etching. One issue resulted from a DRIE process is the so-called RIE lag. This RIE lag causes damage on both front and bottom sides of the released rotor.

Anodic bonding was again used for triple-wafer stack bonding. Wafer preparation was carried out in advance to make an electrical connection between the bottom surface of the glass substrate and a silicon wafer. This was done by sputter coating an aluminium layer on the bottom surface of the glass wafer. The stack was successfully bonded using the following parameters: temperature = 350 °C, ambient pressure = 4×10^{-2} mtorr and applied voltage = 700 V. However, it was found later that the fabricated device had a stiction problem. This is likely because the released rotor was electrostatically bonded to the top glass substrate.

Chapter 7

Feasibility Study of Electrostatic Levitation using Sidewall Electrodes

7.1 INTRODUCTION

During the course of this research project it was found that the fabricated devices suffered from stiction problems. Before the silicon/glass wafer was bonded to the top glass substrate, the released rotor was free to move. However, the rotor was stuck to a substrate after the triple-wafer stack bonding step. This issue could not be resolved during this research project as the entire Southampton University cleanroom facilities were destroyed by a fire. The final device, therefore, could not be tested.

As a result, in this chapter a micromachined device with no top substrate (see Figure 7.1) was considered and an alternative approach to provide electrostatic levitation by sidewall electrodes was explored. These sidewall electrodes are normally used to provide electrostatic forces in order to suspend the rotor along the x- and y-axis directions and maintain it at the centre of the device cavity. By applying a superimposed signal consisting of a DC bias voltage and an AC feedback control signal to the sidewall electrodes, a vertical levitation force in combination with lateral control forces can be generated on the rotor. This levitation effect was first reported in electrostatic comb drive actuators [**150–152**]. Vertical levitation of a microstructure was observed when such devices were driven by interdigitated comb electrodes biased with a DC voltage.

In this chapter, the feasibility of such an approach is investigated. The analysis of side drive electrostatic levitation is described along with the 2D simulation results. An analogue feedback control interface for the lateral motion along the x- or y-axis is discussed. Matlab/Simulink simulations were performed to investigate the control stability.

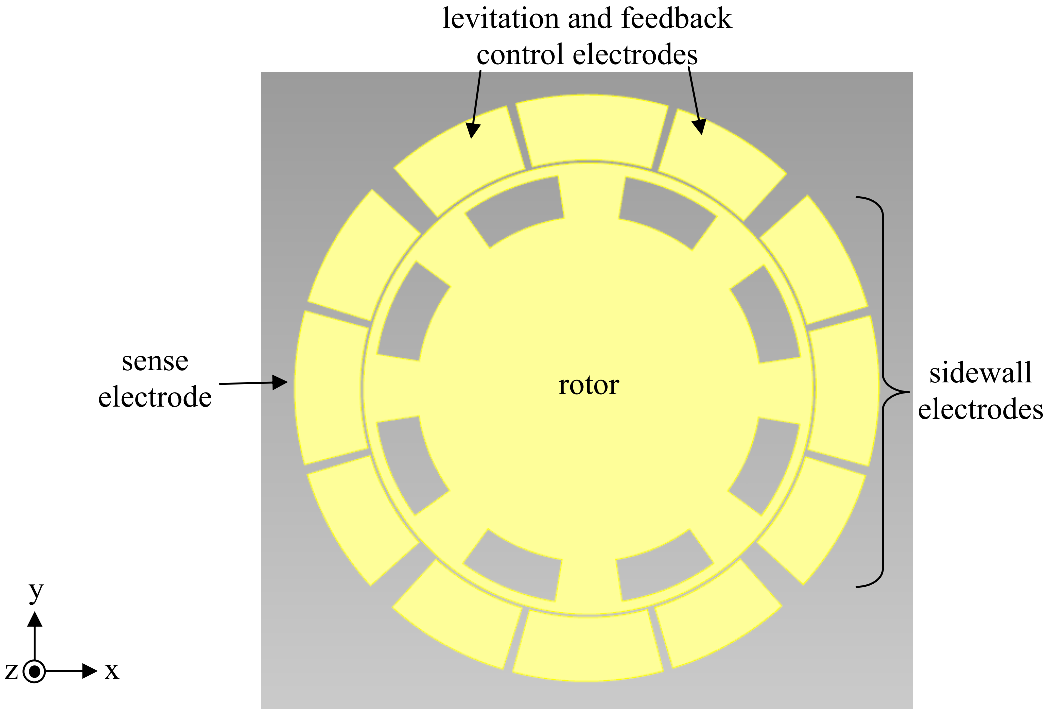

Top view

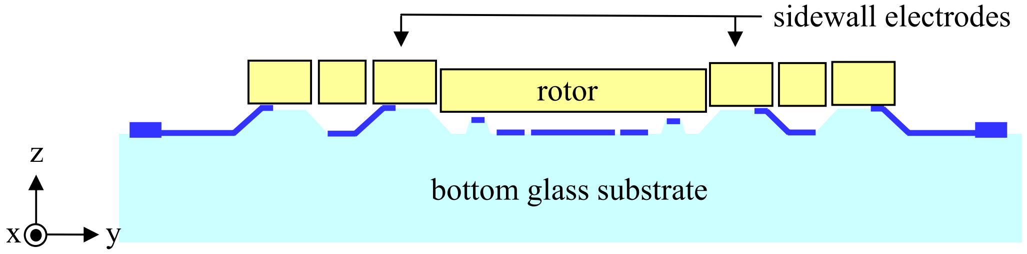

Cross-sectional view

Figure 7.1 Top-viewed and side-viewed schematics of a micromachined device considered in this chapter. Its design configuration and device dimensions are the same as the micromachined ESG discussed in chapter 3, except that it was not capped by a top glass substrate. The sidewall electrodes are employed to provide forces to control lateral motions of the rotor in the x and y directions and also a vertical levitation force along the z axis. The bottom electrodes can be used to measure angular displacements of the rotor about the x and y axis; thus, it may be possible to use it as a dual-axis accelerometer.

7.2 ANALYSIS OF SIDE–DRIVE ELECTROSTATIC LEVITATION

Cross-sectional views of the micromachined device considered in this study are shown in Figure 7.2. Figure 7.2a illustrates the device at rest where the rotor sits on the bottom glass substrate. This occurs at start-up when there is no DC voltage applied to the sidewall electrodes. Figure 7.2b shows the levitated rotor when sufficient DC voltage is applied to the sidewall electrodes. By applying a positive voltage to one electrode and a negative voltage with the same magnitude on the opposite electrode, the potential of the rotor is kept close or equal to zero as explained in more detail in chapter 3. Assuming the rotor is in the middle position between the surrounding sidewall electrodes, the net electrostatic force in the lateral directions (the x and y axes) will become zero and thus there is only a vertical levitation force acting on the rotor.

The vertical levitation force $F_{e,z}$ is, in this case, induced by electrostatic fringe fields. It cannot be modelled using a simple parallel-plate analysis. Therefore, finite element program, i.e. ANSYS, was used to estimate the levitation force acting on the rotor. In ANSYS simulations, a two-dimensional electrostatic analysis was performed to simulate the cross section of the micromachined device (as shown in Figure 7.2). Sidewall electrodes were biased with positive and negative DC voltages, where as bottom electrodes were grounded. Assume that the rotor is made of highly conductive silicon and it is in the centre between both sidewall electrodes. Thus, the potential of the rotor can be assumed as zero.

It is very challenging to run a simulation using the actual device geometry (discussed in chapter 3). The actual device dimension is large compared to the gap, and thus causing a problem during mesh generation. Therefore, the following simulations were carried out with a smaller rotor diameter (400 μm) and thickness (20 μm). Assume that a capacitive gap between the rotor and sidewall electrodes is 10 μm and the rotor is sitting on the stoppers, 1 μm away from the bottom substrate.

Figure 7.3 shows the resulting electric potential when the sidewall electrodes were biased with ±100 V. It reveals a high potential gradient between the sidewall electrodes and the edge of the rotor, and thus the magnitude of the resulting electrostatic force is high in the region close to the rotor edge. Note that the resulting forces obtained from 2D ANSYS approximation are the induced force per unit length of the rotor. Figure 7.4 shows the distribution of the electrostatic forces acting along the top (top graph) and the bottom of the rotor (bottom graph). A positive sign implies that the rotor is pulled up and a negative sign means the rotor is pulled down. The sum of the top and bottom forces is the net vertical levitation force per unit length F_{z0}.

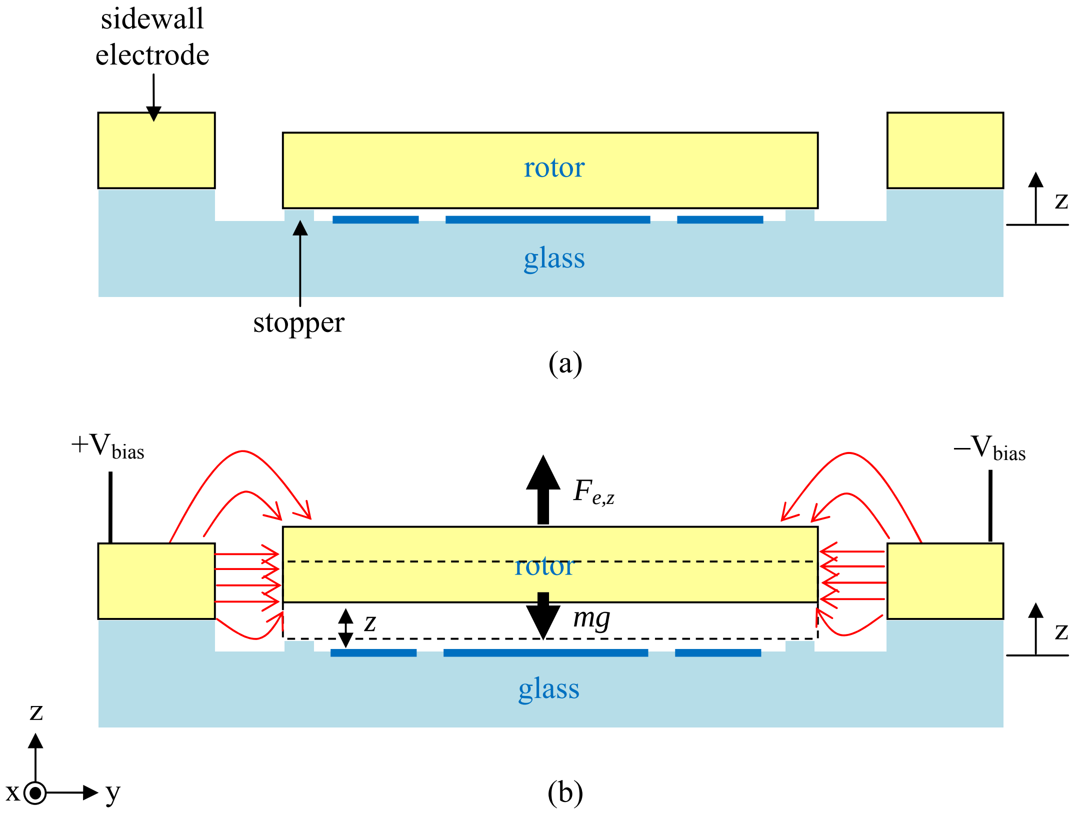

Figure 7.2 Schematic diagrams of a micromachined device considered in this chapter: (a) when no voltage is applied to sidewall electrodes, a rotor sits on a bottom substrate and (b) a rotor is lifted up when sidewall electrodes are biased with DC voltages. By applying a positive voltage +V_{bias} to one electrode and a negative voltage –V_{bias} with the same magnitude to the opposite electrode, the rotor potential is kept close or equal to zero; and thus, only a vertical levitation force is produced on the rotor. Red arrow lines show the corresponding electric field lines.

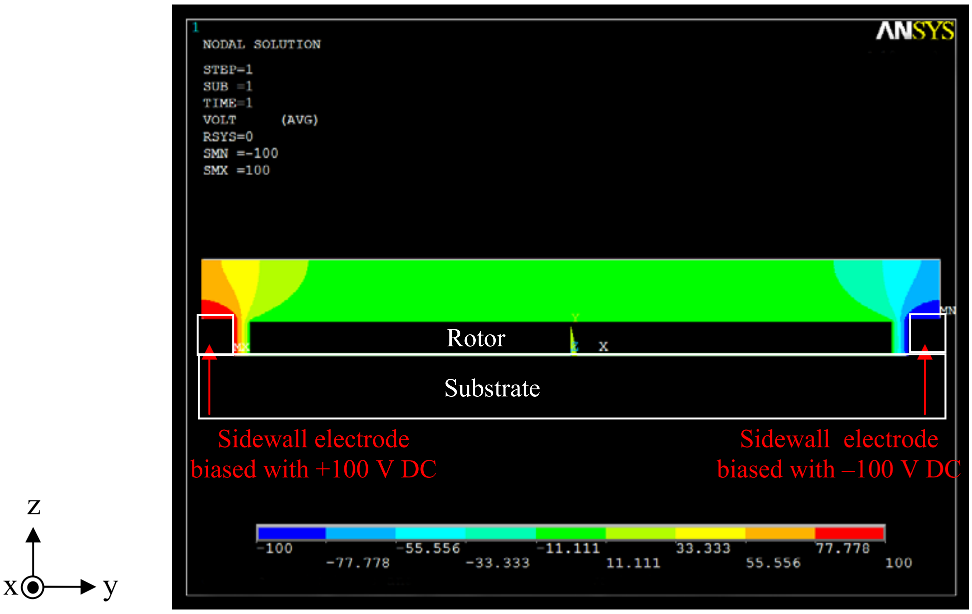

Figure 7.3 The potential distribution obtained from ANSYS 2D electrostatic analysis when the rotor sit on the stoppers and ±100 V was applied to sidewall electrodes.

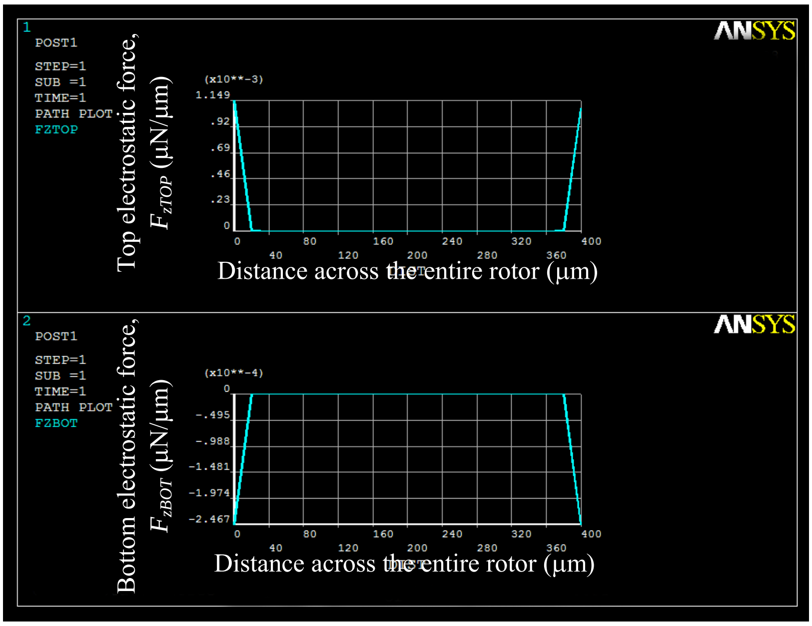

Figure 7.4 Induced electrostatic forces per unit length acting on the top surface (top plot) and bottom surface (bottom plot) of the rotor when it rests on the stoppers and ±100 V is applied to the sidewall electrodes.

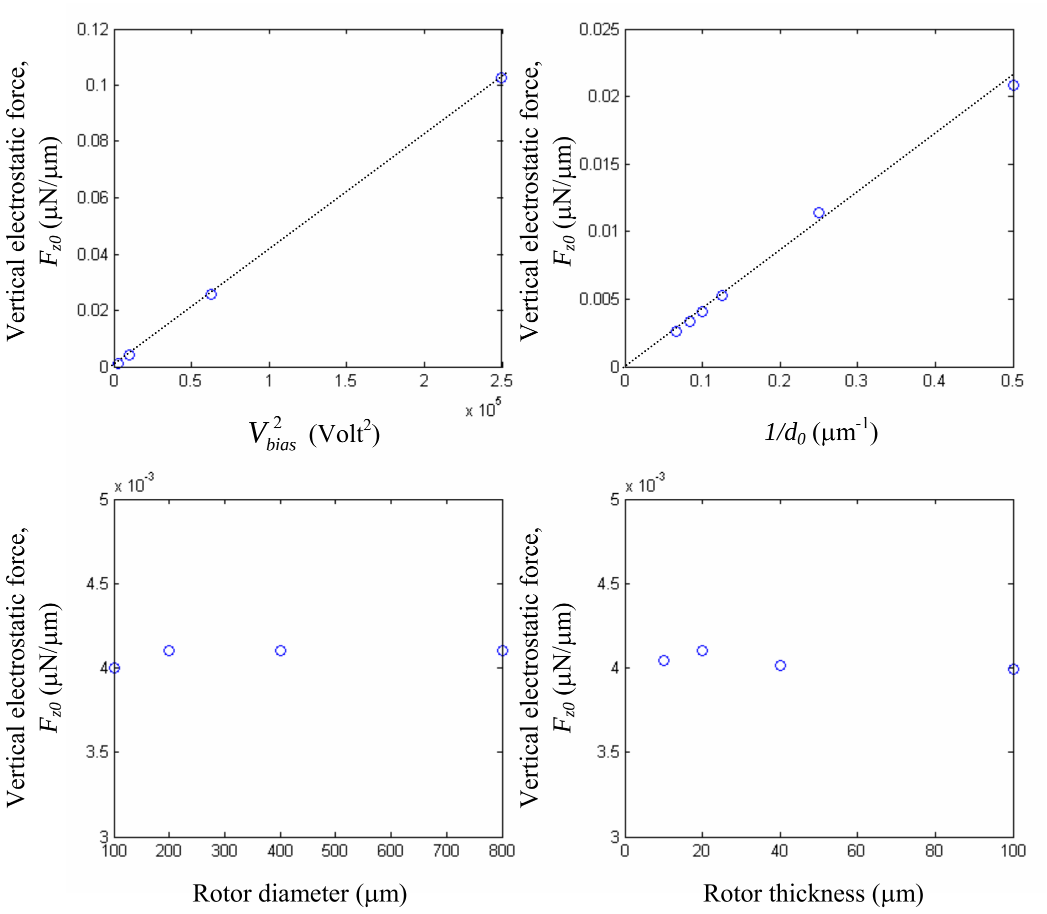

Figure 7.5 Net electrostatic levitation forces as a function of the bias voltage (top, left), distances between the rotor and sidewall electrodes (top, right), rotor diameters (bottom, left) and rotor thickness (bottom, right). These results are obtained from ANSYS simulations by assuming the rotor sitting on the stoppers.

ANSYS simulations were carried out to investigate the net vertical force as a function of various parameters, including the bias voltage V_{bias}, the distance between the rotor and sidewall electrodes d_0, the rotor diameter and the thickness of the rotor. The simulation results are shown in Figure 7.5. It can be seen that the net vertical levitation force is directly proportional to the square of the bias voltage and inversely proportional to the distance between the rotor and sidewall electrodes. However, the net vertical force remains almost constant with regard to the diameter and thickness of the rotor, which implies that the net vertical force is independent of the rotor dimension. The relationship between the net electrostatic levitation force F_{z0} and the displacement of the rotor z along a vertical direction is plotted as shown in Figure 7.6. It can be seen that in the absence of the force of gravity, the rotor will be levitated to a stable equilibrium position z_0 (~ 5.5 μm for this case) upon the application of a bias voltage.

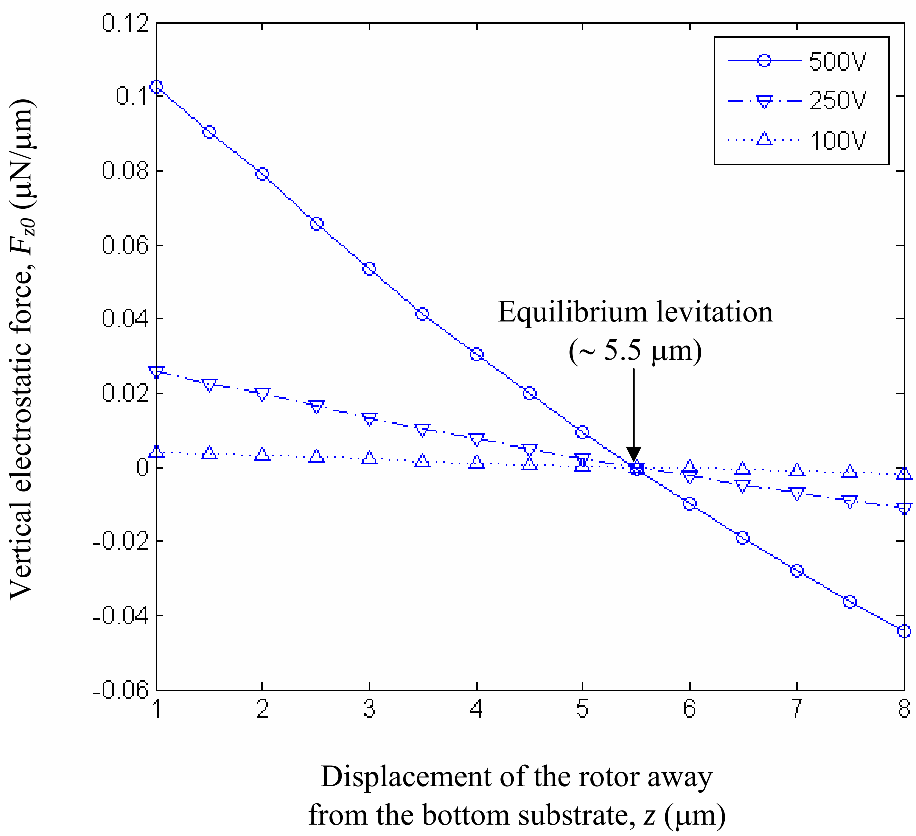

Figure 7.6 Net vertical electrostatic forces corresponding to the displacement of the levitated rotor away from the bottom substrate when the sidewall electrodes were biased with ±100 V, ±250 V and ±500 V, respectively. The results were simulated in ANSYS with the following parameters: a rotor diameter = 400 μm, a rotor thickness = 20 μm, separations from the rotor and the sidewall electrodes = 10 μm and an etched depth in the bottom glass substrate = 3 μm.

The resulting electrostatic force calculated from 2D ANSYS simulations is the force per unit length. In order to obtained the actual electrostatic levitation force acting on the rotor, the resulting vertical force F_{z0} has to be multiplied by the overlap angle between the rotor and the set of the sidewall electrodes. Figure 7.7 is a plot of the actual electrostatic levitation force $F_{e.z}$ as a function of a vertical displacement z for the device dimensions: a rotor having a diameter of 4 mm and a thickness of 200 μm, and the gap between the rotor and sidewall electrodes is 10 μm. The relationship between the levitation force and the vertical displacement for a given V_{bias} can be expressed as:

$$F_{e,z} = \gamma_z V_{bias}^2 (z_0 - z) \tag{7.1}$$

where

z = levitation height,

z_0 = maximum levitation height and

γ_z = geometry factor (~ 8.7214×10^{-10} N μm^{-1} V^{-2} for this case).

The geometry factor depends on design parameters, including the separation between the rotor and the sidewall electrodes and the height of the sidewall electrode relative to the thickness of the rotor. Note that equation (7.1) is justified only for z less than z_0.

In order to levitate the rotor, the net electrostatic force must be large enough to counteract the force of gravity, $F_{e,z} > mg$. Thus, the minimum voltage required to levitate the rotor $V_{lev,\min}$ can be evaluated by solving:

$$F_{e,z} - mg = 0 \tag{7.2}$$

Substituting (7.1) into (7.2) yields:

$$\gamma_z V_{bias}^2 (z_0 - z) - mg = 0 \tag{7.3}$$

The minimum voltage $V_{lev,\min}$ can then be solved by rearranging equation (7.3), which yields:

$$V_{lev,\min} = \sqrt{\frac{mg}{(z_o - z)\gamma_z}} \tag{7.4}$$

For the rotor with a diameter of 4 mm and a thickness of 200 µm, the minimum voltage required to maintain the rotor at 3 µm above the bottom substrate is about 325 V. This level of voltage is below the breakdown voltage under atmospheric pressure, which is about 400 V for a 10 µm separation between the rotor and the sidewall electrodes.

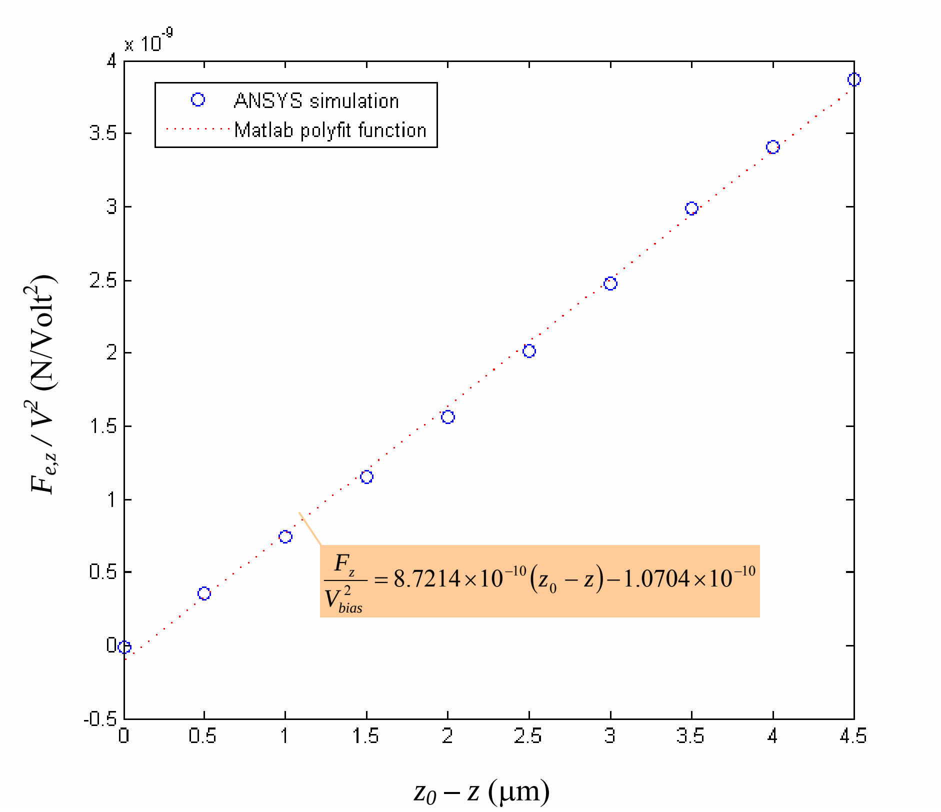

Figure 7.7 A plot of the vertical electrostatic forces divided by the square of the bias voltage as a function of $(z_0 - z)$.

The approach discussed above was based on the assumption that the rotor was kept in the middle position between all sidewall electrodes. If the rotor was off-centre, the potential of the rotor will not be maintained at zero. Furthermore, as can be seen in Figure 7.5, the magnitude of a vertical electrostatic levitation force strongly depends on the distance between the rotor and sidewall electrodes. The off-centred rotor will result in the imbalance between electrostatic forces acting on each side of the rotor. For instance, Figure 7.8 shows the resulting electrostatic forces acting across the rotor when it is off-centre by 0.1 μm. It is obvious that the resulting force on the right hand side is stronger than that on the left side of the rotor and thus causing the rotor to rotate about the x axis. The calculation obtained from ANSYS shows that the moment per unit length acting on the rotor is 0.11×10^{-1} μN. As a consequence, a closed-loop system is required to control the translational motion of the rotor along the x and y axes. Principle, design and simulation of such a closed-loop system are discussed in the next section.

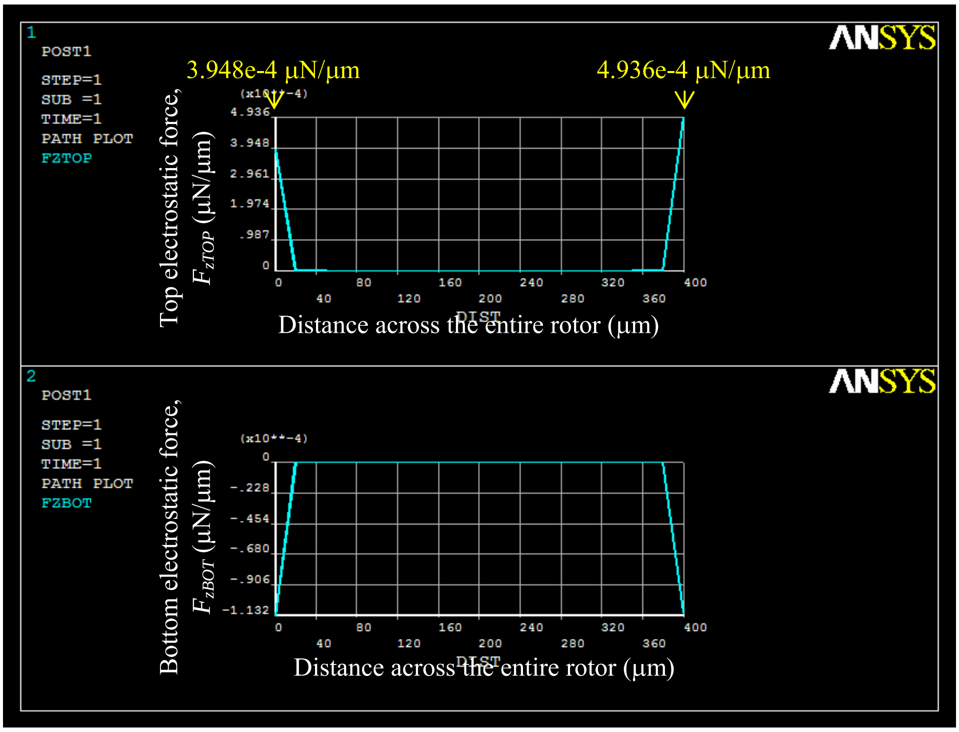

Figure 7.8 Induced electrostatic forces per unit length acting on the top surface (top plot) and bottom surface (bottom plot) of the rotor when the rotor is off-centre by 0.1 μm. The result was obtained from ANSYS simulations with an assumption that the rotor rests on the stoppers and ±100 V is applied to the sidewall electrodes.

7.3 A CLOSED–LOOP SYSTEM FOR CONTROLLING LATERAL MOTIONS OF THE ROTOR

For the micromachined device considered in this chapter, sidewall electrodes are used to provide the vertical electrostatic levitation force acting on the rotor and at the same time also control lateral motions of the rotor along the x and y axes. The levitation force can be realised by biasing the sidewall electrodes with DC voltages as discussed in the previous chapter. On the other hand, in order to maintain the position of the rotor in the centre among the sidewall electrodes, a closed-loop control system is required. Due to the relatively high voltage needed for levitation, a closed-loop control system based on analogue force feedback is preferred. This section discusses the sensing and actuation strategy employed in the closed-loop control system. The principle and analysis of the analogue feedback loop is also presented.

7.3.1 Sensing and actuation strategy

For the sake of simplicity, the lateral motion of the rotor along only one direction, i.e. the y axis, is considered in the following. This assumption is justified due to the symmetrical design of the micromachined device. The sensing strategy relies on a fully differential capacitance measurement using reverse-role half bridge configuration as described in section 3.5.2. As the rotor is floating and has no direct electrical connection to a bond pad, the AC excitation signal is coupled through the rotor via the capacitor formed between the rotor and the excitation electrode, which is located on the bottom glass substrate (see Figure 7.9a). The displacement of the rotor away from the centre position between the left and right sense electrodes (see Figure 7.9b) will cause an imbalance in the capacitance of the two capacitors formed between the rotor and the left and right sense electrodes. The differential of these two capacitances will be picked up and amplified by a front-end amplifier. The position sensing approach is actually similar to that explained in chapter 3, except that the excitation voltage is only applied to the bottom excitation electrode. One disadvantage of this approach is that the amplitude of the coupled excitation signal changes according to the levitation of the rotor along the vertical z axis. However, this common-mode error is cancelled out by a differential capacitive readout scheme.

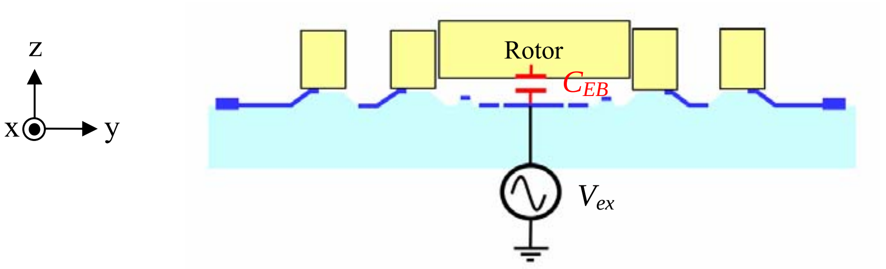

(a) Top view

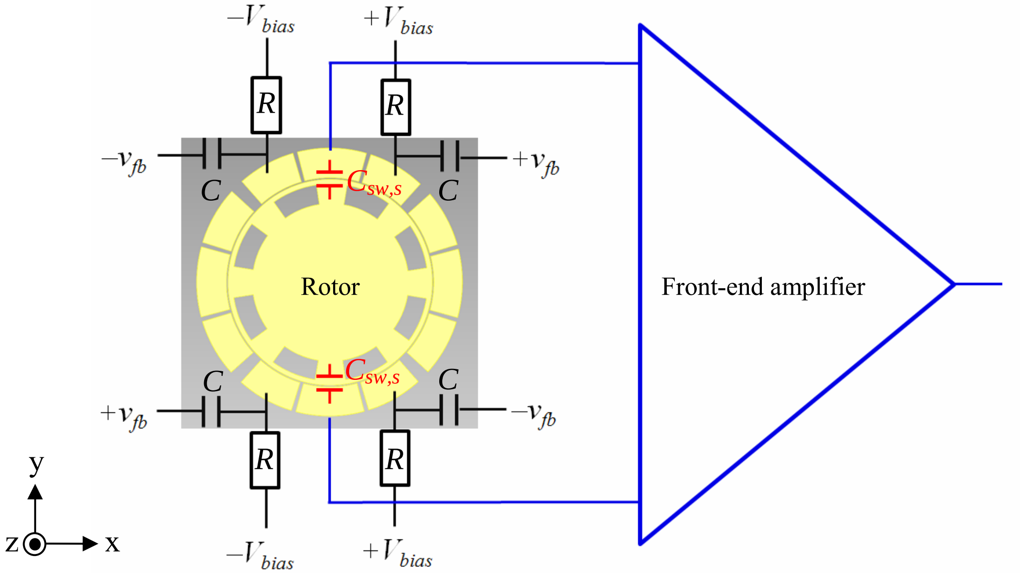

(b) Cross-sectional view

Figure 7.9 Schematic diagram showing the approach employed to control the position of the rotor along the in-plane axes. (a) The AC voltage source is connected to the excitation electrode located on the bottom substrate. This voltage source is required for capacitive position sensing. (b) A front-end amplifier is used to read out the imbalance between the left and right capacitances formed between the rotor and the two sense electrodes. The feedback electrodes are fed by feedback control voltages v_{fb} superimposed on the DC levitation voltages V_{bias}.

The equivalent capacitance network for the capacitive position sensing of the micromachined levitated device considered here is presented in Figure 7.10. The relationship between the rotor potential V_r and the input excitation voltage V_{ex} can be written as:

$$V_r = \frac{V_{ex} C_{EB}(z)}{C_{EB}(z) + \sum C_{sw,s} + \sum C_{sw,fb}} \tag{7.5}$$

where

$C_{sw,s}$ = sense capacitance between the rotor and the sense electrodes,

$C_{sw,fb}$ = feedback capacitances between the rotor and the feedback electrodes,

C_{EB} = capacitance between the rotor and the bottom excitation electrode.

The C_{EB} is a function of the levitation height. However, assuming the rotor is levitated at the equilibrium point, C_{EB} can be treated as a constant. For the considered micromachined device, C_{EB} = 6.25 pF, $C_{sw,s}$ = 0.186 pF and $C_{sw,fb}$ = 0.168 pF. It should be noted that the C_{EB} is relatively larger than the sum of the sense and feedback capacitances and thus $V_r \approx V_{ex}$.

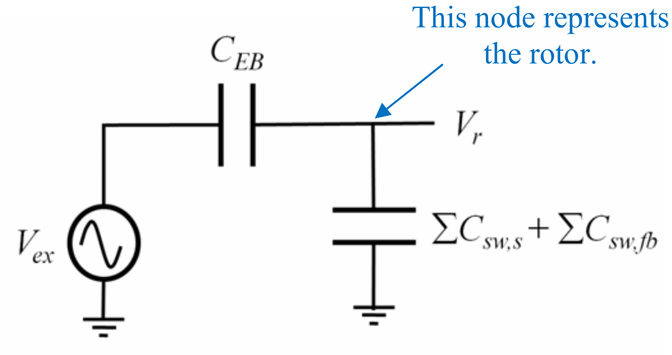

Figure 7.10 Equivalent electronic model of the capacitances formed between the rotor and the electrodes.

The electrostatic actuator is composed of two sets of parallel-plate electrodes as shown in Figure 7.9. Each set has two feedback electrodes: one electrode is connected to a positive bias voltage and the other electrode to a negative bias voltage. The applied bias voltages provide a vertical electrostatic force to levitate the rotor in the z axis. In addition, AC feedback control signals are superimposed on the DC bias voltages. These feedback voltages provide electrostatic forces to control the motion of the rotor along the in-plane directions, i.e. the x and y axes. Figure 7.9b shows a circuit diagram to combine the bias voltage and the feedback control signal. The voltage $V_{feedback}$ at the electrode terminal can be derived by the principle of superposition. It is the sum of the DC and AC components as given by:

$$V_{feedback} = V_{DC} + v_{AC} \tag{7.6}$$

where V_{DC} and v_{AC} are the DC and AC components of the $V_{feedback}$ signal at the electrode terminal. By considering the AC voltage source is disconnected (shorted) from the circuit, V_{DC} can simply be expressed as:

$$V_{DC} = V_{BIAS} \tag{7.7}$$

Similarly, v_{AC} at the electrode terminal can be derived by considering the case where the DC voltage source is disconnected (shorted) from the circuit. Assume that v_{fb} is a sinusoidal signal with an angular frequency ω, v_{AC} as a function of v_{fb} can be expressed in the phasor form as:

$$v_{AC} = \left(\frac{v_{fb}}{1 + j\omega RC} \right) \times j\omega RC \tag{7.8}$$

Note that when ωRC is much greater than 1, the amplitude of the v_{AC} will be equal to that of the v_{fb}. In other words, the impedance of the capacitor becomes small enough and can be neglected at frequencies f much higher than the cutoff frequency $f_c = 1/2\pi RC$. In general, a high value of R (about hundreds kilo-ohm) is chosen to prevent a short circuit occurring between the rotor and the sidewall electrodes. A 100 kΩ resistor and a 0.1 μF capacitor are employed in the design, which yields a 15.9 Hz cutoff frequency.

7.3.2 Analogue feedback control system

Figure 7.11 shows the block diagram and linear model of the considered micromachined levitating device with a force feedback loop. Due to the symmetrical design of the micromachined device in the x and y axes, only one degree of freedom is considered here. The displacement of the rotor due to inertial forces is detected by the imbalance of the sense capacitors. The differential change between the sense capacitors is picked up and converted into a voltage by a front-end amplifier. An electronic controller is added to improve the system stability. An electrostatic force is used as a feedback on the rotor to counteract the displacement caused by inertial forces. Assume small displacements of the rotor due to a closed-loop system (compared to the nominal gap d_0). By applying the feedback voltage v_{fb} together with a DC bias voltage V_{BIAS} to the sidewall electrodes, the electrostatic feedback force F_{fb} on the rotor can be approximated as:

$$F_{fb} \approx -2C_{sw,fb} \frac{v_{fb} V_{BIAS}}{d_0} \tag{7.9}$$

where $C_{sw,fb}$ is the feedback capacitance and d is the nominal distance between the rotor and the sidewall electrodes.

Consider the linear model of the closed-loop system illustrated in Figure 7.11b. The sensing element can be modelled as a proof mass connected in series with a damper (but no spring). This is due to the absence of suspension beam connecting between the rotor and substrate. The displacement-to-capacitance building block and the front-end circuit are modelled with the gains k_x (with dimension pF/m) and k_c (~ 9.74 V/pF, see chapter 4), respectively. According to equation (7.4), the force feedback block can be modelled as the linear gain k_{FB}. The electronic controller employs a lead compensator in order to shift poles of the closed-loop system to the left hand side and thus improve the stability of the system. Its transfer function compensator can be expressed in the Laplace's domain as:

$$C_s = k_p \frac{s+z}{s+p} \tag{7.10}$$

where k_p is the gain, z and p are the zero and pole frequencies in radians per second. For a lead compensator, the pole frequency is normally greater than the zero frequency ($z > p$). Then, the transfer function from the input inertial forces to the output feedback voltage can be expressed as:

$$H(s) = \frac{v_{fb}(s)}{F_{in}(s)} = \frac{k_{po}k_p s + k_{po}k_p z}{ms^3 + mps^2 + \left(b + bp + k_{po}k_p k_{FB} p\right)s + k_{po}k_p k_{FB} z} \tag{7.11}$$

where

$$k_{po} = k_x k_c = \left(\frac{2C_{sw,s}}{d}\right)\left(\frac{C_{EB}}{C_{EB} + \sum C_{sw,s} + \sum C_{sw,fb}} \cdot \frac{2V_{ex}}{C_f}\right),$$

$$k_{FB} = -2C_{sw,fb}\frac{V_{BIAS}}{d}.$$

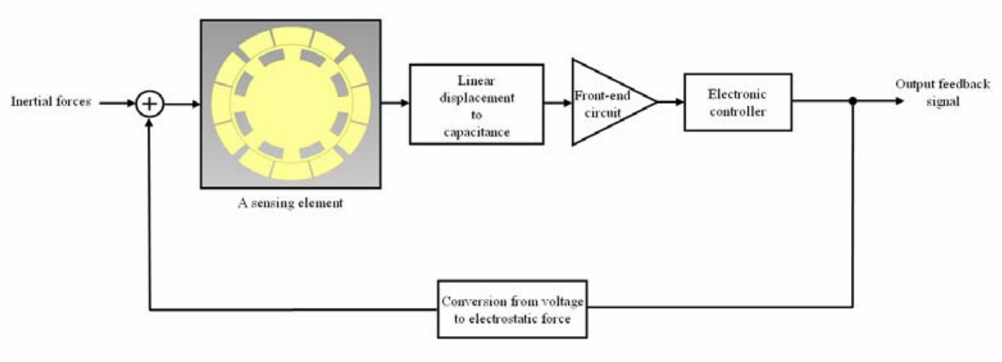

(a)

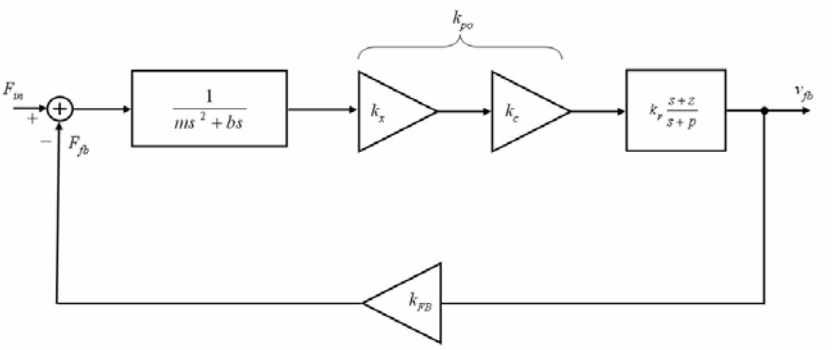

(b)

Figure 7.11 (a) Block diagram and (b) linear model of the micromachined levitating device with an analogue feedback control system.

The lead compensator was designed using Matlab/Simulink and SISO design tools [**153**] where the system parameters were assumed as follows: m = 3.73 mg, $b = 7.65\times10^{-5}$ Ns/m (for air pressure), d = 10 µm, C_{EB} = 6.25 pF, $C_{sw,s}$ = 0.186 pF, $C_{sw,fb}$ = 0.168 pF and V_{bias} = 350. Figure 7.12 shows the root locus diagram of the open-loop transfer function with a lead compensator. The compensator has a gain k_p of 10 and its pole and zero frequencies are located at –50000 rad/s and –35000 rad/s, respectively. The location of pole and zero of the compensator was chosen in such a way as to the poles of the closed-loop system are on the left hand side of the root locus plot and thus improve the stability of the system. Increasing a control gain will result in higher natural frequency and quality factor of the closed-loop system. Figure 7.13 compares the frequency responses of the micromachined levitating device with and without a feedback control loop.

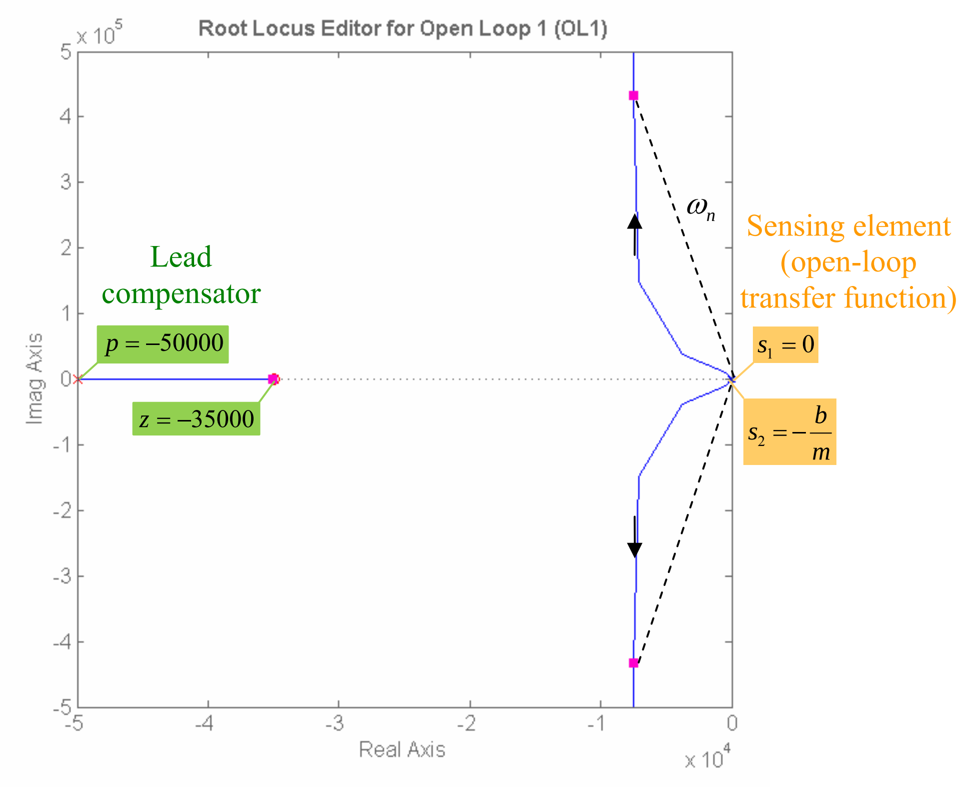

Figure 7.12 Root locus plot of the open-loop transfer function with a lead compensator, which has a pole at –50000 rad/s and a zero at –35000 rad/s. The red dots represent the poles of the closed-loop system with the gain k_p = 10.

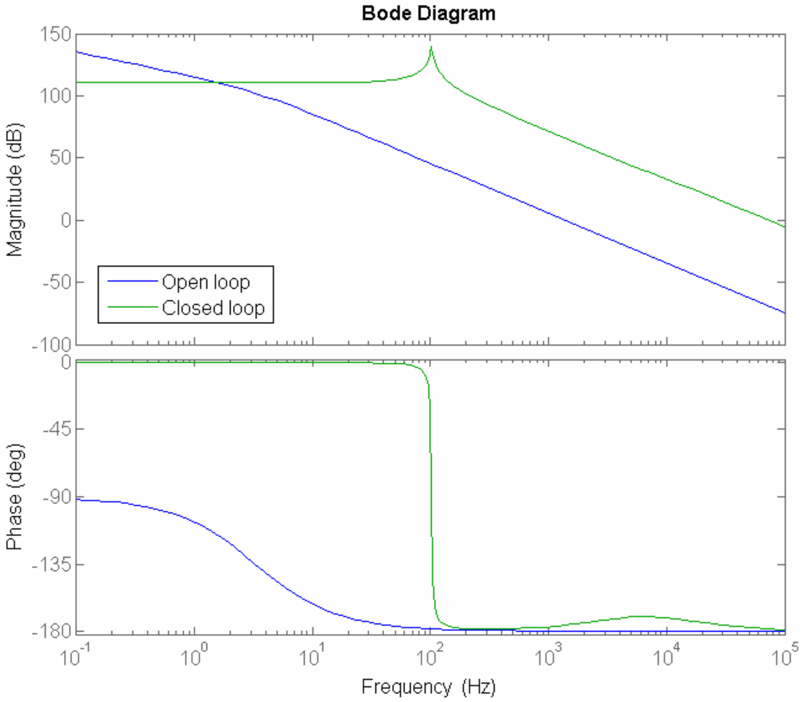

Figure 7.13 Bode plot of the micromachined levitating device with and without a control feedback loop. The closed-loop system employs a lead compensator, which has a pole at –50000 rad/s and a zero at –35000 rad/s as well as a gain of 10.

7.3.3 Simulation of the closed-loop position control system

Simulations of the closed-loop system discussed in the previous section have been performed in Matlab/Simulink to study the system behaviour and to evaluate its stability. Due to the symmetrical design of the micromachined device in the x and y axes, only one degree of freedom of the closed-loop system is considered. The following parameters were assumed for the simulations: m = 3.73 mg, $b = 7.65\times10^{-5}$ Ns/m (for air pressure), d = 10 μm, C_{EB} = 6.25 pF, $C_{sw,s}$ = 0.186 pF, $C_{sw,fb}$ = 0.168 pF, V_{bias} = 350, k_p = 1000, p = –50000 rad/s, z = –35000 rad/s, C_f = 1 pF and V_{ex} = 1 V.

The first issue to be considered is that whether or not the micromachined levitating device is stable when it operates as part of the developed feedback control loop. Recall that the rotor has no mechanical connection to substrate and it is surrounded by sense and feedback control electrodes (see Figure 7.1). Since there are no bearings or pillars to kept the rotor in the middle position among the surrounding electrodes, it can sit anywhere inside the cavity during the start-up. Therefore, the first simulation was carried out to ensure that the closed-loop system is able to cope with this situation. A stable closed-loop system should be able to maintain the rotor in the centre position, i.e. the so-called nominal position.

Simulation assumed that, for the worst case scenario[1], the rotor is off centre by 7 μm at the start-up and no inertial force is applied to the rotor. Simulation results (see Figure 7.14) reveal that the closed-loop system is able to capture the rotor and maintain it at the nominal position. The upper trace in Figure 7.14 shows the displacement of the rotor along the in-plane direction and the bottom trace shows the waveform of the voltage output. At the beginning, the rotor fluctuates about the centre position with displacement amplitude of 7 μm, resulting in the output voltage of the amplifier saturating at its supply voltages of ±12 V. The displacement of the rotor starts converging at the centre position after some period of time. It took about 9 ms for the closed-loop system to settle. At this point, the rotor is maintained at its nominal position.

The system response when the micromachined levitating device experiences acceleration along the in-plane axis is shown in Figure 7.15. The acceleration is a sinusoidal signal and has a peak magnitude of 10 g (1 g = 9.8 m/s^2) and a frequency of 10 Hz. The upper trace shows the input inertial force due to the applied acceleration, the middle trace is the displacement of the rotor along the in-plane direction and the bottom trace is the output feedback voltage. The simulations were carried out by assuming the rotor is already in the middle position between the sidewall electrodes. It can be seen that the output feedback voltage is in-phase to the applied force and the closed-loop system seems stable.

---

[1] If the rotor is off-centre by more than 7 μm, the closed-loop system will become unstable. Therefore, the worst case is defined as the maximum distance of the rotor away from the centre that the control system can handle.

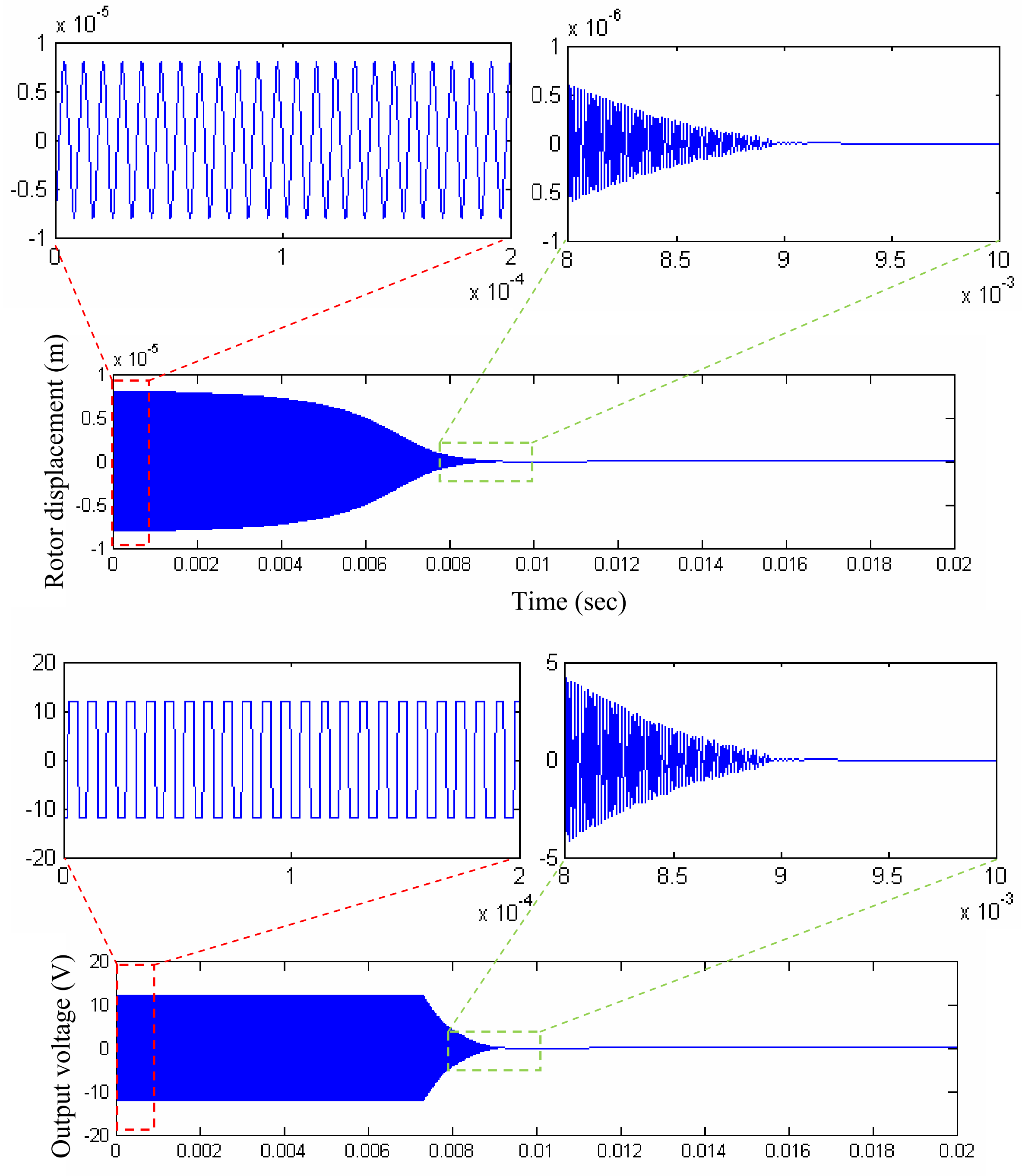

Figure 7.14 System response at the start-up phase, assuming the rotor is off-centre by 7 μm: the upper trace showing the displacement of the rotor and the bottom trace showing the output feedback voltage.

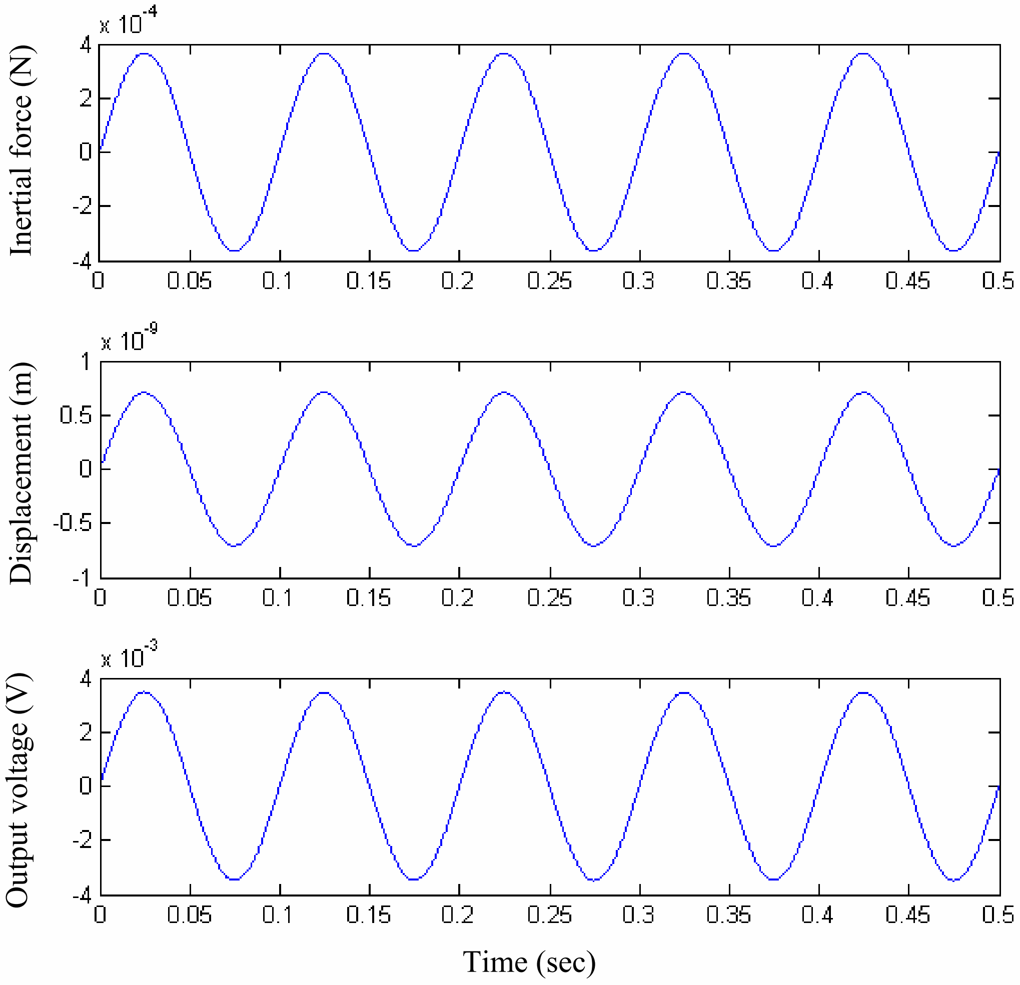

Figure 7.15 Time-domain response of the closed-loop system when an in-plane sinusoidal acceleration with a magnitude of 10 g and a frequency of 10 Hz was applied to the sensing element. Assume that the rotor was initially at the centre position. The upper trace shows the input inertial force, the middle trace showing the displacement of the rotor and the bottom trace showing the output feedback voltage.

To conclude, it can be seen that the designed analogue feedback control loop based on a lead compensator provides a stable closed-loop system. It is able to cope with the situation where the rotor is initially located at the off-centre position. The closed-loop system is still stable under applied inertial force.

7.4 INITIAL TEST

A preliminary measurement of a fabricated prototype sensor was performed to measure the capacitances which are formed between the sidewall electrodes and the released rotor. The measurement was carried out using the prototype sensor with the parameters shown in Table 3.1 and 3.2, except the thickness of the rotor is 80 μm and the gap distance between the rotor and sidewall electrodes is 10 μm.

The experimental setup for measuring the sidewall capacitances is illustrated in Figure 7.16. One probe tip that contacts the rotor is used to maintain the rotor fixed in position. The other probe tip is movable to connect sidewall electrodes to an Agilent 4279A CV meter. The capacitance measurement was carried out using the following procedure. First, the open-circuit and short-circuit calibrations of the CV meter are performed. The probe tips are then moved into contact to the prototype sensor. The position of the rotor is adjusted so that the reading value of each sidewall sense capacitance is as close to each other as possible. The sidewall capacitances were measured using an AC excitation signal with amplitude of 1 V_{rms} and a frequency of 1 MHz at different bias voltages (from –2 to 2 V). This approach, however, cannot be used to measure the exact value of each sidewall capacitance since the actual gap distance between the rotor and each sidewall electrode is difficult to be measured. The measurement only gives an approximation value of the sidewall capacitances

The sidewall capacitance at different bias voltages, as measured by the CV meter, shows small deviations about a constant value. The measured capacitances for each sidewall sense capacitor are then averaged as shown in Table 7.1. It can be seen that the measured values are in the same order of magnitude to the nominal sidewall capacitance calculated from equation (3.51). However, the measured values are relatively smaller. This is because the actual gap between the rotor and the sidewall electrodes is somewhat larger than the designed value (due to undercut etching during photolithography and DRIE processes).

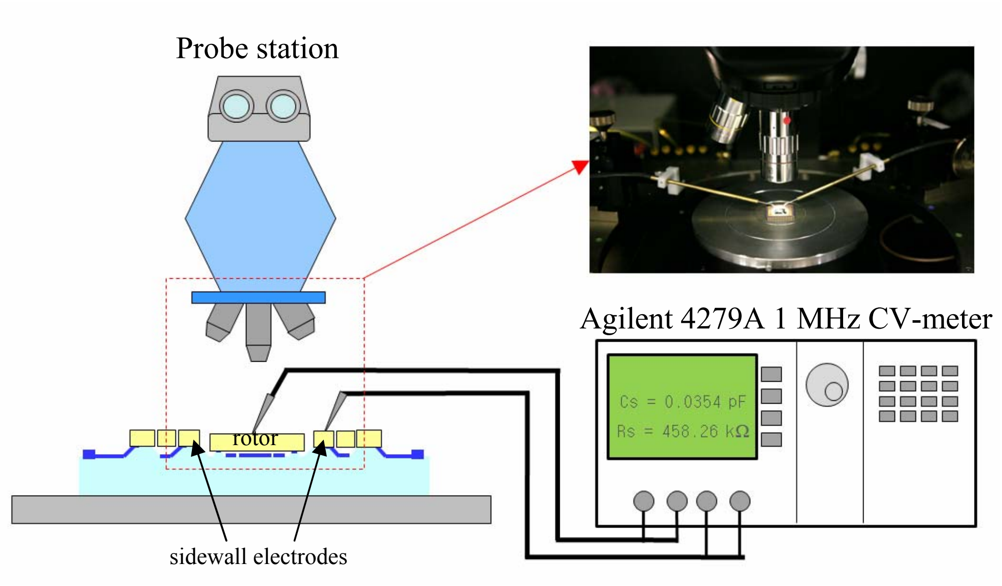

Figure 7.16 Schematic diagram of the experimental setup for measuring capacitances between the rotor and sidewall sense electrodes.

Table 7.1: Measured values of the capacitances between the rotor and the sidewall electrodes in comparison with the theoretical value calculated from equation (3.51).

	Measured (pF)	**Analytical (pF)**
Capacitance between the rotor and the left-hand electrode to sense motion in the x direction	3.44×10^{-2}	7.45×10^{-2}
Capacitance between the rotor and the right-hand electrode to sense motion in the x direction	3.43×10^{-2}	7.45×10^{-2}
Capacitance between the rotor and the left-hand electrode to sense motion in the y direction	4.03×10^{-2}	7.45×10^{-2}
Capacitance between the rotor and the right-hand electrode to sense motion in the y direction	4.36×10^{-2}	7.45×10^{-2}

Furthermore, the prototype sensor implemented with a closed-loop position control circuit was experimentally tested. This aims to evaluate electrostatic levitation resulted from applying high voltages onto the sidewall electrodes. Figure 7.17 depicts a schematic diagram of this experimental setup. A Polytec white light interferometer (micro system analyser MSA-400) is employed to measure the levitation height of the rotor. First, a step height between the top surface of the rotor and the sidewall electrodes were measured as a reference point (see Figure 7.18a). Then, the measurement was carried out to measure a change in the step height when the applied bias voltages (±350 V) were switched on. Two configurations were conducted: (1) the bottom excitation electrode is connected to an AC excitation signal with the amplitude of 1 V and a frequency of 500 kHz and (2) the bottom electrode is grounded.

The measurement results are shown in Figure 7.18. Levitation of the rotor could not be observed on both experiments. The step height between the rotor and the sidewall electrode remains constant even the applied voltages were increased to ±400 V (the maximum output voltage of the high voltage power supply). As the gap between the rotor and the sidewall electrodes is larger than the designed value (due to undercut etching), the applied voltages may not be enough to achieve levitation.

In addition, the designed closed-loop control circuit did not function properly as it was expected. It was found that the rotor was stuck to the sidewall electrodes. This caused the applied levitation voltages to be connected to the input of the front-end circuit. As a result, the pick-off amplifiers of the front-end circuit were damaged.

The test results at this point are not yet conclusive. Further tests need to be performed to investigate the electrostatic levitation.

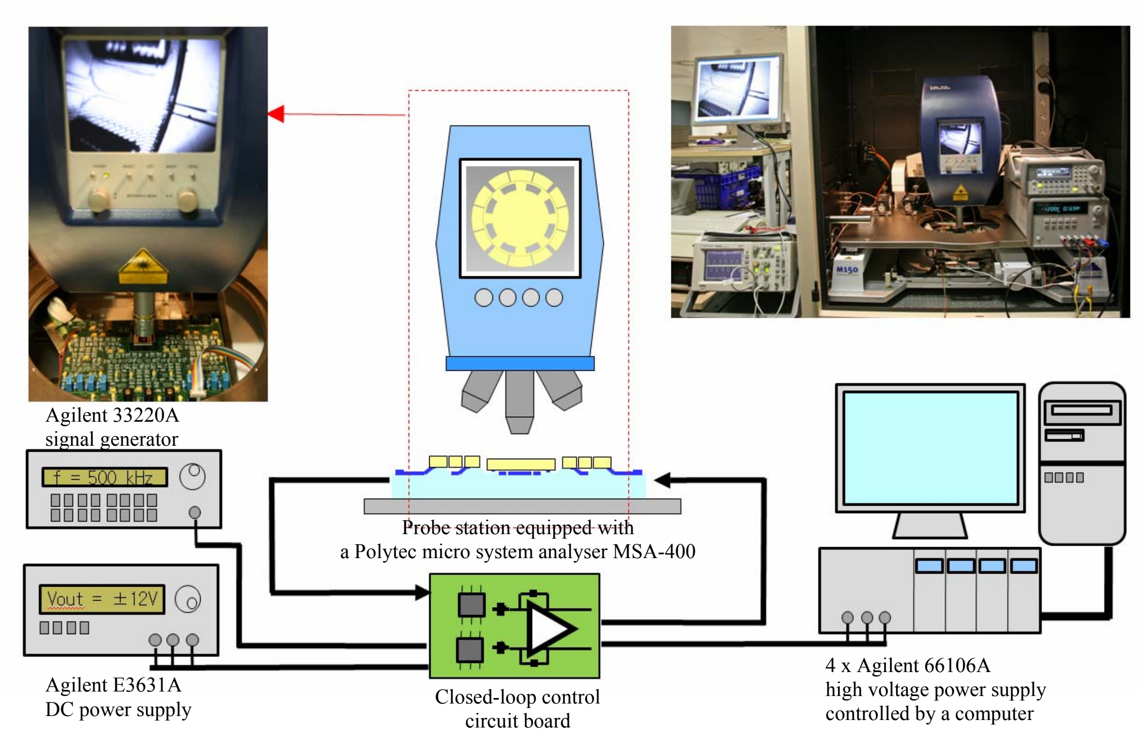

Figure 7.17 Schematic diagram of the experimental setup for a feasibility study of the electrostatic levitation effect. Electrostatic forces are generated by applying high voltages onto sidewall electrodes of the prototype sensor. The levitation is inspected using a Polytec white light interferometer.

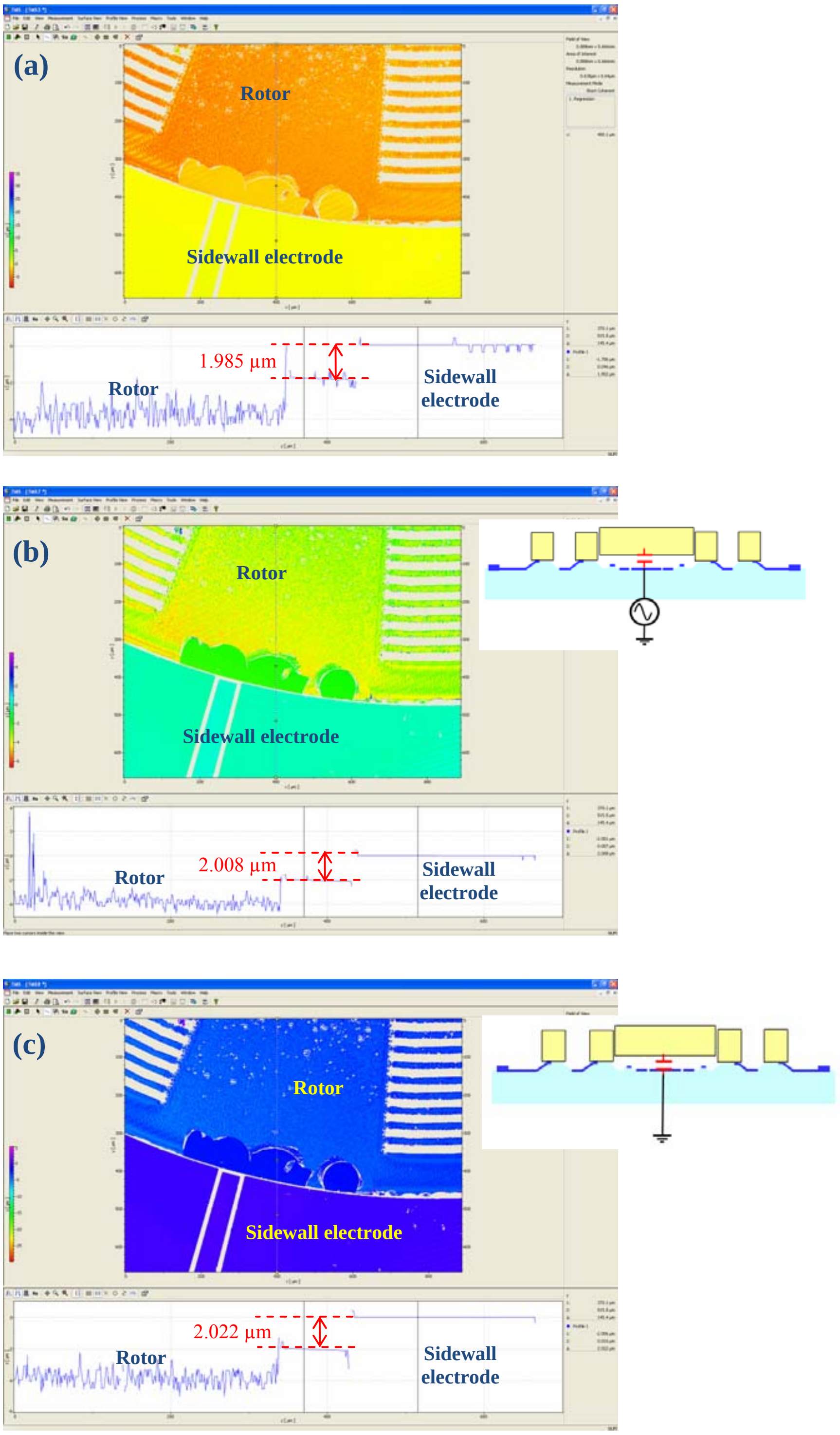

Figure 7.18 Topographical images of the prototype sensor obtained from a Polytec white light interferometer: (a) no high voltage applied to the sidewall electrodes, (b) and (c) are when high voltages are applied to the sidewall electrodes. The bottom electrode is connected to: (b) an excitation signal and (c) ground potential.

7.5 CONCLUSIONS

This chapter presented the feasibility study of a micromachined device in which its sidewall electrodes are used to provide the vertical electrostatic levitation force acting on the rotor; and at the same time also control lateral motions of the rotor along the x and y axes. By applying DC voltages to sidewall electrodes, the levitation force along the z direction can be realised. Feedback control voltages (AC signals) are also superimposed on DC bias and provide electrostatic forces to control the motion of the rotor along the in-plane directions, i.e. the x and y axes.

The analysis of such a micromachined device has been investigated using 2D electrostatic finite element simulations in ANSYS. It can be seen that the net vertical levitation force is directly proportional to the square of a bias voltage and inversely dependent on the distance between the rotor and sidewall electrodes. However, the net vertical force remains almost constant with regard to the diameter and thickness of the rotor. Simulations also showed that the magnitude of a vertical electrostatic levitation force strongly depends on the distance between the rotor and sidewall electrodes. If the rotor was placed off-centre, it will result in the imbalance between electrostatic forces acting on each side of the rotor and thus causing the rotor to rotate out of plane (about the x and y axes). This confirms that such a device requires a closed-loop control system to maintain the rotor in the middle position between sidewall electrodes.

The closed-loop control system for the micromachined device considered in this chapter is based on analogue force feedback. The displacement of the rotor due to inertial forces is detected by the imbalance of the sense capacitors. The different capacitance between the sense capacitors is then picked up and converted into voltage by a front-end amplifier. An electronic lead compensator is added to improve the system stability. An electrostatic force is used as a feedback on the rotor to counteract the displacement caused by inertial forces. Simulations conducted in Matlab/Simulink showed that the designed closed-loop system is able to cope with the situation where the rotor is initially located at the off-centre position. The closed-loop system is also stable under applied inertial force.

Initial tests were carried out to measure sidewall sense capacitances and to evaluate electrostatic levitation. The measured capacitances are in the same order of magnitude to the calculated nominal sidewall capacitance. However, the measured values are relatively smaller, which could be because the distance between the rotor and the sidewall electrode is larger than the designed value. The prototype sensor implemented with the designed closed-loop control was also experimentally evaluated. However, the test results at this point are not yet conclusive.

Chapter 8

Conclusions

8.1 SUMMARY

This thesis presented important issues in the development of a micromachined electrostatically suspended gyroscope (ESG). The micromachined ESG employs a rotor, which has no mechanical connection to a substrate, as a proof mass. Instead, the micromachined rotor is suspended using electrostatic levitation. The operating principle of the micromachined ESG differs from that of conventional MEMS gyroscopes, which are based on detection of rotation-induced Coriolis acceleration of a vibrating structure. Hence, many major problems that limit the performance of vibratory MEMS gyroscopes are inherently ruled out. Furthermore, it is possible to design the micromachined ESG which produces higher gyro sensitivity compared with that obtained from vibratory-type gyroscopes (for more details, see chapter 3). The micromachined ESG cannot operate in open loop; it needs a closed-loop control system. The micromachined ESG, considered in this thesis, employs a digital feedback control loop based on a ΣΔM to avoid the electrostatic latch-up problem of an analogue closed-loop control system,

The micromachined ESG consists of a rotor, which is surrounded by sets of sense, feedback and spin control electrodes. The electrodes located above and underneath the rotor are used to detect and control the position of the rotor in three degrees of freedom: the levitation along the z direction and the rotation about the x and y axes. The in-plane motion of the rotor along the x and y axes is controlled by sets of sense and feedback electrodes at the periphery of the rotor. Each of the surrounding electrodes forms a capacitor with the levitated rotor. In the presence of rotation, the spinning rotor will displace away from its nominal position, perpendicular to the spin and input axes. The displacement of the rotor results in a change in capacitances formed between the rotor and upper/lower sense electrodes. The capacitance imbalance is differentially sensed by a closed-loop electrostatic suspension control system. The system, in turn, produces electrostatic feedback forces to counteract the movement of the rotor, and thus nulling it back to the nominal position. These feedback forces associated with the precession torque provide a measure of the rotation rate.

OrCAD/PSPICE and Matlab/Simulink models were developed in order to investigate the stability of the micromachined ESG implemented with the closed-loop system. The simulations revealed that it is feasible to levitate the rotor at the start-up phase using the closed-loop system if the rotor is initially placed on stoppers at the bottom substrate. Both OrCAD/PSPICE and Matlab/Simulink simulation results show a good correspondence with each other. The output bitstreams of the system showed the expected characteristic of a second-order ΣΔM. The full system model was developed in Matlab/Simulink to evaluate the performance of the micromachined ESG with ΣΔM force feedback. The results confirmed that the micromachined ESG can be used to sense multiple inputs (rotation rates and accelerations) simultaneously. Nevertheless, the level of the noise floor increased when three input signals, i.e. rotation rate about the x and y axes and acceleration along the z direction, were applied to the micromachined ESG at the same time.

The micromachined ESG needs to be operated under vacuum condition for two purposes. One reason is to reduce the squeezed-film damping/spring constants. The other is for the sake of rotor spinning speed. As a result, a Brownian noise floor of the sensor is relatively low. Noise analysis in Matlab/Simulink simulations confirmed that the signal-to-noise ratio of the output bitstream of the sensor system was limited by electronic noise sources. Hence, special care must be taken in the design and development of low-noise electronic interface.

The prototype micromachined ESG was implemented using the glass/silicon/glass bonding technology, which combines high-aspect-ratio deep etching with triple-wafer anodic bonding. Glass etching on top and bottom Pyrex substrate was carried out to define a capacitive gap and stoppers. It was followed by metal deposition and wet chemical etching, respectively, in order to pattern the upper and lower electrodes. Then, a thin bare silicon wafer was anodically bonded to a bottom glass substrate. A high-aspect-ratio DRIE process was used to etch silicon in order to form the sidewall electrodes and also release the rotor. Next, the fabricated top glass wafer was anodically bonded to the etched silicon wafer.

Lastly, the triple-wafer stack was sawed into individual chips and a diced chip was wire bonded to a chip carrier. However, the fabrication of the micromachined ESG with the process flow described above was not successful. All of the fabricated sensors suffered from the so-called stiction problem. Unfortunately, such a problem could not be resolved during the course of this research project because the entire Southampton University cleanroom facilities were destroyed by a fire.

Some fabricated prototype, which has not yet bonded to the top substrate, was used to investigate an alternative approach to provide electrostatic levitation using sidewall electrodes. These sidewall electrodes are normally used to provide electrostatic forces in order to suspend the rotor along the x- and y-axis directions and maintain it at the centre of the device cavity. However, by applying a superimposed signal consisting of a DC bias voltage and an AC feedback control signal to the sidewall electrodes, a vertical levitation force in combination with lateral control forces is generated on the rotor. The analysis of this approach was investigated using 2D electrostatic finite element simulations in ANSYS. Simulation results showed that the net vertical levitation force is directly proportional to the square of the bias voltage and inversely dependent on the distance between the rotor and sidewall electrodes. In contrast, the net vertical force remains almost constant with regard to the diameter and thickness of the rotor. ANSYS simulations also revealed that for the case that the rotor was placed off-centre, electrostatic forces acting on each side of the rotor are imbalanced and thus causing the rotor to rotate out of plane. This confirms that electrostatic levitation using sidewall electrodes requires a closed-loop control system in order to maintain the rotor in the middle position between the sidewall electrodes. A relatively high voltage is required to control the vertical levitation. Thus, a closed-loop system based on analogue force feedback is more suitable and it is used for initial tests. System simulations in Matlab/Simulink were carried out and confirmed that the designed closed-loop system is able to cope with the situation where the rotor is initially located at the off-centre position and it is also stable under applied inertial force.

Initial tests of the prototype sensor with no top substrate were carried out to measure sidewall capacitances and to evaluate electrostatic levitation. The sidewall capacitances were measured using the procedure described in chapter 7. It was found that the measured capacitances are in the same order of magnitude to the designed value. However, the measured values are relatively smaller, which could be because the distance between the rotor and the sidewall electrode is larger than the designed value (due to undercut etching during photolithography and DRIE processes). The prototype sensor was also implemented with the designed analogue feedback control. Experimental test was carried out to evaluate electrostatic levitation using sidewall electrodes. However, the test results at this point are not yet conclusive.

8.2 FUTURE WORK

In this section, suggestions for future work are presented with regard to all main aspects in the development of the micromachined ESG, including (1) design and analysis of the sensor, (2) electrostatic suspension control and (3) device fabrication.

8.2.1 Design and analysis of the micromachined ESG

The analysis of the micromachined ESG presented in this thesis assumed that the net charge on the rotor is always zero and the potential of the rotor always remains at zero. However, in reality the levitated rotor may become charged and the potential of the rotor is not always equal to zero. This can result in the adhesion of the rotor to substrate and, as a consequence, the sensor system will become unstable. For macro-scale electrostatically suspended devices [**154, 155**], this problem is resolved by connecting a relatively light-weight gold wire to a levitated proof mass so that its potential can be controlled through the gold wire. However, this is not suitable for the micromachined ESG, which has a relatively small dimension proof mass and the proof mass also rotates. This charging and discharging of the rotor is the remaining topic that needs to be investigated in more details.

8.2.2 Electrostatic suspension control

The results obtained from Matlab/Simulink and OrCAD/PSPICE simulations have confirmed the expected operation and performance of the micromachined ESG with the designed ΣΔM control system; however, this has not yet been tested experimentally. This is due to unavailability of a working sensor prototype. Therefore, it would be interesting to fabricate a dummy sensor, which has the same design and configuration to the micromachined ESG; but has suspended beams (very low spring constant) connecting a rotor to anchors. Such a dummy sensor can then be used to test the operation and functionalities of the electrostatic suspension control system.

8.2.3 Device fabrication

The prototype sensor has not yet been realised yet due to problems mentioned in chapter 6. Therefore, future work should focus on the development of the fabrication process to overcome considerable problems, for instance the so-called stiction problem and a surface damage on the front and back side of the rotor. Some suggestion to the problems is given in section 8.3.

8.2.4 Further work towards the goal of the project

The *short-term* goal of the project is to realise working prototypes of the micromachined ESG. Other than what mentioned above, the following work should also be addressed:

- Electrostatically spinning the levitated rotor needs to be explored.
- A closed-loop system to control a spin speed of the levitated rotor should also be investigated. This will improve scale factor stability in the micromachined ESG.

8.3 SUGGESTIONS ON DEVICE FABRICATION

The most crucial issue in the development of the micromachined ESG is the fabrication of the sensor. One issue is the so-called *RIE lag* that causes damage on the front and back sides of the rotor. This will cause an imbalance between the upper and lower sense and feedback capacitances. The RIE lag issue can be resolved by designing the micromachined ESG in such a way that it has the same opening area. The other approach is by depositing a thin layer of metal, for example platinum, aluminium or chrome/gold, on both front and bottom surfaces of the rotor (see Figure 8.1). This approach requires two additional steps from the original fabrication of the micromachined ESG (for more details, see chapter 6). Before a silicon wafer is bonded to a bottom glass wafer, a metal layer is deposited and patterned on the front and back sides of the silicon wafer. This will also prevent the released rotor to be bonded to the top and bottom glass substrates during the anodic bonding process. In addition, the metal layer on the top and bottom of silicon feedthroughs can be exploited to make an electrical connection between the top electrodes and the bottom bond pads. When the silicon wafer is bonded to the top glass substrate, these metal layers (one on the silicon wafer and the other on the glass substrate) will be pressed together and forms a *press-on* contact.

The fabricated prototype suffers from the so-called *stiction* problem. This problem may come from: (1) electrostatic bonding of the triple-wafer stack, (2) water and debris getting into a device cavity during wafer dicing and (3) remaining thin photoresist on the released rotor (see chapter 6 for more details). During the triple-wafer stack bonding, the released rotor may become charged and thus will be bonded to glass or silicon substrate. This problem could be avoided by using alternative bonding techniques, for example, soldering bonding [**156, 157**], eutectic bonding [**158, 159**] and thermo-compression bonding [**160, 161**]. Figure 8.2 shows the schematic diagram of the triple-wafer stack bonding using a thermo-compression technique. Gold is normally the material of choice in thermo-compression bonding due to its oxidation resistant property. Basically, Chrome/gold layers are patterned on both top glass and silicon wafers and then bonded together by applying appropriated pressure to the wafers at a temperature of 375 or 400 °C.

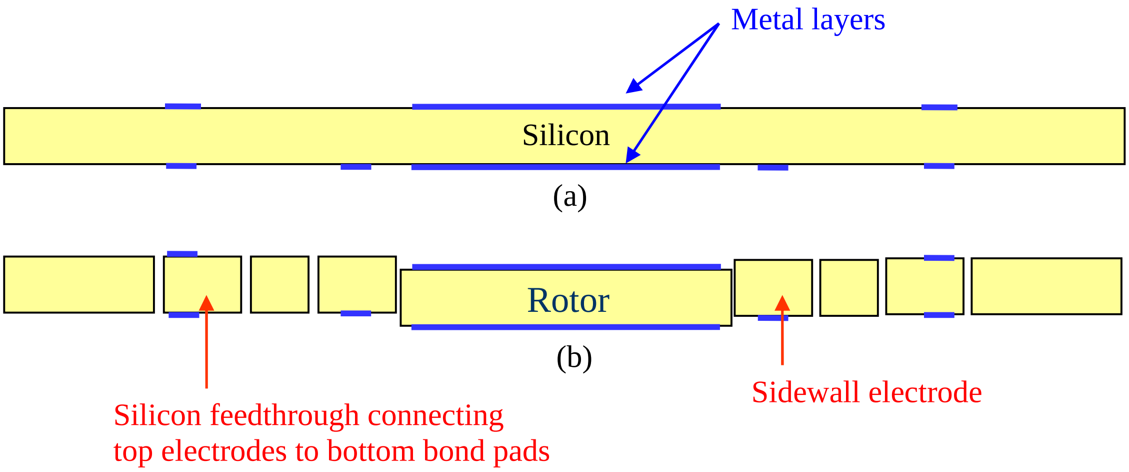

Figure 8.1 Additional steps to the fabrication of the micromachined ESG in order to avoid damage on the front and bottom sides of the rotor. Before a silicon wafer is bonded to a bottom glass wafer, a metal layer is deposited and patterned on the front and back sides of the rotor: (a) prior to etching and (b) after etching.

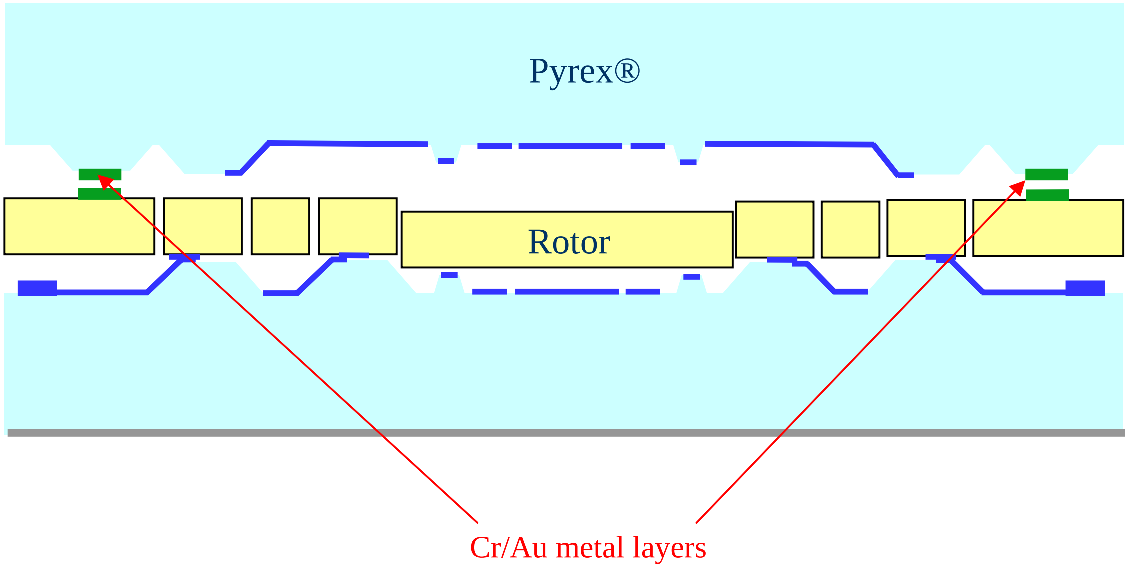

Figure 8.2 Schematic of the triple-wafer stack bonding using a thermo-compression method.

The real bottleneck in the sensor fabrication is that the rotor was completely released in the middle of the fabrication. This not only leads to the rotor stiction problem, but it also makes the wafer cleaning difficult. These issues can be resolved using the sacrificial layer technique that can kept the rotor in its place; and a sacrificial material is then released (a dry release is preferable) at the end of the process flow.

One possible approach is by exploiting the Unity™ polymer as a sacrificial layer. The Unity™ polymer was recently developed by the Promerus to be used together with solid polymer overcoat, Avatel™, for wafer packaging applications [**162, 163**]. It is photo-definable using deep UV exposure (248 nm) and can withstand a high temperature up to 400°C. The Unity™ polymer can then be released by thermal decomposition. The by-products will become volatile gases such as CO_2. Hence, there is no residual remaining in the device cavity.

The proposed process flow for the micromachined ESG based on the Unity™ approach is shown in Figure 8.3. This approach is similar to the fabrication presented in chapter 6. The fabrication process of top and bottom glass wafers remains the same. A thin silicon wafer is replaced by a highly conductive SOI wafer. The SOI wafer is first etched to define a structure, followed by filling Unity™ polymer into the etched trenches. Next, the SOI wafer is bonded to the bottom glass substrate. The thin layer of silicon and buried oxide layer are removed. The top glass wafer is then bonded to the pair of the glass/silicon wafer. The fabricated wafer is diced into small chips and the Unity™ polymer is released at the end of the process.

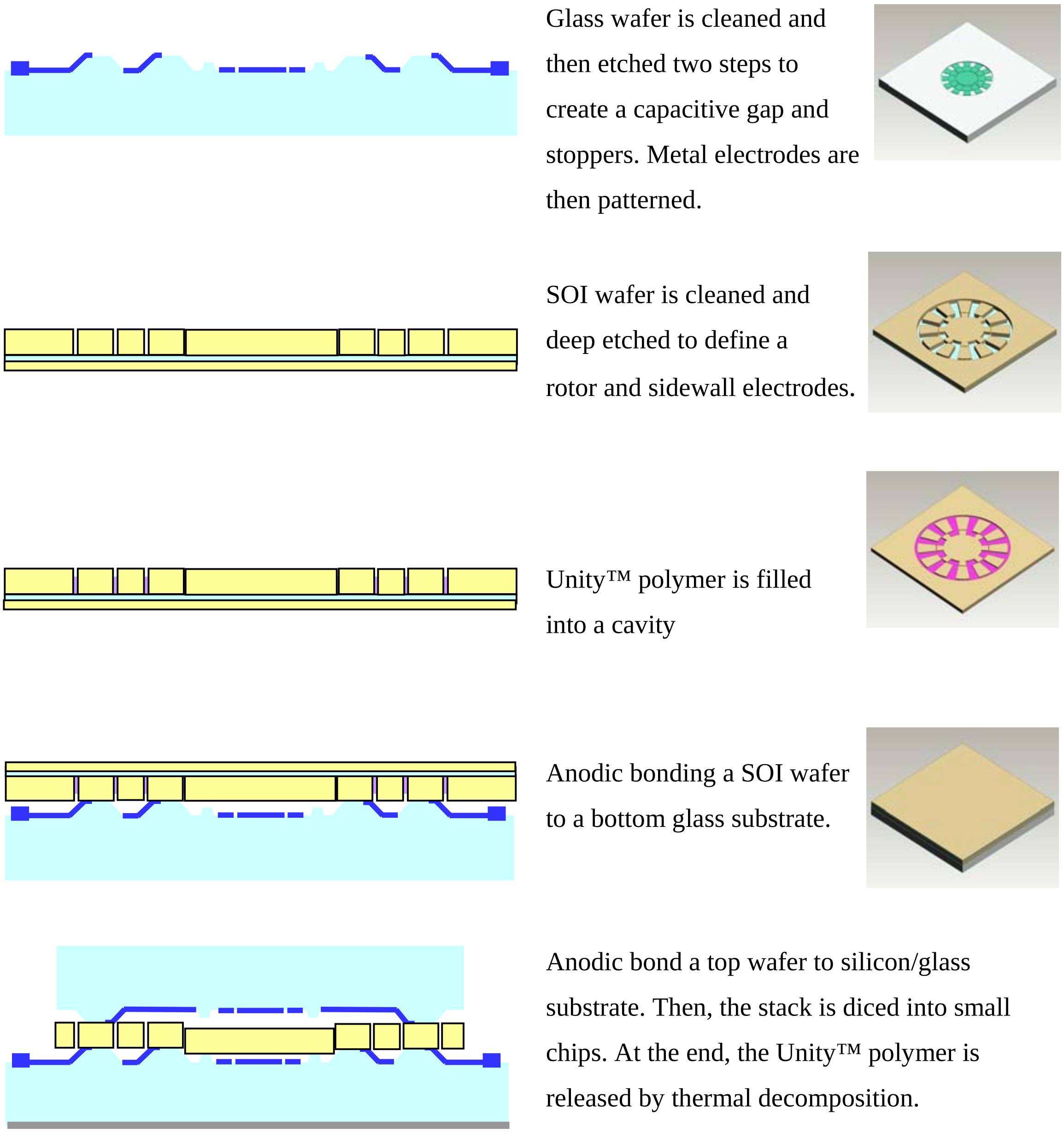

Glass wafer is cleaned and then etched two steps to create a capacitive gap and stoppers. Metal electrodes are then patterned.

SOI wafer is cleaned and deep etched to define a rotor and sidewall electrodes.

Unity™ polymer is filled into a cavity

Anodic bonding a SOI wafer to a bottom glass substrate.

Anodic bond a top wafer to silicon/glass substrate. Then, the stack is diced into small chips. At the end, the Unity™ polymer is released by thermal decomposition.

Figure 8.3 Proposed process flow for the fabrication of the micromachined ESG which utilizes the Unity™ polymer as a sacrificial layer.

Appendix A

ANSYS Parametric Design Language Code

A.1 2D ELECTROSTATIC LEVITATION

A two-dimensional finite element model for calculating electrostatic levitation forces acting on a rotor as it was presented in chapter 3 (Figure 3.26).

```
finish
/clear
/title, 2D electrostatic analysis of a levitated rotor
/prep7

!solid modelling
!================

W = 200
Hd = 20
gap = 5
We = (W-Hd)/2
He = 4
z = 0

Wair = W + (W/4)
Hair = 4*Hd

blc5,0,z,W,Hd,,                                  ! Levitated rotor
blc5,(We/2)+(Hd/4),(Hd/2)+gap+(He/2),We,He,,   ! Top electrodes
blc5,-(We/2)-(Hd/4),(Hd/2)+gap+(He/2),We,He,,
blc5,(We/2)+(Hd/4),-(Hd/2)-gap-(He/2),We,He,,  ! Bottom electrodes
blc5,-(We/2)-(Hd/4),-(Hd/2)-gap-(He/2),We,He,,
blc5,0,0,W+20,Hd+(2*gap),,
blc5,0,0,Wair,Hair,,                             ! Air boundary

aovlap,all
numcmp,area


!material attribute
!==================

et,1,plane121

emunit,epzro,8.854e-6
mp,rsvx,1,0
mp,perx,1,11.7
mp,perx,2,1
asel,s,area,,1                                   ! area 1 = silicon rotor
aatt,1,1,1
asel,s,area,,6,7,1                               ! air
```

```
aatt,2,1,1
allsel

!meshing
!=======

mshape,1
esize,gap/3
amesh,6
esize,3*gap
amesh,7
esize,2*gap
amesh,1
allsel


!loading
!=======

V = 10
GND = 0

asel,s,area,,1
lsel,s,ext
nsll,s,1
cm,cond1,node

asel,s,area,,2
lsel,s,ext
nsll,s,1
cm,cond2,node
d,all,volt,V

asel,s,area,,3
lsel,s,ext
nsll,s,1
cm,cond3,node
d,all,volt,V

asel,s,area,,4
lsel,s,ext
nsll,s,1
cm,cond4,node
!d,all,volt,GND
d,all,volt,-V

asel,s,area,,5
lsel,s,ext
nsll,s,1
cm,cond5,node
!d,all,volt,GND
d,all,volt,-V
allsel

finish

/solu
eqslv,iccg
solve

finish

/post1
set,last
cmsel,s,cond1
emft
```

A.2 3D ELECTROSTATIC ANALYSIS OF THE AXIAL–DRIVE LEVITATED ROTOR

A three-dimensional model for calculating a capacitance forming between the rotor and the upper/lower electrodes as a function of the angular position of the rotor (presented in chapter 3).

```
finish
/clear
/title, 3D electrostatic axial-drive levitated rotor model
/prep7


Ro = 1500                              ! rotor structure
Ri = 1200
Rm = Ro-0
h  = 50                                ! thickness of rotor/stator
Rso = Ro-100
gap = 5
Rb = Ro + 15*gap                       ! air boundary radius
rt = 0                                 ! rotor angle
rotor_theta = rt                       ! rotor angle

*IF,rotor_theta,GT,9,THEN
   rotor_theta = rotor_theta - 45
*ENDIF

theta1 = 18                            ! rotor pole's angle
theta2 = 45 - theta1                   ! space between each rotor pole
theta3 = 18                            ! stator pole's angle
theta4 = 30 - theta3                   ! space between each stator pole
thetaRA = 9 + rotor_theta              ! initial state
thetaRB = 0
thetaSA = 6
thetaSB = 0

md = 90

! Rotor model
!============

cyl4,0,0,Ro,0,0,md,,

*DO,I,1,8
   thetaRB = thetaRA + theta2

   *IF,thetaRB,GE,md,THEN
      thetaRB = md
   *ENDIF
   cyl4,0,0,Rm,thetaRA,Ri,thetaRB,,
   thetaRA = thetaRB + theta1
   asba,1,2
   numcmp,area

   *IF,thetaRA,GE,md,THEN
      *EXIT
   *ENDIF
*ENDDO
vext,all,,,,,h+2*gap
numcmp,volume
```

```
! Air boundary domain
!===================

cylind,Rb,0,0,h+(2*gap),0,md
cylind,Ro,0,0,h+(2*gap),0,md
cylind,Rb,0,h+gap,h+(2*gap),0,md
cylind,Rb,0,0,gap,0,md
vovlap,all
numcmp,volume
vglue,all

! Top/Bottom electrodes
!=====================

thetaSA = 6
thetaSB = 0

*DO,I,1,3
   thetaSB = thetaSA + theta3
   cylind,Ri,Rso,(h+(2*gap))+1,(h+(2*gap))+2,thetaSA,thetaSB
   thetaSA = thetaSB + theta4
*ENDDO

thetaSA = 6
thetaSB = 0

*DO,I,1,3
   thetaSB = thetaSA + theta3
   cylind,Ri,Rso,-1,-2,thetaSA,thetaSB
   thetaSA = thetaSB + theta4
*ENDDO

/color,volume,4,13,18,1
/color,volume,14,1,11,1
/trlcy,volume,1,1,11,1
/trlcy,volume,0.5,13,18,1


! Meshing
!========

et,1,solid122                        ! 3D 10-node electrostatic solid
et,5,mesh200,7                       ! Unsolved element type


!Define physical parameters
!=========================

emunit,epzro,8.854e-6                ! Free space permittivity (uMKSV units)
mp,perx,1,1                          ! air permittivity
mp,perx,2,11.5                       ! silicon permittivity
vsel,s,volume,,12
vatt,2,1,1
vsel,s,volume,,1,11,1
vatt,1,1,1
allsel


type,5
mshape,1
esize,5*gap
amesh,52
amesh,46
amesh,2
amesh,72
```

```
type,1
esize,,3
vsweep,4,52,57
vsweep,3,46,51
vsweep,11,2,93
vsweep,7,72,73
allsel
esize,,4
vsweep,6,57,39
vsweep,5,51,45
vsweep,12,93,90
vsweep,9,73,81
allsel
esize,,3
vsweep,1,39,34
vsweep,2,45,40
vsweep,10,90,1
vsweep,8,81,80
allsel
vclear,12
allsel


!Loading
!=======

V1 = 10                                 ! define driving potential on stator
V0 = 0                                  ! define ground potential on rotor
csys,1

!Define load to rotor node
!=========================

vsel,s,volume,,12
asel,s,ext
nsla,s,1
cm,cond1,node
d,all,volt,V0
sf,all,mxwf
allsel

!Define load to stator nodes
!===========================

theta3 = 18                            ! stator pole's angle (normally = of rotor)
theta4 = 30 - theta3                    ! space between each stator pole

thetaSA = 6
thetaSB = thetaSA + theta3

! Phase A - TOP

nsel,s,loc,x,Ri,Rso
nsel,r,loc,y,thetaSA,thetaSB
nsel,r,loc,z,h+(2*gap)
cm,cond2,node
d,all,volt,V0

! Phase A - BOTTOM

nsel,s,loc,x,Ri,Rso
nsel,r,loc,y,thetaSA,thetaSB
nsel,r,loc,z,0
cm,cond3,node
d,all,volt,V0
```

```
thetaSA = thetaSB + theta4
thetaSB = thetaSA + theta3

! Phase B - TOP

nsel,s,loc,x,Ri,Rso
nsel,r,loc,y,thetaSA,thetaSB
nsel,r,loc,z,h+(2*gap)
cm,cond4,node
d,all,volt,V1

! Phase B - BOTTOM

nsel,s,loc,x,Ri,Rso
nsel,r,loc,y,thetaSA,thetaSB
nsel,r,loc,z,0
cm,cond5,node
d,all,volt,V0
thetaSA = thetaSB + theta4
thetaSB = thetaSA + theta3

! Phase C - TOP

nsel,s,loc,x,Ri,Rso
nsel,r,loc,y,thetaSA,thetaSB
nsel,r,loc,z,h+(2*gap)
cm,cond6,node
d,all,volt,V0

! Phase C - BOTTOM

nsel,s,loc,x,Ri,Rso
nsel,r,loc,y,thetaSA,thetaSB
nsel,r,loc,z,0
cm,cond7,node
d,all,volt,V0

allsel
finish


/solu
solve
!cmatrix,1,'cond',7,1
finish

/post1

set,first
etable,sene,sene
etable,efx,ef,x
etable,efy,ef,y

/number,1

plnsol,volt
plvect,efx,efy
ssum
*GET,W,ssum,,item,sene
C = (W*2)/((V1-V0)**2)
*STATUS,C
```

A.3 2D ANALYSIS OF ELECTROSTATIC LEVITATION USING SIDEWALL ELECTRODES

A two-dimensional finite element model for calculating a resulting electrostatic force acting on a rotor as a function of various parameters as presented in chapter 7.

```
finish
/clear
/title, 2D electrostatic force analysis of a side-drive levitated rotor
/prep7


!solid modelling
!================

xo = 10
yo = 3
z = 4.5
Wsub = 300
Hsub = 60
Wd = 400
Hd = 20
We = 20
He = Hd+yo
Wair = Wd+(2*xo)+(2*We)
Hair = Hsub
blc5,0,Hd/2+z,Wd,Hd,,                              ! rotor
blc5,-(Wd/2)-(We/2)-xo,He/2,We,He,,                ! left side electrode
blc5,(Wd/2)+(We/2)+xo,He/2,We,He,,                 ! right side electrode
blc5,0,Hair/2,Wair,Hair,,                          ! Air boundary
aovlap,all
numcmp,area


!material attribute
!==================

et,1,plane121

emunit,epzro,8.854e-6
mp,perx,1,11.7                                     ! silicon
mp,perx,2,1                                        ! air
asel,s,area,,1,3,1                                 ! silicon
aatt,1,1,1
asel,s,area,,4                                     ! air
aatt,2,1,1
allsel

!meshing
!=======

mshape,1

esize,0.5
amesh,4
allsel


!loading
!=======
```

```
V = 100
GND = 0

asel,s,area,,1
lsel,s,ext
nsll,s,1
cm,rotor,node
d,all,volt,GND

asel,s,area,,2
lsel,s,ext
nsll,s,1
cm,Lelectrode,node
d,all,volt,V

asel,s,area,,3
lsel,s,ext
nsll,s,1
cm,Relectrode,node
d,all,volt,-V

asel,s,area,,4
lsel,s,ext
nsll,s,1
cm,air,node
allsel

finish

/solu
eqslv,iccg
solve

finish

/post1
set,last
cmsel,s,rotor
emft
```

Appendix B

Fabrication Process Flow for Micromachined ESGs

STEP	PROCESS	DESCRIPTION	COMMENTS
1	Materials	*International Wafer Service* Si Wafers, 100mm diameter, <100>±0.5°, N-type, Double Sides Polished (DSP) 0.001 – 0.005Ω cm, Thickness 200μm±5 0.005 – 0.020Ω cm, Thickness 150μm±5 0.005 – 0.020Ω cm, Thickness 75μm±5 *Sensor Prep Services, Inc.* 7740 Pyrex Wafers, 100mm±0.5, DSP, Thickness 0.50mm±0.05, Surface Finish: SI 4–8A°	
		PYREX WAFERS	
2	Piranha clean	H_2SO_4:H_2O_2 3:1 mixture: 15min Spin, rinse and dry (SRD)	
3.1	Evaporate	Cr/Au: 200A°/3000A°	
3.2	Photolithography Mask 1: ***FB*** and ***FT*** (front side)	Dehydration: 15min @140°C in an oven Vapour HMDS or HMDS: 30sec @4krpm S1813: spread 4sec @500rpm, spin 30sec @4krpm Soft bake: 60sec @115°C on a hotplate Expose: MA6 20mW/cm2 4.5sec Hard contact Develop: MIF 319 or Microprofit 351 60sec+10sec SRD Hard bake : 15min @115°C in an oven	***FB***: for bottom glass wafers ***FT***: for top glass wafers Measure the thickness of S1813
3.3	Wet etch Cr/Au	Etch Au: KI-based etchant 1min or ‘til clear Etch Cr: CR-14 etchant 15sec or ‘til clear SRD	Measure the thickness of Cr/Au layer
3.4	Backside protection	S1813: spread 4sec @500rpm, spin 30sec @4krpm Hard bake : 10min @115°C in an oven	Not necessary
4	Etch glass 1.3μm	J.T Baker 7:1 BOE with surfactant or Transene BHF improved or H_2O:HNO_3:HF 10:3:7 mixture SRD Inspect etch depth using step profilometer	
5	Strip photoresist (PR)	Hot PRS-2000: 20min or	Acetone/IPA can be used to

STEP	PROCESS	DESCRIPTION	COMMENTS
		Piranha clean: 15min SRD Inspect etch depth (no PR)	strip PR; but not as good as PRS-2000 and Piranha clean
6	Piranha clean	H_2SO_4:H_2O_2 3:1 mixture: 15min SRD	
7.1	Evaporate	Cr/Au: 200A°/3000A°	
7.2	Photolithography Mask 2: ***SB*** and ***ST*** (front side)	Dehydration: 15min @140°C in an oven Vapour HMDS or HMDS: 30sec @4krpm S1827: spread 4sec @500rpm, spin 30sec @4krpm Soft bake: 60sec @115°C on a hotplate Expose: MA6 20mW/cm2 14sec Hard contact Develop: MIF 319 or Microprofit 351 60sec+10sec SRD Hard bake : 15min @115°C in an oven	***SB***: for bottom glass wafers ***ST***: for top glass wafers Measure the thickness of S1813
7.3	Wet etch Cr/Au	Etch Au: KI-based etchant 1min or 'til clear Etch Cr: CR-14 etchant 15sec or 'til clear SRD	Measure the thickness of Cr/Au layer
7.4	Backside protection	S1813: spread 4sec @500rpm, spin 30sec @4krpm Hard bake : 10min @115°C in an oven	Not necessary
8	Etch glass 2µm	J.T Baker 7:1 BOE with surfactant or Transene BHF improved or H_2O:HNO_3:HF 10:3:7 mixture SRD Inspect etch depth using step profilometer	
9	Strip PR	Hot PRS-2000: 20min or Piranha clean: 15min SRD Inspect etch depth (no PR)	Acetone/IPA can be used to strip PR; but not as good as PRS-2000 and Piranha clean
10	Piranha clean	H_2SO_4:H_2O_2 3:1 mixture: 15min SRD	
11	Photolithography Mask 3: ***MB*** and ***MT*** (front side)	Dehydration: 5min @115°C Vapour HMDS SPR220-3: spread 4sec @500rpm, spin 30sec @3krpm Soft bake: 60sec @95°C Expose: MA6 20mW/cm2 15sec Hard contact Develop: MIF 300 30sec+60sec SRD Optical inspection	***MB***: for bottom glass wafers ***MT***: for top glass wafers Spin on SPR220-3 was done using Suss ACS2000: ***recipe SPR220-3 5µm***
12	Evaporate	Cr/Pt/Au: 200A°/500A°/2500A°	
13	Metal liftoff	Hot 1112A: 20min 1112A + Ultrasonic tank: 5min DI Rinse Acetone + IPA + DI Rinse	

<table>
<tr><th>STEP</th><th>PROCESS</th><th>DESCRIPTION</th><th>COMMENTS</th></tr>
<tr><td></td><td></td><td>SRD
Optical inspection</td><td></td></tr>
<tr><td colspan="4"><i><u>BOTTOM PYREX + SILICON</u></i></td></tr>
<tr><td>14</td><td>Wafer preparation</td><td>Piranha clean: 15min (Si wafers only)
Acetone + Ultrasonic tank: 10min
IPA:10min
DI Rinse
SRD</td><td></td></tr>
<tr><td>15</td><td>Anodic bonding</td><td><i>Recipe :</i>
Top/Bottom temperature : 385°C
Chamber pressure : 1×10^{-4} Torr
Contact force : ~370 N
Voltage: 1min @-250V
1min @-500V
1min @-650V
@-800V ‘til current drops to 10% of I_{max}
3min @-800V
Cool down: 100°C

Optical inspection</td><td><i>EVG501</i> or <i>Suss SB6e</i></td></tr>
<tr><td>16</td><td>Solvent clean</td><td>Acetone + IPA + DI Rinse
SRD</td><td></td></tr>
<tr><td>17.1</td><td>Front side protection</td><td>S1813: spread 4sec @500rpm, spin 30sec @4krpm</td><td></td></tr>
<tr><td>17.2</td><td>Sputter (back side)</td><td>Al or Cr: 2000-5000A°</td><td></td></tr>
<tr><td>18</td><td>Photolithography
Mask 4: <i>DE</i> (front side)</td><td>Dehydration: 15min @115°C
Vapour HMDS or HMDS: 30sec @4krpm
AZ9260: spread 6sec @300rpm, spin 30sec @2krpm
Soft bake: 60sec @90°C on hotplate
Expose: MA6 20mW/cm2 50sec Hard contact
Develop: AZ400k:DI 1:3 30sec+90sec
SRD
Optical inspection</td><td>Backside alignment</td></tr>
<tr><td>19.1</td><td>Attach a handle wafer</td><td>Mix cool grease with IPA
Put a handle wafer on a hotplate, temp = 115°C
Pour cool grease onto a handle wafer
Wait ‘til it looks dried (no IPA left)
Adhere the device wafer to the handle wafer</td><td><i>AIT Technology, INC.</i>
Cool grease 7016, good thermal and electrical conductive</td></tr>
<tr><td>19.2</td><td>DRIE (STS™)</td><td>Target depth: Thru wafer 200µm
UMICH Recipe: PCC-HR
<i>Recipe :</i>
<table>
<tr><th></th><th>Etch</th><th>Passivation</th></tr>
<tr><td>C_4F_8</td><td>-</td><td>85 sccm</td></tr>
<tr><td>SF_6</td><td>130 sccm</td><td>-</td></tr>
<tr><td>O_2</td><td>13 sccm</td><td>-</td></tr>
<tr><td>Coil Power</td><td>800 W</td><td>600 W</td></tr>
<tr><td>Platen Power</td><td>10 W</td><td>-</td></tr>
<tr><td>Time</td><td>12 sec</td><td>7 sec</td></tr>
</table></td><td><i>STS Multiplex ICP ASE System</i>

<i>Inspection:</i>
Optical microscope</td></tr>
</table>

STEP	PROCESS	DESCRIPTION	COMMENTS
		* Passivation step first, then Etch step * APC set to manual 65% - 0.2%/min	ZYGO™ Interferometer SEM
19.3	Remove a handle wafer	Glass wafer might be required to cover the front side Detach the device wafer using a razor blade Clean the back side using IPA + CleanWIPE™	
20	Strip PR	O_2 plasma asher (preferred) or Solvent clean	
PYREX/SILICON + TOP PYREX			
21	Wafer preparation	Acetone + Ultrasonic tank: 10min IPA:10min DI Rinse SRD	Only for top Pyrex wafers
22	Anodic bonding	***Recipe :*** Top/Bottom temperature : 350°C Chamber pressure : 1×10^{-4} Torr Contact force : ~370 N Voltage: 1min @250V 1min @500V 1min @650V @700V 'til current drops to 10% of I_{max} 3min @700V Cool down: 100°C Optical inspection	***Suss SB6e***
23	Dicing	Glass blade 777, 250 microns thick @8.5krpm	
24	Wire bonding	Au wire bonding	

References

[1] J. Soderkvist, “Micromachined gyroscopes,” *Sensors and Actuators A*, volume 43, pp. 65–71, 1994.

[2] N. Yazdi, F. Ayazi and K. Najafi, “Micromachined inertial sensors,” *Proceedings of IEEE*, volume 86, pp. 1640–1659, 1998.

[3] A.M. Shkel, “Micromachined gyroscopes: Challenges, design solutions, and opportunities,” in Proc. of SPIE: Smart Electronics and MEMS, volume 4334, pp. 74–85, 2001.

[4] H. Xie and G.K. Fedder, “Integrated microelectromechanical gyroscopes,” *Journal of Aerospace Engineering*, volume 16, pp. 65–75, 2003.

[5] M.S. Weinberg and A. Kourepenis, “Error sources in in-plane silicon tuning-fork MEMS gyroscopes,” *Journal of Microelectromechanical Systems*, volume 15, pp. 479–491, 2006.

[6] T. George, “Overview of MEMS/NEMS technology development for space applications at NASA/JPL,” in Proc. of SPIE: smart sensors, actuators and MEMS, volume 5116, pp. 136–148, 2003.

[7] S.Y. Bae, K.J. Hayworth, K.Y. Yee, K. Shcheglov and D.V. Wiberg, “High performance MEMS micro-gyroscope,” in Proc. of SPIE: design, test, integration and packaging of MEMS/MOEMS, volume 4755, pp. 316–324, 2002.

[8] R.C. Langford, “Unconventional inertial sensors,” in AIAA second annual meeting, pp. 1–66, San Francisco, CA, USA, July 1965.

[9] S. Bennett, “Modern Gyroscopes,” in AIAA Guidance, Navigation and Control Conference and Exhibit, pp. 1–20, Montreal, Canada, August 2001.

[10] Marshall Space Flight Center Fact Sheets, “Gravity Probe B: Testing Einstein’s universe,” NASA Technical Report, Pub 8-40360, April 2005, available at: http://www.nasa.gov/centers/marshall/pdf/114043main_gpb_fs.pdf.

[11] M. Kraft, M.M. Farooqui and A.G.R. Evans, “Modelling and design of an electrostatically levitated disk,” *Journal of Micromechanics and Microengineerings*, volume 11, pp. 423–427, 2001.

[12] R. Houlihan, A. Kukharenka, H. Sehr and M. Kraft, “Optimisation, design and fabrication of a novel accelerometer,” in IEEE Int. Conf. on Solid-State Sensors, Actuators and Microsystems (Transducers’03), Boston, USA, June 2003.

[13] B. Damrongsak and M. Kraft, **“**A micromachined electrostatically suspended gyroscope with digital for feedback,” in Proc. IEEE Sensors, pp. 401-404, Irvine, CA, USA, October 2005.

[14] B. Damrongsak, M. Kraft, S. Rajgopal and M. Mehregany, “Design and fabrication of a micromachined electrostatically suspended gyroscope,” *Proc. IMechE Part C: Journal of Mechanical Engineering Science.*, vol. 222, no. 1, pp. 53–63, 2008.

[15] W.Q. Yang, “Electrostatic suspension system for gyroscopes with minimum electrical disturbing torque via non-linear pre-compensation,” *Proc. IMechE Proc. Instn. Mech. Engineers*, vol. 210, pp. 123–127, 1996.

[16] K. Fukatsu, T. Murakoshi and M. Esashi, “Electrostatically levitated inertia measurement system,” in Tech. Digest of the 18th Sensors Symp., pp. 285–288, Tokyo, Japan, 2001.

[17] T. Murakoshi, Y. Endo, K. Fukatsu, S. Nakamura and M. Esashi, “Electrostatically levitated ring-shaped rotational-gyro/accelerometer”, *Jpn. J. Appl. Phys.*, volume 42, no. 4B, pp. 2468–2472, 2003.

[18] M. Kraft, “Closed loop digital accelerometer employing oversampling conversion,” PhD thesis, Coventry University, Coventry, U.K., 1997.

[19] B. Damrongsak and M. Kraft, “Electrostatic suspension control for micromachined inertial sensors employing a levitated-disk proof mass,” in Proc. MME 2005 Conference, pp. 240-243, Sweden, September 2005.

[20] B. Damrongsak and M. Kraft, **“**Design and simulation of a micromachined electrostatically suspended gyroscope,” in Proc. IET Seminar on MEMS Sensors and Actuators, pp. 267-272, London, UK, May 2006.

[21] B. Damrongsak and M. Kraft, “Performance Analysis of a Micromachined Electrostatically Suspended Gyroscope employing a Sigma-Delta Force Feedback,” in Proc. of MME 2007 Conference, pp. 269–272, Portugal, September 2007.

[22] Yole development, **MEMS gyro markets**, report from Yole Developpement, April 2006.

[23] ADXRS613 yaw rate gyroscope datasheet, available at: http://www.analog.com/

[24] M. Lutz, W. Golderer, J. Gerstenmeier, J. Marek, B. Maihofer, S. Mahler, H. Munzel, and U. Bischof, “A precision yaw rate sensor in silicon micromachining,” in Tech. Dig. 9th Int. Conf. Solid-State Sensors and Actuators (Transducers’97), Chicago, IL, June 1997, pp. 847–850.

[25] B.L. Lee, S.W. Lee, K.D. Jung, J.H. Choi, T.R. Chung and Y.C. Cho, “A de-coupled vibratory gyroscope using a mixed micro-machining technology,” in Proc. of IEEE Int. Conf. on Robotics and Automation, pp. 3412–3416, Seoul, Korean, May 2001.

[26] J. Bernstein, S. Cho, A.T. King, A. Kourepenis, P. Maciel and M. Weinberg, “A micromachined comb-drive tuning fork rate gyroscope,” in Proc. of IEEE Micro Electro Mechanical Systems (MEMS’93), pp. 143–148, Florida, USA, February 1993.

[27] M. Weinberg, J. Bernstein, S. Cho, A. T. King, A. Kourepenis, P. Ward and J. Sohn, “A micromachined comb-drive tuning fork gyroscope for commercial applications,” in Proc. Sensor Expo, Cleveland, OH, 1994, pp. 187–193.

[28] A.M. Madni, L.E. Costlow and S.J. Knowles, “Common design techniques for BEI gyro chip quartz rate sensors for both automotive and aerospace/defense markets,” *Journal of IEEE Sensors*, Vol. 3, pp.569–578, 2003.

[29] W.J. Bencze, Y. Xiao, D.N. Hipkins, G.F. Franklin and B.W. Parkinson, “Gyroscope spin axis direction control for the Gravity Probe B satellite,” in Proc. of the 35th IEEE Decision and Control, pp. 480–485, Kobe, Japan, 1996.

[30] C. Acar, “Robust micromachined vibratory gyroscopes,” PhD dissertation, University of California, Irvine, California, USA, 2004.

[31] T.B. Gabrielson, “Mechanical-thermal noise in micromachined acoustic and vibration sensors,” *IEEE Trans. on Electron Devices*, volume 40, pp. 903–909, 1993.

[32] J. Soderkvist, “Design of a solid-state gyroscopic sensor made of quartz,” *Sensors and Actuators A*, volume A21/A23, pp. 293–296, 1990.

[33] M. Hashimoto, C. Cabuz, K. Minami, and M. Esashi, “Silicon resonant angular rate sensor using electromagnetic excitation and capacitive detection,” *Journal of Micromechanics and Microengineerings*, pp. 219–225, 1995.

[34] F. Paoletti, M. A. Gretillat, and N. F. de Rooij, “A silicon micromachined vibrating gyroscope with piezoresistive detection and electromagnetic excitation,” in Proc. IEEE Micro Electro Mechanical Systems Workshop (MEMS’96), San Diego, CA, 1996, pp. 162–167.

[35] W. A. Clark, R. T. Howe and R. Horowitz, “Surface micromachined -axis vibratory rate gyroscope,” in Tech. Dig. Solid-State Sensor and Actuator Workshop, Hilton Head Island, SC, June 1996, pp. 283–287.

[36] S. An, Y. S. Oh, B. L. Lee, K. Y. Park, S. J. Kang, S. O. Choi, Y. I. Go and C. M. Song, “Dual-axis microgyroscope with closed-loop detection,” in Proc. IEEE Micro Electro Mechanical Systems Workshop (MEMS’98), Heidelberg, Germany, Feb. 1998, pp. 328–333.

[37] W. Geiger, B. Folkmer, J. Merz, H. Sandmaier, and W. Lang, “A new silicon rate gyroscope,” in Proc. IEEE Micro Electro Mechanical Systems Workshop (MEMS’98), Heidelberg, Germany, Feb. 1998, pp. 615–620.

[38] F. Ayazi and K. Najafi, “A HARPSS polysilicon vibrating ring gyroscope,” *Journal of Microelectromechanical Systems*, volume 10, pp. 169–179, 2001.

[39] M.F. Zaman, A. Sharma and F. Ayazi, “High performance matched–mode tuning fork gyroscope,” in Tech. Dig 19th IEEE International Conference on Micro-Electormechanical Systems Conference 2006 (MEMS 2006), Istanbul, Turkey, Jan. 2006, pp. 66-69.

[40] M. Putty and K. Najafi, “A micromachined vibrating ring gyroscope,” in Solid State Sensor and Actuator Workshop, pp 213–220, Hilton Head Island, SC, USA, 1994.

[41] M. Niu, W. Xue, X. Wang, J. Xie, G. Yang and W. Wang, “Design and characteristics of two-gimbals micro-groscopes fabricated with quasi-LIGA process,” in Tech. Dig. 9th Int. Conf. Solid-State Sensors and Actuators (Transducers’97), Chicago, IL, June 1997, pp. 891–894.

[42] H. Xie and G.K. Fedder, “Fabrication, characterization and analysis of a DRIE CMOS–MEMS gyroscope,” *Journal of IEEE Sensors*, volume 3, pp. 622–631, 2003.

[43] A. Trusov, C. Acar and A.M. Shkel, “Comparative analysis of distributed mass micromachined gyroscopes fabricated in SCS-SOI and EFAB,” in Proc. of SPIE 6174, 61742A, Smart Structures and Materials 2006, San Diego, CA, USA

[44] C. Song, B. Ha and S. Lee, “Micromachined inertial sensors,” in Proc. of IEEE/RSJ Int. Conf. on Intelligent Robots and Systems, pp. 1049–1056, 1999.

[45] M. Kraft, “Micromachined inertial sensors: The state-of-the-art and a look into the future,” *Measurement and Control*, volume 33, pp. 164–168, 2000.

[46] P. Ward, “Electronics for Coriolis force and other sensors,” U.S. Patent 5481914, Jan. 9, 1996.

[47] S. Park and R. Horowitz, “Adaptive control for the conventional mode of operation of MEMS gyroscopes,” *J. of Microelectromechanical Systems*, volume 12, pp. 101-108, 2003.

[48] M.S. Weinberg, K. Kumar and A.T. King, “Dynamically balanced micromechanical devices,” U.S. Patent 6571630 B1, June 3, 2003.

[49] M. Braxmaier, A. Gaiber, A. Schumacher, I. Simon, J. Frech, H. Sandmaier and W. Lang, “Cross-coupling of the oscillation modes of vibratory gyroscopes,” in Proc. of International Conference on Solid State Sensors, Actuators, and Microsystems (Transducers’ 03), pp. 167–170, Boston, USA, June 2003.

[50] S.E. Alper and T. Akin, “A symmetric surface micromachined gyroscope with decoupled oscillation modes,” *Sensors and Actuators A*, volume 97-98C, pp. 337-348, 2002.

[51] S. E. Alper and T. Akin , “A symmetrical and decoupled nickel microgyroscope on insulating substrate,” *Sensors and Actuators A* , volume 115/2-3, pp. 336-350, 2004.

[52] S. E. Alper and T. Akin , “A Single-Crystal Silicon Symmetrical and Decoupled MEMS Gyroscope on an Insulating Substrate,” *Journal of Microelectromechanical Systems* , Vol. 14, No. 4, pp. 707-717, August 2005.

[53] S. E. Alper, K. Azgin and T. Akin, “A high-performance silicon-on-insulator MEMS gyroscope operating at atmospheric pressure,” *Sensors and Actuators A*, volume 135/1, pp. 34-42, 2007.

[54] W. Geiger, J. Merz, T. Fischer, B. Folkmer, H. Sandmainer and W. Lang, “The silicon angular rate sensor system DAVED®,” *Sensors and Actuators A*, volume 84, pp. 280-284, 2000.

[55] W. Geiger, W.U. Butt, A. Gaiber, J. Frech, M. Braxmaier, T. Link, A. Kohne, P. Nommensen, H. Sandmaier, W. Lang and H. Sandmaier, “Decoupled microgyros and the design principle DAVED,” *Sensors and Actuators A*, volume 95, pp. 239-249, 2002.

[56] C.C. Painter and A.M. Shkel, “Active structural error suppression in MEMS rate integrating gyroscopes,” *Journal of IEEE Sensors*, Vol. 3, Number 5, pp. 595-606, October 2003

[57] C.C.Painter and A.M. Shkel, “Structural and thermal modeling of a z-axis rate integrating gyroscope" *Journal of Micromechanics and Microengineering*, Institute of Physics Publishing, Vol. 13, pp.229-237, 2003

[58] C. Acar and A.M. Shkel, “Non-resonant micromachined gyroscopes with structural mode-decoupling,” *Journal of IEEE Sensors*, Vol. 3, No. 4, pp. 497-506.

[59] C. Acar and A.M. Shkel, “Structural design and experimental characterization of torsional micromachined gyroscopes with non-resonant drive-mode,” *Journal of Micromechanics and Microengineering*, Vol. 14, January 2004, pp. 15-25

[60] C. Acar and A.M. Shkel, “An approach for increasing drive-mode bandwidth of MEMS vibratory gyroscopes,” *Journal of Microelectromechanical Systems*, Vol. 14, No. 3, pp. 520-528, 2005

[61] A.R. Schofield, A.A. Trusov, C. Acar and A.M. Shkel, “Anti-phase driven rate gyroscope with multi-degree of freedom sense mode," in International Conference on Solid-State Sensors, Actuators and Microsystems (TRANSDUCERS '07), pp. 1199-1202, Lyon, France, June 10-14, 2007

[62] L. Oropeza-Ramos, C.B. Burgner, C. Olroyd, and K. Turner, “Inherently robust micro gyroscope actuated by parametric resonance”, in IEEE International Conference on Micro Electro Mechanical Systems (MEMS’08), Tucson, AZ, Jan 2008.

[63] K.E. Petersen, N. Maluf, W. McCulley, J. Logan, E. Klaasen and J.M. Noworolski, “Single crystal silicon sensor with high aspect ratio and curvilinear structures,” U.S. Patent 6084257, 1995

[64] F. Laermer and A. Schilp, “Method of anisotropically etching silicon,” U.S. Patent 5501893, 1996.

[65] M.F. Zaman, A. Sharma, B.V. Amini and F. Ayazi, “Towards inertial grade vibratory microgyros: A high-Q in-plane silicon-on-insulator tuning fork device,” in Tech. Dig. Solid-State Sensors, Actuators, and Microsystems Workshop, Hilton Head, SC, June 2004, pp. 384-385.

[66] A. Sharma, M.F. Zaman, B.V. Amini and F. Ayazi, “A high Q in-plane silicon-on-insulator tuning-fork gyroscope,” in Proc. of IEEE Sensors, Vienna, Austria, Oct. 2004.

[67] C. Acar and A.M. Shkel, “Post-release capacitance enhancement in micromachined devices,” in Proc. of IEEE Sensors 2004, pp. 268-271, Vienna, Austria, Oct 2004.

[68] S. Lee, S. Park and D.D. Cho, “The surface/bulk micromachining (SBM) process: a new method for fabricating released microelectromechanical systems in single crystal silicon,” *Journal of Microelectromechanical Systems*, volume 8, ppl 409-416, 1999.

[69] S. Lee, S. Park, J. Kim, S. Yi and D.D. Cho, “Surface/bulk micromachined single-crystalline silicon microgyroscope,” *Journal of Microelectromechanical Systems*, volume 9, pp. 557-567, 2000.

[70] J. Kim, S. Park, D. Kwak, H. Ko and D.D. Cho, “An x-axis single-crystalline silicon microgyroscope fabricated by the extended SBM process,” *Journal of Microelectromechanical Systems*, volume 14, pp. 444-455, 2005.

[71] S.E. Alper, I.E. Ocak and T. Akin, "Ultra-thick and high-aspect-ratio nickel microgyroscope using EFAB^{TM} multi-layer additive electroforming," *Journal of Microelectromechanical Systems,* volume 16, pp. 1025-1035, 2007.

[72] K. Yang, J. Zhou and G. Yan, "The research on MEMS fang-bar fluidic angular rate sensor," in Proc. Of 7th Int. Conf. on Solid-State and Integrated Circuits Technology 2004, pp. 1808-1811, Beijing, China, October 2004.

[73] J. Zhou, G. Yan, Y. Zhu, Z. Xiao and J. Fan, "Design and fabrication of a microfluid angular rate sensor," in 18th IEEE Int. Conf. on Micro Electro Mechanical Systems 2005 (MEMS 2005), pp. 363-366, Miami Beach, FL, USA, January/February 2005.

[74] V.T. Dau, T.X. Dinh, D.V. Dao, O. Tomonori and S. Sugiyama, "Design and fabrication of a convective 3-DOF angular rate sensor," in Proc. of IEEE Sensors 2007, pp. 915-918, Atlanta, Georgia, USA, October 2007.

[75] V.K. Varadan, W.D. Suh, P.B. Xavier, K.A. Jose and V.V. Varadan, "Design and development of a MEMS-IDT gyroscope," *Smart Material Structures,* volume 9, pp. 898-905, 2000.

[76] H. Johari and F. Ayazi, "Silicon-on-insulator bulk acoustic wave disk resonators," in Tech. Dig. IEEE Int. SOI Conference, pp. 153-154, Niagara Falls, NY, USA, October 2006.

[77] H. Johari and F. Ayazi, "Capacitive bulk acoustic wave silicon disk gyroscopes," in Tech. Dig. IEEE Int. Electron Devices Meeting (IEDM 2006), pp. 513-516, San Francisco, CA, USA, December 2006.

[78] S.W. Lee, J.W. Rhim, S.W. Park and S.S. Yang, "A novel micro rate sensor using a surface-acoustic-wave (SAW) delay-line oscillator," in Proc. of IEEE Sensors 2007, pp. 1156-1159, Atlanta, Georgia, USA, October 2007.

[79] A.M. Shkel, "Innovations in design of chip-scale gyroscopes," in MicroMechanics Europe Workshop (MME 2006), pp. 231-233, Southampton, UK, September 2006.

[80] E.J. Eklund and A.M. Shkel, "Glass blowing on a wafer level," *Journal of Microelectromechanical Systems,* volume 16, pp.232-239, 2007.

[81] R.A. Patterson, E.L. Goldner, D.M. rozelle, N.J. Dahlen and T.L. Caylor, "IFOG technology for embended GPD/INS applications," in Proc. of SPIE: Fiber Optic Gyros, volume 2837, pp. 113-123.

[82] M.N. Armenise, C. Ciminelli, F. De Leonardis, R. Diana, V. Passaro and F. Peluso, "Gyroscope technologies for space applications," in 4th Round Table on Micro/Nano Technologies for Space, Noordwijk, Netherlands, May 2003.

[83] B. Miao, “Design, fabrication and characterization of microring resonators used in micro gyroscopes,” Ph.D. thesis, University of Delaware, Newark, Delaware, USA, 2006.

[84] W.J. Bencze, R.W. Brumley, M.L. Eglington and S. Buchman, “Precision electrostatic suspension system for the Gravity Probe B Relativity Mission’s science gyroscopes,” in SICE Annual Conference 2003, pp. 2726-2731, Fukui, Japan, August 2003.

[85] M. Mehregany, S.F. Bart, L.S. Tavrow, J.H. Lang, S.D. Senturia and M.T. Schlecht, “A study of three microfabricated variable-capacitance motors,” *Sensors and Actuators A*, volume 21, pp. 173–179, 1990.

[86] M. Mehregany, S.F. Bart, L.S. Tavrow, J.H. Lang and S.D. Senturia, “Principles in design and microfabrication of variable-capacitance side-drive motors,” *Journal of Vacuum Science and Technology A*, volume 8, pp. 3614–3624, 1990.

[87] W. Wrigley, W.M. Hollister and W.G. Denhard, **Gyroscopic Theory, Design, and Instrumentation**, The M.I.T. Press, Massachusetts, U.S., 1969.

[88] T.J. Hawkey and R.P. Torti, “Integrated microgyroscope,” in Proc. of SPIE, volume 1694, pp. 199–207, 1992.

[89] R. Torti, V. Gondhalekar, H. Tran, B. Selfors, S. Bart and B. Maxwell, “Electrostatically suspended and sensed micro-mechanical rate gyroscope,” in Proc. of SPIE, volume 2220, pp. 27–38, 1994.

[90] D.J. Alladi, M.L. Nagy and S.L. Garverick, “An IC for closed-loop control of a micromotor with an electrostatically levitated rotor,” in Proc. of IEEE Int. Symp. On Circuits and Systems 1999 (ISCAS’99), pp. 489-492, Orlando, FL, USA, May/June 1999.

[91] S.L. Garverick , M.L. Nagy, N.K. Rao, D.K. Hartsfield and A. Purushotham, “A capacitive sensing integrated circuit for detection of micromotor critical angles,” *Journal of Solid-State Circuits*, volume 31, pp. 23–30, 1997.

[92] M.A.N. Eyoum, “Modularly integrated MEMS technology,” Ph.D. Thesis, University of California, Berkeley, 2006.

[93] C. Shearwood, C.B.Williams, P.H. Mellor, R.B. Yates, M.R.J. Gibbs and A.D. Mattingley, “Levitation of a micromachined rotor for application in a rotating gyroscope,” *Electronic Letters*, volume 31, pp.1845–1846, 1995.

[94] C.B. Williams, C. Shearwood, P.H. Mellor, A.D. Mattingley, M.R.J. Gibbs and R.B. Yates, “Initial fabrication of a micro-induction gyroscope,” *Microelectronic Engineering*, volume 30, pp. 531–534, 1996.

[95] C.B. Williams, C. Shearwood, P.H. Mellor and R.B. Yates, “Modelling and testing of a fictionless levitated micromotor,” *Sensors and Actuators A*, volume 61, pp. 469–473, 1997.

[96] C. Shearwood, K.Y. Ho, C.B. Williams and H. Gong, “Development of a levitated micromotor for application as a gyroscope,” *Sensors and Actuators A*, volume 83, pp. 85–92, 2000.

[97] X. Wu, W. Chen, X. Zhao and W. Zhang, “Development of a micromachined rotating gyroscope with electromagnetically levitated rotor,” *Journal of Micromechanics and Microengineerings*, volume 16, pp. 1993–1999, 2006.

[98] K. Fukatsu, T. Murakoshi and M. Esashi, “Electrostatically levitated micro motor for inertia measurement system,” in Tech. Dig. of the 10th Int. Conf. on Solid-state Sensors and Actuators (Transducers’99), pp. 1558–1561, Sendai, Japan, 1999.

[99] S. Karasawa, T. Murakoshi and K. Fukatsu, “Acceleration detection type gyro device,” U.S. Patents 6668648, December 2003.

[100] S. Nakamura, “MEMS inertial sensor toward higher accuracy & multi-axis sensing,” in Proc. of IEEE Sensors 2006 Conference, pp. 939–942, Irvine, CA, USA, October 2006.

[101] W. Frey, Z. Pan and A. Niendorf, “Device and method for electrostatically levitating a disk and method for using an electrostatic levitated disk as a sensor,” U.S. Patents 6856067, February 2005.

[102] M.E. Greene and V.S. Trent, “Motion sensor and method for detecting motion,” U.S. Patents 2006/0090564, May 2006.

[103] M. Kraft, C.P. Lewis, T.G. Hesketh and S. Szymkowiak, “A novel micromachined accelerometer capacitive interface,” *Sensors and Actuators*, volume A68, pp. 466–473, 1998

[104] M.V. Gindila and M. Kraft, “Electronics interface design for an electrically floating micro-disc,” *Journal of Micromechanics and Microengineerings*, volume 13, pp. S11–S16, 2003.

[105] Y. Dong, M. Kraft and W. Redman-White, “Micromachined vibratory gyroscopes controlled by a high order band-pass sigma delta modulator,” *Journal of IEEE Sensors*, volume 7, pp. 50–69, 2007.

[106] R. Houlihan and M. Kraft, “Modelling of an accelerometer based on a levitated proof mass,” *Journal of Micromechanics and Microengineerings,* volume 12, pp. 495–503, 2002.

[107] A. Kukharenka, M.M. Farooqui, L. Grigore, M. Kraft and N. Hollinshead, "Electroplating moulds using dry film thick negative photoresist," *Journal of Micromechanics and Microengineerings*, volume 13, pp. S67–S74, 2003.

[108] A. Kukharenka and M. Kraft, "Realisation of electroplating moulds with thick positive SPR 220-7 photoresist," *Journal of Materials Science: Materials in Electronics*, volume 14, pp. 319–322, 2003.

[109] T.N. Juneau, "Micromachined dual input axis rate gyroscope," PhD dissertation, University of California, Berkeley, California, USA, 1997.

[110] E.A. Avvallone, T. Baumeister, A. Sadegh and L.S. Marks, **Marks' Standard Handbook for Mechanical Engineers**, 11th edition, McGraw-Hill, New York, 2006.

[111] W.S.N. Trimmer and K.J. Gabriel, "Design considerations for a practical electrostatic micromotor," *Sensors and Actuators*, volume 11, pp. 189–206, 1987.

[112] L.S. Fan, Y.C. Tai and R.S. Muller, "IC-processed electrostatic micromotors," in Tech. Digest IEEE Int. Electron Device Meeting (IEDM '88), pp. 666–669, San Francisco, Calif., December 1988.

[113] R.R. Warzynski and R.L. Ringo, "The evolution of ESG technology," in the 15th Meeting of the Guidance and Control Panel of AGARD, pp. 13-1–13-8 Florence, Italy, October 1972.

[114] N. Takeda, "Ball semiconductor technology and its application to MEMS," in the 13th IEEE Int. Conf. on Micro Electro Mechanical Systems (MEMS 2000), pp. 11–16, Miyazaki, Japan, January 2000.

[115] R. Toda, N. Takeda, T. Murakoshi, S. Nakamura and M. Esashi, " Electrostatically levitated spherical 3-axis accelerometer," in the 15th IEEE Int. Conf. on Micro Electro Mechanical Systems (MEMS 2002), pp. 710–713, Los Vagas, NV, USA, January 2002.

[116] M.J. Madou, **Fundamentals of Microfabrication: The Science of Miniaturization**, 2nd edition, CRC press, 2002.

[117] R. Houlihan and M. Kraft, "Modelling squeeze film effects in a MEMS accelerometer with a levitated proof mass," *Journal of Micromechanics and Microengineering*, volume 15, pp. 893–902, 2005.

[118] S.F. Bart, T.A. Lober, R.T. Howe, J.H. Lang and M.T. Schlecht, "Design considerations for micromachined electric actuators," *Sensors and Actuators*, volume 14, pp. 269–292, 1988.

[119] J.J. Blech, “On isothermal squeeze films,” *Journal of Lubrication Technology*, volume 105, pp. 615–620, 1983.

[120] D. Zwillinger, **CRC Standard Mathematical and Formulae**, 30th edition, CRC press, 1996.

[121] D. Ostergaard, “Using a heat transfer analogy to solve for squeeze film damping and stiffness coefficients in MEMS structures,” 2003, Online: http://www.ansys.com/assets/tech-papers/mems-thermal-analogy-fsi-damping.pdf.

[122] G.T. Kovacs, **Micromachined Transducers Sourcebook**, McGraw-Hill, New York, 1998.

[123] R. Houlihan, “ Design and analysis of a levitated proof mass accelerometer ,” PhD thesis, University of Southampton, Southampton, UK, 2005

[124] A. Burstein and W.J. Kaiser, “Mixed analog-digital highly sensitive sensor interface circuit for low cost microsensors,” The 8th Int. Conf. on Solid-State Sensors and Actuators (Transducers’95), pp. 162–165, Stockholm, Sweden, June 1995.

[125] M. Lemkin, “Micro accelerometer design with digital feedback control,” PhD dissertation, University of California (Berkeley), U.S.A, 1997.

[126] S.J. Woo, J.U. Jeon, T. Higuchi and J. Jin, “Electrostatic force analysis of electrostatic levitation system,” Proceeding of the 34th society of instrument and control engineers (SICE) annual conference, pp. 1347–1352, Sapporo, Japan, July 1995.

[127] J. Jin, T. C. Yih, T. Higuchi and J.U. Jeon, “Direct electrostatic levitation and propulsion of silicon wafer,” *IEEE Trans. on Industry Applications*, volume 34, pp. 975–984, 1998.

[128] S.C. Brown, **Introduction to Electrical Discharges in Gases**, Wiley, New York, 1966.

[129] C.H. Chen, J.A. Yeh and P.J. Wang, “Electrical breakdown phenomena for devices with micron separations,” *Journal of Micromechanics and Microengineering*, volume 16, pp. 1366–1373, 2006.

[130] M.P. Omar, M. Mehregany and R.L. Mullen, “Electric and fluid field analysis of side-drive micromotors,” *Journal of Microelectromechanical Systems*, volume 1, pp. 130–140, 1992.

[131] W. Daniau, S. Ballandras, L. Kubat, J. Hardin, G. Martin and S. Basrour, “Fabrication of an electrostatic wobble micromotor using deep-etch UV lithography, nickel

electroforming and a titanium sacrificial layer," *Journal of Micromechanics and Microengineering*, volume 5, pp. 270–275, 1995.

[132] S.M. Huang, A.L. Stott, R.G. Green and M.S. Beck, "Electronic transducers for industrial measurement of low value capacitances," *J. Phys. E: Sci. Instrum.*, volume 21, pp. 242–250, 1998.

[133] W.C. Heerens, "Application of capacitance techniques in sensor design," *J. Phys. E: Sci. Instrum.*, volume 19, pp. 897–906, 1986.

[134] **OrCAD PSpice User's Guide**, Chapter 6, pp.147 – 192, November 1998

[135] OPA2107 datasheet, available at: http://www.ti.com/

[136] W.K. Chen (editor-in-chief), The Circuits and Filters Handbook, 2nd edition, CRC press, Florida, 2003.

[137] R.P. van Kampen, "Bulk-micromachined capacitive servo-accelerometer," PhD dissertation, Delft University, Netherland, 1995.

[138] M. van Paemel, "Interface circuit for capacitive accelerometer," *Sensors and Actuators*, volume 17, pp. 629–637, 1989.

[139] M. Kraft, "Chapter 5 – Case study: control system for capacitive inertial sensors," **Smart MEMS and sensor systems** by E. Gaura and R. Newman, Imperial College Press, UK, 2006.

[140] S. R. Norsworthy, R. Schreier and G. C. Temes, **Delta-sigma data converters: Theory, Design and Simulation**, IEEE Press, 1997.

[141] J. A. Cherry and W. M. Snelgrove, **Continuous-time delta-sigma modulators for high-speed A/D conversion**, Kluwer Academic Publishers, New York, 2002.

[142] I.M. Wilson, "Analog behavioral model using PSPICE," in Proc. of the 32rd Midwest Symp. on Circuit and System 1989, pp. 981–984, Champaign, IL, USA, August 1989.

[143] C.P. Lewis and M. Kraft, "Simulation of a micromachined digital accelerometer in SIMULINK and PSPICE," in UKACC Int. Conf. on Control, pp. 205–209, Exeter, UK, 1996.

[144] ADG441 quad SPST switch datasheet, available at: http://www.analog.com/

[145] Y. Dong, M. Kraft and C.O. Gollasch, "A high performance accelerometer with fifth order sigma delta modulator," *Journal of Micromechanics and Microengineerings*, volume 15, pp. S22–S29, 2005.

[146] T. Arakawa, Y. Sato, T. Ueno, T. Funatsu and S. Shoji, “Pinhole-free Pyrex glass etching using HF-H_2SO_4 mixed acid and its applications for a PDMS microflow system,” in 13th Int. Conf. on Solid-State Sensors, Actuators and Microsystems (Transducers’05), pp. 1489 – 1492, Seoul, Korea, June 2005.

[147] J.K. Bhardwaj and H. Ashraf, “Advanced silicon etching using high density plasmas,” in Proc. of SPIE Micromachining and Microfabrication Process Technology, volume 2639, pp. 224 – 233, 1995.

[148] J.K. Bhardwaj, H. Ashraf and A. McQuarrie, “Dry silicon etching for MEMS,” in the Symp. On Microstructures and Microfabricated Systems, pp. 1–13, Montreal, Quebec, Canada, May 1997.

[149] J. Hopkins, H. Ashraf, J.K. Bhardwaj, A.M. Hynes, I. Johnston and J.N. Shepherd, “The benefits of process parameter ramping during the plasma etching of high aspect ratio silicon structure,” in Proc. of the Materials Research Fall Meeting, pp. 1–7, Boston, Massachusetts, USA, December 1998.

[150] W.C. Tang, M.G. Lim and R.T. Howe, “Electrostatic comb drive levitation and control method,” *Journal of Microelectromechanical Systems*, volume 1, pp. 170–178, 1992.

[151] A.P. Lee, C.F. McConaghy, P.A. Krulevitch, E.W. Campbell, G.E. Sommagren and J.C. Trevino, “Electrostatic comb drive for vertical actuation,” in Proc. of SPIE Micromachined Devices and Components III, pp. 109-119, Austin, Texas, September 1997.

[152] S.J. Timpe, D.A. Hook, M.T. Dugger and K. Komvopoulos, “Levitation compensation method for dynamic electrostatic comb-drive actuators,” *Sensors and Actuators A*, volume 143, pp. 383–389, 2008.

[153] J.J. D’Azzo, C.H. Houpis and S.N. Sheldon, **Linear Control System Analysis and Design with Matlab**, 5th edition, CRC Press, 2003.

[154] E. Willemenot and P. Touboul “On-ground investigation of space accelerometers noise with an electrostatic torsion pendulum,” *Review of Scientific Instruments*, volume 71, pp. 302–309, 2000.

[155] E. Willemenot and P. Touboul “Electrostatically suspended torsion pendulum,” *Review of Scientific Instruments*, volume 71, pp. 310–314, 2000.

[156] G. Humpston, “Flip-chip solder bonding for microsystems,” in IEE Colloquium on Assembly and Connections in Microsystems, pp. 3/1–3/3, February 1997.

[157] C.C. Hu, S.Y. Wen, C.P. Hsu, C.W. Chang, C.T. Shih and H.W. Lee, “Solder bonding with a buffer layer for MOEMS packaging using induction heating,” Microsystem Technologies, volume 12, pp. 1011–1014, 2006.

[158] D.J. Yao, G. Chen and C.J. Kim, “Low temperature eutectic bonding for in-plane type micro thermoelectric cooler,” in Proc. of ASME Int. Mechanical Engineering Congress and Exposition, pp.1–4, New York, NY, USA, 2001.

[159] L. Lin, Y.T. Cheng and K. Najafi, “Formation of silicon-gold eutectic bond using localized heating method,” *Jpn. J. Appl. Phys.*, volume 37, pp. L1412–L1414, 1998.

[160] C.H. Tsau, S.M. Spearing and M.A. Schmidt, “Fabrication of wafer-level thermocompression bonds,” *Journal of Microelectromechanical Systems*, volume 11, pp. 641–647, 2002.

[161] M.M.V. Taklo, P. Storas, K. Schjolberg-Henriksen, H.K. Hasting and H. Jakobsen, “Strong, high-yield and low-temperature thermocompression silicon wafer-level bonding with gold,” *Journal of Micromechanics and Microengineering*, volume 14, pp. 884–890, 2004.

[162] P. Monajemi, P.J. Joseph, P.A. Kohl and F. Ayazi, “A low cost wafer-level MEMS packaging technology,” in Proc. of IEEE MicroElectroMechanical Systems 2005, pp. 634–637, Miami, FL, USA, February 2005.

[163] P. Monajemi, P. Joseph, P. A. Kohl and F. Ayazi, “Wafer-level packaging of MEMS via thermally released metal-organic membranes,” *Journal of Micromechanics and Microengineering*, volume 16, pp. 742–750, 2006.